UNIVERSITY OF COPENHAGEN

PHD THESIS

Partonic collectivity in large and small systems at the LHC

Author:
Zuzana MORAVCOVÁ

Supervisor:
assoc. prof. You ZHOU

High Energy Heavy-Ion Group
Niels Bohr Institute

UNIVERSITY OF COPENHAGEN

This PhD thesis has been submitted to the PhD School of the Faculty of Science, University of Copenhagen on October 30, 2022.

Abstract

Under extreme conditions, such as high temperature and density, quarks and gluons can be deconfined. The deconfined matter, quark-gluon plasma (QGP), that existed within the first microsecond after the Big Bang, can be recreated in ultra-relativistic heavy-ion collisions at particle accelerators. One way to investigate the initial conditions and the dynamic evolution of such a collectively expanding medium is by studying the anisotropic flow, quantified by flow coefficients v_n. Experimental measurements of the QGP from various flow observables show remarkable agreement with the hydrodynamic calculations, suggesting the QGP behaves like a nearly ideal fluid.

The collective behaviour associated with the presence of QGP is also observed in small collision systems at very high multiplicities with significantly more produced particles than in an average small system collision. Based on the existing studies, it is known that the anisotropic flow in small systems is mainly driven by the initial geometry of the system. However, the development of flow from the initial geometry through the dynamic evolution is still under discussion.

In this thesis, the anisotropic flow is studied using different observables and across different collision systems. A new generic algorithm is developed to formulate multi-particle cumulants of arbitrary order in Pb–Pb collisions at $\sqrt{s_{\rm NN}} = 5.02$ TeV. The measurements of multi-particle cumulants of single and mixed harmonics are reported. Mixed harmonic cumulants $MHC(v_m^k, v_n^l)$ have a unique sensitivity to the initial conditions. Thus, the results are compared to the calculations from hydrodynamical models in order to constrain initial conditions and transport properties of the QGP. The flow coefficients $v_2(p_{\rm T})$ are calculated using the two- and four-particle cumulants method. With these observables, it is possible to study the first two moments of the probability density function of elliptic flow, the mean $\langle v_2 \rangle$ and variance σ_{v_2}, and the relative flow fluctuations of identified particles for the first time in heavy-ion collisions. Moreover, the elliptic flow $v_2(p_{\rm T})$ with various identified particle species is studied in Pb–Pb collisions to further probe the initial conditions and properties of QGP, in particular, the particle production mechanisms, e.g., quark coalescence.

The flow measurements of identified particles in heavy-ion collisions bring a unique insight into initial conditions and the properties of QGP. Therefore, such a study in small collision systems can contribute to understanding the role of initial conditions and the state of the recreated matter. However, the study of flow coefficients in small systems is more challenging due to significant non-flow contamination. The measurement is performed in p–Pb and pp collisions at $\sqrt{s_{\rm NN}} = 5.02$ and 13 TeV, respectively. Thanks to the unique pseudorapidity coverage of ALICE, the flow coefficients with sufficient non-flow suppression are obtained using ultra-long-range two-particle correlations and the template fit method. Many similarities are observed in flow in large and small systems.

The measured $v_2(p_T)$ coefficients exhibit mass ordering in the low transverse momentum region. Such a phenomenon originates from the radial expansion of the system. The baryon-meson grouping at the intermediate transverse momentum, which in Pb–Pb is typically associated with partonic collectivity and quark coalescence, is also reported in p–Pb and pp collisions. These observations are discussed in the context of models with and without the contribution of quark coalescence. The similarities between large and small systems show strong evidence that a droplet of QGP is created in small collision systems at high multiplicities.

Dansk resumé

Under ekstreme forhold, såsom høj temperatur og densitet, vil kvarker og gluoner være frie og ubundne. Dette ubundne stof, kvark-gluon plasma (QGP), som eksisterede inden for det første mikrosekund efter Big Bang, kan blive genskabt ved ultrarelativistiske tung-ions kollisioner i partikelacceleratorer. En metode hvormed man kan undersøge begyndelsestilstandene og den dynamiske udvikling af det kollektivt udvidende medium, er det anistropiske flow, som er kvantificeret ved flow koefficienterne v_n. Eksperimentelle målinger af QGP fra forskellige flow observable viser en bemærkelsesværdig god overensstemmelse med hydrodynamiske beregninger, hvilket antyder at QGP opfører sig som en ideel væske.

Den kollektive opførsel forbundet med tilstedeværelsen af QGP er også set i små kollisionssystemer ved meget høj multiplicitet med betydeligt flere producerede partikler end i et gennemsnitligt småt kollisionssystem. Baseret på eksisterende studier er det vidst, at det anisotropiske flow i små systemer primært er drevet af geometrien af systemet i begyndelsen af kollisionen. Dog er udviklingen af flow fra den indledningsvise geometri og igennem den dynamiske udvikling stadig til diskussion.

I denne afhandling, studeres det anisotropiske flow med forskellige observable og i forskellige kollisionssystemer. En ny generisk algoritme udvikles til at formulere multipartikelkumulanter af vilkårlig orden i Pb–Pb kollisioner ved $\sqrt{s_{\mathrm{NN}}} = 5.02$ TeV. Målingerne af multi-partikelkumulanter af enkelte og blandede harmoniske flow koefficienter rapporteres. Kumulanter af blandede harmoniske koefficienter $MHC(v_m^k, v_n^l)$ har en unik følsomhed over for begyndelsestilstandene. Derfor bliver resultaterne sammenlignet med beregninger fra hydrodynamiske modeller for at afgrænse begyndelsestilstandene og QGP's transport egenskaberne. Flow koefficienterne $v_2(p_{\mathrm{T}})$ beregnes med to- og firpartikel kumulantmetoden. Med disse observable er det muligt at studere de første to momenter af sandsynlighedstæthedsfunktionen af det elliptiske flow, middelværdien $\langle v_2 \rangle$ og variansen σ_{v_2}, og den relative flowfluktuation af identificerede partikler for første gang i tung-ions kollisioner. Ydermere, undersøges det elliptiske flow $v_2(p_{\mathrm{T}})$ med forskellige identificerede partikelarter studeres i Pb–Pb kollisioner for yderligt at undersøge begyndelsestilstandene og QGP's egenskaber, især partikelproduktionsmekanismerne, f.eks. kvark-sammensmeltning.

Flow målingerne af identificerede partikler i tung-ions kollisioner giver unik indsigt i begyndelsestilstandene og QGP's egenskaber. Derfor kan sådan et studie af små kollisionssystemer bidrage til forståelsen af begyndelsestilstandenes rolle og det genskabte stofs tilstand. Dog er undersøgelsen af flow koefficienter i små systemer mere udfordrende på grund af betydeligt non-flow. Målingerne udføres for p–Pb og pp kollisioner ved henholdsvis $\sqrt{s_{\mathrm{NN}}} = 5.02$ og 13 TeV. Takket være ALICE's unikke pseudorapiditetsdækning, kan flow koefficienterne opnås med tilstrækkelig undertrykkelse

af non-flow ved hjælp af ultra-lang-distance to-partikel korrelationer og template fit metoden. Mange ligheder observeres mellem flow i store og små systemer. Det målte $v_2(p_{\mathrm{T}})$ udviser et massehierarki ved lavt transverst momentum. Dette fænomen har oprindelse i den radiale udvidelse af systemet. Baroyn-meson gruppering ved mellemliggende transverst momentum, som i Pb–Pb tilskrives partonisk kollektivitet og kvarksammensmeltning, er også observeret i p–Pb og pp kollisioner. Lighederne mellem store og små systemer er stærkt bevis for at en dråbe af QGP er skabt i små kollisionssystemer med høj multiplicitet.

Acknowledgements

First, I would like to thank my supervisor, You, for his supervision and fruitful physics discussions, sometimes at unexpected times or places. I do not think I would be able to obtain so many results without your guidance and curiosity. Good luck with your future endeavours!

A big thanks to all the first-floor members of the HEHI group — Jens Jørgen for keeping the group in touch even when the whole world was in lockdown, Børge for all my detector questions, Ian for always being supportive and willing to listen, Christian Holm for all my statistics and FMD questions (I'm still impressed by the overnight secondary contamination code!), and Kris for my math and correlations questions.

I would like to thank my "other half" (of ALICE PhD students in Denmark) and my favourite office mate, Emil, for all the coffee breaks, friendly chats, and for listening to all my complaints. Good luck with the rest of your PhD! Additionally, I would like to thank all the master's students from the past I worked with for contributing to the friendly atmosphere in the offices. Especially to Mathias, my friend and first official student.

My beginning in the institute would be much harder without the guidance and help I got from Vojta. Thanks for everything! Furthermore, thanks to you, Freja, for helping me navigate around in the early days.

Furthermore, the beginning of my PhD would be much harder without the solid ground I was able to build on. So – thank you, Jaro, Lukas, and the rest of team STAR in Prague, for all the wisdom and skills I moved to Denmark with.

I would like to extend my thank to my ALICE colleagues from different groups. The biggest one goes to Lucia, who was of incredible help in recent months when she basically took over my analysis and gave me some time to write this thesis. Without you, the paper proposal and/or the thesis would not happen. Next, to Laura, for great discussions and questions. We (and I personally) had a great time with you around. To Katarína, ARC of all my analyses, for all the great comments and ability to discuss physics in our first language, but also for words of encouragement. To Ya, for a fruitful work at the analysis and a nice time in Copenhagen. To Panos, for your great contribution in the flow and flow fluctuations paper. To Siyu, for being very helpful when I was switching analysis techniques. And finally, to Yuko, for her enormous help with all the FMD-related things.

Being in the ALICE collaboration was not just about the work, and while I didn't travel as much as I thought I would (thanks again, Covid!), I was happy to meet again and/or get to know many amazing people and physicists. So thanks for keeping me sane and keeping the conferences and ALICE weeks more fun! So thanks – Dianka, Tomáš, Jana, Basti, Jerome, Tea, Adrian, Jakub, Simone, Fernando, Hannah, ... and many more!

I would like to express my deepest gratitude to Vytautas. You helped me with so many things, both work-related and not, it is hard to count them. Thank you for your support and patience, for all the rides and trips, for helping me to live outside the work, and, mostly, for always being by and on my side.

Life is, fortunately, not just about work. For that reason, I would like to thank my friends in the Copenhagen area, Joachim, Katinka, Étienne, Ari, Oliver, Emilie, Lais, Meera, Veronika, Joanna, Balász, István, Kelly, and many more. Thanks for making me forget about the work and stress and for all the fun we had. Thanks to my friends outside Scandinavia, mostly to Dianka for always being just one call away, and to Alča, Filip, Christian, Bea, Zuzka, Klárka, and more.

Finally, I would like to thank my family, most notably my mum and dad and my siblings. Thanks for always being there for me. Additionally, I would like to thank my little sister Katka for the fantastic front-page illustration. Thanks for making my idea alive.

Preface

The following section serves as an overview of my work throughout my PhD. The description of my contribution to the publications, listed on page xiii, is also provided.

Disclaimer: No explanation of different terms used in this overview is provided, as it can be found across the thesis. It is assumed that the reader is familiar with the topic or has already read the thesis and wants to evaluate the author's work over the course of her PhD.

I joined the high-energy heavy-ion physics group at the Niels Bohr Institute (NBI), University of Copenhagen, on the first of August 2019. In parallel, I became a member of the ALICE Collaboration.

At the very beginning, after getting familiar with the ALICE framework, I started reconstructing the published results of two- and multi-particle cumulants in heavy-ion collisions. This exercise was to get to understand the methods and the analysis environment. A great help was the finishing PhD student V. Pacík from whom I inherited the UniFlow framework.

Once I became more familiar with the framework, I started extending it by implementing the online and offline code for Mixed Harmonic Cumulants (MHC) calculation. I created an independent set of results that contributed to the systematic evaluation of the final MHC, published with ALICE. The paper proposal within the ALICE Collaboration, chaired by Y. Zhou, followed shortly after. Once the paper was approved, we started the writing process I contributed to. The paper was published in Physics Letters B in 2021.

In parallel to the experimental paper, we started working on the theoretical paper on the generic algorithm for multi-particle cumulants. However, I did not directly contribute to the development of the algorithm itself. I implemented the Toy Monte Carlo simulation that tested the algorithm. During that time, I also worked on optimization of the algorithm and the whole calculation as it was very CPU demanding. I significantly improved the speed of the calculation, much needed for calculating high orders of multi-particle correlations in many different events. In addition, I calculated high orders of single particle cumulants and different mixed harmonic cumulants from the data simulated with the HIJING event generator. The analysis framework had to be modified as the on-the-fly type of simulation was used instead of an already existing simulated production.

At the end of 2019, in parallel to the two aforementioned activities, I took over the analysis of flow and flow fluctuations of identified particles from V. Pacík, who was about to leave the collaboration. Together with Y. Zhu, we proceeded with the analysis and aimed for the paper proposal. The paper includes the flow measurements of inclusive charged particles and many different identified species, $\pi^{\pm}$, $\mathrm{K}^{\pm}$, $\mathrm{p}(\bar{\mathrm{p}})$, $\mathrm{K}^0_{\mathrm{S}}$, $\Lambda(\bar{\Lambda})$, ϕ, $\Xi(\bar{\Xi})$, and $\Omega(\bar{\Omega})$. As multi-strange particles $\Xi(\bar{\Xi})$and $\Omega(\bar{\Omega})$were done entirely by Y. Zhu as a part of this PhD project, it is not discussed in the thesis. However, with the remaining particle species, I worked on the analysis and evaluation of statistical and systematic uncertainties. A considerable progress in the analysis with respect to the ALICE preliminary results approved by V. Pacík has been made by me. Once the results for the paper received the final approval from the collaboration, the paper committee started the writing process with me serving as the chair. We successfully finished the paper in the spring of 2022, with the paper now being accepted by the Journal of High Energy Physics.

While improving the results of the flow of identified particles and calculating the flow fluctuations, I noticed a potential issue in the flow coefficients of identified particles. The solution, figured out together with V. Vislavičius, provides a correction of the generic framework. The particle weights are used for compensating the non-uniform detector acceptance. In the measurement of the flow of identified particles, the Q-vector of the reference flow has to contain the weights of identified particles already. Otherwise, the self-correlations of particles are not properly removed.

Alongside studying flow in large collision systems, in this case in Pb–Pb collisions, I also started looking into small systems. It is mentioned in several places in this thesis that the study of these systems is highly non-trivial due to the significant non-flow contribution that needs to be suppressed before the flow measurement. I started by reproducing results from V. Pacík with two-particle cumulants and suppression of non-flow by subtracting low multiplicity collisions. The scaling he used was only using p_{T}-integrated mean multiplicities. First, I tried applying a p_{T}-dependent subtraction, as the non-flow contribution increases with p_{T}. However, this approach did not provide the results we hoped for. Inspired by the measurement of p_{T}-integrated higher-order cumulants, I developed and implemented p_{T}-differential four-particle cumulants with three sub-event method for identified particles. I used this method to obtain flow coefficients $v_n\{4\}_{3-\mathrm{sub}}$ across all collision systems of different sizes (pp, p–Pb, Pb–Pb) in the same multiplicity region. Together with the measurements of two-particle cumulants with subtraction, also obtained in all three systems and the same multiplicity region, I prepared the results for a collaboration approval. However, as the behaviour of $v_n\{4\}_{3-\mathrm{sub}}$ as a function of p_{T} was not understood well enough, I did not proceed with such an analysis. Now it is believed an additional suppression with jet contribution removal is needed. Both $v_n\{4\}_{3-\mathrm{sub}}$ and jet veto are implemented in my codes. The efforts will continue by future PhD students.

Instead, I started to study the flow of identified particles in small systems using a new framework I developed, where di-hadron correlations are used instead of cumulants. I first used central barrel detectors to reconstruct published results of the flow of identified particles using the peripheral subtraction method. With the help of Y. Sekiguchi, and, later on, S. Tang, I added the Forward Multiplicity Detector in order to calculate the correlations over the wide pseudorapidity range. I added the template fit method, and subsequently also the improved template fit method, to the collection of the post-processing methods I was using. With these two methods, I was able to obtain the flow of identified particles in pp and p–Pb collisions for $\pi^{\pm}$, $K^{\pm}$, $p(\bar{p})$, K^0_S, and $\Lambda(\bar{\Lambda})$. I fully finished the results, including evaluating systematic uncertainties and different corrections and prepared them for the collaboration approvals. My results were approved in spring 2022, and I presented them as ALICE preliminaries at the Quark Matter 2022. Shortly after this conference, I was joined by L. A. Tarasovičová, who helped me further improve the results and finalize them for the collaboration paper proposal that took place at the very end of my PhD in October 2022. The paper, currently chaired by me, aims for a high-profile journal, as it brings a new understanding of the collectivity in small systems, clearly showing the partonic collectivity in both pp and p–Pb collisions.

In addition to the aforementioned activities, I contributed to two publications with proposals for future LHC runs. My projection figures are shown in the outlook chapter.

While the thesis summarizes my scientific activities, outside my main project, flow of identified particles in large and small collision systems, I spent the time of my PhD with several different work-related activities. They mainly included teaching at the University of Copenhagen, the collaboration service task, participation at the data collection with the ALICE experiment, and serving as a junior representative of the ALICE collaboration. Additionally, I attended a few international conferences and workshops/schools. However, due to the covid-related travel restrictions, the majority of them took place only online.

I started my teaching duties in block 3 (the first half of the summer semester) of the academic year 2019/2020. I was a teaching assistant in the course Radioactive Isotopes and Ionizing Radiation, taught by prof. J. J. Gaardhøje. I was teaching calculations of different exercises related to the course, and I served as a lab assistant, which also included reviewing the lab reports of our students. I repeated the course as a teaching assistant also in the academic year 2020/2021, when the lab exercises took place in person in smaller groups and with strict corona restrictions. However, the classroom calculation exercises were entirely online. My final teaching assistant duty was in block 2 of the academic year 2020/2021 in the course of Applied Statistics, taught by prof. T. C. Petersen. At the same time, I was also attending the course, as it helped me deepen my understanding of statistics and improved my programming in python.

In spring 2020, I was supposed to spend three months at CERN to work with M. Puccio on my collaboration service task. The time was also supposed to be the change of environment, mandatory for all the PhD students enrolled at the University of Copenhagen. However, it was not possible due to the global pandemic, CERN closure, ban on travel, and home office order in Denmark and most of the world. In consequence, the project was then done fully remotely. I was working on the development of an offline ALICE high multiplicity trigger for LHC Run 3 using ITS. For this project, I had to switch from the framework I was using before (AliPhysics) to the new framework developed for LHC Run 3 (O^2). Using the simulation I created, I studied the resolution and efficiency of such a trigger.

Finally, between April 2020 and April 2022, I served as an elected junior representative of the ALICE Collaboration. Connected to this function, I was a member of the ALICE Management Board and a voting member of the ALICE Collaboration Board. Together with my two colleagues (considering the rotation, my colleagues included F. A. Flor, T. Herman, H. Bossi, and C. A. Reetz), we served as a connection between juniors and the management and addressed relevant questions or issues. As my most significant achievement, I consider a contribution to the kick-start of the ALICE Mental well-being campaign.

List of Publications

1. **Observation of partonic flow in proton–proton and proton–nucleus collisions**
   ALICE Collaboration [PC: Z. Moravcová (chair), L. A. Tarasovičová, Y. Zhou, C. Cheshkov]
   in preparation, to be submitted to Nature Physics

2. **Anisotropic flow and flow fluctuations of identified hadrons in Pb–Pb collisions at $\sqrt{s_{\mathrm{NN}}} = 5.02$ TeV**
   ALICE Collaboration [PC: Z. Moravcová (chair), Y. Zhu, Y. Zhou, V. Pacík, P. Christakoglou, A. Dobrin]
   accepted by JHEP, arXiv:2206.04587 [nucl-ex]

3. **Measurements of mixed harmonic cumulants in Pb–Pb collisions at** $\sqrt{s_{\mathrm{NN}}} = 5.02$ TeV
   ALICE Collaboration [PC: Y. Zhou (chair), Z. Moravcová, K. Gulbrandsen]
   Phys. Lett. B 818 (2021) 136354, arXiv:2102.12180 [nucl-ex]

4. **Generic algorithm for multiparticle cumulants of azimuthal correlations in high energy nucleus collisions**
   Z. Moravcová, K. Gulbrandsen, Y. Zhou
   Phys. Rev. C 103, 024913 (2021), arXiv: 2005.07974 [nucl-th]

List of Contributions

1. **Flow of identified hadrons in p–Pb and pp collisions with ALICE**
   Invited online plenary talk on behalf of the ALICE Collaboration at the International workshop on Multiple Partonic Interactions at the LHC
   November 2022, Madrid, Spain

2. **Probing partonic collectivity in large and small collision systems with strange hadrons in ALICE**
   Parallel talk on behalf of the ALICE Collaboration at the International Conference on Hypernuclear and Strange Particle Physics
   June 2022, Prague, Czech Republic

3. **Observation of partonic flow in small collision systems with ALICE at the LHC**
   Parallel talk on behalf of the ALICE Collaboration at the Quark Matter International Conference on Ultra-relativistic Nucleus-Nucleus Collisions
   April 2022, Kraków, Poland

4. **Anisotropic flow in small collision systems**
   Parallel talk at the Dansk Fysisk Selskab Årsmøde
   June 2021, Middelfart, Denmark

5. **Constraining transport properties of quark-gluon plasma using non-linear hydrodynamic response**
   Online parallel talk at the European Physical Society Conference on High Energy Physics
   May 2021, DESY, Hamburg, Germany

6. **Flow fluctuations in heavy-ion collisions measured with ALICE**
   Online parallel talk on behalf of the ALICE Collaboration at the International conference on Critical Point and Onset of Deconfinement
   March 2021, Online

7. **Investigation of anisotropic flow in large and small collision systems with ALICE**
   Online parallel talk on behalf of the ALICE Collaboration at the Zimányi School Winter Workshop on Heavy Ion Physics
   December 2020, Budapest, Hungary

8. **Generic algorithm for multi-particle cumulants of azimuthal correlations in high energy nucleus collisions**
   Online parallel talk at the International Conference on New Frontiers in Physics
   September 2020, Kolymbari, Crete, Greece

9. **Collectivity (not only) in heavy-ion collisions**
   Parallel talk at the Epiphany Conference
   January 2020, Bratislava, Slovakia

Contents

It is the time you have wasted for your rose
that makes your rose so important.

– *ANTOINE DE SAINT-EXUPÉRY*

Introduction and overview

In normal conditions, quarks and gluons are confined in protons and neutrons. However, at extreme temperature or density, nucleons become deconfined, creating a nuclear matter called the quark-gluon plasma (QGP). This state of matter existed within the first microsecond after the Big Bang and exists in the cores of neutron stars. It can be recreated in ultra-relativistic collisions of heavy ions at particle accelerators, for example, with ions of lead ^{208} at the LHC.

The lifetime of the QGP is very short, ≈ 10 fm$/c$, hence the medium cannot be studied directly. One of the ways how to probe the initial conditions of the system and the dynamic evolution of the collectively expanding medium is by studying the anisotropic flow, quantified by flow coefficients v_n. The evolution of QGP can be described by hydrodynamics, which allows for extraction of the the shear viscosity to entropy density η/s of the medium. The very low viscosity of QGP suggests it behaves as a nearly ideal fluid. The initial conditions and the transport properties of QGP created in Pb–Pb collisions at $\sqrt{s_{\mathrm{NN}}} = 5.02$ TeV are studied using anisotropic flow coefficients and correlations between different moments of different flow harmonics using mixed harmonic cumulants, which are studied as a function of event centrality. Moreover, the measurement is compared to a hydrodynamic model with different initial conditions and transport properties in order to constrain the properties of the QGP.

Small collision systems, such pp at the LHC, used to be considered as a baseline in the measurements of heavy-ion collisions. This understanding was challenged by the collective behaviour of the medium observed in small systems at high multiplicities, as such behaviour is associated with the creation of QGP in large systems. Nowadays, several similarities are observed between large and small collision systems, including the anisotropic flow measurements. The initial geometry of the colliding system contributes to the creation of flow. However, the possible physics mechanisms that contribute to the development of flow in small systems through the dynamic evolution of the medium are still under debate.

The measurements of anisotropic flow coefficients $v_n(p_{\mathrm{T}})$ of various identified particle species are performed in both large and small collision systems with ALICE at the LHC. The study in Pb–Pb collisions at $\sqrt{s_{\mathrm{NN}}} = 5.02$ TeV is motivated by studying the initial conditions and transport properties of QGP and by probing particle production mechanisms, such as the quark coalescence. The observations of two phenomena in the flow of identified particles, mass ordering and baryon-meson grouping, contributed to the discovery of QGP in large collision systems. Thus, the measurements of flow coefficients $v_n(p_T)$ of identified particles in p–Pb collisions at $\sqrt{s_{NN}} = 5.02$ TeV and pp collisions at $\sqrt{s} = 13$ TeV is performed in order to study the development of flow from the initial geometry through the dynamic evolution of the system. Both mass ordering and baryon-meson grouping phenomena are observed in p–Pb and pp collisions. The presented measurement is the first observation of baryon-meson splitting in pp collisions. Thanks to the striking similarities across all studied systems described in detail, the evidence of partonic collectivity in p–Pb and pp collisions is discussed, which proves the creation of a droplet of QGP in small collision systems at high multiplicities.

The first chapter of this thesis is dedicated to the theoretical introduction and presents the theoretical background needed for describing the obtained results. It starts with a brief introduction to the Standard model of particle physics, the theory of elementary particles and the fundamental interactions between them. It focuses on quantum chromodynamics (QCD) that describes the interaction between quarks and gluons. Using the QCD phase diagram, the quark-gluon plasma is introduced. The QGP can be recreated in ultra-relativistic heavy-ion collision. Such collisions are used for probing the created medium, thus, the evolution of a heavy-ion collision is described. Moreover, several experimental observables to probe QGP in heavy-ion collisions are discussed, including the anisotropic flow and the measurements of different observables. The chapter is ended with the studies of small collision systems at high multiplicities that show signs of collectivity. Various measurements of flow coefficients in such systems are discussed.

The second chapter introduces the experimental framework needed to collect the data for measuring the presented results. The Large Hadron Collider (LHC) and the entire CERN accelerator complex are introduced. The chapter later focuses on the general-purpose heavy-ion experiment at the LHC, the ALICE experiment. The sub-detectors of ALICE used for reconstructing the data discussed in the analysis chapter of this thesis are introduced. A short overview of the ALICE upgrade for the current data collection is also provided.

The third chapter introduces various methods used to calculate flow coefficients from the experimental data. It introduces the calculation of multi-particle correlations using the generic framework and, subsequently, the calculation of flow coefficients from multi-particle cumulants, i.e., genuine multi-particle correlations, out of multi-particle correlations. Using flow coefficients from two- and four-particle cumulants, it is possible to approximate the variance and mean of the probability density function of the flow. Furthermore, the calculation of relative flow fluctuations is introduced. Besides the method using multi-particle cumulants, di-hadron correlations are introduced from which the flow coefficient can also be extracted. The chapter ends with an overview of non-flow suppression methods, crucial for studying flow in small collision systems, including pseudorapidity separation between different sub-events and explicit and implicit subtraction of low multiplicity collisions, i.e., peripheral subtraction and template fit methods.

The methods introduced in the third chapter are independent of the experiment or the analysis framework. The fourth chapter introduces the analysis procedure needed for implementing the aforementioned methods. First, the analysis frameworks used for obtaining the results are briefly discussed, and the data samples used in the analysis are introduced. Second, the selection criteria used in the analysis are discussed in detail, including the event selection, track selection, and particle identification of different types of particles – primary identified particles $\pi^{\pm}$, $K^{\pm}$, and $p(\bar{p})$, and reconstructed particles K^0_S, $\Lambda(\bar{\Lambda})$, and ϕ. The chapter discusses various corrections used in the analysis, including the non-uniform detector acceptance correction and corrections of the reconstruction efficiency and secondary contamination. Furthermore, the in-depth Monte Carlo closure test is presented for different pseudorapidity regions. Finally, the evaluation of statistical and systematic uncertainties is presented and illustrated with examples. The systematic variations are discussed as well.

The fifth chapter contains the most important part of the thesis – the summary of results obtained during the course of the PhD. It first introduces a discussion on the novel implementation of the calculation of multi-particle correlations. Subsequently, it presents tests of the new generic algorithm for calculating an arbitrary number of multi-particle cumulants with both single and mixed harmonics. Flow coefficients are presented from up to twelve-particle cumulants. In addition, multi-particle cumulants are compared to a model that contains non-flow only to test the non-flow suppression. Mixed harmonic cumulants are discussed in detail for various combinations of different moments of different flow harmonics. A comparison with hydrodynamic models with different initial conditions is presented, which can help constrain the initial conditions and the transport properties of the flow coefficients, as it is not possible with single flow harmonics only. The result chapter continues with the flow of identified particles in Pb–Pb collisions where $v_2\{2\}$ and $v_2\{4\}$ are shown, including the scaling with the number of constituent quarks. The approximate first two moments of the v_2 probability functions and relative flow fluctuations are also discussed. A comparison with hydro-inspired models follows. First, a hydrodynamic model with two sets of initial conditions is used. However, such a model cannot describe the entire studied transverse momentum region. For that reason, a hybrid model that combines hydrodynamics, quarks coalescence, and jet fragmentation mechanisms is used. A comparison of all studied variables is discussed with such a model. Finally, the flow of identified particles is discussed in small collision systems. As non-flow contamination dominates such systems, the calculation is more challenging. For that reason, flow coefficients from different methods are reported. The chapter ends with the results of flow coefficients of identified particles from ultra-long-range correlations and template fit method. The observations in the data and the scaling with the number of constituent quarks show the same behaviour as in large collision systems. Furthermore, a comparison to various models is discussed in order to study the contribution of quark coalescence mechanisms in small collision systems.

Finally, the thesis ends with a short conclusion of the main observations and possible outlook, including the projection study for future LHC runs.

1 Theoretical background

In ancient Greece, alongside the concept of matter being created by the four elements, water, earth, fire, and air, a philosophical concept of matter from indivisible atoms was created. Atomic theory was reintroduced by J. Dalton in 1808. In 1897, J. J. Thomson showed the existence of negative electrons inside an atom. His work was followed by a series of experiments by E. Rutherford, H. Geiger, and E. Marsden, clearly showing a positive nucleus in the centre of the atom. Finally, N. Bohr added quantum theory into the picture by formulating the planetary model of an atom [1–3].

It took almost 20 years to discover that the nucleus is made not only of positive protons but also of neutral neutrons discovered by J. Chadwick in 1932. Another 20 years later, many short-lived particles were discovered with the first high-energy experiments. At that point, it started to be clear that a classification system was needed, and not all the observed particles were elementary. M. Gell-Mann named their constituents *quarks* [4]. At the time, quarks were a purely mathematical concept that followed the SU(3) group symmetry and helped classify all the particles observed in experiments. Nevertheless, in the 1970s, quarks were observed at the Stanford Linear Accelerator Center [5] in deep inelastic scattering experiments, yet always confined in hadrons. In 1979, the theory of strong interactions, quantum chromodynamics, , was confirmed by the discovery of gluons in three-jet events thanks to gluon bremsstrahlung [6], which explained why quarks are always confined in hadrons.

The following chapter presents the Standard model of particle physics with a focus on the strong interaction between quarks and gluons, and presents the conditions under which it is possible to deconfine the nuclear matter and create the quark-gluon plasma. A description of its evolution and experimental studies is provided, emphasising the study of collectivity and azimuthal anisotropy.

1.1 Standard model of particle physics

The Standard model of particle physics describes all the elementary particles and the fundamental forces between them. All the particles considered as elementary are point-like and in an unexcited state. They are grouped into two types of particles based on their spin – fermions and bosons have half-integer and integer spin, respectively. Spin, or spin angular momentum, is an internal property of a particle not connected to its

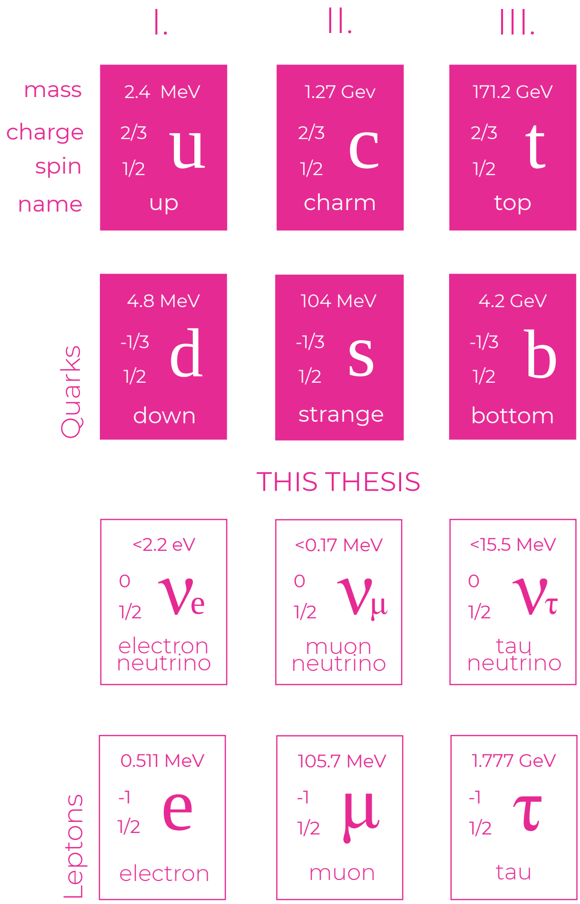

FIGURE 1.1: Three generations of fermions.

coordinates, momenta, or eigenstates. It represents an additional degree of freedom of a quantum mechanical particle [7]. As their names suggest, fermions follow Fermi-Dirac statistics while bosons follow Bose-Einstein statistics [8].

Fermions are subsequently divided into leptons and quarks. Both groups are subsequently organised into three generations with each generation containing two particles. Particles in the second and the third generation have the same electromagnetic charge as the particles in the first generation, only the masses increases with increasing generation[1]. The summary table with names of all the fundamental fermions, their masses, and electric charges is shown in Fig. 1.1. In addition to the listed particle, every particle has an associated antiparticle with the same properties but opposite electromagnetic charge. Antiparticles are marked with a bar above the symbol of a particle, e.g. antiproton $\bar{p}$ is

[1]Assuming the standard mass hierarchy of neutrinos. The inverted mass hierarchy of neutrinos is out of the scope of this thesis.

an antiparticle of proton p. The only exceptions in this notation are the charged leptons for which the charge is usually explicitly stated in the symbol, e.g. the antiparticle of electron e^- is positron e^+.

Every generation of leptons consists of a neutrally charged lepton and associated neutral neutrino. Their overall number is connected with a lepton number. For the first generation, it is calculated as

$$L_e = N(e^-) - N(e^+) + N(\nu_e) - (\bar{\nu}_e), \tag{1.1}$$

where $N(e^-/e^+)$ is a number of electrons/positrons and $N(\nu_e/\bar{\nu}_e)$ is a number of electron (anti)neutrinos. Analogically, the lepton number is constructed for the second and the third generation. In every observed reaction, the lepton number of each generation is conserved [2]. However, charge conjugation symmetry C is not conserved for neutrinos, as the spin projection into momentum direction, known as helicity, is opposite for neutrinos. Only left-handed neutrinos ν_L and right-handed antineutrinos $\bar{\nu}_R$ are observed in experiments. All the neutrinos are considered to have zero mass within the Standard model [9]. Nevertheless, it is observed that their mass is very small but non-zero, which allows the neutrino oscillation [10, 11]. A mass of an observed neutrino is a superposition of mass eigenstates of neutrinos of all three generations. While significant progress has been made in neutrino physics in recent years, the masses of neutrinos remain unknown. Nevertheless, the upper limits of their masses, differences between masses Δm^2_{21} and Δm^2_{32}, and parameters of the mixing matrix are known with 3σ confidence level [12].

The second type of fermions, quarks, also comes in six types. These types are typically referred to as flavours. Under normal conditions, such as temperature and density, they only exist in bound states called hadrons – either baryons that consist of three quarks qqq or antiquarks $\bar{q}\bar{q}\bar{q}$ or mesons that consist of a quark-antiquark pair $q\bar{q}$ [2]. Hadrons have an integer electromagnetic charge (in the units of an elementary charge e), while the charge of quarks is fractional. Every generation consists of a quark with an electromagnetic charge of 2/3 and -1/3. The overview of all flavours is shown in Fig. 1.1. Due to their masses, also shown in Fig. 1.1, quarks c, b, and t are commonly referred to as heavy flavour quarks. Bound states from a heavy quark and its antiquark, e.g. J/Ψ from $c\bar{c}$, are typically referred to as quarkonia. Due to its large mass, the t quark decays before forming a bound state.

Similarly to the lepton numbers, it is possible to define six flavour numbers in every reaction as

$$N_f = N(f) - N(\bar{\mathrm{f}}), \tag{1.2}$$

[2] Alongside baryons and mesons, experimental evidence of tetraquarks made of $qq\bar{q}\bar{q}$ was confirmed in 2003 by the Belle collaboration [13] and while the pentaquarks made of $q\bar{q}qqq$ was discovered in 2015 at the LHCb experiment [14].

where $N(f/\bar{f})$ stands for a number of valence (anti)quarks of a certain flavour. Analogically, a total quark number is defined as

$$N_q = N(q) - N(\bar{q}). \tag{1.3}$$

Charmonia, a quarkonium out of c quarks, is said to have a hidden charm, as it contains c quark, but its quark number $N_c = 0$. If $N_c \neq 0$, the hadron is referred to as open charm, e.g. D^0 from $c\bar{u}$. Due to the confinement of quarks in baryons in ordinary matter, it is convenient to define a baryon number as

$$B = N_q/3 = [N(q) - N(\bar{q})]/3. \tag{1.4}$$

Baryon number is conserved in all known interactions [2]. For example, the neutron is stable only when inside a nucleus. A mean lifetime of a free neutron is $t \approx 880$ s [15]. Due to the conservation of a baryon number, it cannot decay to a lighter meson which has $B = 0$. Instead, the neutron with $m_n = 939$ MeV$/c^2$ decays to a proton with $m_p = 931$ MeV$/c^2$, an electron, and an electron antineutrino. The decay without electron or electron neutrino is not allowed due to the lepton number and charge conservation. The proton is the lightest and only stable baryon.

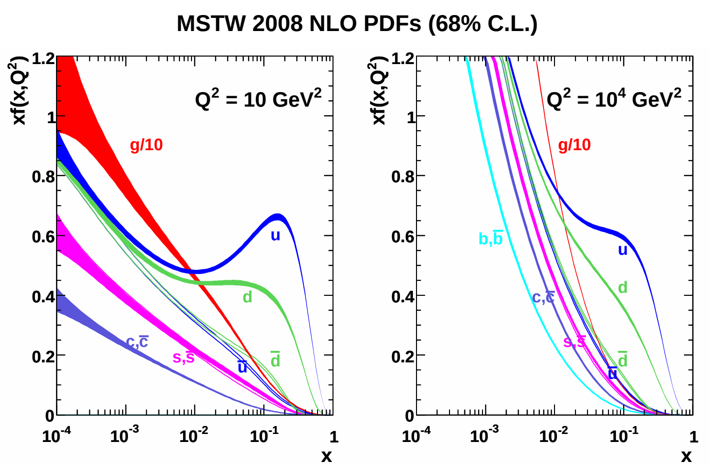

FIGURE 1.2: Next-to-leading order of parton distribution functions in a proton at two different transferred momenta Q^2 as a function of the fraction of the proton's momentum x, also known as Bjorken-x. Taken from [16].

Masses of nucleons, protons (uud) and neutrons (udd), are significantly greater compared to the sum of their constituent (or valence) quarks. In addition to these quarks, virtual (or sea) quarks are present. Together with gluons, described in Sec. 1.2, they make up a hadron and can be referred to as partons based on [17]. While there is a limit on the number of quarks inside a hadron, no such limit exists for the number of partons. The probability of finding a parton of a particular type in a proton is shown in Fig. 1.2 in so-called parton distribution functions.

In addition to nucleons, there is a plethora of unstable hadrons. They can be organised into multiplets with the same spin, baryon number and parity P. An example of an octet of pseudoscalar mesons with spin-parity $J^P = 0^-$ is shown in Fig. 1.3. It is possible to observe $\pi^\pm$ and $\mathrm{K}^\pm$ directly in the particle detectors. However, for neutral K^0 and $\bar{\mathrm{K}}^0$, only their physical states can be observed – K^0_S and K^0_L that are a superposition of K^0 and $\bar{\mathrm{K}}^0$ and CP (charge-parity) eigenstates. The observation of K^0_S showed the breaking of CP symmetry [18]. A full list of the hadrons with their properties, including decay modes, can be found in [9]. Aforementioned mesons $\pi^\pm$, $\mathrm{K}^\pm$, and K^0_S are used in this thesis's analysis and result parts. Moreover, ϕ meson with $J^P = 1^-$ made out of $s\bar{s}$ valence quarks, and Λ baryon with $J^0 = \frac{1}{2}^+$ from uds quarks are used.

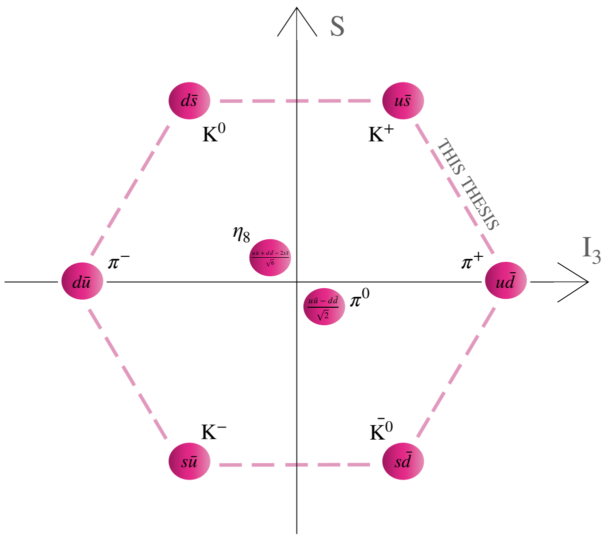

FIGURE 1.3: Octet of pseudoscalar mesons with $J^P = 0^-$. Particles are organised based on their strangeness S and isospin I_3. The last pseudoscalar meson with $J^P = 0^-$ is singlet η_1 with quark composition $(u\bar{u} + d\bar{d} + s\bar{s})/\sqrt{3}$.

Alongside described elementary particles, there are three fundamental interactions in the Standard model – electromagnetic, weak, and strong[3]. All of them are associated with fundamental particles as the interactions occur by exchanging the force carrier. All of the carriers are gauge bosons with spin 1.

[3]The last fundamental interaction, the gravitational one, is not part of the Standard model of particle physics, therefore, is not discussed.

The first interaction, electromagnetic, affects all charged particles and is described by quantum electrodynamics (QED). The electromagnetic charge is conserved in all the interactions and all the vertices of the Feynman diagrams. The force carrier is a photon γ, with a typical interaction being a photon emission or absorption. Due to the zero mass of γ, the interaction range is infinite. However, as the Coulomb potential is proportional to $1/r$, thus the strength of the electromagnetic interaction becomes smaller at large distances. In addition, a highly energetic charged particle can polarise the vacuum and create a virtual particle-antiparticle pair. This pair then shields the charge of the original particle in a phenomenon referred to as screening.

The second interaction, the weak one, can be split into charged currents, carried by $W^{\pm}$ bosons, and neutral currents, carried by Z^0. Both $W^{\pm}$ and Z^0 are very massive, with $m_W = 80.4$ GeV$/c^2$ and $m_Z = 91.2$ GeV$/c^2$ [9]. Due to their large masses, the range of the interaction is very short. $W^{\pm}$ and Z^0 interact with both quarks and leptons. A typical example of weak interaction is a β decay of a nucleus, which is in fact a reaction $d \to u + e^- + \nu_e$ via the W^- boson. This interaction is the only way of detecting neutrinos. Moreover, both parity [19, 20] and charge are not conserved while their combination is mostly conserved. The only known exception is the flavour mixing of neutral hadrons (such as K^0_S).

The unification of electromagnetic and weak interactions, known as electroweak interaction, occurs at high energies [21, 22]. Moreover, it predicts the existence of a spinless Higgs boson as a consequence of spontaneous symmetry breaking. It addresses a difference between masses of massless γ and very massive $W^{\pm}$ and Z^0. Masses of all the fermions also originate from the interaction with the Higgs field. Higgs boson, theoretically predicted in 1964 [23, 24] and experimentally confirmed in 2012 independently by the ATLAS and CMS collaborations [25, 26], was the last missing piece of the Standard model.

The third and the last fundamental interaction, the strong one, is the interaction between quarks. Its carriers are massless electromagnetically neutral gluons with spin 1. The following section is dedicated to the theory describing the strong interaction, quantum chromodynamics (QCD).

1.2 Quantum chromodynamics

Quarks are fermions and follow the Pauli exclusion principle. The existence of a baryon with three identical valence quarks with all their spins aligned exists, e.g. Ω^- (sss) with spin $J = 3/2$, would not follow this principle if quarks did not carry a colour charge which gives them an additional degree of freedom in QCD. The possible colour states are red, green, and blue for quarks, and their anticolours for antiquarks.

The carriers of the strong force are called gluons. When interacting with quarks, they exchange the colour charge. They also carry a colour, therefore, can interact with other gluons as well. Gluons exist in eight colour states in total. The colour charge of gluons leads to a phenomenon referred to as asymptotic freedom [27, 28]. Similarly to the screening effect in the electromagnetic field, a gluon can create a virtual quark-antiquark pair out of a vacuum and produce a screening effect in which the original colour charge is shielded and thus felt weaker. However, as the self-coupling of gluons is possible, a gluon can also produce a virtual gluon-gluon pair. Therefore a particle with a colour charge will interact not only with the original charge but also with a strong coloured cloud of virtual gluons. The produced effect of antiscreening is stronger than the one from screening. Consequently, quarks can behave as free particles at short distances but cannot be separated. The strength of the strong interaction increases rapidly as the distance between two quarks is getting closer to the nucleon radius, $r \sim 10^{-15}$ m, which is why quarks are confined in hadrons under normal conditions. For this reason, all the observed hadrons are colour singlets (or colour neutral), which is referred to as colour confinement.

The strength of the interaction can also be expressed in terms of the running coupling constant α_s [29], following

$$\alpha_s(Q^2) \propto \frac{1}{\ln(Q^2),} \tag{1.5}$$

where Q^2 is the momentum transfer. The QCD running coupling is shown in Fig. 1.4 with measured values from different experimental approaches and different calculations. At the large Q^2 and short distances, perturbative QCD calculations can describe the interaction. As the processes with large momentum transfer are also referred to as hard processes, high-Q^2 QCD is also commonly called hard QCD. The large increase of α_s and in the strength of the interaction occurs in the soft QCD region with the lower Q^2 and larger distances where the description with the perturbative theory is not possible anymore. For that reason, lattice QCD, a numerical approximation in which the calculation is done on a very large four-dimensional grid, takes place. This approach was first introduced in [30].

If the distance between two quarks becomes large enough, i.e., if the colour field becomes strong enough, it can create $q\bar{q}$ pair out of vacuum as it is energetically favourable. One prescription for such $q\bar{q}$ production is the Lund string model [31], in which the colour field is constrained into thin strings. The process of creating new quark-antiquark pairs repeatedly occurs in high-energy collisions. In the model, all the quarks hadronise and form a narrow cone of hadrons – a jet. The initial partons fragment into more partons before the hadronisation process takes place in the phenomenon referred to as jet

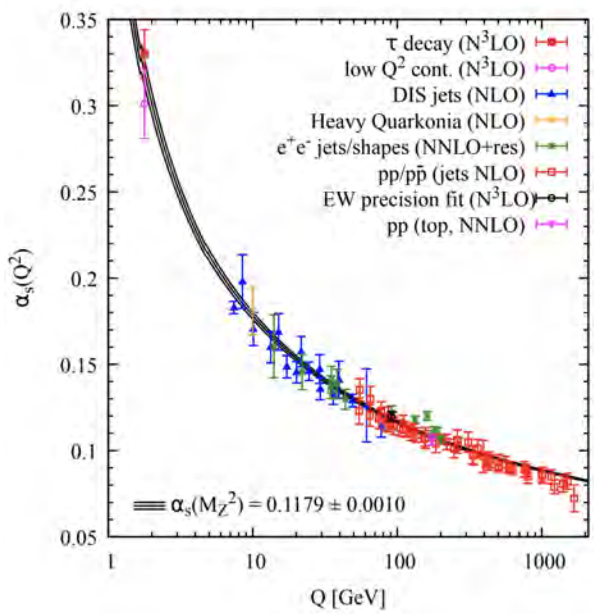

FIGURE 1.4: Running coupling constant α_s of the strong interaction as a function of momentum transfer Q^2. Taken from [9].

fragmentation. The direction of the jet, obtained from the sum of momenta of all particles within the jet, closely corresponds to the direction of the parton of origin. In the majority of observed collisions (or events) with jets, only two jets are observed. Due to the momentum conservation laws, the created jets point in opposite directions in the transverse plane with respect to the beam direction, and are referred to as back-to-back jets. However, in certain conditions, e.g. if a high energy gluon is emitted from the quark of origin before the fragmentation, a three jets event can be observed.

1.3 Quark-gluon plasma

Under normal conditions, quarks and gluons are confined in hadrons. However, the QCD matter also exists under extreme conditions, e.g. in the core of neutron stars, where the density is greater than the density of nucleons. Therefore it was assumed, first in [32], that a quark soup of deconfined quarks and gluons might be created. A similar theory on the quark liberation was proposed in [33], introducing a critical temperature above which normal hadronic matter cannot exist. Nowadays, the name *quark-gluon plasma* (QGP), introduced in [34], is used to describe this very hot and dense state of matter in which quarks and gluons are essentially deconfined. Experimental evidence of its creation was first found during the heavy-ion program at the Super Proton Synchrotron at

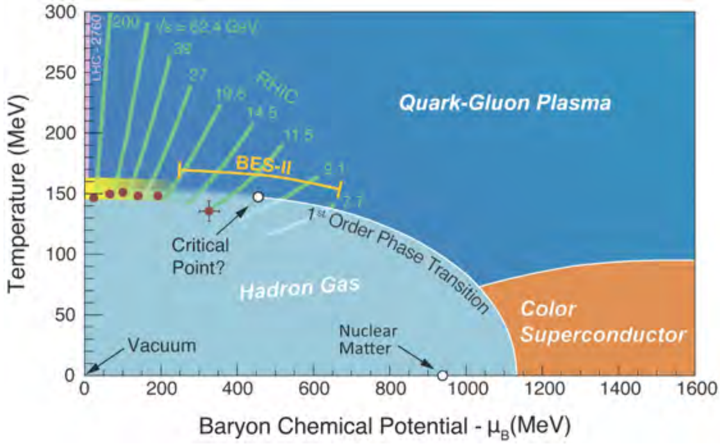

FIGURE 1.5: Scheme of the QCD phase diagram. Taken from [40].

CERN [35]. The discovery was confirmed by four main experiments at the Relativistic Heavy Ion Collider (RHIC) at BNL [36–39]. This section describes the experimental studies of the QGP using ultra-relativistic collisions of heavy ions. Moreover, an evolution of such a collision is described.

The QCD phase diagram in Fig. 1.5 shows the transition between the hadron gas and the QGP as a function of temperature T and baryon chemical potential μ_B. The region with low μ_B and very high$T$ is believed to exist in the very early Universe, right after the Big Bang. To study this region, the lattice QCD calculations at the baryochemical potential $\mu_B = 0$, where $\mu_B \propto \rho_{\text{baryon}}$, are used together with experimental results from ultra-relativistic heavy-ion collisions at the highest possible energies. Currently, CERN's Large Hadron Collider collides ions of lead ($^{208}_{82}$Pb) at the center of mass collision energy per nucleon-nucleon pair $\sqrt{s_{\text{NN}}} = 5.02$ TeV while BNL's RHIC collides gold ($^{197}_{79}$Au)) at $\sqrt{s_{\text{NN}}} = 200$ GeV. A dedicated program called the Beam Energy Scan with heavy-ion collisions at different energies between $\sqrt{s_{\text{NN}}} = 7.7$ GeV and 62.4 GeV was running at RHIC in recent years in order to map the QCD phase diagram in lower temperatures and intermediate-to-high μ_B [41]. One of its goals was to put constraints on the position of the critical point – its position is crucial as the transition between confined and deconfined matter is different for regions on either side of this point. For $\mu_B < \mu_c$, where μ_c is the baryochemical potential of the critical point, the transition between the hadronic gas and QCP is a rapid crossover and can be calculated using lattice QCD [42]. The first order phase transition is assumed for $\mu_B > \mu_c$. The position of this point is expected at $\mu_C \geq 300$ MeV [43]. The critical temperature $T_c(0)$, i.e. the temperature of the phase transition at $\mu_b = 0$, is estimated to be $T_c(0) = (156.5 \pm 1.5)$ MeV [44].

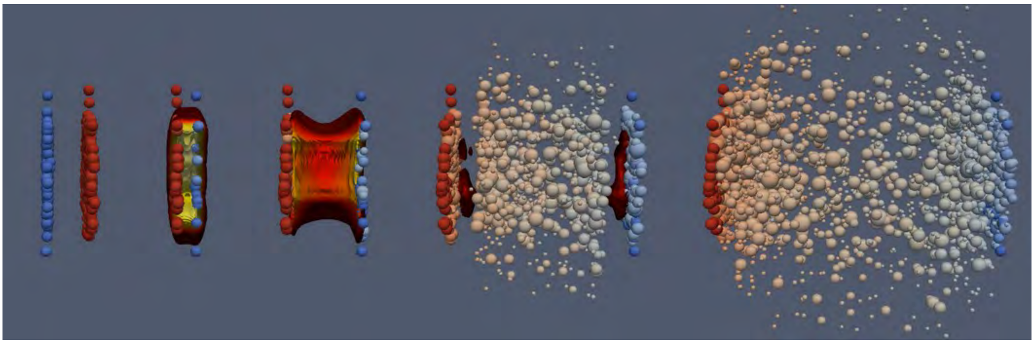

FIGURE 1.6: Different stages of the space-time evolution of a heavy-ion collision. Taken from [45].

The QGP expands and cools down very quickly, thus, it is not observed directly. However, its production and evolution affect the final distributions of observed particles.

1.3.1 Evolution of a heavy-ion collision

Accelerated to ultra-relativistic energies, heavy nuclei are Lorentz contracted, which is shown in the first panel of Fig. 1.6. The impact parameter b, defined as the distance between centres of both colliding nuclei, describes the collision geometry. Small b corresponds to central (or head-on) collisions, while larger b collisions are referred to as peripheral. Only participant nucleons participate in the collisions while spectators continue in the initial direction of the beam. The number of participants and spectators is essential as it is strongly correlated with b, which cannot be experimentally obtained.

In addition to b, the distribution of nucleons inside the colliding nuclei affects the initial geometry of the collision. The distribution can be described by the Woods-Saxon nuclear density potential [46]

$$\rho(r) = \frac{\rho_0}{1 + \exp(\frac{r - r_0}{c})}, \tag{1.6}$$

where r and r_0 are the distance from the centre of the nucleus and the mean radius of the nucleus, respectively, ρ_0 nuclear density, and c the surface thickness. It can be simulated using the Monte Carlo Glauber model [47]. An example of such a distribution is shown in Fig. 1.7. In both, the real collision and the simulation, this distribution fluctuates event-by-event. The geometry of the collision, e.g., distributions of nucleons at the moment of the collision and the impact parameter, affects the initial state of the collisions.

Right after the collision, shown in the second panel of Fig. 1.6, the stage of pre-equilibrium dynamics takes place at $\tau \approx< 1$ fm/c [48]. During this time, hard scattering

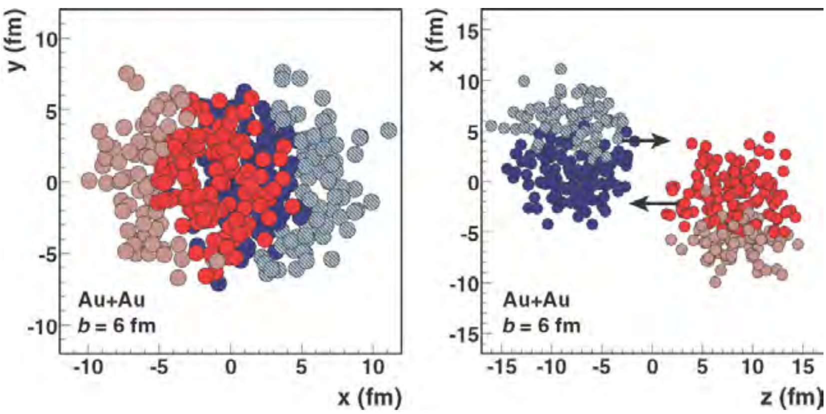

FIGURE 1.7: Glauber Monte Carlo Au+Au collision at $\sqrt{s_{\mathrm{NN}}} = 200$ GeV in the transverse (left) and longitudinal (right) planes. Participants are shown in darker shades. Taken from [47].

processes occur, creating partons with large transverse momentum p_{T} or large masses. Jets created from high p_{T} partons or hadrons containing a heavy flavour quark (c, b) are referred to as hard probes and are crucial for studying the QGP as the hard partons are formed prior the QGP.

After the pre-equilibrium, a local equilibrium is created via the thermalisation process within the deconfined QCD matter, and the quark-gluon plasma is formed (middle panel in Fig. 1.6). Its evolution can be very precisely described by relativistic hydrodynamics. Hence, it can be concluded that the created matter behaves as a nearly ideal fluid. From the hydrodynamical laws of conservation of energy-momentum and charged current

$$\delta_\mu T^{\mu\nu} = 0, \tag{1.7}$$

$$\delta_\mu N_i^\mu = 0, \tag{1.8}$$

where $T^{\mu\nu}$ is the energy-momentum tensor and N_i^μ the current, e.g. baryon number or strangeness in this case. $T^{\mu\nu}$ can be decomposed as

$$T^{\mu\nu} = \epsilon u^\mu u^\nu - (P_s + \Pi)\Delta^{\mu\nu} + W^\mu u^\nu + W^\nu u^\mu + \pi^{\mu\nu}, \tag{1.9}$$

where ϵ is the energy density, u^μ flow velocity of the fluid, $P_s + \Pi$ hydrostatic and bulk pressure, W^μ the heat current, and $\pi^{\mu\nu}$ shear stress tensor. $\Delta^{\mu\nu} = g^{\mu\nu} - u^\mu u^\nu$ is the projector transverse to u and $g^{\mu\nu}$ the Minkowski matrix. Adding the entropy current $S^\mu = su^\mu$ to the system, where s is the entropy, and assuming no charge in the system, it is possible to deduce the equation of motion of the system that describes the time evolution of the energy density ϵ [49, 50]

$$\frac{\mathrm{d}\epsilon}{\mathrm{d}\tau} = -\frac{\epsilon + P_s}{\tau}\left(1 - \frac{4}{3\tau T}\frac{\eta}{s} - \frac{1}{\tau T}\frac{\zeta}{s}\right), \tag{1.10}$$

where τ is the time, T is the temperature, and the transport coefficients η and ζ are shear and bulk viscosity, respectively. In the case of ideal hydrodynamic, only the first term is kept [51]. Dimensionless ratios η/s, ζ/s are important parts of hydrodynamical models. The QGP has $\eta/s \approx 1/4\pi$, which corresponds to the theoretical limit of the perfect fluid [52]. Formulating additional equations that help stabilise the description using the relaxation time terms is possible. However, at both RHIC and LHC energies, their contribution is negligible [53]. To solve the hydrodynamic equations, a relation between the pressure and the energy density has to be provided, which is provided by the equation of state typically taken from the lattice QCD.

As QGP expands and cools down rapidly, a hadronisation process occurs (fourth panel in Fig. 1.6), converting all quarks and gluons into hadrons. The created hadrons are still allowed to interact both elastically and inelastically for a short time. After a further expansion, a local chemical freeze-out takes place, i.e. the system is in local chemical equilibrium, and no inelastic scattering takes place anymore, i.e. all the hadron yields are fixed. One of the ways how to describe this process is using a thermal macroscopic Statistical Hadronization Model [54] which uses the grand canonical ensemble to describe the medium and is in excellent agreement with particle yields obtained from heavy-ion collisions [55].

Finally, the kinetic freeze-out (last panel in Fig. 1.6) occurs when all the hadron scatterings are over, and the momentum of all the particles does not change anymore. After this stage, particles continue towards the detector, with heavier (less stable) particles undergoing weak decays to more stable particles. Subsequently, particles can interact with the detector which allows their detection. The final state particle information obtained from the detectors are available for the experimental studies of the QGP that are presented in the following subsection.

1.3.2 Experimental studies of the QGP

Experimental observables can be divided into two groups – hard and soft probes. The former, as mentioned above, are created shortly after the collision and thus can bring information from the early stage. Hard probes, created in the processes with the large momentum transfers, either carry large p_{T} or have a large mass. The soft probes use the majority of produced particles, i.e. low transverse momenta (soft) particles, and describe the collective behaviour of the medium that evolves as a bulk. Selected important examples of both hard and soft probes are described below. Nevertheless, it is essential

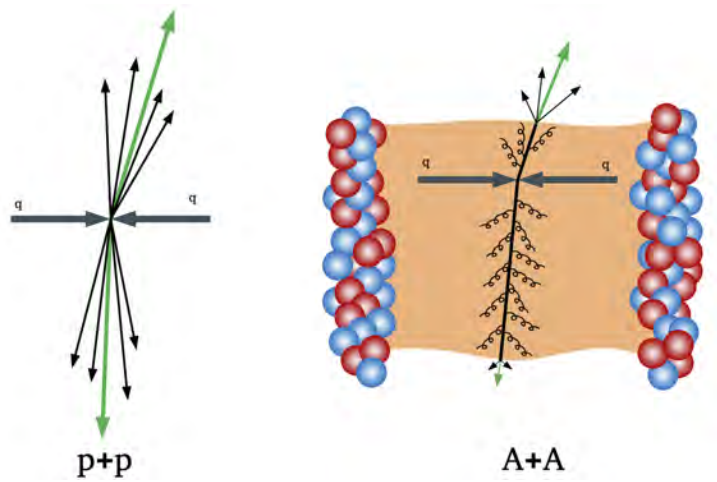

FIGURE 1.8: Hard scattering of two partons in proton-proton (left) and heavy-ion (right) collisions. Taken from [56].

to note that there are more possibilities for experimentally studying QGP, such as using dileptons, photons, or hypernuclei, that are not described in this thesis.

Jet quenching

A hard scattering of two partons at a large angle can occur in high energy collision of both protons and heavy nuclei. In pp collisions, as shown in the left panel of Fig. 1.8, the scattered high p_{T} partons travel in the opposite direction in the transversal plane. Along the way, they radiate gluons that can split into quark-antiquark pairs or more gluons in the fragmentation process, creating two back-to-back jets. The gluon emission is different if the initial parton is a heavy quark. Then the radiation is suppressed in the angle $\theta < m/E$ with respect to the direction of the heavy quark with mass m and energy E. This phenomenon, known as the dead cone effect, has been recently experimentally confirmed by the ALICE Collaboration [57].

However, in a heavy-ion collision, both leading partons interact with the medium they are crossing, as shown in the right panel of Fig. 1.8. The in-medium energy loss takes place via both collisional and radiative processes. The former is through the elastic scatterings, while the latter is through the inelastic ones. The dominant process is the radiative energy loss via medium-induced emission of multiple gluons [58]. As a consequence, unlike the situation in pp collisions, two same back-to-back jets are not observed as one of them is significantly suppressed (quenched).

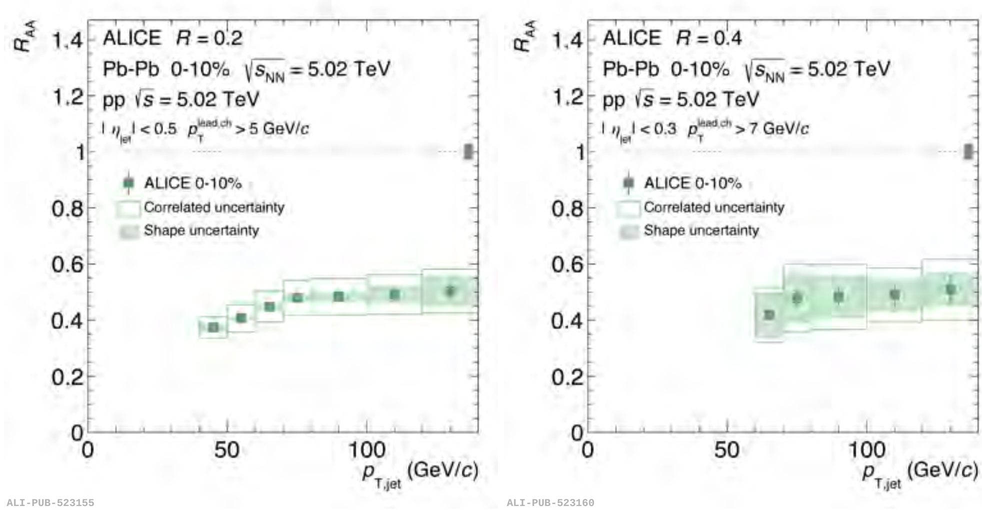

FIGURE 1.9: Nuclear modification factor $R_{\mathrm{AA}}(p_{\mathrm{T}},\mathrm{jet})$ in central Pb–Pb collisions at $\sqrt{s_{\mathrm{NN}}} = 5.02$ TeV with two different jet resolution parameters R. Taken from [60].

The phenomenon of jet quenching can be quantified using a nuclear modification factor, R_{AA}, defined as [59]

$$R_{\mathrm{AA}} = \frac{\frac{1}{N_{\mathrm{event}}} \frac{\mathrm{d}^2 N}{\mathrm{d}p_{\mathrm{T,jet}} \mathrm{d}\eta_{\mathrm{jet}}}|_{\mathrm{AA}}}{\langle T_{\mathrm{AA}} \rangle \frac{\mathrm{d}^2 \sigma}{\mathrm{d}p_{\mathrm{T,jet}} \mathrm{d}\eta_{\mathrm{jet}}}|_{\mathrm{pp}}}, \tag{1.11}$$

where $\frac{\mathrm{d}^2 N}{\mathrm{d}p_{\mathrm{T,jet}} \mathrm{d}\eta_{\mathrm{jet}}}|_{\mathrm{AA}}$ is the per event yield in nucleus-nucleus (AA) collision, $\frac{\mathrm{d}^2 \sigma}{\mathrm{d}p_{\mathrm{T,jet}} \mathrm{d}\eta_{\mathrm{jet}}}|_{\mathrm{pp}}$ cross section in pp collision, and $\langle T_{\mathrm{AA}} \rangle = \frac{\langle N_{\mathrm{coll}} \rangle}{\sigma_{\mathrm{inel}}^{NN}}$, N_{coll} is the number of binary nucleon-nucleon collisions, and $\sigma_{\mathrm{inel}}^{NN}$ is the inelastic nucleon-nucleon cross section. In other words, it expresses how much the jet is suppressed in AA collision with respect to the pp collision considering the scaling with N_{coll}. An example of such a measurement in central Pb–Pb collisions is shown in Fig. 1.9 with two different jet radius R. In both cases, the strong suppression is clearly visible. In the case with $R = 0.2$, a p_{T} dependence is also visible, with stronger suppression at the smaller p_{T} of the jet. No p_{T} dependence is visible in the case of $R = 0.4$ due to the larger uncertainties.

Analogically, it is possible to calculate the nuclear modification factor for inclusive charged particles and different identified species. An example of R_{AA} of open charm mesons D^0, D^+, and D^{*+} is shown in Fig. 1.10 (left). In the left panel, a comparison of R_{AA} in three different centralities of Pb–Pb collisions at $\sqrt{s_{\mathrm{NN}}} = 5.02$ TeV is shown. The largest suppression is at intermediate p_{T} ($6 < p_{\mathrm{T}} < 10$ GeV/c). For most central collisions, the suppression with respect to the pp collisions is by a factor of 5. A comparison

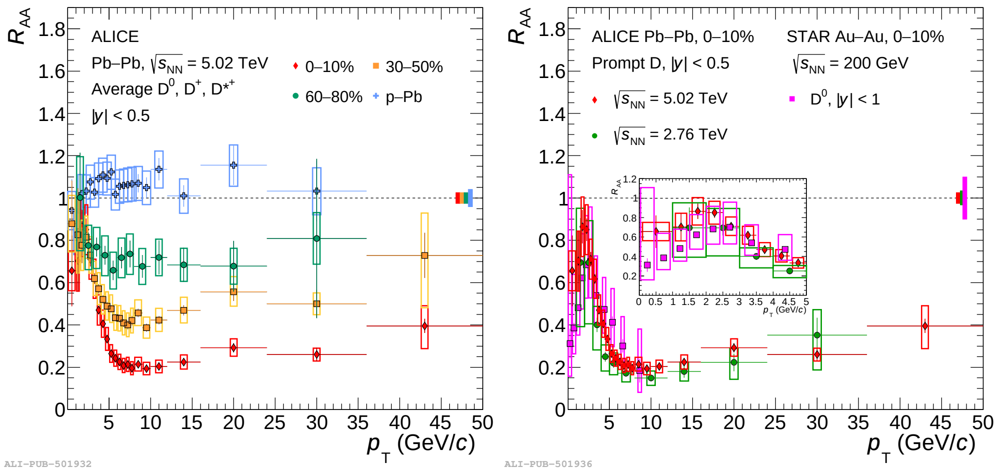

FIGURE 1.10: Nuclear modification factor $R_{AA}(p_T)$ of D mesons in Pb–Pb collisions at $\sqrt{s_{NN}} = 5.02$ TeV in different centrality classes (left) and in two different nuclei-nuclei collision systems at three different energies (right). Taken from [61].

of R_{AA} of D^0 in two different collision energies of central Pb–Pb collisions, specifically at $\sqrt{s_{NN}} = 5.02$ TeV and $\sqrt{s_{NN}} = 2.76$ TeV, and R_{AA} of D^0 from central Au–Au collisions at $\sqrt{s_{NN}} = 200$ GeV, is shown in the right panel of Fig. 1.10. Despite the differences between these measurements, especially at the small p_T, they agree with the conclusion of the strong suppression in the heavy-ion collisions, caused by the energy loss via the interaction with the medium.

Quarkonia

Bound states of $c\bar{c}$ and $b\bar{b}$ are called charmonia and bottomia, or overall, quarkonia. Mesons J/Ψ and Υ are the ground state of charminoum and bottomium, respectively. They are relatively stable, as they can only decay via an OZI-suppressed decay due to the energy conservation and $M_{J/\Psi} < 2M_D$. Moreover, they have large binding energies, therefore they are smaller than a typical hadron radius of ≈ 1 fm, with only $r(J/\Psi) = 0.25$ fm and $r(\Upsilon) = 0.14$ fm. Their excited states are within the range 0.22 – 0.45 fm [62]. Because of the colour screening in the deconfined QCD matter, quarkonia melts at a temperature higher than the phase transition of the hadron gas [63]. Thus it is used to measure the temperature of the QGP.

A comparison of invariant mass of $\Upsilon(nS)$ states reconstructed from $\mu^+\mu^-$ pairs in pp and Pb–Pb collisions at the same collision energy of $\sqrt{s_{NN}} = 2.76$ TeV is shown in Fig. 1.11. It can be seen that the suppression of bottomia occurs in Pb–Pb collisions. However, as different bound states have different binding energies and thus dissociation

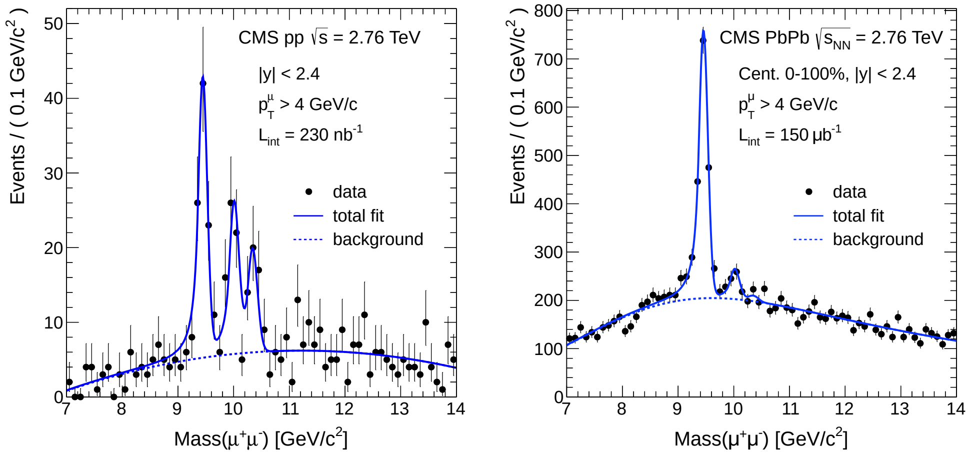

FIGURE 1.11: Invariant mass distributions of $\mu^+\mu^-$ pairs with a fit of $\Upsilon(nS)$ in pp (left) and Pb–Pb (right) collisions at $\sqrt{s_{\mathrm{NN}}} = 2.76$ TeV. Taken from [64].

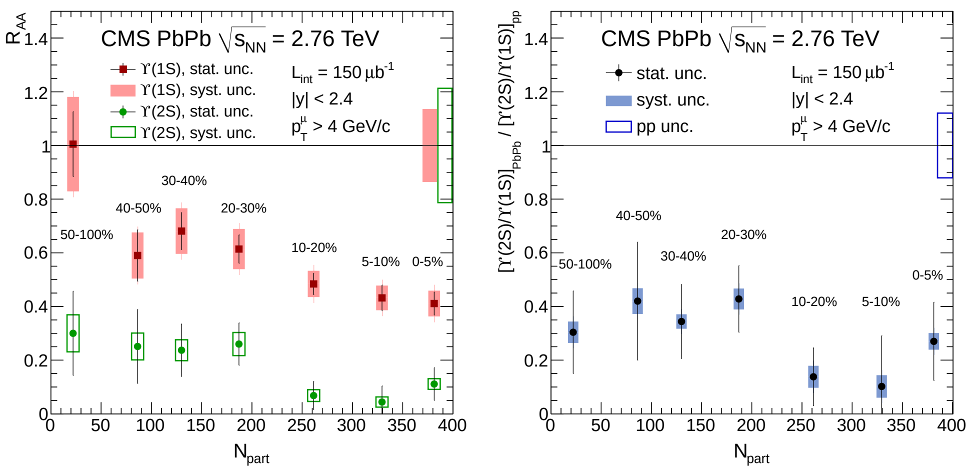

FIGURE 1.12: Nuclear modification factor R_{AA} (left) and double ratios of $\Upsilon(nS)$ (right) as a function of multiplicity N_{part} in Pb–Pb collisions at $\sqrt{s_{\mathrm{NN}}} = 2.76$ TeV. The corresponding event centrality is shown as well. Taken from [64].

temperatures, it is important to quantify this suppression. Nuclear modification factor R_{AA} is shown for $\Upsilon(1S)$ and $\Upsilon(2S)$ in Fig. 1.12 (left). The peak of $\Upsilon(3S)$ in Fig. 1.11 cannot be distinguished from the background. It corresponds to the hypothesis of $\Upsilon(3S)$ being suppressed the most while $\Upsilon(1S)$ the least. The suppression of both $\Upsilon(1S)$ and $\Upsilon(2S)$ becomes more significant towards the most central collision. There is no observed suppression in peripheral collisions for $\Upsilon(1S)$. In addition, a double ratio of $\Upsilon(nS)$ states

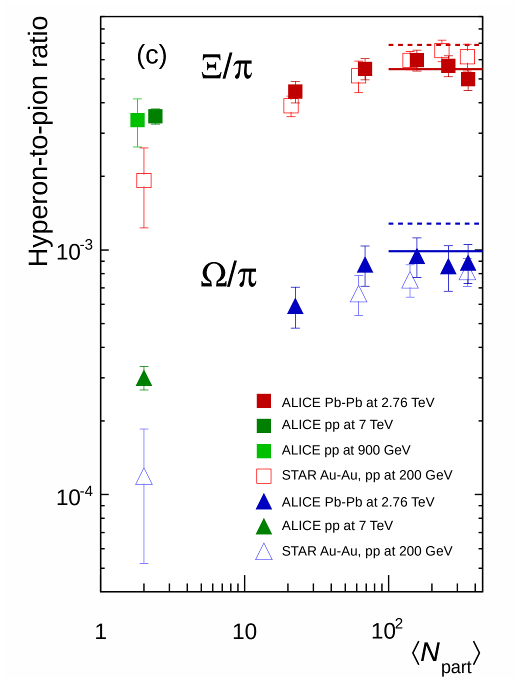

FIGURE 1.13: Ratio of multi-strange baryons (hyperons) to pions as a function of mean multiplicity $\langle N_{\text{part}} \rangle$ in different colliding systems at different collision energies. Taken from [65].

can be defined as [64]

$$d.r. = \frac{\Upsilon(2S)/\Upsilon(1S)|_{\text{PbPb}}}{\Upsilon(2S)/\Upsilon(1S)|_{\text{pp}}}, \tag{1.12}$$

in which all remaining detector effects, such as efficiency or acceptance, are cancelled out. The double ratio is shown in Fig. 1.12 (right). It further confirms a significant suppression of the $\Upsilon(nS)$ bound states and its ordering connected to their melting temperature within the QGP.

Strangeness enhancement

The enhanced production of strange quarks as a signature of QGP has been proposed in [66]. Unlike u and d quarks, s does not directly enter the interaction as a valence quark of colliding particles in both pp and heavy-ion collisions. In the deconfined QCD matter, thermal gluons have enough energy to produce $s\bar{s}$ pairs. The thermal production is the dominant process of the strangeness formation in heavy-ion collisions, while in the small collision systems, only fragmentation is possible. Thus, strange and multi-strange hadrons are enhanced in heavy-ion collisions due to the presence of the QGP [65].

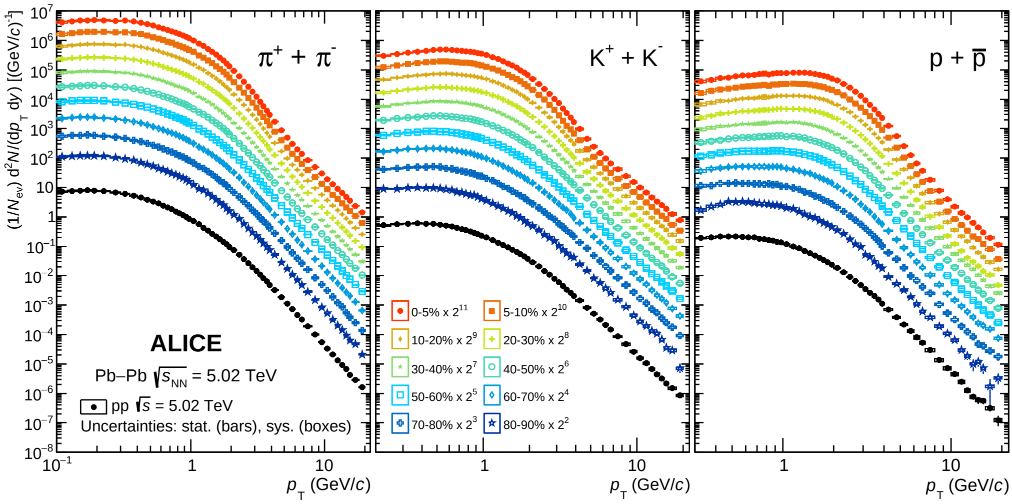

FIGURE 1.14: Transverse momentum p_T spectra of $\pi^{\pm}$(left), $K^{\pm}$(middle), and $p(\bar{p})$(right) in pp and Pb–Pb collisions at $\sqrt{s_{NN}} = 5.02$ TeV. Taken from [67].

An example of strangeness enhancement in Pb–Pb collisions is shown in Fig. 1.13 as a ratio of two hyperons[4] to $\pi^{\pm}$ that contain only u and d quarks. The same ratio is shown for pp collisions as well. Selected hyperons have $N_s = 2$ and 3, respectively, as Ξ^- is made of dss quarks while Ω^- is made only of s quarks, i.e. sss. The production enhancement in the most central Pb–Pb collisions with respect to pp collisions is ~ 1.6 and 3.3 for Ξ and Ω, respectively [65].

Collective flow

A heavy-ion collision is not a simple superposition of many proton-proton collisions. The created strongly interacting QCD matter, QGP, behaves as a nearly ideal fluid and hydrodynamically expands as a bulk. The collective motion of correlated particles is referred to as collective flow.

Radial flow provides insight into the transverse expansion of the QGP. The transverse momentum p_T spectra of $\pi^{\pm}$, $K^{\pm}$, and $p(\bar{p})$ is shown in Fig. 1.14 for different centrality classes of Pb–Pb collisions and minimum bias pp collisions. The spectra' maximum and shape are modified in different centralities, with the maximum being larger for more central collisions, which agrees with the hydrodynamics predictions. In more central collisions, the created QGP fireball expands isotropically and more rapidly than in peripheral collisions, thus producing more radial flow [68]. Moreover, heavier particles are affected more by the radial flow.

[4] A hyperon is defined as a baryon containing at least one strange s quark.

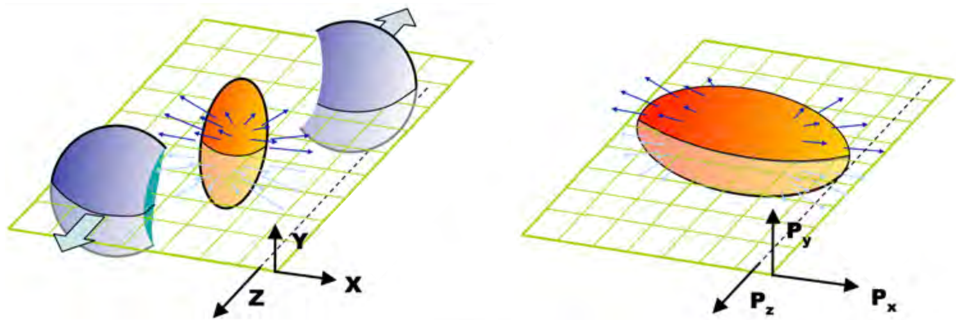

FIGURE 1.15: Scheme of non-central heavy-ion collision and the subsequent expansion of the created medium. Taken from [70].

In addition to radial flow, which is more significant in central collisions, a phenomenon known as anisotropic flow is observed in heavy-ion collisions. A scheme of a non-central collision in which the anisotropic flow is more pronounced is shown in the left panel of Fig. 1.15. The initial geometry, i.e. the shape of overlap between colliding heavy nuclei, is mostly of an ellipsoid shape that can be quantified with its eccentricity defined as

$$\varepsilon = \frac{\langle y^2 + x^2 \rangle}{\langle y^2 - x^2 \rangle}. \tag{1.13}$$

The initial azimuthal anisotropy creates a difference in the pressure gradients of the created medium that is expanding. A collective motion of all the produced partons is enhanced in a preferred direction along the horizontal axis, as shown in the right panel of Fig. 1.15. Thus, the momentum anisotropy of the final state particles is observed. Due to its origin in the ellipsoid shape, it is referred to as elliptic flow. Besides the ellipsoid shape, the distributions of nucleons in the nuclei that fluctuate event-by-event, shown in Fig. 1.7, contribute to the anisotropic flow [69]. Different geometrical components are described by the initial eccentricities ε_n.

Overall, the anisotropic flow can be quantified using different harmonics n of flow coefficients v_n, with first three harmonics being called directed, elliptic, and triangular flow, respectively. Flow coefficients are obtained from the Fourier expansion of the azimuthal distributions of final state particles [71],

$$E\frac{\mathrm{d}^3N}{\mathrm{d}^3p} = \frac{1}{2\pi}\frac{\mathrm{d}^2N}{p_\mathrm{T}\mathrm{d}p_\mathrm{T}\mathrm{d}y}\left(1 + 2\sum_{n=1}^{\infty} v_n \cos n(\varphi - \Psi_n)\right), \tag{1.14}$$

where Ψ_n is the n-th flow symmetry plane. In addition, a n-th flow vector can be constructed as $\vec{V}_n = v_n e^{in\Psi_n}$, where v_n is its magnitude and Ψ_n its phase. For $n = 2, 3$, the flow coefficients v_n are linearly related to the initial eccentricities ε_n in non-peripheral

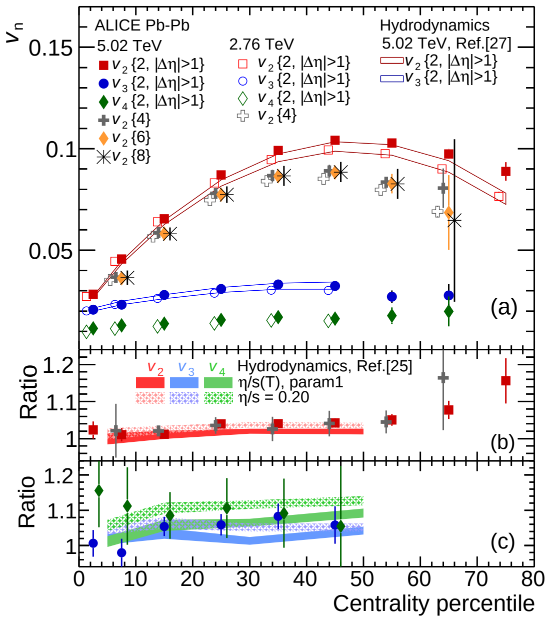

FIGURE 1.16: Top: Anisotropic flow coefficients $v_n\{m\}$ for different harmonics n and from different orders of m-particle correlations as a function of centrality in Pb–Pb collisions at $\sqrt{s_{\mathrm{NN}}} = 5.02$ TeV and $\sqrt{s_{\mathrm{NN}}} = 2.76$ TeV. The hydrodynamical predictions originate from [75]. Bottom: Ratio of $v_2\{2, |\eta| > 1\}$ (red), $v_2\{4\}$ (gray), $v_3\{2, |\eta| > 1\}$ (blue), and $v_4\{2, |\eta| > 1\}$ (green) at $\sqrt{s_{\mathrm{NN}}} = 5.02$ TeV to results at $\sqrt{s_{\mathrm{NN}}} = 2.76$ TeV. The hydrodynamical predictions originate from [76]. Taken from [77].

collisions, as in

$$v_n \propto \varepsilon_n. \tag{1.15}$$

Higher harmonics v_n with $n \geq 4$ do not display a linear response to their initial eccentricity. Besides the linear term, leading contributions from lower terms are present [72–74]. Besides the initial geometry, flow coefficients are sensitive to the transport coefficients of the QGP, such as η/s and ζ/s.

Anisotropic flow coefficients of different harmonics n are shown in Fig. 1.16 as a function of collision centrality. The coefficients are calculated using two- and multi-particle cumulants, noted $v_n\{m\}$, where m is the order of the cumulant. To suppress non-flow contribution from correlations that do not originate from the collective behaviour of the medium, a pseudorapidity separation (η gap of 1) is used in the case of two-particle cumulants, noted as $v_2\{2, |\Delta\eta| > 1\}$. Different methods of v_n calculation are described in detail in Chap. 3.

It can be seen that the elliptic flow v_2 is the dominant harmonic of anisotropic flow

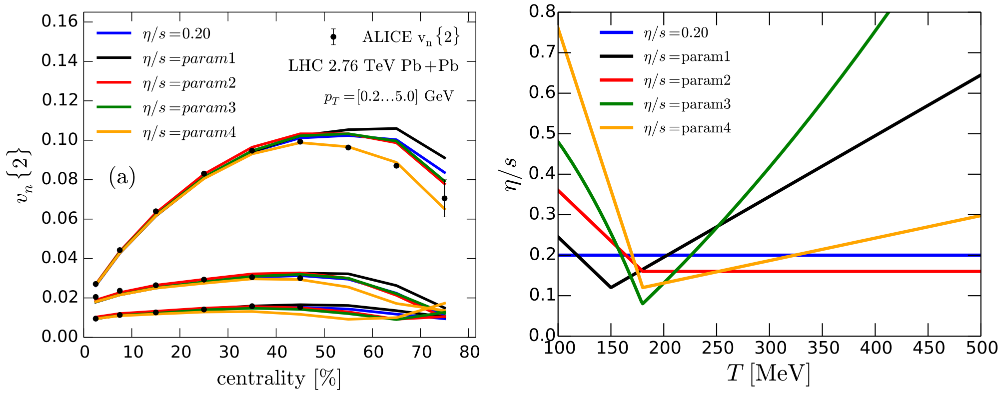

FIGURE 1.17: Left: Elliptic flow coefficients $v_n\{2\}$ as a function of centrality in Pb–Pb collisions at $\sqrt{s_{\mathrm{NN}}} = 2.76$ TeV compared to hydrodynamic calculations with different parametrisations. Right: Shear viscosity to entropy ratio η/s as a function of temperature T in different hydrodynamic models parametrisations. Taken from [78].

in non-central collisions. Nonetheless, the difference between v_2 and higher harmonics is smaller in central collisions. For all the presented flow harmonics n, results at two different collisions energies are shown – $\sqrt{s_{\mathrm{NN}}} = 2.76$ TeV and $\sqrt{s_{\mathrm{NN}}} = 5.02$ TeV. The ratios of flow coefficients at different collision energies are shown in the bottom panels of Fig. 1.16.

The difference between $v_2\{2, |\eta| > 1\}$ and $v_2\{4\}$ originates from the flow fluctuations and non-sufficient non-flow suppression in $v_2\{2, |\eta| > 1\}$. The difference between $v_2\{4\}$ and higher order of multi-particle cumulants, $v_2\{6\}$ and $v_2\{8\}$, is only at the level of the systematic uncertainty. Thus, it can be concluded that the four-particle cumulant sufficiently suppresses the non-flow contamination.

The measured flow coefficients $v_n\{2, |\eta| > 1\}$ are compared to hydrodynamic calculations in order to extract information on the initial state and the transport properties of the created medium. Such an extraction is illustrated on an example of a comparison of $v_n\{2, |\eta| > 1\}$ from the Pb–Pb collisions at $\sqrt{s_{\mathrm{NN}}} = 2.76$ with hydrodynamic calculations, shown in Fig. 1.17. The model combines the EKRT framework [79] in which perturbative QCD and the saturation of gluons are used to calculate the initial conditions for the (2+1) dimensional viscous hydrodynamic model. In addition, different parametrizations of η/s are used in the model, shown in Fig. 1.17 (right panel) as a function of temperature. It can be seen in the data-to-model comparison that it is not possible to distinguish between different parametrisations using only v_n data. Nevertheless, when doing a simultaneous fit of LHC and RHIC v_n data, the best agreement is for the first parametrisation of $\eta/s(T)$, denoted as *param*1, and $\eta/s = 0.2$, i.e. constant η/s with respect to the temperature [78], while it is not directly visible at the aforementioned

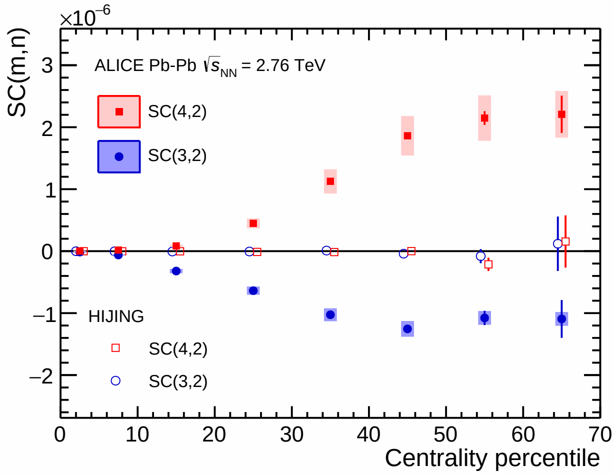

FIGURE 1.18: Symmetric cumulants $SC(3,2)$ and $SC(4,2)$ in Pb–Pb collisions at $\sqrt{s_{\text{NN}}} = 2.76$ TeV compared to HIJING calculations. Taken from [82].

figure.

As various parametrisations of the model are all in agreement in with the data in most of the shown centrality classes, pinning down the best parametrisation is not possible while using v_n coefficients only. Therefore, it is necessary to extend the measurement and construct a new observable, for example, symmetric cumulant $SC(m,n)$. It expresses the correlations between different harmonics of flow coefficients that fluctuate event-by-event in magnitude. $SC(m,n)$ is defined as [80]

$$SC(m,n) = \langle v_m^2 v_n^2 \rangle - \langle v_m^2 \rangle \langle v_n^2 \rangle, \tag{1.16}$$

where $m \neq n$. The first measurement of $SC(m,n)$ in Pb–Pb collisions is shown in Fig. 1.18 for $SC(3,2)$ and $SC(4,2)$. A negative correlation is observed for all the presented centrality classes for the $SC(3,2)$. That can be related to the shape of the initial state – a stronger elliptic shape corresponds to a weaker triangular shape, and vice versa. The measured $SC(4,2)$ shows a positive correlation which can be explained by the non-linear contribution of v_2 in v_4 [81].

In addition to the data collected with ALICE, $SC(m,n)$ in Fig. 1.18 is also shown for the HIJING Monte Carlo simulation [83]. HIJING, or the Heavy Ion Jet Interaction Generator, contains different mechanisms, e.g. multijet production in different collision systems. However, it does not contain any collective flow, therefore, it can be used for

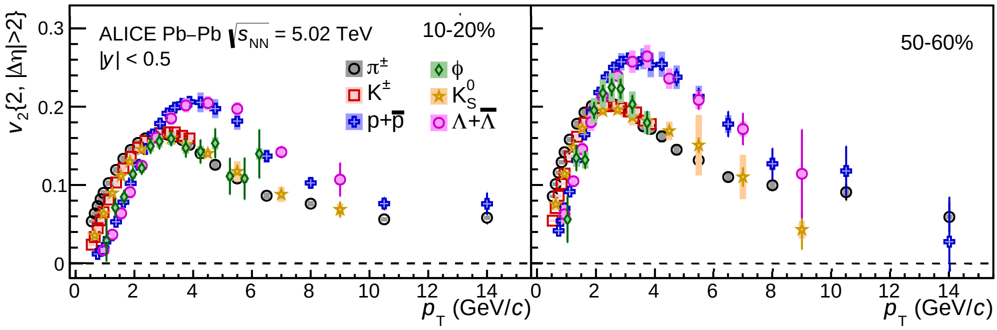

FIGURE 1.19: Elliptic flow v_2 of various identified particles in Pb–Pb collision at $\sqrt{s_{NN}} = 5.02$ TeV in (semi)central (left) and peripheral (right) collisions. Taken from [86].

testing non-flow suppression, crucial for the study of flow in small collision systems, discussed in the following section. As can be seen, both $SC(3,2)$ and $SC(4,2)$ are consistent with zero. It suggests that this observable is not sensitive to non-flow in Pb–Pb collisions.

The presented measurements can be extended by adding an extra dimension – instead of studying p_T-integrated flow coefficients as a function of centrality, a fixed centrality region is selected, and the flow coefficient is calculated as a function of p_T. Moreover, the p_T-differential flow can be studied for different particle species. Such a measurement is shown in Fig. 1.19 in (semi)central collisions (10-20%) and in peripheral (50-60%) Pb–Pb collisions. In both centrality classes, two important phenomena are observed – mass ordering at the low p_T region ($p_T \lesssim 3$ GeV/c), and baryon-meson grouping at the intermediate p_T region ($3 < p_T \lesssim 10$ GeV/). The mass ordering, in which lighter particle species have greater v_2 than heavier particles, can be explained by the interplay between the radial and elliptic flow and is predicted by the hydrodynamical model[84]. The baryon-meson grouping shows clear grouping based on the number of constituent quarks that the partonic collectivity can explain, i.e. it supports the idea of collective flow at the partonic phase and subsequent hadron production via the quark coalescence [85]. The crossing between these two phenomena occurs at a different p_T in different centralities due to the stronger radial flow in central collisions [86].

Moreover, the collective behaviour can be studied using two-dimensional di-hadron correlations. The calculation of the correlation function $C(\Delta\eta, \Delta\varphi)$ and the subsequent extraction of flow coefficients is described in Sec. 3.4 in detail. An example of $C(\Delta\eta, \Delta\varphi)$ in Pb–Pb collisions is shown in Fig. 1.20 in three different centrality classes. The shape of $C(\Delta\eta, \Delta\varphi)$ evolves with centrality. The correlation function can be divided into two regions – near-side at $|\Delta\varphi| < \pi/2$, and away-side at $\pi/2 < \Delta\varphi < 3\pi/2$. Around $(\Delta\eta, \Delta\varphi) \approx (0, 0)$, a peak of near-side jet that originates from correlations of particles in

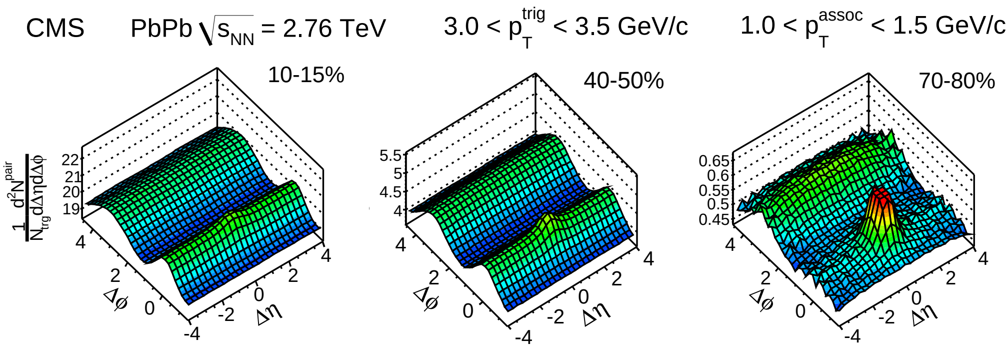

FIGURE 1.20: Correlation function $C(\Delta\eta, \Delta\varphi)$ in Pb–Pb collisions at $\sqrt{s_{NN}} = 2.76$ TeV in different centrality classes. Taken from [87].

the same jet is more visible towards the peripheral collisions. In contrast, only a hint of the peak is visible in central collisions. The away-side peak from correlations of particles from the opposite jets is visible in all selected centralities in the shape of away-side ridge at $\Delta\varphi \approx \pi$. The smearing in $\Delta\eta$ is caused by the fact that the jets are back-to-back only in transversal direction, i.e. they can have non-zero longitudinal momentum alongside the beam axis. Finally, the collective behaviour of the medium explains the near-side ridge at $\Delta\varphi \approx 0$ extended over the whole studied $\Delta\eta$ region. Correlation extended over a large $\Delta\eta$ represents the long-range correlations. The elliptic flow signal is visible as the cosine shape (modulation) within $\Delta\varphi$ direction (outside the jet peak region) and is more pronounced in the peripheral collisions.

1.4 From large to small collision systems

The aforementioned near-side ridge in heavy-ion collisions is connected with the collective expansion and the hydrodynamic evolution of the produced QCD medium. Therefore it was somewhat surprising when the CMS collaboration showed in [88] that the ridge appears in pp collisions with very high multiplicity. It was expected that high multiplicity pp collisions would follow the trend of minimum bias pp collisions in which there si no near-side ridge. The measurement, shown in Fig. 1.21, provided the first hint of collective behaviour in small collision systems with the ridge from long-range correlations covering a wide range of pseudorapidity of up to $|\Delta\eta| = 4$. Such a measurement in high multiplicity collisions can not be reproduced by the PYTHIA model [90] without any collective effects. An analogical measurement in p–Pb collisions is shown in Fig. 1.22. The results agree with the one in the pp collisions – the near-side ridge, typical for

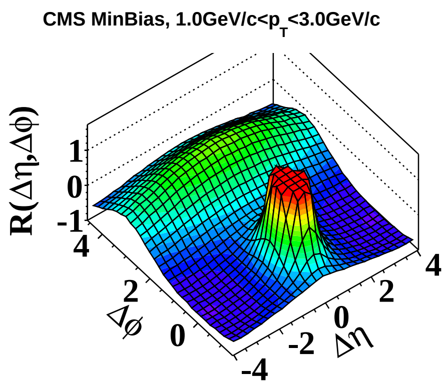

FIGURE 1.21: Correlation function $C(\Delta\eta, \Delta\varphi)$ in minumum bias (left) and high multiplicity (right) pp collisions at $\sqrt{s} = 7$ TeV. Taken from [88].

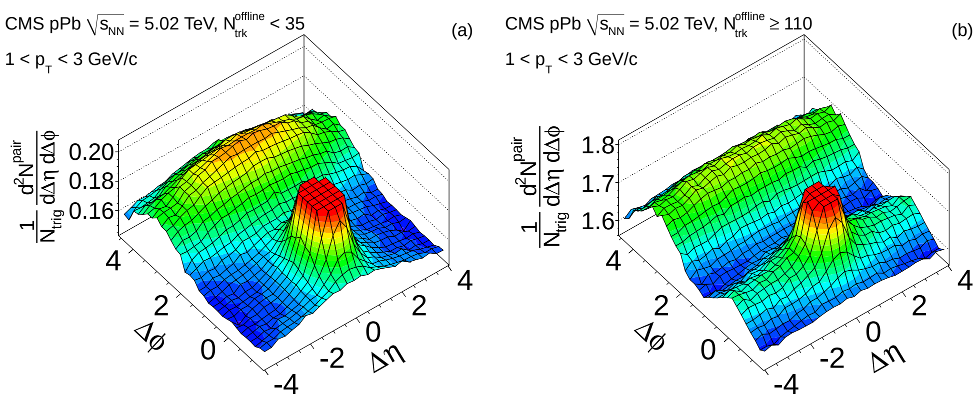

FIGURE 1.22: Correlation function $C(\Delta\eta, \Delta\varphi)$ in low (left) and high (right) multiplicity p–Pb collisions at $\sqrt{s_{\rm NN}} = 5.02$ TeV. Taken from [89].

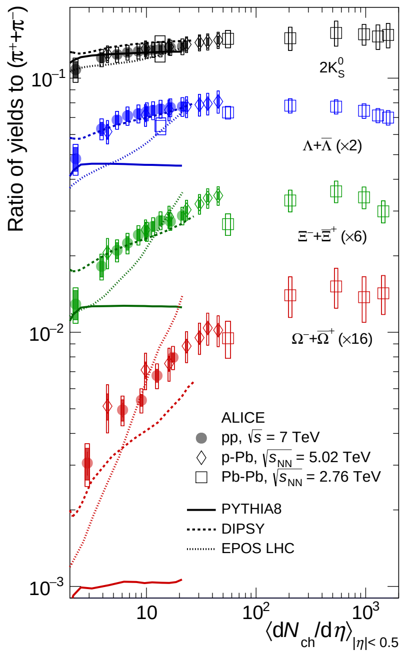

FIGURE 1.23: Ratios of p_T-integrated yield of various hyperons to $\pi^{\pm}$ in pp, p–Pb, and Pb–Pb collisions as a function of the multiplicity compared to MC calculations. Taken from [91].

heavy-ion collisions, where it is connected with the collective behaviour of the created medium, is observed.

Before these observations, the heavy-ion community considered the small collision systems a reference in measuring the large systems. Nevertheless, the similarities between small and large systems opened a discussion on the possibility of creating a droplet of QGP in high multiplicity pp and p–Pb collisions. The observation of strangeness enhancement further confirmed the similarities in high multiplicity pp and p–Pb collisions. The ratios of various hyperons to $\pi^{\pm}$ are shown in Fig. 1.23 in three different collision systems. It can be seen that the strangeness increases with multiplicity. Moreover, the results in the same multiplicity class are in agreement within the uncertainty despite originating from a different collision system. For these reasons, only the minimum bias pp collisions are used nowadays as a baseline in the measurements of heavy-ions.

While the collectivity and strangeness enhancement are observed in the high multiplicity collisions of pp and p–Pb collisions, it is not the case for other probes described in the previous section. Both systems have no jet quenching nor dijet asymmetry, and the nuclear modification factor R_{AA} is consistent with unity [92]. Thus, the medium-induced parton energy loss is compatible with zero. However, it does not exclude the possibility of medium creation – the produced QCD matter is expected to be significantly smaller

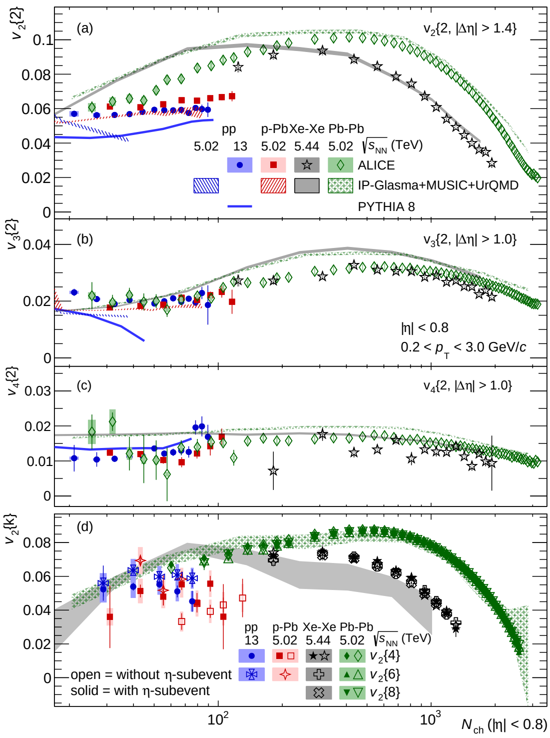

FIGURE 1.24: Multiplicity dependence of flow coefficients $v_n\{m\}$ for different collision systems – pp, p–Pb, Xe–Xe, and Pb–Pb collisions. Taken from [93].

than the one created in heavy-ion collisions. Therefore, the parton energy loss might not be sensitive enough to detect a QGP droplet with the current uncertainties of the measurements. Nevertheless, it is important to emphasize the experimental measurements help to point out the similarities between large and small systems, but the conclusion about underlying physics mechanism is typically obtained by comparing the obtained results with various models with and without deconfined medium and fluid-like dynamics.

1.4.1 Anisotropic flow in small collision systems

The measurements of anisotropic flow in large collision systems significantly contributed to the discovery of the QGP in such systems. Therefore, this observable, quantified by flow coefficients $v_n\{m\}$, is selected to study the anisotropic collectivity in small systems as well. The long-range multi-particle correlations are used for its investigation as the collectivity is understood as the correlated movement of many particles at larger distances. Nevertheless, other effects can mimic a similar behaviour. For that reason, all correlations not associated with the common symmetry planes, referred to as non-flow, must be suppressed.

The measurements of different flow harmonics n obtained from different orders of m-particle cumulants in four collision systems as a function of multiplicity is shown in Fig. 1.24. The collisions energies are similar for p–Pb, Xe–Xe, and Pb–Pb collisions. The collision energy of pp collisions is higher, however, no collision energy dependence is expected [93]. The v_2 coefficients in large systems depend on the collision multiplicity, which can be explained by the dependence of v_2 on the initial eccentricity. Only weak dependence is observed in small collision systems as the initial eccentricity ε_2 is driven mostly by the sub-nucleon fluctuations. However, the magnitude and the ordering of harmonics, i.e., $v_2\{2\} > v_3\{2\} > v_4\{2\}$, are the same at the same multiplicities in all reported collision systems. The bottom panel of Fig. 1.24 shows $v_2\{m\}$ measured using m-particle cumulants with and without pseudorapidity separation between correlated particles. Such a measurement is important as by using higher order cumulants and the pseudorapidity separation, the non-flow effects, dominant in small systems, are suppressed. Different methods of non-flow suppression are described in detail in Sec. 3.5.

Furthermore, the measurement is compared with two different models – PYTHIA for pp collisions and a hybrid model for all the collision systems, including pp collisions. The hybrid model contains IP-Glasma simulation that describes the initial state dynamics by following the colour glass condensate prescription of gluon saturation in the initial state [94]. The evolution of the medium is described by the (3+1)D hydrodynamic model MUSIC [95]. The hadronic rescattering is addressed using the UrQMD model [96]. The calculations from the hybrid model are in good agreement with the experimental data points in high multiplicities of the large collision systems. In small systems, the agreement between the data and the model is worse. The model qualitatively describes the experimental data in p–Pb collisions, but fails to describe pp collisions. A new hydrodynamic calculations at the same collision energy as the data, available in [97], significantly underestimate the data as well. Finally, the model without any collective effects (PYTHIA) does not represent the data as it cannot describe the ordering of harmonics nor the dependence on the multiplicity [93].

The measurement can be extended to study the p_{T}-dependence of the flow coefficients. The results of $v_n(p_{\mathrm{T}})$ in three different collision systems, p+Au, d+Au, and ^{3}He+Au, are shown in Fig. 1.25. The systems are selected as they all have different initial geometries. From the average system eccentricities shown in Ref. [98], d+Au and ^{3}He+Au are driven mostly by the geometry of the projectiles (d and ^{3}He, respectively). However, p+Au collisions are driven by the fluctuations of the initial state as the projectile (p) is on average circular. Thus, it can be concluded that the hydrodynamics translates the initial geometry into the final flow coefficients, as the ordering

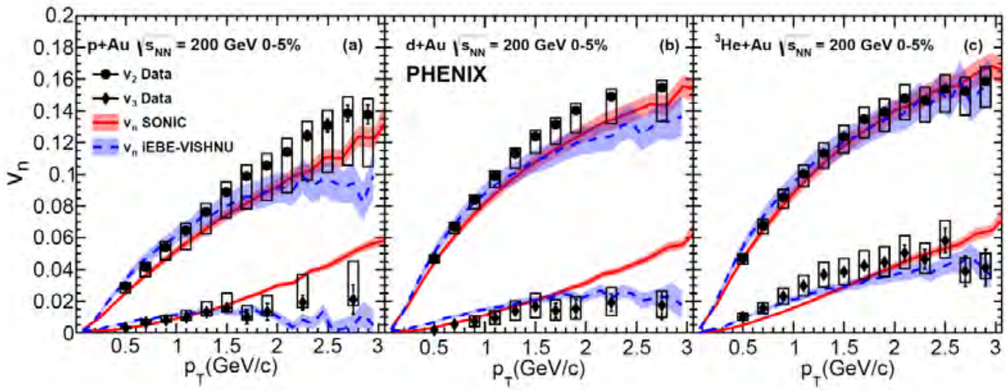

FIGURE 1.25: Flow coefficients $v_n(p_T)$ for different collision systems: p+Au (a), d+Au (b), and ^{3}He+Au (c) in the centrality class 0–5% at $\sqrt{s_{NN}} = 200$ GeV compared to models. Taken from [98].

$v_2^{p+Au} > v_2^{d+Au} > v_2^{^3He+Au}$ is observed. Nevertheless, the v_3 coefficients in p+Au, d+Au, and ^{3}He+Au collisions are system independent when correlating only the particle from the central pseudorapidity, $|\eta| < 0.9$ [99]. Such a measurement proves the importance of sub-nucleon fluctuations in the description of the initial state. To further study the measured $v_2(p_T)$ and $v_3(p_T)$ across three different geometries, a comparison with two different models is provided – hybrid hydrodynamic models SONIC [100] and iEBE-VISHNU with tuning for small systems [101]. In both models, the hydrodynamic evolution is applied on the initial conditions with $\eta/s = 0.08$. Both hydrodynamic models qualitatively describe the data in all shown systems, supporting the hypothesis of the dependence of flow coefficients v_n on the initial eccentricity. Moreover, the predicted difference in magnitude between different harmonics v_2 and v_3 is comparable to the one that is observed.

The study of flow coefficients as a function of p_T can be extended by measuring flow of identified particles, in analogy to the measurement in Pb–Pb collisions, shown in Fig. 1.19. Such a measurement in high multiplicity p–Pb and pp collision are shown in Figs. 1.26 and 1.27, respectively. Flow coefficients are reported for $\pi^{\pm}$, $K^{\pm}$, and $p(\bar{p})$ with the peripheral subtraction method in p–Pb collisions and K^0_S and $\Lambda(\bar{\Lambda})$ with and without peripheral subtraction method in pp collisions[5]. A hint of mass ordering, typical for heavy-ion collisions, can be observed in the low p_T region in both systems. In reported p–Pb collisions, no baryon-meson grouping is observed due to the large statistical uncertainties and the measurement covering only the p_T region up to $p_T = 4$ GeV/c. In pp collisions with larger p_T coverage, the uncertainties of the flow coefficients are significant as well. Therefore, no baryon-meson grouping (or splitting) is observed. Such

[5]The peripheral subtraction method is described in detail in Sec. 3.5.

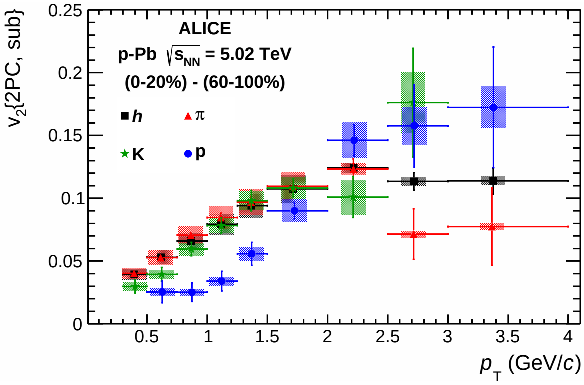

FIGURE 1.26: Flow coefficients $v_2(p_T)$ for $\pi^{\pm}$, $K^{\pm}$, and $p(\bar{p})$ in high multiplicity p–Pb collisions at $\sqrt{s_{NN}} = 5.02$ TeV. Taken from [102].

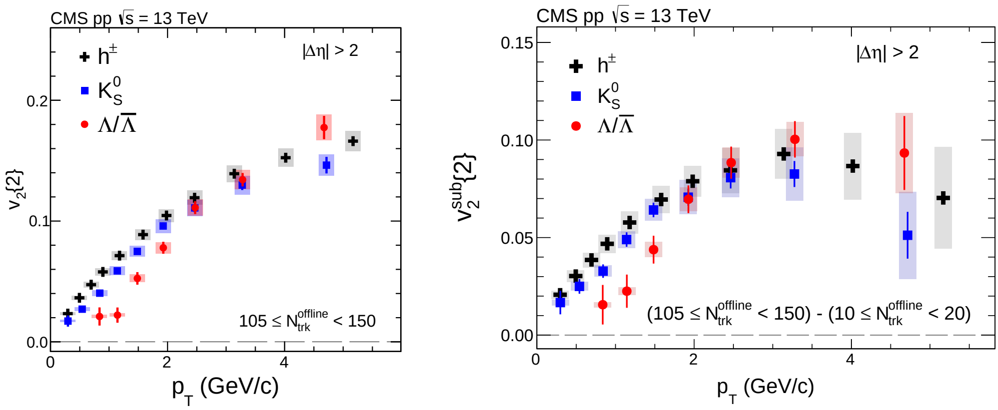

FIGURE 1.27: Flow coefficients $v_2(p_T)$ for K^0_S and $\Lambda(\bar{\Lambda})$ without (left) and with (right) peripheral subtraction in high multiplicity pp collisions at $\sqrt{s} = 13$ TeV. Taken from [103].

an observation has a potential to prove whether the partonic collectivity occurs in small collision systems as well.

2 Experimental background

The European centre for nuclear research (CERN), founded in 1954, is a particle physics organisation and the home of the largest particle accelerator in the world, the Large Hadron Collider (LHC). Situated across the Swiss-French borders, CERN has 23 member states and several associate member states and observers [104]. It is a global organisation with many international collaborations, including four major experiments at LHC – ALICE, ATLAS, CMS, and LHCb. This chapter introduces the CERN accelerator complex and the ALICE experiment.

2.1 CERN accelerator complex

The CERN accelerator complex, illustrated in Fig. 2.1, offers many different experimental programs and contains various experimental facilities, including e.g. the antiproton decelerator (AD) or studies of new acceleration techniques, such as the plasma wakefield (AWAKE). Due to the variety of physics programs and differences in their constructions, specifications, including technical details of different pre-accelerators, are out of the scope of this thesis.

Circular accelerators in this complex generally use older, smaller, and less powerful circular accelerators as their pre-accelerator. In case of the Large Hadron Collider (LHC) [106], the chain conists of the Proton Synchrotron (PS) [107], Super Proton Synchrotron (SPS) [108], and finally, LHC, the largest and the most powerful part of the system [106]. The first one in this complex, PS, is filled with particles from a circular accelerator Booster and a linear accelerator Linac2[1] for protons, or from a circular accelerator Leir and a linear accelerator Linac3 for ions. The sources of Linac2 and Linac3 are hydrogen and lead atoms, respectively, that have been stripped of their electrons before entering the linear accelerators [109].

The LHC was built in a tunnel initially made for the Large Electron-Positron Collider (LEP) [110], between 45 and 170 m under the ground. It is 26.7 km in circumference with two rings where particles are accelerated in the opposite directions, with eight straight sections and eight arcs [106]. Special "twin-bore" magnets (or two-in-one) are used with the magnetic flux circulating in the opposite directions. LHC uses superconducting magnets cooled down by super-fluid helium below 2 K which creates a magnetic field of

[1] Linac2 was replaced during the Long Shutdown 2 by Linac4, however, the data in this work were collected before that, i.e. data from LHC Run 2 was used.

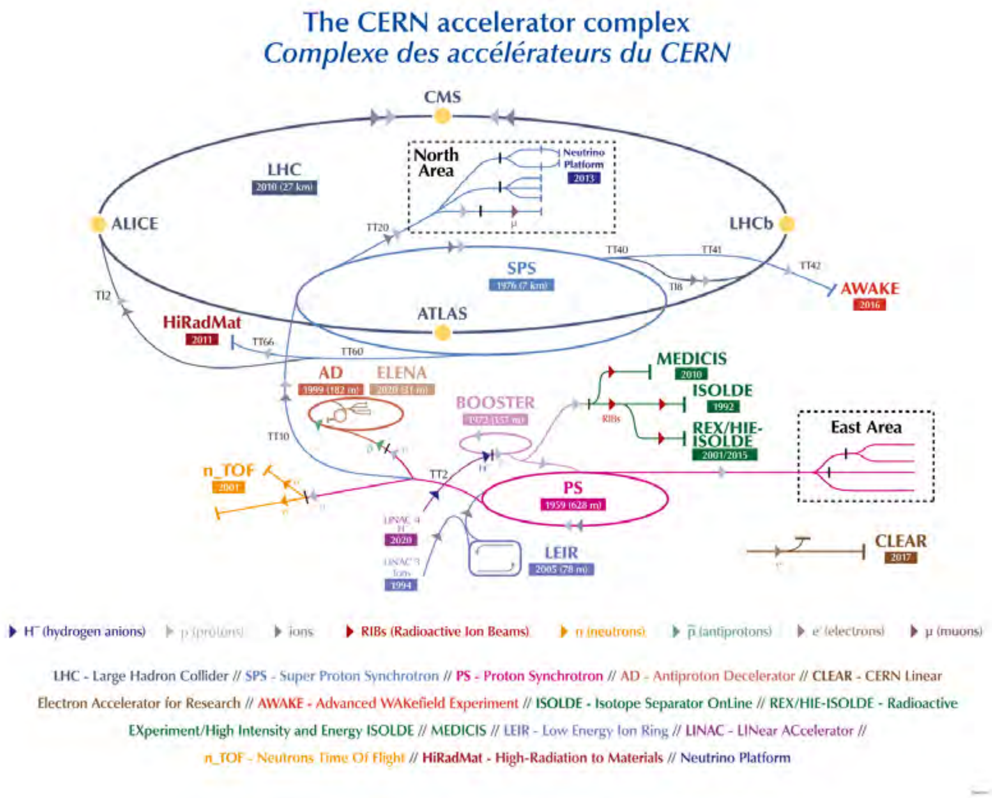

FIGURE 2.1: A scheme of the CERN acceleration complex as of February 2022 [105].

around 8 T. For bending the trajectory of accelerated particles, 1232 dipole magnets are used, each 16.5 m long with a mass of approximately 27.5 t. All interconnected dipole magnets cannot have the relative variations of the magnetic field greater than 10^{-4} [106], i.e. the imperfections have to be reduced to the minimum in each of them, which makes the manufacturing and the construction very difficult. The beam pipe, magnets, and several thermal shields are all in a cylindrical vacuum vessel with 914 mm outer diameter in order to maintain the magnetic coils at the super-cooled state.. A high-quality vacuum is needed inside the beam pipe to prevent any kind of interaction of the environment with the beam particles.

Quadrupole magnets are used to focus particle beams with two pairs of magnets rotated by 90°. Higher orders of magnetic multipoles are used for additional corrections of different types. In addition, before each interaction point, a set of inner triplet magnets is used to focus the bunch of particles into even smaller sizes. These magnets also correct the effects of the spectrometer dipoles at specific interaction points, including ALICE.

LHC is injected with up to 2808 proton bunches with an energy of 450 GeV, with each bunch containing approximately $1.15 \cdot 10^{11}$ protons. During a lead LHC run, 592 bunches with $7 \cdot 10^{7}$ lead ions are accelerated from initial energy of 177 GeV per nucleon at the injection up to 2.7 TeV. The acceleration is done using radiofrequency cavities at 400 MHz [106]. When the LHC is fully filled with protons, the bunch crossing rate is 25 ns (125 ns for Pb–Pb). Once accelerated to the final 7 TeV per beam, the beam can stay in the LHC before being dumped for 10 hours or more which is known as the beam lifetime.

Beams of particles in opposite directions are crossing at specific points, noted as interaction points (IP). The main LHC experiments are placed at IP1 (ATLAS), IP2 (ALICE), IP5 (CMS), and IP8 (LHCb). The remaining IPs are used, e.g. for beam instrumentation or beam dumping.

Different experiments have different physics programmes and goals. The two biggest experiments, ATLAS (A Toroidal LHC ApparatuS) [111] and CMS (Compact Muon Solenoid) [112], are both general-purpose detectors. One of their main goals, the search for the Higgs boson, was successfully reached in 2012 [25, 26]. In addition, they study the Standard model and search for dark matter and new physics. LHCb (Large Hadron Collider beauty) [113] focuses on symmetry breaking, e.g. differences between matter and antimatter, by studying particles containing the b quark. Finally, ALICE (A Large Ion Collider Experiment) [114] is a general-purpose high-energy heavy-ion detector. Its main aim is to study strongly interacting matter at extreme energy densities. The following sections in this chapter are dedicated to describing various ALICE subdetectors.

2.2 ALICE experiment

The ALICE experiment is a detector and an international collaboration consisting of more than 100 full-member institutes from around the world with more than 2000 active members, of which approximately 1000 are on the author list. The main physics goal of the ALICE experiment, defined in [115, 116], is to measure all the parameters related to the formation of QGP, e.g. the size of the system and the energy density, via studying ultra-relativistic Pb–Pb collision. In addition to heavy ions, ALICE was supposed to study small collision systems, including pp and p–Pb collisions, that would "provide reference data for the nucleus-nucleus collisions" [116]. It was shown later on, and it will also be shown later in this thesis that small collision systems are not only reference data anymore.

For measuring high multiplicity, the acceptance in both rapidity and azimuthal angle had to be relatively large – the central part of the detector covers $|\eta| < 0.9$ in the full azimuthal angle. The scheme of the experiment (used for LHC Run 2) is shown in Fig.

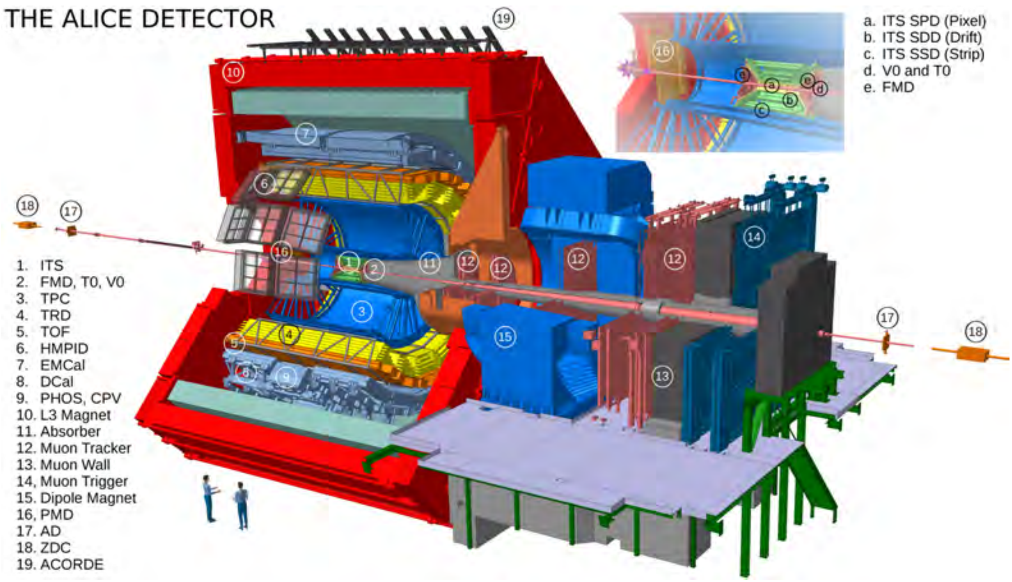

FIGURE 2.2: A scheme of ALICE experiment for LHC Run 2.

2.2. The central region is placed in a uniform magnetic field of 0.5 T created by a solenoid magnet reused from the L3 experiment at the LEP collider [114]. Such a magnetic field allows tracking and particle identification starting from approximately 0.1 GeV/c. In this region, ALICE consists of several subdetectors, such as the Inner Tracking System (ITS), Time Projection Chamber (TPC), and Time Of Flight (TOF). The overall dimensions of ALICE are $16 \times 16 \times 26$ m^3, and the total weight of the detector is approximately 10 000 t. More details about individual subdetectors can be found in the following sections, focusing on the subdetectors that are used in the data analysis. The description is done for detectors as used in LHC Run 2, as the results in this thesis originate from the data collected between 2015 and 2018. Nevertheless, the Sec. 2.9 is dedicated to the ALICE upgrade for LHC Run 3.

2.3 Triggering

The trigger system of the ALICE experiment, also known as the Central Trigger Processor (CTP), is used for selecting events fulfilling specific requirements and for optimising the usage of detectors with different speed and running modes [114, 116]. The trigger is formed in three levels with three latencies. In L0, the fastest part of the system, the signal latency is only 1.2 μs. It combines 24 different inputs from different detectors, e.g. signals from both sides of the V0 detector. Individual conditions are typically checked faster and the decision is made within ≈ 100 ns. The following trigger level, L1, also combines 24 inputs, e.g. it selects only the events with two muon candidates above a certain p_T threshold and checks the centrality information from V0. This is done in 6.5 μs. In the last level, L2, 12 inputs are considered, and a different set of algorithms can be applied based on the running mode of the whole detector. As the detector has to wait for its slowest components, e.g. TPC with its sensitive window of 88 μs, L2 works approximately 100 μs after the collision. Moreover, L2 contains "past-future protection" for Pb–Pb collisions – it rejects an event if any other event occurs within the same time window, i.e. it makes sure TPC reads out one event at a time. This protection works differently in pp collisions where is usually more than one event read out at the time, however, with much lower multiplicities. One must then ensure that all the reconstructed tracks in the event originated in the same primary vertex.

2.3.1 High-multiplicity trigger in pp collisions in Run 3

For LHC Run 3, the Fast Interaction Trigger (FIT) is used as the primary online trigger of the ALICE experiment. As a part of my collaboration service task, I worked on the development of the software trigger for high multiplicity collisions in pp using the ITS detector only, i.e. without the need for FIT preselection. The study's motivation was that the first obtained results were auspicious, with the efficiency and the purity of triggering high multiplicity collisions around 90%. However, those results originated from a toy Monte Carlo study only. The complication in Run 3 is a much higher interaction rate and continuous read-out of many detectors. For ITS, it is expected to have five events on average per read-out frame. We defined the pile-up in ITS as a situation in which two or more vertices are closer than n times the resolution, and these vertices are reconstructed as one. Such a vertex is much more likely to fulfil high multiplicity vertex requirements. My contribution was primarily to help develop the ITS vertex reconstruction using Online-Offline (O^2) analysis tools. Once the vertices were reconstructed, I was able to study the full reconstructed read-out frames with individual events and test the software trigger using ITS. Nevertheless, it is important to say that no final results were obtained as the project was conducted before the final tuning of pp event reconstruction was available, i.e. the event reconstruction in O^2 was done using Pb–Pb tuning. That significantly modified the efficiency and purity of the software trigger. However, more technical details of this project are out of the scope of this thesis.

2.4 V0 detector

V0 is a forward disk-shaped array of plastic scintillator counters on both sides of the ALICE central barrel. It covers pseudorapidity $2.8 < \eta < 5.1$ (V0A) and $-3.7 <$

$\eta < -1.7$ (V0C) [117] which corresponds to 340 cm and 90 cm from the IP along the z-direction, respectively. The disks are divided into eight sectors, each covering 45°in azimuthal angle, in total covering the full azimuth. In the radial direction, it is split into four rings, which makes then 32 counters in total. In the two outer rings of V0C, each segment is split in half in azimuth, creating 48 counters in total. The total multiplicity is measured using the deposited energy per segment with prior knowledge of the average deposited energy per charged particle.

V0 can also measure the luminosity in pp collision and help eliminate false events created by collision with the residual gas in the vacuum chamber or beam-induced background.

A minimum bias (MB) collision is recorded if there is a signal from a charged particle in both V0A and V0C simultaneously and in a coincidence with the beam crossing. The expected time of the signal is considered, 3 ns and 11 ns after the collision for V0C and V0A, respectively [117]. In addition, V0 can serve as a centrality estimator using the multiplicity information from the forward and backward regions [114]. The sum of deposited energy in V0A and V0C (known as V0M amplitude) is used for the classification into the centrality classes using the Glauber model as the information about the impact parameter of the collision is not experimentally known. The model assumes the heavy-ion collision being a superposition of binary nucleon-nucleon collisions. The percentiles of the centrality come from the hadronic cross sections [118]. The method is limited by requiring high purity and efficiency of the selected events, which is approximately at 90% of the hadronic cross section with the V0 detector. This point is then fixed (as a so-called anchor point) as the absolute scale of the centrality using the Glauber Monte Carlo fit of the experimental particle multiplicity. The distribution of V0M amplitude with a Glauber MC fit, and different centrality classes of Pb–Pb collisions at ALICE is shown in Fig. 2.3.

With the information from the V0 detector, a specific trigger configuration can be created to enhance a specific data class. For example, in Pb–Pb data taking in 2018, two specialised triggers were used, a central (0—10%) and a semi-central (30–50%) one. In these cases, the recording of the collision was triggered once the charge deposited in V0 surpassed a certain threshold. The same approach can also be used for triggering high multiplicity pp collisions. With the prior information of the mean V0M amplitude $\langle V0M \rangle$, one can configure the high multiplicity trigger to accept only events with $V0M/\langle V0M \rangle > 4$. With this selection, only approximately 0.1% of minimum bias collisions are selected with significantly higher mean multiplicity in the central region. This can be seen in the distribution of $V0M/\langle V0M \rangle$ and forward multiplicity classes in pp collisions at ALICE in Fig. 2.4.

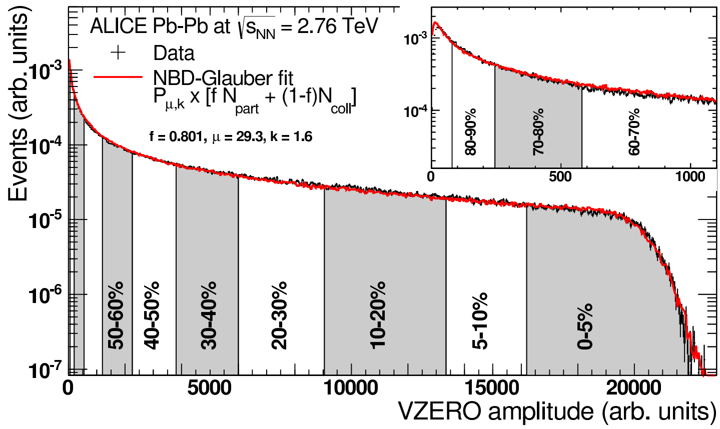

FIGURE 2.3: Distribution of the V0M amplitude with a Glauber Monte Carlo fit used for the centrality determination of Pb–Pb collisions at ALICE. Taken from [118].

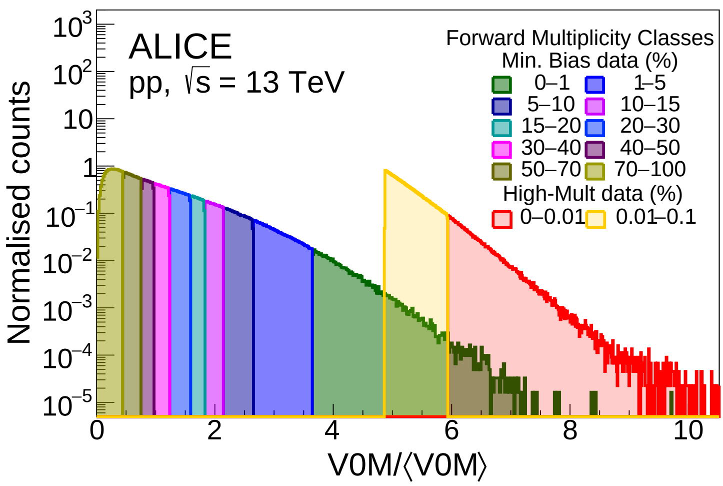

FIGURE 2.4: Distribution of the V0M amplitude scaled by the mean V0M amplitude $\langle V0M \rangle$ that is used for determination of forward multiplicity classes and high multiplicity triggering in pp collisions at ALICE. Taken from [119].

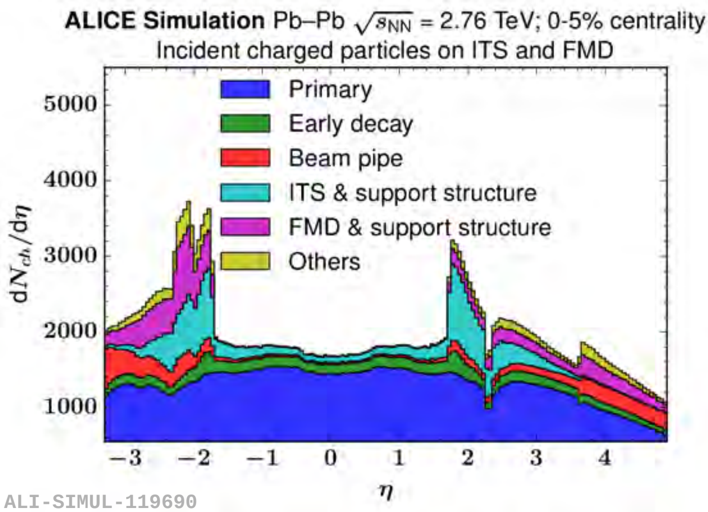

FIGURE 2.5: Origin of signal in the FMD detector.

2.5 Forward Multiplicity Detector

Forward Multiplicity Detector (FMD) is also situated in the forward region of the ALICE detector complex, in the pseudorapidity range $1.7 < \eta < 5.0$ (FMD1,2) and $-3.4 < \eta < -1.7$ (FMD3). Together with ITS in the central pseudorapidity region, it provides multiplicity information across the whole ALICE coverage. FMD consists of 5 ring-shaped one-sided silicon strip detectors with 10200 strips each. The choice of the segmentation was made based on the distribution of particles in the most central Pb–Pb collisions – on average, there should be one charged particle in every strip of the FMD [114]. Individual strips can read up to 20 particles before saturating. Each FMD ring is divided into 20 and 40 azimuthal sectors for inner (FMD1,2,3) and outer (FMD2,3) rings, respectively. The radius of the inner and outer ring is 4.2 – 17.2 and 15.4 – 28.4 cm, respectively.

Similarly to V0, the information on the charged particle multiplicity originates from the deposited energy in individual segments with the prior knowledge of the average deposited energy per charged particle from the Landau distribution, which is also dependent on the angle of the particle with respect to the detector and affected by the signal overflow to neighbouring strips. The information on multiplicity is also significantly affected by the presence of secondary particles that comes, e.g. from the scattering of primary particles on different materials along the way, such as the beam pipe, ITS and its cables, T0 and V0 detectors and the muon absorber [117]. The origin of the signal in the FMD, including different sources of secondary particles, is shown as a function of η in Fig. 2.5. Such a study is essential as a correction for the secondaries is needed to obtain a real multiplicity. The correction is generally obtained using a Monte Carlo simulation.

Unlike V0, FMD is not used as a multiplicity trigger but only provides offline information due to its read-out time of more than 1.2 μs.

2.6 Inner Tracking System

The Inner Tracking System (ITS) is the innermost central detector of ALICE, made out of six layers of silicon detector. Its main physics goal is to reconstruct the primary vertex (PV) of the collision and all the secondary and tertiary vertices from weak decays of heavier particles. The resolution of the vertex reconstruction is better than 100 μm. Additionally, it provides precise tracking and particle identification via the specific energy loss ($\mathrm{d}E/\mathrm{d}x$) of tracks with $100 < p < 200$ MeV/c (non-relativistic region). The relative momentum resolution is around 2% for $\pi^{\pm}$ with $0.1 < p_{\mathrm{T}} < 3$ GeV/c [114].

ITS surrounds the beam pipe with its six layers of cylindrical silicon detectors covering a radius between 3.9 and 43.0 cm from the interaction point (IP). The two innermost layers are made of silicon pixel detector (SPD) with a very large granularity – 3 276 800 and 6 553 600 channels in the first and second layer, respectively. It is necessary to obtain the exact 2D information considering the high particle density. For the innermost layer, there can be up to 50 particles/cm^2. The spatial resolution in this layer is 12 μm. As the read-out is binary, the first two layers do not contribute to the particle identification.

The third and the fourth layer are made of silicon drift detector (SDD) with 43 008 and 90 112 channels, respectively. The particle density is significantly smaller compared to the innermost layer, with approximately 7 particles/cm^2. With the maximum drift time of 6.3 μm, its average resolution is 25 and 35 μm along the anode (z) and the drift ($r\varphi$) direction, respectively.

The last two layers of ITS, made of double-sided silicon strip detectors (SSD), have 1 148 928 and 1 459 200 channels, respectively, with the spatial resolution of 20 and 820 μm for $r\varphi$ and z, respectively. The particle density is less than one particle/cm^2. The precision of these two layers is essential as it serves to match the reconstructed tracks with the tracks from the TPC sub-detector (see next section for TPC). The read-out of the four outer layers is analogue and therefore allows the particle identification via $\mathrm{d}E/\mathrm{d}x$.

Pseudorapidity coverage of ITS is $|\eta| < 0.9$ for all its layers, but for the first layer it is $|\eta| < 1.98$. The overlap with FMD in pseudorapidity secures continuous information of the charged particle multiplicity in η. Each layer is longer than the previous one (going from the innermost layer), ranging from $\pm z$ 14.1 to 28.9 cm [114].

The read-out time of the silicon detector is generally very short, therefore, ITS (mostly SPD) contributes to the L0 trigger (by Fast-OR pixel trigger), e.g. by rejecting the background events in low multiplicity pp data-taking. Based on the configuration of the CTP, ITS can contribute to each trigger level (L0, L1, L2).

2.7 Time Projection Chamber

The Time Projection Chamber (TPC) is the main tracking detector of ALICE located in the central barrel with the pseudorapidity coverage of $|\eta| < 0.9$ or $|\eta| < 1.5$ with a reduced momentum resolution. It has a cylindrical shape covering the full azimuthal angle, and its active volume is 90 m^3 in between the radius of 85 and 250 cm. The total length in z is 500 cm [114]. In addition to tracking, it contributes to the particle identification, track separation and momentum measurement of charged particles in the range $0.1 < p_{\mathrm{T}} < 100$GeV/$c$. The active volume is able to contain up to 20 000 charged tracks (primary and secondary) as the most central Pb–Pb collisions have $\mathrm{d}N_{ch}/\mathrm{d}\eta \approx 8000$.

TPC is filled with $Ne/CO_2/N_2$ (90/10/5) mixture operating at a high drift field of 400 V/cm. The $r\varphi$ coordinate is obtained from the ionization electrons drifting to the end-plate cathodes with the resolution of 1100 and 800 μm for the inner and outer radius, respectively. In total, there are 557 568 read-out channels (pads) grouped in 18 sectors. The z coordinate is obtained from the drift time with an average drift velocity in the aforementioned gas mixture of 2.7 cm/μs. The resolution in z varies between 1100 and 1250 μm [120]. Due to the relatively slow drift time with a maximum of 92 μs, it is the slowest detector at ALICE.

For the precise calibration of the TPC, a laser system with a pulsed laser beam with a UV wavelength of 266 nm is used [121]. Through beam splitters and mirrors, the beam with a diameter of 25 mm is split into in total 336 beams of 1 mm diameter. They enter the TPC and create a signal in the shape of straight lines at known positions. It is a crucial part of TPC as it provides information on the drift velocity that changes over time depending on the gas density.

The reconstruction of charged particle tracks is done by combining individual space points reconstructed by the TPC using the Kalman filter procedure [114]. The reconstruction starts at the outermost pad of TPC because of the smaller charged particle density and continues towards the inner part of TPC, where the particle density is larger. In total, a maximum of 159 space points can be used for every track. Once all the possible points from the TPC are used, the track candidate is propagated to the ITS spatial points. In every step, a candidate is required to match with a prolongation of the track based on the previously reconstructed space points. A χ^2 parameter is calculated from the difference between the space point candidates and the reconstructed tracks and can be used for high-quality track selection. Numerous fake tracks with at least one point wrongly assigned are reconstructed during the process of combined TPC-ITS track reconstruction. Nevertheless, the probability of creating a fake track is always below 10% and decreases to approximately 1% in higher p_{T}. That leads to the efficiency of the track reconstruction of approximately 90% at $p_{\mathrm{T}} = 0.2$ GeV/c and increases up to 95% in higher p_{T} region.

The reconstruction efficiency is connected with a p_{T} precision. The relative momentum resolution is around 1.5% when using combined TPC-ITS track reconstruction in both Pb–Pb and pp collisions for $p_{\mathrm{T}} < 20$ GeV/c. The best relative resolution can be obtained at the low p_{T} region (around $p_{\mathrm{T}} \approx 0.5$ GeV/c). At $p_{\mathrm{T}} \approx 1$ GeV/c, the spatial resolution in the transverse plane is 100 μm when using TPC-ITS reconstructed tracks. This is essential for the reconstruction of secondary vertices originating from weak decays.

Finally, TPC significantly contributes to the particle identification (PID), which is done via the prior knowledge of the total energy loss per unit path length of a specific particle species in the studied medium, described by the Bethe-Bloch formula

$$\langle \frac{\mathrm{d}E}{\mathrm{d}x} \rangle \propto -\frac{1}{\beta^2} \ln[\beta^2\gamma^2 - \beta^2], \tag{2.1}$$

where β is the particle velocity and γ is the relativistic Lorentz factor [9]. The resolution of $\langle \frac{\mathrm{d}E}{\mathrm{d}x} \rangle$ measurement with the TPC varies from 5.5% in pp collisions to 6.5% in central Pb–Pb collisions. In addition to the particle density, it also depends on the number of clusters (space points) in the TPC that have been used for the track reconstruction as $\sigma \propto 1/\sqrt{n_{cl}}$. The calibration is done approximately once a year by injecting radioactive isotope ^{83}Kr with a known spectrum.

The distribution of specific energy loss of tracks reconstructed by the TPC is shown in Fig. 2.6 together with the theoretical lines of individual particle species. The relative difference between the measured and calculated $\langle \frac{\mathrm{d}E}{\mathrm{d}x} \rangle$ is expressed in terms of $n\sigma$ which can be used in the data analysis for selecting specific particle species. Nevertheless, as can also be seen in Fig. 2.6, the discriminating power is dependent on the p_{T} of the particle, and it is the highest in the lower p_{T} region ($p_{\mathrm{T}} < 1.0$ GeV/c) where $1/\beta^2$ dominates the Bethe-Bloch relation and where the particles are well separated. In the relativistic region of the Bethe-Bloch equation $p_{\mathrm{T}} > 3.0$ GeV/c, TPC can be used for PID with the usage of the statistical unfolding method [122]. However, in the intermediate p_{T} ($1.0 < p_{\mathrm{T}} < 3.0$ GeV/c) which is the region of the minimum ionising region, TPC cannot be reliably used for PID as it cannot separate different particle species.

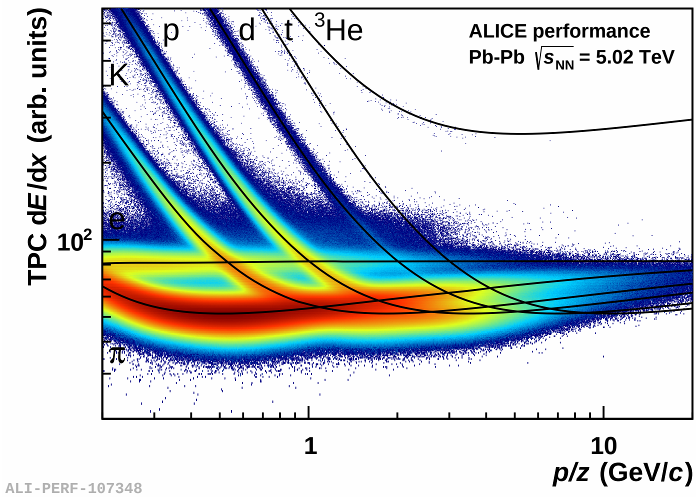

FIGURE 2.6: The distribution of specific energy loss of tracks reconstructed by the ALICE TPC in Pb–Pb collisions at $\sqrt{s_{\rm NN}} = 5.02$ TeV together with theoretical lines for selected particle species.

2.8 Time-Of-Flight detector

The Time-Of-Flight (TOF) detector is also situated in the central barrel ($|\eta| < 0.9$), covering the whole azimuthal angle. It has an internal and outer radius of 370 cm and 399 cm, respectively [114]. Its main physics goal is to identify charged particles in the intermediate $p_{\rm T}$ region where TPC cannot separate different species. Moreover, it can be used as a trigger for cosmic ray events and ultra-peripheral collisions.

Similarly to the ITS and the TPC, high multiplicity in the central Pb–Pb collisions had to be considered when designing TOF. For that reason, TOF is made out of 1539 Multi-gap Resistive-Plate Chambers (MRPC) strip detectors, grouped into 18 symmetric modules in the azimuthal direction and 5 modules (with different lengths) in z direction. Individual MRPC strips are divided into 48 pads with two rows each. In total, 157 248 read-out pads are available.

MRPC were tested to provide outstanding efficiency ($\approx 99\%$) and time resolution ($\sigma_t \approx 50$ ps, including the electronics). The material budget affects the final efficiency of TOF, primarily by detectors between the IP and TOF, especially the Transition Radiation Detector (TRD). In addition, low $p_{\rm T}$ tracks ($p_{\rm T} < 0.3$ GeV/c) do not reach TOF due to the curvature of their trajectory caused by the magnetic field within ALICE.

TOF contributes to the PID by measuring the particle velocity β from its time of flight. The prior knowledge of the time of the collision t_{col} is needed. It is typically obtained from the T0 detector situated in the forward region ($-3.3 < \eta < -2.9$ and $4.5 < \eta < 5.0$)

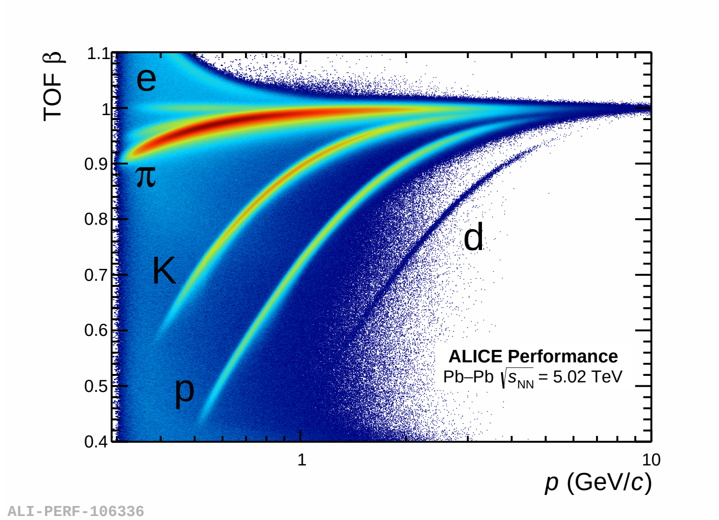

FIGURE 2.7: The distribution of particle velocity as reconstructed by the ALICE TOF in Pb–Pb collisions at $\sqrt{s_{\mathrm{NN}}} = 5.02$ TeV.

and using photomultiplier tube technology [117]. Nevertheless, as the signal from T0 is not always available, the signal from TOF itself can also be used as t_{col}, with its resolution getting better with the larger multiplicity [123]. The final time resolution of TOF then considers the resolution of the t_{col} as well and is 56 ps[2]. For the final PID, the expected time of a selected species with corresponding p_{T} is needed. Then one can calculate $n\sigma$ as the relative distance from the calculated value. This approach extends the p_{T} region of the PID up to $p_{\mathrm{T}} < 3$ GeV/c and $p_{\mathrm{T}} < 5$ GeV/c for π-K and K-p separation with more than 3σ [114, 123]. The distribution of β as a function p_{T} in Pb–Pb collisions is shown in Fig. 2.7 together with the labels of the corresponding identified particle species.

2.9 Upgrade

ALICE was taking data during the LHC Run 1 (2009–2012) and LHC Run 2 (2015 – 2018). During the Long Shutdown 2 (LS2), a major upgrade of the ALICE detector took place. The LS2 has been extended due to the complications caused by the global COVID-19 crisis at CERN. With a small delay, the physics programme of the LHC Run 3 successfully started on 5 July 2022. In this section, a brief summary of the ALICE upgrade is presented.

Before LS2, Pb–Pb data were recorded by ALICE with a maximum of 500 Hz readout rate. For Run 3, the collision rate of 50 kHz is expected [125] which brings several

[2] As a CERN Summer Student, I tested the time resolution using μ from cosmic rays events and using pp collisions. The final report can be found at [124].

challenges, considering, e.g. very slow read-out time of TPC ($\sim 100\ \mu$s). The major upgrade consisted of replacing the ITS detector and upgrading the TPC read-out chambers, improvement of triggering by introducing a new Forward Interaction Trigger (FIT) detector, improvement of the data collection and reconstruction, and the addition of a new detector in the forward region – the Muon Forward Tracker.

Inner Tracking System

Run 2 ITS, described in Sec. 2.6, consisted of 6 layers of a combination of SPD, SDD, and SSD. The new ITS consists of 7 layers, all made from ALPIDE (ALICE Pixel Detector) Monolithic Active Pixel Sensors (MAPS), and covers an extended pseudorapidity range of $|\eta| < 1.22$. Thanks to MAPS, the material budget is reduced seven times compared to the old ITS, and the thickness of the innermost layers is only 50 μm [126]. Additionally, the distance between the IP and the first layer is currently only 22.4 mm, as the size of the beam pipe has been reduced. This allows high precision tracking and vertex determination. The former was improved especially in the low p_{T} region. The intrinsic spatial resolution is now 5 μm and consistent across all the ITS layers, with the detector efficiency of > 99 % [127]. The latter is crucial for the heavy flavour physics, which is a major part of the ALICE Run 3 programme. Two read-out modes are possible, continuous and triggered, with both of them being able to record the collision up to 100 kHz for Pb–Pb , which is twice the expected collision rate (50 kHz).

Time Projection Chamber

To be able to collect the data at the increased collision rate, TPC was changed from MWPC to gas electron multipliers (GEM) stack that prevents charge accumulation in the active detector volume [128]. To reduce ion backflow, a gating grid was used in LHC Run 1 and Run 2. For Run 3, the GEM stacks were designed to keep it at approximately 1%. The upgraded TPC operates with a continuous read-out which brings a challenge for the read-out hardware. For that reason, specialised GPU-based data reduction has to be introduced.

The new design of the TPC has been chosen to keep high tracking and PID capabilities with values similar to Run 2. The tracking efficiency is high and stable for $p_{\mathrm{T}} > 0.2\mathrm{GeV}/c$. The relative resolution of $\langle \frac{\mathrm{d}E}{\mathrm{d}x} \rangle$ is better than 10%.

Fast Interaction Trigger

The Fast Interaction Trigger (FIT) is situated in the forward region and covers a large pseudorapidity region replacing FMD, V0, and T0 detectors from Run 2. It consists of several parts – FT0, FV0, and FDD. FT0 is organized into 28 and 24 Cherenkov modules, covering $-3.4 < \eta < -2.3$ and $3.8 < \eta < 5.0$, respectively. It provides a central trigger in Pb–Pb collisions and a minimum bias trigger for pp and p–Pb collisions. It also measures the collision time, crucial for PID from the TOF detector, with a resolution of around 33 ps, and an online luminometer. FV0 consists of 50 plastic scintillators organized in pseudorapidity range $2.2 < \eta < 5.1$ into 5 rings. It provides centrality information (from the forward multiplicity) in Pb–Pb collisions. FDD, made from two arrays of double-layers scintillators covering the range $-4.9 < \eta < -6.9$ and $4.7 < \eta < 6.3$, is used for triggering and an online beam monitoring as well as for ultra-peripheral and diffractive studies [125, 129].

Muon Forward Tracker

The Muon Spectrometer, covering $-4.0 < \eta < -2.5$, provided identification and measurement of muons in the LHC Run 1 and Run 2 with certain limitations in the resolution, mainly in the vertex region. To improve the measurement, for Run 3, the Muon Forward Tracker (MFT) was added to the region $-3.6 < \eta < -2.5$. MFT is a silicon pixel detector made of MAPS that significantly improves the precision of the vertexing and muon tracking [130].

3 Methodology

Anisotropic flow, introduced in Sec. 1.3.2, can be quantified by flow coefficients v_n, which are obtained from the Fourier expansion of the azimuthal distributions of final state particles,

$$\frac{\mathrm{d}N}{\mathrm{d}\varphi} \propto 1 + 2\sum_{n=1}^{\infty} v_n \cos n(\varphi - \Psi_n). \tag{3.1}$$

Ψ_n is the n-th flow symmetry plane defined by the impact parameter b and the beam direction driven by the initial symmetry plane Φ_n [131, 132]. As b cannot be experimentally obtained on an event-by-event basis, the real symmetry plane is also unknown. The experimental estimation of the flow symmetry plane is referred to as the event plane Ψ_{EP}. As it is an approximation, its resolution has to be considered when calculating v_n coefficients [71]. Alternatively, one can eliminate Ψ_n by considering two particles

$$\langle\langle \cos[n(\varphi_1 - \varphi_2)]\rangle\rangle = \langle\langle \cos n[(\varphi_1 - \Psi_n) - (\varphi_2 - \Psi_n)]\rangle\rangle = \langle v_n^2\rangle + \delta_n, \tag{3.2}$$

where δ_n represents a contribution of the non-flow in the two-particle correlations [133]. Non-flow is generally used to describe the azimuthal angle correlations that are not associated with the common symmetry planes[1]. If the non-flow contribution can be suppressed well enough, two- and multi-particle correlations can be used for calculating the flow coefficients v_n.

This chapter presents individual steps for obtaining v_n coefficients from two- and multi-particle cumulants, both differential and integrated over the transverse momentum p_{T}. For the former, it is possible to study flow coefficients for different particle species as well. For the latter, the correlations between different moments of different flow harmonics can be measured. In addition, a method of constructing the two-dimensional correlation function, used for the flow calculation in the small systems, is presented in this chapter as well. Finally, the methods of the non-flow suppression are presented, such as the pseudorapidity separation or the subtraction using the low multiplicity collisions.

[1]Typical examples of the contribution to the non-flow are decays of the resonances or correlations between particles that originate from the same jet cone.

3.1 Multi-particle correlations

A single event average of two-particle correlation of the same harmonic n is defined as [131]

$$\begin{aligned}\langle 2\rangle_{n,-n} =& \langle e^{in(\varphi_1-\varphi_2)}\rangle = \langle\cos[n(\varphi_1-\varphi_2)]\rangle \\ =& \frac{1}{M(M-1)}\sum_{i,j=1;\, i\neq j}^{M}\cos[n(\varphi_i-\varphi_j)],\end{aligned} \tag{3.3}$$

where M is the event multiplicity (number of particles in the studied event) and the condition $i \neq j$ ensures self correlations are not included in the final term. Nevertheless, the implementation of a double loop (or multiple nested loops for the case of multi-particle correlations) is computationally challenging. For that reason, a method that requires a single loop over the particles has been proposed in [133]. It introduces Q-vectors that are used for calculating two- and multi-particle cumulants.

3.1.1 Generic framework

Aforementioned Q-vectors can be further extended as introduced in [80]. The extension consists of an addition of particle weights w, used for the correction of the non-uniform detector acceptance or reconstruction efficiency[2]. The Q-vector is defined as

$$Q_{n,p} \equiv \sum_{i\in\mathrm{RFP}}^{M} w_i^p e^{in\varphi_i}, \tag{3.4}$$

where n, p are its harmonic and power, respectively, and φ_i, w_i are the azimuthal angle and the weight of i-th particle. The RFP is an acronym for reference flow particles that are typically integrated over a certain p_{T}. The two-particle correlation can be expressed using Q-vectors as

$$\langle 2\rangle_{n_1,n_2} = \frac{Q_{n_1,1}\cdot Q_{n_2,1} - Q_{n_1+n_2,2}}{Q_{0,1}^2 - Q_{0,2}}. \tag{3.5}$$

Typically, when calculating the flow coefficient of harmonics n, we are interested in the case where $n_1 = n, n_2 = -n$. From the definition of the Q-vector, it is clear that

$$Q_{-n,p} = Q_{n,p}^{*}. \tag{3.6}$$

Then Eq. 3.5 becomes

$$\langle 2\rangle_{n,-n} = \frac{|Q_{n,1}|^2 - Q_{0,2}}{Q_{0,1}^2 - Q_{0,2}}. \tag{3.7}$$

[2]More about different corrections is discussed in Sec. 4.7.

Similarly, one can express four-particle correlation in terms of Q-vectors as

$$\langle 4\rangle_{n_1,n_2,n_3,n_4} = \frac{\mathrm{N}\langle 4\rangle_{n_1,n_2,n_3,n_4}}{\mathrm{D}\langle 4\rangle_{n_1,n_2,n_3,n_4}}, \tag{3.8}$$

where N and D stands for numerator and denominator, respectively, and

$$\begin{aligned} \mathrm{N}\langle 4\rangle_{n_1,n_2,n_3,n_4} &= Q_{n_1,1}Q_{n_2,1}Q_{n_3,1}Q_{n_4,1} - Q_{n_1+n_2,2}Q_{n_3,1}Q_{n_4,1} - Q_{n_2,1}Q_{n_1+n_3,2}Q_{n_4,1} \\ &- Q_{n_1,1}Q_{n_2+n_3,2}Q_{n_4,1} + 2Q_{n_1+n_2+n_3,3}Q_{n_4,1} - Q_{n_2,1}Q_{n_3,1}Q_{n_1+n_4,2} \\ &+ Q_{n_2+n_3,2}Q_{n_1+n_4,2} - Q_{n_1,1}Q_{n_3,1}Q_{n_2+n_4,2} + Q_{n_1+n_3,2}Q_{n_2+n_4,2} \\ &+ 2Q_{n_3,1}Q_{n_1+n_2+n_4,3} - Q_{n_1,1}Q_{n_2,1}Q_{n_3+n_4,2} + Q_{n_1+n_2,2}Q_{n_3+n_4,2} \\ &+ 2Q_{n_2,1}Q_{n_1+n_3+n_4,3} + 2Q_{n_1,1}Q_{n_2+n_3+n_4,3} - 6Q_{n_1+n_2+n_3+n_4,4}\,, \end{aligned} \tag{3.9}$$

$$\begin{aligned} \mathrm{D}\langle 4\rangle_{n_1,n_2,n_3,n_4} &= \mathrm{N}\langle 4\rangle_{0,0,0,0} \\ &= Q_{0,1}^4 - 6Q_{0,1}^2Q_{0,2} + 3Q_{0,2}^2 + 8Q_{0,1}Q_{0,3} - 6Q_{0,4} \end{aligned} \tag{3.10}$$

For calculating p_{T}-differential two-particle correlations, a variation of Q-vector is introduced – if all the contributions originate only from particles of interest (POI) in a specific kinematic region, such as p_{T}, p-vector is defined as

$$p_{n,p} \equiv \sum_{i\in\mathrm{POI}}^{M} w_i^p e^{in\varphi_i}. \tag{3.11}$$

If the phase space between RFP and POI overlaps, it results in self correlations that have to be removed. This is addressed by constructing a q-vector as

$$q_{n,p} \equiv \sum_{i\in(\mathrm{RFP}\cap\mathrm{POI})}^{M} w_i^p e^{in\varphi_i}. \tag{3.12}$$

Then the differential two-particle correlation is

$$\langle 2'\rangle_{n,-n} = \frac{p_{n,1}\cdot Q_{-n,1} - q_{0,2}}{p_{0,1}\cdot Q_{0,1} - q_{0,2}}, \tag{3.13}$$

where $'$ is used for denoting the correlation being differential.

Analogically, one can obtain p_{T}-differential four-particle correlation by replacing relevant terms that contain n_1 in Eq. 3.8 using $p-$ and $q-$ vectors as

$$\begin{aligned} \mathrm{N}\left\langle 4' \right\rangle_{n_1,n_2,n_3,n_4} = & \ p_{n_1,1}Q_{n_2,1}Q_{n_3,1}Q_{n_4,1} - q_{n_1+n_2,2}Q_{n_3,1}Q_{n_4,1} - q_{n_1+n_3,2}Q_{n_2,1}Q_{n_4,1} \\ & - p_{n_1,1}Q_{n_2+n_3,2}Q_{n_4,1} + 2q_{n_1+n_2+n_3,3}Q_{n_4,1} - q_{n_1+n_4,2}Q_{n_2,1}Q_{n_3,1} \\ & + q_{n_1+n_4,2}Q_{n_2+n_3,2} - p_{n_1,1}Q_{n_3,1}Q_{n_2+n_4,2} + q_{n_1+n_3,2}Q_{n_2+n_4,2} \\ & + 2q_{n_1+n_2+n_4,3}Q_{n_3,1} - p_{n_1,1}Q_{n_2,1}Q_{n_3+n_4,2} + q_{n_1+n_2,2}Q_{n_3+n_4,2} \\ & + 2q_{n_1+n_3+n_4,3}Q_{n_2,1} + 2p_{n_1,1}Q_{n_2+n_3+n_4,3} - 6q_{n_1+n_2+n_3+n_4,4} \, , \end{aligned} \tag{3.14}$$

an analogically for $\mathrm{D}\left\langle 4' \right\rangle_{n_1,n_2,n_3,n_4}$.

Generally, using Q-, p-, and q-vectors, one can express any order of the correlation. However, the number of terms that are used for m-particle correlations follow a Bell sequence [80]

$$1, 2, 5, 15, 52, 203, 877, 4140, ... \tag{3.15}$$

For that reason, a recursive algorithm, that can be found in [80], is typically used. Using this algorithm, any order of correlation can be expressed using lower order correlations. A further optimization that performs better in terms of CPU consumption by calling the main recursive function fewer times is introduced in [134].

3.2 Multi-particle cumulants

Once the single-event average of two- and multi-particle correlation is calculated, an averaging over all the events takes place. This is done as

$$\langle\langle 2 \rangle\rangle_{n,-n} = \sum_i \frac{(W_{\langle 2 \rangle} \langle 2 \rangle_{n,-n})_i}{(W_{\langle 2 \rangle})_i} = c_n\{2\}, \tag{3.16}$$

where $(W_{\langle 2 \rangle})_i$ is the event weight that is dependent on the event multiplicity, and $c_n\{2\}$ is the two-particle cumulant. In the generic framework notation, the event weight is

$$(W_{\langle 2 \rangle})_i = \mathrm{D}\langle 2 \rangle = \sum_{k_1 \neq k_2}^{M} w_{k_1} w_{k_2}. \tag{3.17}$$

The flow coefficient obtained from the two-particle cumulant is denoted as $v_n\{2\}$ and calculated as

$$v_n\{2\} = \sqrt{c_n\{2\}}. \tag{3.18}$$

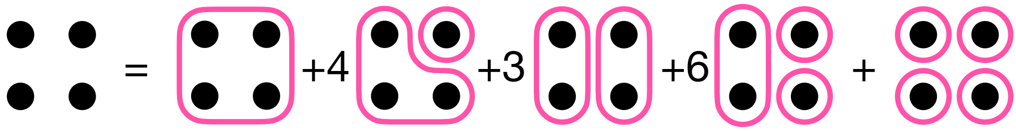

FIGURE 3.1: Sketch of different contributions into four-particle correlations.

For the p_{T}-differential case, where $\langle 2' \rangle$ is obtained from Eq. 3.13, the event-average two-particle correlation and two-particle cumulant are

$$\langle\langle 2' \rangle\rangle_{n,-n} = \sum_i \frac{W_i \langle 2' \rangle_{i,n,-n}}{W_i} = d_n\{2\}(p_{\mathrm{T}}). \tag{3.19}$$

The flow coefficient dependent on p_{T} is calculated as

$$v_n\{2\}(p_{\mathrm{T}}) = \frac{d_n\{2\}(p_{\mathrm{T}})}{\sqrt{c_n\{2\}}}, \tag{3.20}$$

where $c_n\{2\}$ is the p_{T}-integrated cumulant. As the p_{T}-differential flow is calculated with respect to the p_{T}-integrated $v_n\{2\}$, $v_n\{2\}$ is often referred to as the reference flow.

For four-particle correlations, the event-average is, analogically to Eq. 3.16,

$$\langle\langle 4 \rangle\rangle_{n,n,-n,-n} = \sum_i \frac{(W_{\langle 4 \rangle} \langle 4 \rangle_{n,n,-n,-n})_i}{(W_{\langle 4 \rangle})_i} \tag{3.21}$$

and, similarly to Eq. 3.17,

$$(W_{\langle 4 \rangle})_i = D\langle 4 \rangle = \sum_{k_1 \neq k_2 \neq k_3 \neq k_4}^{M} w_{k_1} w_{k_2} w_{k_3} w_{k_4}. \tag{3.22}$$

The four-particle correlations, and all higher order multi-particle correlations, contain a contribution from lower orders, sketched in Fig. 3.1. However, thanks to the symmetry in the azimuthal direction, some terms vanish[3]. The genuine four-particle correlation, known as four-particle cumulant, is then [131]

$$c_n\{4\} = \langle\langle 4 \rangle\rangle_{n,n,-n,-n} - 2 \cdot \langle\langle 2 \rangle\rangle^2_{n,-n}. \tag{3.23}$$

In the Eq. 3.23, all the non-vanishing contributions from lower orders are explicitly subtracted. Thus, the obtained cumulant contains only the physical correlations.

[3]Generally, if the vector of harmonics of m-particle correlation is $\{n_1, n_2, n_3, ..., n_m\}$, only the terms with $\sum_i^m n_i = 0$ remain non-zero. For m-particle correlation of a single harmonic, $|n_i| = n$, all the terms with odd m are trivially zero.

The flow coefficient from the four-particle cumulant is

$$v_n\{4\} = \sqrt[4]{-c_n\{4\}}. \tag{3.24}$$

Analogically to the two-particle case, one can obtain $d_n\{4\}$ as

$$d_n\{4\}(p_\mathrm{T}) = \langle\langle 4' \rangle\rangle_{n,n,-n,-n} - 2 \cdot \langle\langle 2' \rangle\rangle_{n,-n} \cdot \langle\langle 2 \rangle\rangle_{n,-n}. \tag{3.25}$$

Finally, the p_T-differential flow coefficient is

$$v_n\{4\}(p_\mathrm{T}) = \frac{-d_n\{4\}(p_\mathrm{T})}{(-c_n\{4\}^{3/4})}. \tag{3.26}$$

3.2.1 Generic algorithm

To obtain arbitrary high order of multi-particle cumulant, one must subtract all the lower order correlations, analogically to Eq. 3.23. The number of all the terms in a cumulant follows the Bell sequence (Eq. 3.15), and can be seen in the above example (Fig. 3.1) with the four-particle cumulant. For calculating six- and eight-particle cumulants, 203 and 4140 terms are needed, respectively. For this reason, a generic algorithm has been developed [134] at the Niels Bohr Institute[4]. Using the recursive algorithm, an arbitrary order of a multi-particle cumulant can be calculated. With removing all the terms that are zero thanks to the azimuthal symmetry and for simplicity assuming the single harmonic $|n_i| = n$, a six-particle cumulant is calculated as

$$c_n\{6\} = \langle\langle 6 \rangle\rangle_{n,n,n,-n,-n,-n} - 9\langle\langle 4 \rangle\rangle_{n,n,-n,-n}\langle\langle 2 \rangle\rangle_{n,-n} + 12\langle\langle 2 \rangle\rangle^3_{n,-n}. \tag{3.27}$$

The flow coefficient is then

$$v_n\{6\} = \sqrt[6]{\frac{c_n\{6\}}{4}}. \tag{3.28}$$

Analogically, it is possible to calculate any higher orders of cumulants and flow coefficients. The formulas for flow coefficients $v_n\{m\}$ for $m = 2, 4, 6, 8, 10, 12$ are explicitly stated in Sec. 5.1.2 together with results of multi-particle cumulants and flow coefficients.

Furthermore, with the generic algorithm, it is possible to calculate any combination of harmonics of a m-particle cumulant. Then a study of correlation between different moments $2k, 2l$ of different flow harmonics m, n can be obtained by constructing the observable Mixed harmonic cumulant $MHC(v_m^{2k}, v_n^{2l})$. The formulas for mixed harmonic cumulants of different orders are explicitly stated in Sec. 5.1.3 together with their measurements.

[4]My contribution to the paper is described in the preface.

3.3 Flow fluctuations

As introduced at the beginning of the chapter, calculation of the flow coefficient using two- and multi-particle cumulants is only an approximation. The real flow coefficients of the n-th harmonic also include a contribution from the non-flow, denoted as δ_n. Flow coefficients from two- and four-particle cumulants can then be expressed as [135]

$$v_n\{2\} = \langle v_n^2 \rangle^{1/2} + \delta_n, \tag{3.29}$$

$$v_n\{4\} = [2\langle v_n^2 \rangle^2 - \langle v_n^4 \rangle]^{1/4}, \tag{3.30}$$

In non-central heavy-ion collisions, after the non-flow is sufficiently suppressed, the event-by-event flow fluctuations $\sigma_{v_n}^2$ follow $\sigma_{v_n} << v_n$. Then [136]

$$v_n^2\{2\} = \langle v_n \rangle^2 + \sigma_{v_n}^2, \tag{3.31}$$

$$v_n^2\{4\} \approx \langle v_n \rangle^2 - \sigma_{v_n}^2. \tag{3.32}$$

Using these relations, it is possible to construct approximate first two moments of the probability density function ($p.d.f.$) of the flow coefficients, i.e. the mean $\langle v_n \rangle$ and the variance σ_{v_n} as

$$\langle v_n \rangle \approx \sqrt{\frac{v_n^2\{2\} + v_n^2\{4\}}{2}}, \tag{3.33}$$

$$\sigma_{v_n} \approx \sqrt{\frac{v_n^2\{2\} - v_n^2\{4\}}{2}}. \tag{3.34}$$

The relative flow fluctuations $F(v_n)$ can then be defined as

$$F(v_n) = \frac{\sigma_{v_n}}{\langle v_n \rangle} \approx \sqrt{\frac{v_n^2\{2\} - v_n^2\{4\}}{v_n^2\{2\} + v_n^2\{4\}}}. \tag{3.35}$$

3.4 Di-hadron correlations

The methods introduced above are effective and commonly used for calculating flow coefficients from two- and multi-particle cumulants in large collision systems, such as Pb–Pb collisions. Nevertheless, the small collision systems, such as pp and p–Pb collisons, are dominated by so-called non-flow contamination, described in the following section. For that reason, it is useful to construct standard two-particle correlations. The nested loop needed for its calculation is computationally more challenging compared to the Q-vector approach introduced before that requires a single loop over the particles. However, it provides additional information about the shape of the correlation function.

Therefore, in small collision systems, flow extraction using di-hadron correlation is typically the preferred approach of the flow measurement.

The correlation function $C(\Delta\eta, \Delta\varphi)$ is a distribution of particle pairs as a function of difference between their pseudorapidities $\Delta\eta$ and azimuthal angles $\Delta\varphi$. As the angle is circular, for simplicity it is recalculated to the range $-\pi/2, 3\pi/2$. Every pair consists of a leading particle, referred to as the trigger particle, and an associated particle. The shape of $C(\Delta\eta, \Delta\varphi)$ depends on p_{T} of both trigger and associated particles and the centrality/multiplicity class of the event. Moreover, the shape is significantly affected by the acceptance of the detector. For this reason, an event mixing technique is commonly used. The correlation function $\Delta\eta$ and $\Delta\varphi$ is calculated in two steps. Firstly, in the same event from all the pairs of different trigger and associated particles. Secondly, in different events, but with similar proprieties, such as the position within the detector (primary vertex) or the collision centrality. The trigger particles originate from the studied event, while the associated particles are reconstructed in different events. Using this technique, the raw shape of the correlation function is significantly modified as the raw $C(\Delta\eta, \Delta\varphi)$ contains both physics correlation and effects of the limited detector acceptance. After the event mixing, the final correlation function can be described as [102]

$$C(\Delta\eta, \Delta\varphi) = \frac{1}{N_{\mathrm{trig}}} \sum_{\mathrm{PV}_z} \frac{SE(\Delta\eta, \Delta\varphi)}{\alpha\, ME(\Delta\eta, \Delta\varphi)}, \tag{3.36}$$

where SE and ME are acronyms for same and mixed events, α is a normalisation factor, and N_{trig} is the number of trigger particles. An example of distributions of $SE(\Delta\eta, \Delta\varphi)$ (left) and $ME(\Delta\eta, \Delta\varphi)$ in peripheral (60–10%) p–Pb collisions is shown in Fig. 3.2. In the analysis presented in this thesis, N_{trig}, $SE(\Delta\eta, \Delta\varphi)$, $ME(\Delta\eta, \Delta\varphi)$ are corrected for the detector efficiency[5]. The correlation function $C(\Delta\eta, \Delta\varphi)$ after the event mixing is shown in Fig. 3.3 for central (left) and peripheral (right) p–Pb collisions.

The event mixing is performed separately for collisions with different vertex positions along the beam axis (primary vertex PV_z) as the detector effects may vary. The normalisation factor α is obtained from the $ME(\Delta\eta, \Delta\varphi)$ distribution as an integral along the plateau in $\Delta\varphi$ (normalised by the number of bins) at the maximum in $\Delta\eta$. The integral is used to avoid statistical fluctuations. As it can be seen in Fig. 3.2, the plateau in $\Delta\eta \approx 0$ along $\Delta\varphi$ is uniform except the region around the $\Delta\varphi \approx 0$. To avoid statistical instability, the region around $\Delta\varphi \approx 0$ is not considered in the integral along $\Delta\varphi$.

Furthermore, the correlation function calculated from trigger and associate particles from the central pseudorapidity region, $|\eta| < 0.8$, has to be further corrected. The pairs of correlated particles are required to fulfill an additional criterion to ensure a sufficient

[5] See Sec. 4.7 for more details about the reconstruction efficiency correction.

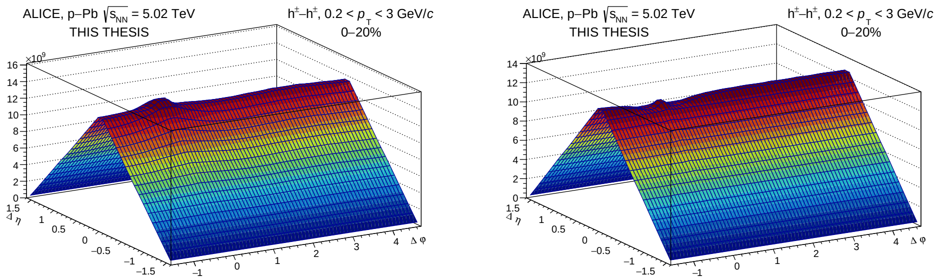

FIGURE 3.2: Distribution of $SE(\Delta\eta, \Delta\varphi)$ (left) and $ME(\Delta\eta, \Delta\varphi)$ (right) from the same and mixed events, respectively, in peripheral (60–10%) p–Pb collisions. Both trigger and associate particles are measured within the central pseudorapidity, $|\eta| < 0.8$. The typical triangular shape, caused by the detector acceptance, can be observed.

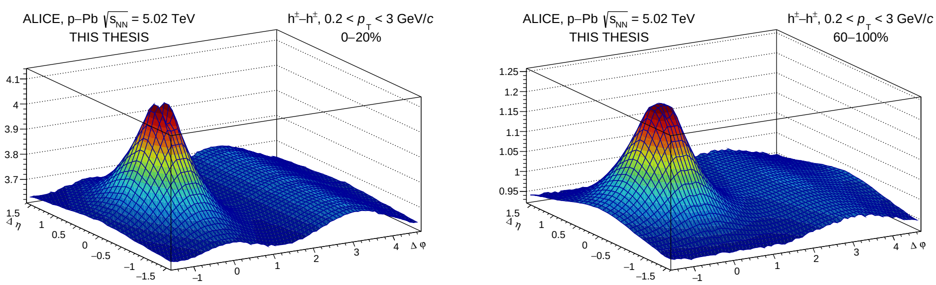

FIGURE 3.3: Correlation function $C(\Delta\eta, \Delta\varphi)$ of central (left) and peripheral (right) p–Pb collisions. Both trigger and associate particles are measured within the central pseudorapidity, $|\eta| < 0.8$.

quality of the track reconstruction. In particular, the cases of two particles being reconstructed as a single track are removed. Such requirement can be obtained using the selection criterion on $\Delta\varphi*$, which is an actual angular distance between two particles at a given radius R, defined as

$$\Delta\varphi* = \varphi_1 - \varphi_2 + \arcsin(\frac{z_1 e B_z R}{2p_{\mathrm{T1}}}) - \arcsin(\frac{z_2 e B_z R}{2p_{\mathrm{T2}}}), \tag{3.37}$$

where $\varphi_{1,2}$, $z_{1,2}$ and $p_{\mathrm{T1,2}}$ are the azimuthal angle at the vertex, charge, and transverse momentum of tracks 1 and 2. B_z is the magnetic field in the z direction and e is the elementary charge [137]. Then for the case when $|\Delta\eta| < 0.02$, an additional criterion of $|\Delta\varphi*| > 0.02$ is required for both mixed and same event correlation functions within the active volume of TPC[6] ($0.8 < R < 2.5$ m) to correct for the reconstruction inefficiency, especially the track merging.

In the next step, the two-dimensional correlation function $C(\Delta\eta, \Delta\varphi)$ is projected into the $\Delta\varphi$ axis. For the flow studies, it is typical to avoid the central region ($|\Delta\eta| < \eta_{\mathrm{lim}}$, typically $\eta_{\mathrm{lim}} \approx 0.8$) in order to suppress possible non-flow contamination from the jet peak region that has a center at $(\Delta\eta, \Delta\varphi) \approx (0, 0)$. The projected distribution $Y(\Delta\varphi)$ can be described by a Fourier decomposition as

$$Y(\Delta\varphi) = a_0 + 2\sum_{n=1}^{\infty} a_n \cos(n\Delta\varphi). \tag{3.38}$$

For practical reasons, the decomposition only goes up to $n = 3$. We can then define $V_{n\Delta}$ as

$$V_{n\Delta} = \frac{a_n}{a_0} \tag{3.39}$$

Assuming the p_{T} region of both the trigger and the associated particle is the same, the integrated (reference) flow in this p_{T} region can then be calculated as

$$v_n\{2\mathrm{PC}\} = \sqrt{V_{n\Delta}}. \tag{3.40}$$

For the p_{T}-differential flow coefficients, the fitting procedure and extraction of $V_{n\Delta}(p_{\mathrm{T}})$ coefficients have to be done separately for every p_{T} region, selecting the associate particles from the same kinematic region (in p_{T}) as the reference flow in the cumulant analysis. The trigger particles are selected from a narrow p_{T} interval of interest. The calculation of the flow coefficient then becomes

$$v_n\{2\mathrm{PC}\}(p_{\mathrm{T}}) = V_{n\Delta}(p_{\mathrm{T}})/\sqrt{V_{n\Delta}}. \tag{3.41}$$

[6]See Sec. 2.7 for more details about the TPC detector.

For specific cases, e.g. for the study of flow vector fluctuations [138, 139], it is convenient to define

$$v_n[2\mathrm{PC}](p_\mathrm{T}) = \sqrt{V_{n\Delta}(p_\mathrm{T})}, \tag{3.42}$$

where both the trigger and associated particles are taken from the same, usually narrow, p_T region. It can be noticed that it is the same relation as introduced in Eq. 3.40 which nevertheless is typically used for the reference flow from an integrated p_T region.

3.5 Non-flow treatment

To use the two- and multi-particle correlations for calculating the flow coefficients, the non-flow contamination might be non-negligible and therefore should be removed. It is essential especially in small collision systems, such as pp and p–Pb.

There are several ways how to suppress non-flow contamination. To obtain the best possible results, combining more than one method of non-flow suppression can be helpful. The first method uses the higher order of multi-particle cumulants for calculating the flow coefficients, and has been introduced in Sec. 3.2. This section then introduces two additional methods of non-flow treatment. Firstly, it is possible to separate correlated particles, i.e. correlate particles from different pseudorapidity regions. Secondly, it is possible to subtract (explicitly or implicitly) the non-flow contribution using the low multiplicity collisions of small systems in which very little to no flow signal is assumed.

3.5.1 Pseudorapidity separation

The first non-flow suppression technique consists of correlating two or more particles from different pseudorapidity regions. In this section, three different approaches are presented – two-particle cumulants measurement with two sub-events, also known as η gap method, four-particle cumulants measurement with three sub-events, and pseudorapidity separation in the measurement of di-hadron correlations.

Two- and four-particle cumulants with two sub-events method

The Q-vectors, introduced in Sec. 3.1.1 and defined by Eq. 3.4, are used for calculating two- and multi-particle correlation. Without any specification of pseudorapidity region η, it is assumed they originate from the whole studied η region and are only constrained by the acceptance of the detector. Nevertheless, it is possible to divide the acceptance region into so-called sub-events, as introduced in [140, 141]. It can be illustrated as

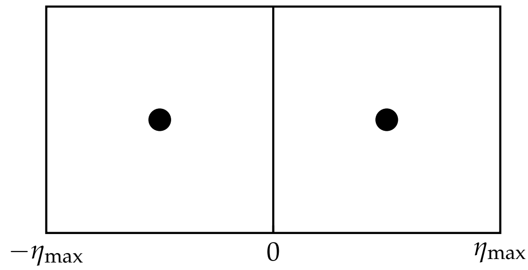

It the sketch, $|\eta_{\text{max}}|$ is the full acceptance of the detector. The new Q-vector can be defined, including contributions only from the positive sub-event, i.e. from reference particles (RFP) only from the positive pseudorapidity $\eta > 0$, as

$$Q^{+}_{n,p} \equiv \sum_{i \in \text{RFP}^{+}}^{M} w_i^p e^{in\varphi_i}. \tag{3.43}$$

Analogically, $Q^{-}_{n,p}$ contains contribution only from particles with $\eta < 0$[7]. The Eq. 3.7 then becomes

$$\langle 2 \rangle_{n_1,n_2} = \frac{Q^{+}_{n_1,1} \cdot Q^{-}_{n_2,1}}{Q^{+}_{0,1} \cdot Q^{-}_{-0,1}}. \tag{3.44}$$

It is important to notice that unlike Eq. 3.7, where all the correlated particle originate from the same sub-event, no term is subtracted (in both numerator and denominator) as no self correlation occurs. For p_{T}-differential case, the equation is modified analogically, i.e. no self correlation is removed,

$$\langle 2' \rangle_{n_1,n_2} = \frac{p^{+}_{n_1,1} \cdot Q^{-}_{n_2,1}}{p^{+}_{0,1} \cdot Q^{-}_{-0,1}}. \tag{3.45}$$

The final $\langle 2' \rangle_{n,-n}$ is an average of two cases with the particle of interest in the positive and negative sub-events, respectively.

Analogical simplification of the calculation can be made for four-particle correlations with self correlations being removed only in the case when two particles are within the same sub-event. To calculate the numerator of four-particle correlations with two sub-events, the equation

$$\begin{aligned} \mathrm{N}\langle 4 \rangle_{n_1,n_2,n_3,n_4} = {} & Q^{+}_{n_1,1} Q^{+}_{n_2,1} Q^{-}_{n_3,1} Q^{-}_{n_4,1} - Q^{+}_{n_1+n_2,2} Q^{-}_{n_3,1} Q^{-}_{n_4,1} \\ & - Q^{+}_{n_1,1} Q^{+}_{n_2,1} Q^{-}_{n_3+n_4,2} + Q^{+}_{n_1+n_2,2} Q^{-}_{n_3+n_4,2} \end{aligned} \tag{3.46}$$

[7]Generally, the splitting between sub-events does not have to be in $\eta = 0$. However, the most common approach is to split the event into sub-events with respect to the positive and negative pseudorapidity.

is used instead of Eq. 3.9 that was used for the case when all the particles originated from the same phase-space. The same notation is used as in the case of two-particle correlations, i.e. Q^+ and Q^- contain contribution only from particles from positive and negative sub-events, respectively. The illustration below shows an event with four particles and two sub-events schematically.

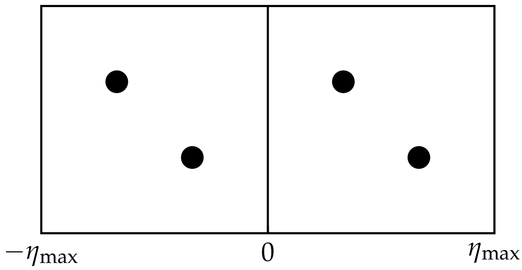

The calculation of two- and four-particle cumulants and flow coefficients out of two- and four-particle correlations continues exactly the same as described in Sec. 3.2. The standard notation used to mark flow coefficients obtained using the two sub-event method is $v_n\{m, |\Delta\eta| > x\}$, where x represents the separation between sub-events, that is also the minimum separation between two particles. For the illustration above, $x = 0$.

Four-particle cumulants with three sub-events method

This method can be extended to the three sub-events method [142], typically used with four-particle correlation. It has been shown that the three sub-events method suppresses the non-flow contamination better [143], thus it is essential for the flow measurements in small collision systems.

Analogically to the case with two sub-events, the sub-events are defined at different η ranges, $\eta < \eta_1$ (marked as left or L), $\eta_1 < \eta < \eta_2$ (marked as middle or M), and $\eta_2 < \eta$ (marked as right or R). Then the Q-vector with contributions only from left, middle, or right sub-event, marked as Q^{L}, Q^{M}, and Q^{R}, respectively, is defined analogically to Q^+ defined by Eq. 3.43. An example of four-particle correlation with three sub-events is shown in the illustration bellow.

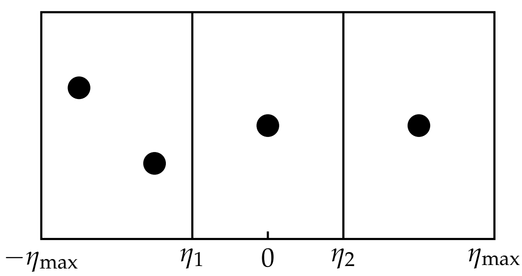

Similarly, the case with two particles in the middle or right sub-event can be visualized. For the sketched case, the numerator of four-particle correlation becomes

$$N\langle 4\rangle^{\mathrm{LLMR}}_{n_1,n_2,n_3,n_4} = \left(Q_{n_1,1}Q_{n_2,1} - Q_{n_1+n_2,2}\right)^{\mathrm{L}} \cdot Q^{\mathrm{M}}_{n_3,1} \cdot Q^{\mathrm{R}}_{n_4,1}, \tag{3.47}$$

and analogically for LMMR and LMRR, based on the configuration of the calculation.

To calculate four-particle cumulant out of four-particle correlations, lower order correlations have to be subtracted – in this case, two-particle correlations. In the calculation, the geometry of the calculated case has to be kept in mind in order to subtract correct two-particle correlations. For the case illustrated above,

$$c_n\{4\}^{\mathrm{LLMR}}_{3-\mathrm{sub}} = \langle\langle 4\rangle\rangle^{\mathrm{LLMR}}_n - 2\langle\langle 2\rangle\rangle^{\mathrm{LM}}_n\langle\langle 2\rangle\rangle^{\mathrm{LR}}_n, \tag{3.48}$$

where for simplicity $|n_i| = n$. The two-particle correlations are calculated analogically to Eq. 3.44 by replacing $+$ and $-$ with L, M, and R.

For the p_{T}-differential four-particle cumulant with three sub-events, even more geometrical combinations are needed. The particle of interest (POI, in pink) can be either in a different different sub-event than the sub-event with two particles, or in the the same. The former case is illustrated in the sketch below.

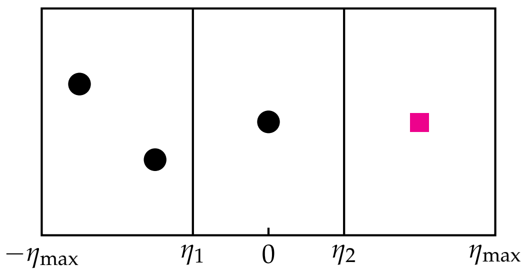

The numerator of p_{T}-differential four-particle correlation is

$$N\langle 4'\rangle^{\mathrm{LLMR}'}_n = \left(Q_{n,1}Q_{n,1} - Q_{2n,2}\right)^{\mathrm{L}} \cdot Q^{\mathrm{M}}_{-n,1} \cdot p^{\mathrm{R}'}_{-n,1}, \tag{3.49}$$

with p-vector defined by Eq. 3.11, considering only particles from the selected sub-event. Subsequently, the four-particle cumulant is calculated as

$$d_n\{4\}^{\mathrm{LLMR}'}_{3-\mathrm{sub}} = \langle\langle 4'\rangle\rangle^{\mathrm{LLMR}'}_n - 2\langle\langle 2\rangle\rangle^{\mathrm{LM}}_n\langle\langle 2'\rangle\rangle^{\mathrm{LR}'}_n, \tag{3.50}$$

where $'$ explicitly marks the p_{T}-differential parts.

The latter case, with POI in the same sub-event as two particle, is sketched below.

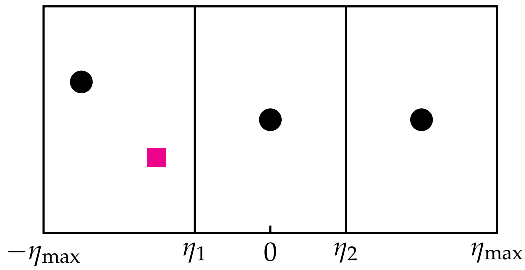

The calculation of four-particle correlation becomes

$$N\langle 4' \rangle_n^{\mathrm{L'LMR}} = (p_{n,1}Q_{n,1} - q_{2n,2})^{\mathrm{L'}} \cdot Q^{\mathrm{M}}_{-n,1} \cdot Q^{\mathrm{R}}_{-n,1}, \tag{3.51}$$

with q-vector being an overlap of Q- and p-vector, defined by Eq. 3.12. The four-particle cumulant is calculated as

$$d_n\{4\}^{\mathrm{L'LMR}}_{3-\mathrm{sub}} = \langle\langle 4' \rangle\rangle_n^{\mathrm{L'LMR}} - \langle\langle 2' \rangle\rangle_n^{\mathrm{L'M}} \langle\langle 2 \rangle\rangle_n^{\mathrm{LR}} - \langle\langle 2 \rangle\rangle_n^{\mathrm{LM}} \langle\langle 2' \rangle\rangle_n^{\mathrm{L'R}}. \tag{3.52}$$

Analogically, it is possible to obtain formulas for all the geometrical combinations. The final flow coefficient can be calculated as an average of all nine different geometrical configurations. It has been tested that they are compatible within uncertainties. Nevertheless, it is important to note that when calculating the flow coefficient $v_n\{4\}_{3-\mathrm{sub}}$ using Eq. 3.26, one has to be careful to use the correct geometrical combination for both $c_n\{4\}$ and $d_n\{4\}$.

Pseudorapidity separation in the measurement of di-hadron correlations

In the di-hadron correlation method, two options of pseudorapidity separation are possible. In the first method, the correlation function $C(\Delta\eta, \Delta\varphi)$ is constructed from the pairs of particles that both originate from the central pseudorapidity, $|\eta| < 0.8$. Then, the projection into $Y(\Delta\varphi)$ is done excluding $|\Delta\eta| < \eta_{\mathrm{lim}}$, as described in Sec. 3.4. In the second method, similarly to the three sub-events method, the trigger and associate particles originate from different η regions. Then the projection into $Y(\Delta\varphi)$ is done over the entire studied $\Delta\eta$ region, and $V_{n\Delta}$ is obtained as described above. The procedure is repeated for three different geometrical combinations, obtaining correlation functions from particle pairs from LM, MR, and LR regions.

In the analysis presented in this thesis, the limitation of the used detectors are considered. For obtaining the p_{T}-dependent flow coefficient using the three sub-events method, the p_{T}-dependent particle originates from the central (middle) pseudorapidity region, $|\eta| < 0.8$. The p_{T}-integrated associated particles originate from the forward (right) and backward (left) pseudorapidity regions. The p_{T}-dependent flow coefficient

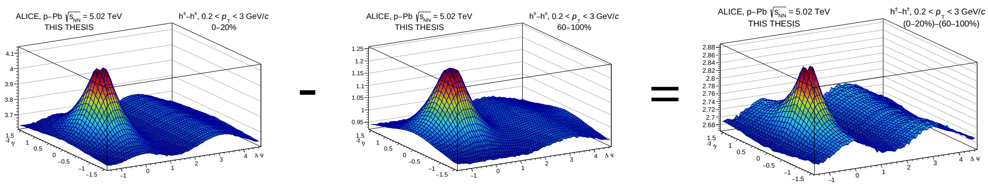

FIGURE 3.4: The correlation function $C(\Delta\eta, \Delta\varphi)$ in high (left) and low (middle) multiplicity, and correlation function $C(\Delta\eta, \Delta\varphi)^{\text{sub}}$ obtained by their subtraction (right) in p–Pb collisions. Both trigger and associate particles are measured within the central pseudorapidity, $|\eta| < 0.8$.

is calculated as

$$v_n\{2\text{PC}\}(p_{\text{T}}) = \sqrt{\frac{V_{n\Delta}^{\text{LM}}(p_{\text{T}})V_{n\Delta}^{\text{MR}}(p_{\text{T}})}{V_{n\Delta}^{\text{LR}}}}. \tag{3.53}$$

3.5.2 Subtraction of low multiplicity collisions

Assuming weak to no flow signal in low multiplicity (LM) collisions of small systems and the dominance of non-flow, it is possible to subtract LM collisions from high multiplicity (HM) collisions in order to gain a sample with suppressed non-flow contribution. Thus, the LM collisions are used to estimate the non-flow in HM collisions. The subtraction is done at the level of two-dimensional correlation functions $C(\Delta\eta, \Delta\varphi)$ as the knowledge of the shape of the subtracted correlation function $C(\Delta\eta, \Delta\varphi)^{\text{sub}}$ is important to confirm whether there the non-flow treatment was sufficient. It can be noted as

$$C(\Delta\eta, \Delta\varphi)^{\text{sub}} = C(\Delta\eta, \Delta\varphi)^{\text{HM}} - k \cdot C(\Delta\eta, \Delta\varphi)^{\text{LM}}, \tag{3.54}$$

where k is the scaling factor. Nevertheless, in a plethora of analyses, including the one presented in later chapters, $k = 1$. For historical reasons, as the method was firstly used in p–Pb collisions where peripheral collisions were used as the LM base, the method is commonly referred to as the peripheral subtraction [102]. An example of the subtraction with $k = 1$ is shown in Fig. 3.4. The double-ridge structure, a sign of collectivity, becomes better visible after the subtraction of the dominant non-flow contribution using the LM collisions.

The projection of $C(\Delta\eta, \Delta\varphi)^{\text{sub}}$ into $Y(\Delta\varphi)^{\text{sub}}$ and its fit is done as described in Sec. 3.4. An example of $Y(\Delta\varphi)^{\text{sub}}$ together with the fit function is shown in Fig. 3.5. The only difference in the procedure is the calculation of $V_{n\Delta}$ to compensate the different magnitude of $Y(\Delta\varphi)^{\text{sub}}$ after the subtraction. The calculation of $V_{n\Delta}$ becomes

$$V_{n\Delta} = \frac{a_n}{b}, \tag{3.55}$$

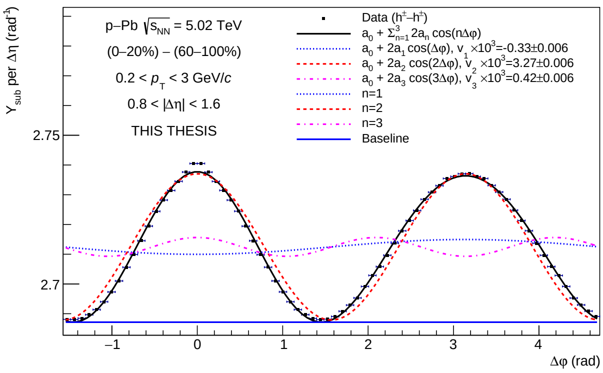

FIGURE 3.5: An example of the fit of $Y(\Delta\varphi)^{\text{sub}}$ for the extraction of flow coefficients.

where b is either the baseline of HM collisions or $b = b' + a_0$ where b' is the baseline of LM collisions and a_0 is from the fit of subtracted $Y(\Delta\varphi)^{\text{sub}}$. The baseline is the integral of $C(\Delta\eta, \Delta\varphi)$ in its minimum (typically $|\Delta\varphi - \pi/2| < 0.2$) alongside the full $\Delta\eta$ range, scaled with the number of bins. It has been tested that the choice of b does not affect the final flow coefficients that are calculated out of $V_{n\Delta}$ as described in Sec. 3.4.

Similarly, it is possible to subtract LM collisions from HM collisions when calculating the flow coefficients v_n using two-particle cumulants. The subtraction has to take place in both c_n and d_n with the same scaling factor k as [144]

$$v_n\{2\}^{\text{sub}}(p_{\text{T}}) = \frac{d_n\{2\}(p_{\text{T}})^{\text{HM}} - k \cdot d_n\{2\}(p_{\text{T}})^{\text{LM}}}{\sqrt{c_n\{2\}^{\text{HM}} - k \cdot c_n\{2\}^{\text{LM}}}}. \tag{3.56}$$

It is possible to use different scaling, for example, using mean multiplicity $\langle M \rangle$ of studied collisions

$$k = \frac{\langle M \rangle^{\text{LM}}}{\langle M \rangle^{\text{HM}}}, \tag{3.57}$$

as it is assumed the non-flow changes inversely with the multiplicity. This has been tested with both $\langle M \rangle$ and $\langle M \rangle(p_{\text{T}})$. Similarly, it is possible to use jet yield from HM and LM collisions for calculating the scaling factor k.

3.5.3 Template and improved template fit

In the low multiplicity (peripheral) subtraction method, it is assumed that there is weak to no flow signal. If this assumption is not valid, during the subtraction process, the flow signal is subtracted from the signal, i.e. an over subtraction occurs. For that reason a template fit method has been introduced in [145]. The correlations from high multiplicity (HM) collisions are assumed to be a superposition of scaled correlation from low

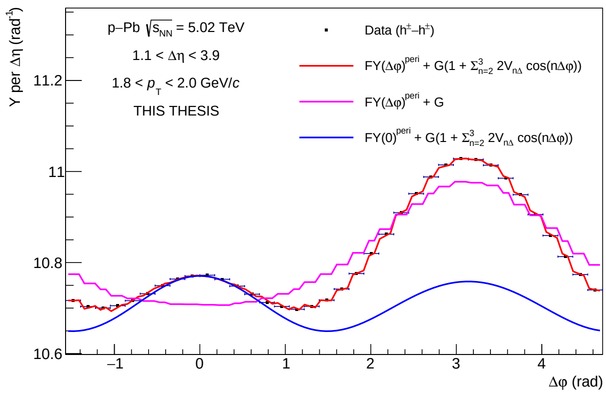

FIGURE 3.6: An example of the template fitting method for the extraction of flow coefficients in p–Pb collisions.

multiplicity (LM) collisions and a cosine modulation that represents the flow contribution, i.e.

$$Y(\Delta\varphi)^{\mathrm{HM}} = FY(\Delta\varphi)^{\mathrm{LM}} + G^{\mathrm{tmp}}\left[1 + 2\sum_{n=2}^{\infty} V_{n\Delta}^{\mathrm{tmp}}\cos(n\Delta\varphi)\right], \tag{3.58}$$

where F is the scaling factor of the LM collisions, and $V_{n\Delta}$ is used for calculating the flow coefficients $v_n\{2\mathrm{PC}\}$ as in Eq. 3.41. Similarly to the fit with a Fourier decomposition in the explicit subtraction method, in the data analysis, the decomposition usually goes only up to $n = 3$. An example of the template fit procedure is shown in Fig. 3.6 for the $Y(\Delta\varphi)$ from HM p–Pb collisions. The di-hadron correlations is obtained with the p_{T}-dependent trigger particle from the central pseudorapidity region and the associated particle from the forward pseudorapidity region. The low multiplicity template is shown in pink and shifted for the visibility. The blue line represents the cosine modulation.

This procedure can be extended to parametrise for the multiplicity dependence of the flow coefficients as introduced in [146]. It originates from the assumption that both HM and LM collisions are made from a jet component and a flow component that are completely independent

$$Y^{\mathrm{HM}}(\Delta\varphi) = Y_{\mathrm{jet}}^{\mathrm{HM}}(\Delta\varphi) + G^{\mathrm{HM}}[\left[1 + 2\sum_{n=2}^{\infty} V_{n\Delta}^{\mathrm{HM}}\cos(n\Delta\varphi)\right] \tag{3.59}$$

$$Y^{\mathrm{LM}}(\Delta\varphi) = Y_{\mathrm{jet}}^{\mathrm{LM}}(\Delta\varphi) + G^{\mathrm{LM}}\left[1 + 2\sum_{n=2}^{\infty} V_{n\Delta}^{\mathrm{LM}}\cos(n\Delta\varphi)\right] \tag{3.60}$$

When introducing the method in [146], it has been assumed that $Y(\Delta\varphi)$ in the two lowest multiplicity bins have the same jet component. However, it has been shown in

[147] that this assumption is broken in pp collisions as the jet component strongly depends on the event multiplicity. Therefore, the procedure from [146] is slightly modified. Nevertheless, a jet component of any multiplicity class can be expressed using a different jet component with an appropriate scaling factor. For that reason,

$$Y_{\text{jet}}^{\text{LM}}(\Delta\varphi) = F^{\text{LM}} Y_{\text{jet}}(\Delta\varphi) \tag{3.61}$$

$$Y_{\text{jet}}^{\text{HM}}(\Delta\varphi) = F Y_{\text{jet}}^{\text{LM}}(\Delta\varphi) = F F^{\text{LM}} Y_{\text{jet}}(\Delta\varphi) \tag{3.62}$$

It is possible to substitute $Y(\Delta\varphi)^{\text{LM}}$ in Eq. 3.58 with components from 3.60 and substitute both jet components using $Y_{\text{jet}}(\Delta\varphi)$ from Eqs. 3.61 and 3.62. Then comparing Eqs. 3.58 to 3.59, it is possible to get

$$F F^{\text{LM}} Y_{\text{jet}}(\Delta\varphi) + (F G^{\text{LM}} + G^{\text{tmp}}) + 2\sum_{n=2}^{\infty}\left(G^{\text{tmp}} V_{n\Delta}^{\text{tmp}} + F G^{\text{LM}} V_{n\Delta}^{\text{LM}}\right)\cos(n\Delta\varphi) =$$

$$F F^{\text{LM}} Y_{\text{jet}}(\Delta\varphi) + G^{\text{HM}}\left[1 + 2\sum_{n=2}^{\infty} V_{n\Delta}\cos(n\Delta\varphi)\right] \tag{3.63}$$

By comparing the left and right sides of the equation, the parametrised $V_{n\Delta}$ is obtained as

$$V_{n\Delta}^{\text{HM}} = V_{n\Delta}^{\text{tmp}} - \frac{F G^{\text{LM}}}{G^{\text{HM}}}(V_{n\Delta}^{\text{tmp}} - V_{n\Delta}^{\text{LM}}), \tag{3.64}$$

assuming $G^{\text{HM}} = F G^{\text{LM}} + G^{\text{tmp}}$ which is true for the case of no modulation.

As we do not know the real modulation, the template fitting procedure, as described by Eq. 3.58 is done twice, once in the second lowest multiplicity bin to approximately find LM parameters and then in the HM bin with respect to the second lowest multiplicity bin to obtain tmp parameters. The final $V_{n\Delta}$ is obtained using Eq. 3.64.

4 Analysis procedure

While the previous chapter introduced how two- and multi-particle correlations can be calculated, in the data analysis, several steps have to be taken prior to the calculation, such as selecting the proper events and tracks used for the analysis. Therefore, this chapter provides a description of the analysis procedure.

Once the track is successfully reconstructed, it is used to calculate the flow coefficients. If the identification of the selected track is possible, it also contributes to the calculation of the flow of identified particles. As a detector's acceptance and efficiency is generally not perfect, a set of corrections used in this analysis is also described in this chapter. Lastly, a description of methods used for obtaining the statistical and systematic uncertainty on results is discussed.

4.1 Analysis framework

The analysis is written in an object-oriented programming language C++ using the framework AliPhysics developed by the ALICE Collaboration. The framework used for calculating the results presented in this thesis is written and included in the AliPhysics repository at GitHub [148]. Every analysis task is written as a C++ class. Moreover, it uses classes from AliRoot, which is an extension of ROOT [149] created by the ALICE Collaboration and provides processed information. By using this framework, the analyzer does not have to reconstruct tracks from individual space point hits as described in Sec. 2.7. Instead, one can directly load the `AliVParticle` object and use its attributes from the public member functions to obtain, e.g. p_{T} or φ. Analogically, one can access information about selected events or generated Monte Carlo particles from anchored productions.

Two different analysis tasks from individual classes are used for the analysis presented in this thesis. Both can be found in `AliPhysics/PWGCF/FLOW/GF`. The `AliAnalysisTaskUniFlow` framework is used for calculating both p_{T} integrated and differential multi-particle correlations using Q, p, and q vectors. This framework can calculate an arbitrary order of multi-particle correlations using the generic algorithm presented in Sec. 3.2.1. Calculating both p_{T} integrated and p_{T} differential correlations is possible. For the latter, it is possible to specify an identified particle species that should be calculated, such as $\pi^{\pm}$, $\mathrm{K}^{\pm}$, $\mathrm{p}(\bar{\mathrm{p}})$, $\mathrm{K}^0_{\mathrm{S}}$, $\Lambda(\bar{\Lambda})$, ϕ. A possibility to add a pseudorapidity separation, including the 3 sub-events method, is also implemented. This framework has been first introduced in [144]. Further optimization and many additions are included in later versions. In the online part of the analysis, event-averaged two- and multi-particle correlations are calculated. The post-processing, i.e. calculating multi-particle cumulants out of multi-particle correlations and the flow coefficients extraction, as described in Sec. 3.2, takes place offline.

Di-hadron correlations are calculated using `AliAnalysisTaskCorrForFlowFMD` class. With this framework, the user can calculate both the long-range correlations, where both trigger and associated particles originate from the central rapidity, and the ultra-long-range correlations, where the associated particle originates from the forward region. The former is later noted as TPC – TPC correlations while the latter consists of TPC – FMD and FMD – FMD correlations. Details about TPC and FMD detectors are described in Sec. 2.7 and Sec. 2.5, respectively. Besides the correlations of inclusive charged particles, the framework is capable to calculate the correlations of nine different identified species, $\pi^{\pm}$, $\mathrm{K}^{\pm}$, $\mathrm{p}(\bar{\mathrm{p}})$, K^0_S, $\Lambda(\bar{\Lambda})$. In the online part of the analysis, the correlation functions $C(\Delta\eta, \Delta\varphi)$ are calculated for both same and mixed events. The multi-dimensional information is required as for every particle pair, in addition to $\Delta\eta$ and $\Delta\varphi$, the primary vertex position along the z axis (PV_z) is required for the event mixing procedure. In the case of the p_T-differential analysis, the information on p_T of the trigger particle is added as well. If the trigger particle is a V^0 particle, the invariant mass of the trigger particle candidate is needed. Finally, a random number is assigned to every analyzed event in order to calculate the statistical uncertainty, as described in Sec. 4.9.1. The offline part of the analysis starts with applying the event mixing, described in Sec. 3.4. Once the correlation function $C(\Delta\eta, \Delta\varphi)$ is obtained, the procedure follows as described in Sec. 3.4 with the projection over $\Delta\eta$ and subsequent fitting for obtaining the flow coefficients.

4.2 Data sample

For the analysis described in this thesis, the data collected from the ALICE experiment between 2015 and 2018 during the Run 2 campaign are used. Additionally, simulated events corresponding to the analyzed data in the event reconstruction, so-called anchored Monte Carlo (MC) productions, are used for estimating detector efficiency (Sec. 4.7.2), calculating the contamination from secondary particles (Sec. 4.7.3), and for the MC closure test (Sec. 4.8).

For both the calculation of flow and flow fluctuations of identified particles using two- and multi-particle cumulants and the calculation of mixed harmonic cumulants in Pb–Pb collisions at $\sqrt{s_\mathrm{NN}} = 5.02$ TeV, the `LHC15o` period is used.

For the calculation of flow in small systems, p–Pb collisions at $\sqrt{s_{\rm NN}} = 5.02$ TeV and pp collisions at $\sqrt{s} = 13$ TeV are used. For the former, periods `LHC16q,t` are considered. There is a known issue with the high busy time of the SDD detector in both p–Pb periods. Therefore the data are divided (during the reconstruction phase) into sub-groups based on the trigger clusters. Only the data without known issues are used. For the later, all available periods are used.

Adequate data quality is ensured using so-called run tags created by the data reconstruction experts (Data Preparation Group) obtained from the data quality control – both online during the data taking and offline during the data reconstruction. The data-taking runs used in this analysis are tagged with `central barrel tracking` which corresponds to correctly reconstructed particles in the ALICE central barrel detectors (ITS, TPC). Additionally, a tag requiring the high-precision particle identification is required for the analyses using identified particles. Furthermore, if the FMD detector is used, only runs tagged as `FMD good` are analyzed.

4.3 Event selection

In all the studied systems, only the triggered collisions are analyzed. The minimum bias (MB) trigger requiring a coincidence signal in both sides of the V0 detector, V0A and V0C, as described in Sec. 2.4, is used. In addition to the MB trigger, in pp collisions, a special high multiplicity (HM) trigger is used to select only events to follow the condition of the event multiplicity to be greater than four times the average (MB) multiplicity. In the terms of event amplitude V0M, the condition is commonly expressed as $\mathrm{V0M}/\langle\mathrm{V0M}\rangle > 4$.

A significant part of the event selection is done using a standard ALICE procedure with the `AliEventCuts` class. First, the quality of the primary vertex along the beam axis (PV_z) reconstruction is checked with both SPD and TPC detectors. If the PV_z measured with two different detectors is incompatible, the event is rejected. If the position of PV_z is compatible, it is required to be within 10 cm of the centre of the detector, i.e. $|\mathrm{PV}_z| < 10$ cm. This requirement is connected with the detector acceptance within the pseudorapidity and secures the high quality of reconstructed tracks within the central barrel.

The beam-induced background suppression and pile-up rejection are done in several steps. The former, that originates from the beam–gas interactions, is rejected using the information about the signal from V0 and ZDC (zero degree calorimeter) detectors. Pile-up events from different bunch crossings (out-of-bunch pile-up) are removed by applying a selection based on the correlation of multiplicities obtained from SPD and V0 detectors. In Pb–Pb collisions, out-of-bunch pile-up is further suppressed using the

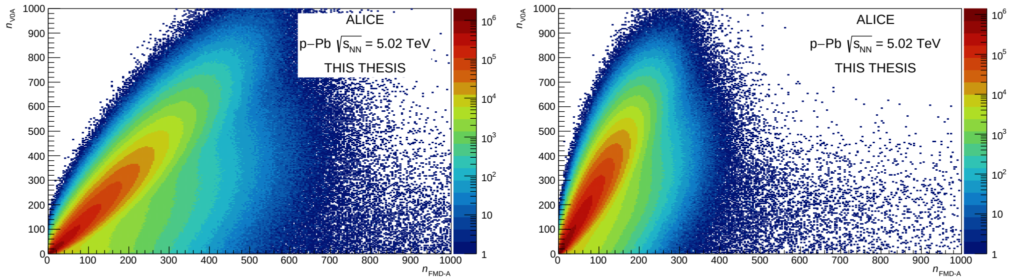

FIGURE 4.1: Correlation between the multiplicity obtained from FMD and V0 detectors before the additional criteria on their correlation.

information from the TOF detector. Moreover, the difference between two centrality estimators CE_1, CE_2 is compared using the known correlation between them. The estimators need to follow the requirement

$$CE_1 > 0.973488 \cdot CE_2 + 0.0157497 - 5\sigma, \tag{4.1}$$

$$CE_1 < 0.973488 \cdot CE_2 + 0.0157497 + 5.5\sigma, \tag{4.2}$$

where

$$\sigma = 0.67361 + 0.0290718 \cdot CE_2 - 0.000546728 \cdot CE_2^2 + 5.82749 \cdot 10^{-6} \cdot CE_2^3. \tag{4.3}$$

Finally, an additional criterion is required to remove contamination in the FMD detector if it is used in the analysis. The contamination is mostly caused by the pile-up due to the slow read-out time of the FMD. As written in Sec. 2.4 and Sec. 2.5, FMD and V0 detectors have similar η coverage. Therefore, the removal of the contaminated events is done by using the correlation between the FMD and V0 multiplicity, separately on both sides, as

$$n_{\mathrm{V0}} > s \cdot n_{\mathrm{FMD}} - 3o, \tag{4.4}$$

where n_{V0} and n_{FMD} stand for the multiplicity in V0 and FMD detector at forward or backward pseudorapidity, s is the slope of their correlation, and o is its width. The slope is obtained as $s = cov(\mathrm{V0}, \mathrm{FMD})/\sigma(\mathrm{V0})\sigma(\mathrm{FMD})$ [150]. The correlation between FMD and V0 on both sides before and after the cuts can be seen in Fig. 4.1 and Fig. 4.2. The specific values for s and o are taken from [150].

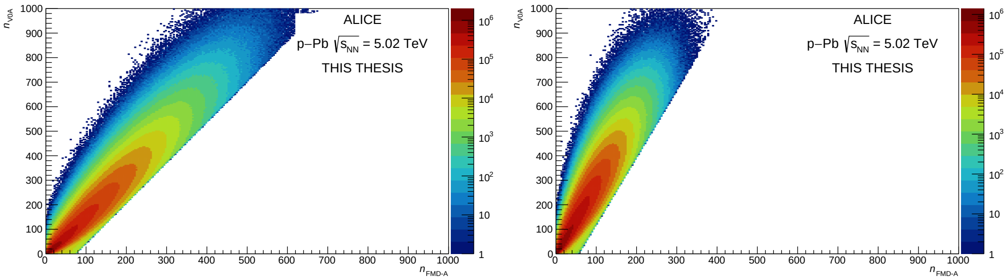

FIGURE 4.2: Correlation between the multiplicity obtained from FMD and V0 detectors after the additional criteria on their correlation.

4.3.1 Selection of high multiplicity collisions of small systems

In the study of flow systems, a selection of high multiplicity collisions is needed. In p–Pb collisions, the correlation between central and forward multiplicity is strong. Therefore, only selection based on V0A forward centrality estimator is used. In particular, 0–20% most central collisions are considered.

In pp collisions, it is known the correlation between central and forward multiplicity is weak. For that reason, considering high multiplicity triggered collisions as described which correspond to 0–0.1% most central collisions as selected by V0M estimator is not sufficient. Additionally, an overlap in central multiplicity, i.e. number of reconstructed charged tracks between high multiplicity triggered and minimum bias collisions is non-negligible. The effect might negatively affect low multiplicity subtraction methods, described in Sec. 3.5. Therefore, an additional event selection criterion is applied on high multiplicity pp collisions. The criterion is selected in order to obtain the same mean multiplicity as in 0–20% p–Pb collisions, similarly to results from Ref. [98]. The distribution of uncorrected number of charged particles within the central pseudorapidity in 0–0.1% centrality class of pp collisions and 0–20% centrality class of p–Pb collisions is shown in Fig. 4.3. The correctness of such distributions and obtained mean multiplicity is in agreement with published results from Ref. [151] and [152] for pp and p–Pb collisions, respectively. It can be seen the mean multiplicity, marked in the figure as $\langle N_{ch} \rangle$, is almost the same with the aforementioned additional criterion of $N_{ch} > 25$ in pp collisions.

In the template fit method, with results reported in Sec. 5.2.6, the low multiplicity base is peripheral (60–100%) p–Pb collisions and minimum bias (0–100%) pp collisions in the measurement p–Pb and pp collisions, respectively. In order to avoid potential overlap of multiplicity within the central pseudorapidity, a criterion of $N_{ch} < 20$ is applied in both cases.

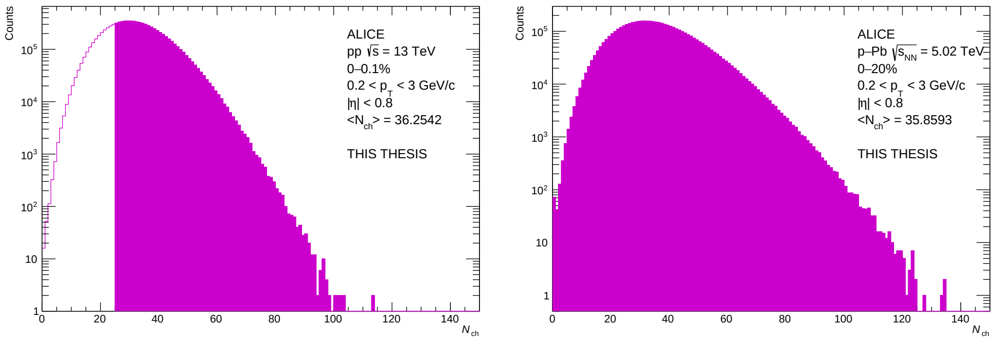

FIGURE 4.3: Distribution of uncorrected number of charged particles N_{rmch} reconstructed in the central pseudorapidity $|\eta| < 0.8$ in pp (right) and p–Pb (left) collisions.

4.4 Track selection

Inclusive charged particles are all the charged particles that pass the selection criteria. They are reconstructed using a combined information from ITS and TPC. In this analysis, charged particles from $p_{\mathrm{T}} > 0.2$ GeV/c within the central pseudorapidity $|\eta| < 0.8$ are considered. As described in Sec. 2.7, a charged track can create a maximum of 159 space points within the active volume of TPC. In order to obtain a high-quality reconstruction, it is required to have at least 70 out of 159 reconstructed space points. Additionally, to ensure the optimal balance between the track quality and abundance of primary particles, a requirement on the distance of the closest approach (DCA) is applied. The DCA between the track and the primary vertex (PV) in the longitudinal (z) direction has to be within 2 cm, and in the transverse (xy) direction within 7σ of the expected value as a function of p_{T}. Finally, a χ^2 criterion per space point in TPC is required to be smaller than 4. In addition to the high quality of the reconstructed tracks, these selection criteria remove most of the products of weakly decaying hadrons. In Pb–Pb collisions, this selection criteria leads to the reconstruction efficiency of approximately 80% for tracks with $p_{\mathrm{T}} > 0.5$ GeV/c. The secondary contamination is approximately 5% at $p_{\mathrm{T}} = 1$ GeV/c [135] and can be seen for primary identified particles in Fig. 4.5.

If a charged primary track passes all the aforementioned criteria, it is used in the analysis. Firstly, if the charged particle is within a specific kinematic range ($0.2 < p_{\mathrm{T}} < 3.0$ GeV/c if not stated otherwise),

- it contributes to the Q-vector that is used for the calculation of the reference flow using the cumulant method as described in Sec. 3.1,
- it is used as an associated particle in the TPC – TPC di-hadron correlations analysis.

Secondly, if the charged particle is within the kinematic range $0.2 < p_{\mathrm{T}} < 10.0$ GeV/c,

- it contributes to the p_{T}-differential p- and q-vectors for the calculation of the p_{T}-differential cumulants,
- it is used as a trigger particle in both TPC – TPC and TPC – FMD di-hadron correlations for calculating the p_{T}-differential flow of inclusive charged particles,
- if it can be identified (see the next section), it contributes to the p_{T}-differential p- and q-vectors and acts as a trigger particle in the calculation of the p_{T}-differential flow coefficients of the specfic identified particle species.

4.5 Particle identification

Selected charged primary track that passed all the aforementioned criteria can be subsequently identified using the TPC and TOF detectors. In the former, it is done via specific energy loss in an environment $\langle \frac{\mathrm{d}E}{\mathrm{d}x} \rangle$, as described by Eq. 2.1 in Sec. 2.7. In the latter, the velocity of the charged particle β is used, as described in Sec. 2.8. The identification of certain neutral particles is possible by reconstructing them from their decay products using a set of topological and kinematic requirements.

Identification of $\pi^{\pm}$, $\mathrm{K}^{\pm}$, and $\mathrm{p}(\bar{\mathrm{p}})$

From the $\langle \frac{\mathrm{d}E}{\mathrm{d}x} \rangle$ and β reconstructed with TPC and TOF, respectively, it is possible to calculate $n\sigma$, where σ is the relative difference between the measured and calculated signal for a specific particle species and p_{T}. The identification criterion is a requirement on $n\sigma$, typically $n\sigma < 3$ for both TPC and TOF if the signal from the latter is available.

Nevertheless, it has been shown in [153] that by combing the particle identification from different detectors, it is possible to obtain improved purity of the selected sample. The purity represents a fraction of particles of a certain species that is correctly identified. It can be seen in Fig. 4.4 that the separation in two dimensions is more significant compared to the case of using one detector (dimension) at the time. A combined probability is calculated for every reconstructed particle by combining the identification probability obtained from individual detectors. In this analysis, only TPC and TOF detectors are used for the particle identification, without an additional contribution from a different detector. The threshold for the combined probability is 95% for pions, and 85% for both kaons and protons across the full studied p_{T} range. Fig. 4.5 (right) shows the obtained purities of identified particles in p–Pb collisions. The purity of an individual species is calculated as

$$purity = \frac{N_{\mathrm{identified,true}}}{N_{\mathrm{identified}}}, \tag{4.5}$$

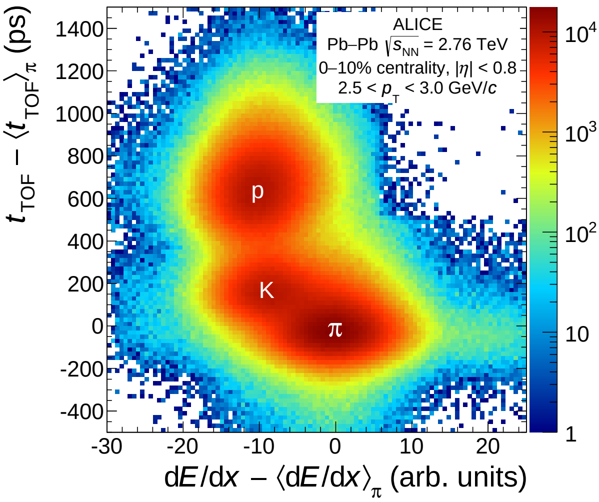

FIGURE 4.4: The difference between the measured and calculated signal of a particle from TPC and TOF detectors. Taken from [153].

i.e. it represents the fraction of particles that are correctly identified. A Monte Carlo (MC) simulation is used for obtaining $N_{\mathrm{identified,true}}$ and $N_{\mathrm{identified}}$ using a general purpose production with EPOS-LHC event generator [154]. The GEANT4 transport code [155] for simulating the passage of particles through matter is used to represent as closely as possible the LHC Run 2 p–Pb collisions recorded with the ALICE experiment. It can be seen that the purity is very high in the studied p_T region. The left panel of the same figures shows the fraction of primary identified particles. It can be seen that for $\pi^{\pm}$ and $K^{\pm}$, the contamination is rather low. The largest contamination can be seen for $p(\bar{p})$ at the low p_T region where its origin is mostly from the interactions of the primary particles with the material, and from the weak decays, such as Λ decay discussed in the following section.

Reconstruction of K^0_S and $\Lambda(\bar{\Lambda})$ particles

K^0_S and $\Lambda(\bar{\Lambda})$ are neutral particles reconstructed directly from their decay products. They are commonly referred to as V^0 particles due to the typical V-shape of their decay, shown in Fig. 4.6. The reconstruction is done using the most probable decay channel, $K^0_S \to \pi^+ + \pi^-$ with branching ratio (B.R.) 69.2% and $\Lambda(\bar{\Lambda}) \to p(\bar{p}) + \pi^{\mp}$ with B.R. 63.9% [9]. The reconstruction is done on a statistical basis, the signal is mixed with a combinatorial background. In ALICE, the first preselection of V^0 candidates is performed online during the data taking.

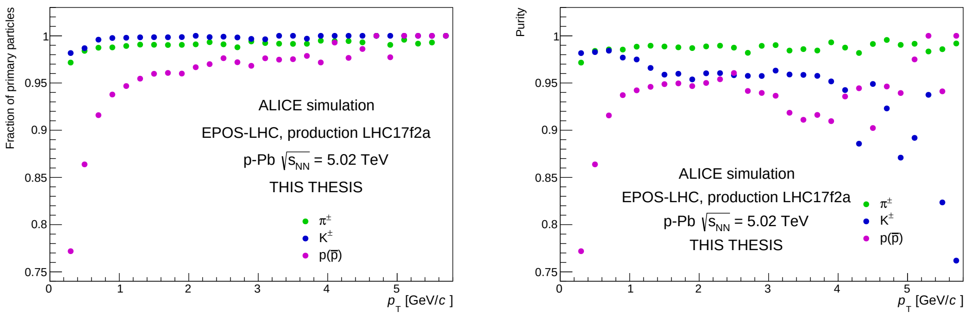

FIGURE 4.5: A fraction of primary particles (left) and purity (right) of $\pi^{\pm}$, $K^{\pm}$, and $p(\bar{p})$.

In small collision systems, such pp and p–Pb collisions, the topological criteria are the same. The rapidity of the V^0 candidate has to be within $|y| < 0.5$ with secondary vertex (SV) placed within a radial distance from the beam line between 0.5 and 200 cm. The combinatorial background is suppressed by applying several topological criteria for the decay products and the V^0 candidate. The used variables are illustrated in Fig. 4.6. First, for the candidate itself, the cosine of the pointing angle (PA), which is the angle between the line connecting primary and V^0 vertices and the V^0 momentum vector, has to be bigger than 0.97 and 0.995 for K^0_S and Λ, respectively. The proper lifetime $c\tau$ should be less than 20 and 30 cm for K^0_S and Λ, respectively. Secondly, a set of selection criteria is applied to the daughter tracks. They have to be within $|\eta| < 0.8$ and follow the same quality criteria besides the DCA that are required for the inclusive charged particles, described in Sec. 4.4. An additional requirement on the ratio between the number of space points and the number of crossed rows in the TPC is applied with the ratio being larger than 0.8. Daughter tracks of opposite charges have to fulfill the particle identification criteria as well. Only the information on the specific energy loss $\langle \frac{dE}{dx} \rangle$ from the TPC detector is used for the particle identification in this case. For K^0_S, both daughter tracks have to be within 3σ of $\pi^{\pm}$ hypothesis. For $\Lambda(\bar{\Lambda})$, positive (negative) daughter has to be within 3σ of $p(\bar{p})$ hypothesis, while negative (positive) daughter has to be within 3σ of $\pi^-(\pi^+)$ hypothesis. Finally, the DCA of a daughter track to the PV in the z direction has to be more than 0.06 cm, and the DCA between daughter tracks has to be below $1\sigma_r$ where σ_r is the combined resolution of the tracks.

The analysis is done within certain invariant mass windows, which are 0.44 – 0.56 GeV/c for K^0_S and 1.08 – 1.15 GeV/c for Λ. Invariant mass is calculated from the momenta of daughter particles and their masses obtained from the particle identification. Nevertheless, the identification is not always correct. For that reason, when reconstructing, e.g., a K^0_S candidate, its invariant mass is calculated assuming both daughter tracks

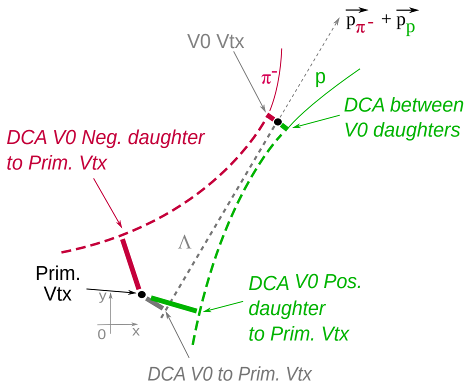

FIGURE 4.6: A scheme of decay of $\Lambda \rightarrow \mathrm{p} + \pi^-$ with selected topological criteria used in the reconstruction. Taken from [156].

are $\pi^\pm$. The invariant mass is then calculated also assuming one of the daughter tracks is $\mathrm{p}(\bar{\mathrm{p}})$, obtaining the invariant masses of both $\Lambda(\bar{\Lambda})$. If the difference between calculated and real invariant mass of $\Lambda(\bar{\Lambda})$ is < 0.005 GeV/c, the K^0_S candidate is rejected. The criterion, known as invariant mass cross rejection, is < 0.01 GeV/c when reconstructing $\Lambda(\bar{\Lambda})$ candidates, with the invariant mass of K^0_S used in the calculation.

Unlike the purity for primary identified particles that is obtained from the MC simulation, the purity for V^0 particles is calculated from the data. More specifically from the fit of the invariant mass distribution in every p_T bin. The distribution is fitted with

$$f(x) = p_1 + p_2 x + p_3 x^2 + p_4 x^3 + p_5 \left[p_6 e^{-\frac{1}{2}\left(\frac{x-\mu_1}{\sigma_1}\right)^2} + (1 - p_6) e^{-\frac{1}{2}\left(\frac{x-\mu_2}{\sigma_2}\right)^2} \right], \tag{4.6}$$

i.e. the double Gaussian and the third order polynomial functions to describe the signal and background, respectively. Parameters p_i for $i = 1, 2, ..., 6$ are obtained from the fit as well as mean value and the width of Gaussians, i.e. $\mu_{1,2}$ and $\sigma_{1,2}$. The purity is then calculated as

$$purity = \frac{\text{signal} - \text{background}}{\text{signal}}, \tag{4.7}$$

where the signal is obtained as an integral of the fit function within $\mu \pm 3\sigma$ around the invariant mass μ taken from Ref. [9]. The σ is the greater of $\sigma_{1,2}$ from the fit. The background is in $[\mu - 8\sigma, \mu - 5\sigma]$ and $[\mu + 5\sigma, \mu + 8\sigma]$ intervals. The purity of V^0 particles K^0_S and $\Lambda(\bar{\Lambda})$is shown in Fig. 4.7.

In order to be in agreement with the published results in different collision systems, the selection criteria are adjusted for the analysis in Pb–Pb collisions. The only difference in previously described criteria is that the DCA to PV has to be greater than 0.06 cm

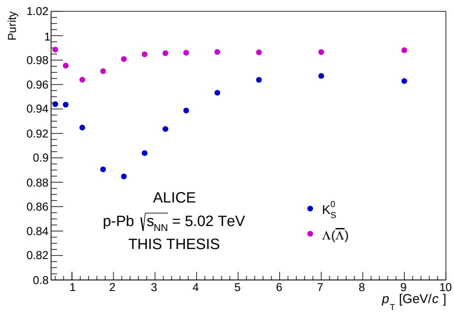

FIGURE 4.7: Purity of reconstructed V^0 particles in p–Pb collisions.

for both daughter tracks of K^0_S and greater than 0.1 cm and 0.25 cm for the positive and negative daughter track of Λ, respectively. However, in addition to aforementioned selection criteria, a criterion using the Armenteros-Podolanski variables is applied [86, 157] instead of using the cross rejection of V^0 invariant masses. With this requirement, the contamination from Λ and electron-positron pairs originated from γ conversions is removed from the K^0_S sample. Tracks with $q \leq |\alpha|/5$ are rejected, where q is the momentum of the positive daughter track projected to the plane perpendicular to the V^0 momentum. The α parameter is obtained from the projection of positive and negative daughter track into the V^0 momentum $p_L^{\pm}$ as $\alpha = (p_L^+ - p_L^-)/(p_L^+ + p_L^-)$. Moreover, the invariant mass window is extended to 0.4 – 0.6 GeV/c and 1.08 – 1.16 GeV/c for K^0_S and Λ, respectively.

Reconstruction of ϕ meson

For the analysis presented in this thesis, the reconstruction of ϕ meson is done in its decay channel $\varphi \rightarrow K^+ + K^-$ with B.R. 49.2% [9]. Unlike K^0_S and $\Lambda(\bar{\Lambda})$ candidates, no preselection is done as it is not possible to distinguish between primary particles and secondary particles that originate from the ϕ decays. Instead, the candidates are reconstructed directly from K^+K^- pairs, where $K^{\pm}$ are selected as described in Sec. 4.5. The only condition applied on ϕ candidate is on its invariant mass that is required to be within the mass window of 0.99 – 1.07 GeV/c. Both like-sign (K^+K^-) and unlike-sign (K^+K^+, K^+K^-) pairs are needed. The former is used for the combinatorial background estimation while the latter contains both the signal and the combinatorial background, which is significantly higher compared to the one of V^0 particles where the secondary vertex can be identified. The invariant mass spectrum of ϕ candidates is described using a sum of Breit-Wigner function for the signal and the third order polynomial for the residual background.

4.6 Mass-dependent correlations

The reconstruction of particles such as K^0_S, Λ, or ϕ out of their decay products mean the obtained sample contains candidates of two types – the real signal and the combinatorial background. The background contamination needs to be addressed in order to obtain the correlation of the signal only. The correction is done using p_T-differential event-averaged correlations, $\langle\langle 2' \rangle\rangle_{n_1,n_2}$, or generally $\langle\langle m' \rangle\rangle_n$ for single harmonic n and m-particle correlations. The contamination is expressed as [135, 144]

$$\langle\langle X' \rangle\rangle_n^{\text{total}}(m_{\text{inv}}) = f^{\text{signal}}(m_{\text{inv}})\langle\langle X' \rangle\rangle_n^{\text{signal}} + (1 - f^{\text{signal}}(m_{\text{inv}}))\langle\langle X' \rangle\rangle_n^{\text{bg}}(m_{\text{inv}}), \quad (4.8)$$

where f^{signal} is a fraction of the signal calculated from the invariant mass distribution (m_{inv}) in each p_T bin as

$$f^{\text{signal}}(m_{\text{inv}}) = \frac{N^{\text{signal}}(m_{\text{inv}})}{N^{\text{signal}}(m_{\text{inv}}) + N^{\text{bg}}(m_{\text{inv}})}. \quad (4.9)$$

N^{signal} and N^{bg} are numbers of signal particles and combinatorial background entries, respectively. They are obtained as an integral of the fit function of the signal and background. A common function of choice to describe the signal distribution is a double-Gaussian function. The background can be either n-th order polynomial or an exponential function [158]. The specific function is selected based on the studied particle. In this analysis, for K^0_S, Λ, and ϕ, the third order polynomial function is used.

The fits of the invariant mass spectrum and the multi-particle correlations are done simultaneously. An example of such a procedure is shown in Fig. 4.8. In the fits, multi-particle correlation of the background $\langle\langle X' \rangle\rangle_n^{\text{bg}}(m_{\text{inv}})$ can vary with m_{inv} while the extracted signal correlation $\langle\langle X' \rangle\rangle_n^{\text{signal}}$ is constant. The extracted $\langle\langle X' \rangle\rangle_n^{\text{signal}}$ is subsequently used to calculate the flow coefficients, as described in Sec. 3.2.

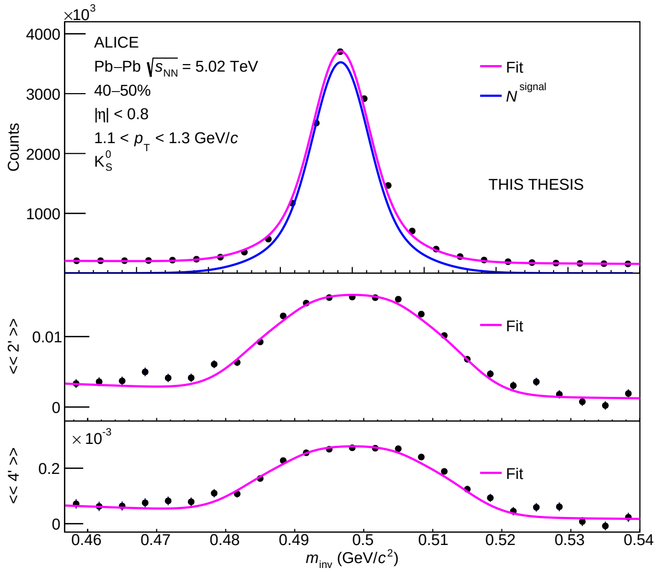

FIGURE 4.8: Simultaneous fit of the invariant mass of K^0_S meson, $\langle\langle 2' \rangle\rangle$, and $\langle\langle 4' \rangle\rangle$.

4.7 Corrections

The ALICE detector and its subdetectors are described in Sec. 2.2. Nevertheless, the acceptance of the detector and the efficiency of the reconstruction are not perfect. Therefore, it is essential to apply certain corrections in order to avoid any kind of additional effects during the data analysis . This section presents different corrections applied during the analysis procedure.

4.7.1 Non-uniform acceptance

ALICE detector does not have a perfectly uniform acceptance in both the azimuthal direction and the pseudorapidity. The most significant contribution to the nonuniformity is caused by the TPC detector located in the central barrel of ALICE. As the calculation of correlation depends on the azimuthal angle, such a discrepancy can negatively affected the obtained flow coefficients. The data-driven correction of the non-uniform acceptance (NUA) is applied in a form of particle weight $w(\eta, \varphi)$, calculated as

$$w(\eta, \varphi) = \frac{N^{\max}(\eta)}{N(\eta, \varphi)}, \tag{4.10}$$

where $N(\eta, \varphi)$ stands for number of particles in a specific η and φ bin, and $N^{\max}(\eta)$ is the maximum number of entries per φ slice. Moreover, the weight is species dependent,

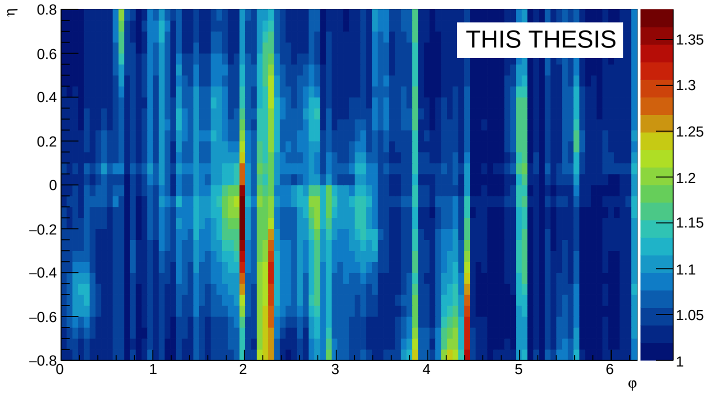

FIGURE 4.9: Particle weights for non-uniform acceptance correction of inclusive charged particles in Pb–Pb collisions at $\sqrt{s_{\mathrm{NN}}} = 5.02$ TeV.

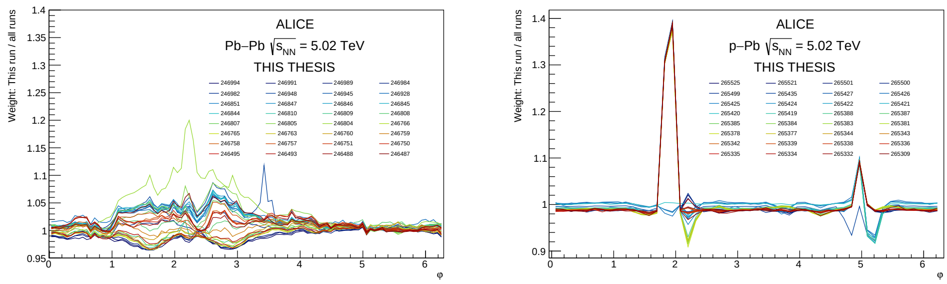

FIGURE 4.10: Ratio of particle weight $w(\eta, \varphi)$ of individual runs to the average weight across the whole data-taking for inclusive charged particles in Pb–Pb (left) and p–Pb (right) collisions at $\sqrt{s_{\mathrm{NN}}} = 5.02$ TeV.

i.e. it is calculated individually for every particle species. A distribution of $w(\eta, \varphi)$ in Pb–Pb collisions at $\sqrt{s_{\mathrm{NN}}} = 5.02$ TeV is shown in Fig. 4.9 for inclusive charged particles. There is no significant p_{T} dependence observed in the NUA correction for the studied p_{T} ranges, therefore the calculation is done for the whole studied p_{T} range.

In addition to the η and φ, the detector acceptance correction is studied for different periods of data taking. The projection of the weight, $w(\varphi)$, is shown in Fig. 4.10 for Pb–Pb (left) and p–Pb (right) collisions. It can be seen that the performance of different data-taking runs is different. For that reason, applying particle weights is done for individual Pb–Pb runs to allow more precise overall correction. In both p–Pb and pp collisions, runs with similar distributions are grouped in order gain higher statistical stability.

The application of the weight is done using the generic framework (GR) [80]. With this framework, two- and multi-particle correlations are calculated using Q-vectors. While the detailed description of the GF is provided in Sec. 3.1.1, a short example is provided for an illustration of the weight usage. The Q-vector is defined as

$$Q_{n,p} \equiv \sum_{i \in \mathrm{RFP}}^{M} w_i^p e^{in\varphi_i}, \tag{4.11}$$

where n, p are its harmonic and power. Analogically to the Q-vector, which contains reference particles (RFP), the p-vector contains particles of interest (POI). The q-vector contains all the particle from the overlap between RFP and POI. The two-particle correlation is calculated as

$$\langle 2' \rangle_{n,-n} = \frac{\mathrm{N}\langle 2' \rangle_{n,-n}}{\mathrm{D}\langle 2' \rangle_{n,-n}} = \frac{\mathrm{N}\langle 2' \rangle_{n,-n}}{\mathrm{N}\langle 2' \rangle_{0,0}} = \frac{p_{n,1} \cdot Q_{-n,1} - q_{0,2}}{p_{0,1} \cdot Q_{0,1} - q_{0,2}}, \tag{4.12}$$

where the subtracted terms in both numerator $\mathrm{N}\langle 2' \rangle$ and denominator $\mathrm{D}\langle 2' \rangle$ explicitly remove the self correlations of particles.

If the POI is an inclusive charged particle, the weight used in the definition of Q, p, and q, is the same. An example can be made by supposing the Q-vector containing 4 particles with weights $Q : w_1, w_2, w_3, w_4$ and p-vector being its subset, $p = q \subset Q$ with $p : w_3, w_4$. Then the denominator of 4.12 with explicitly multiplied terms is

$$\begin{aligned} \mathrm{D}\langle 2' \rangle &= p_{0,1} \cdot Q_{0,1} - q_{0,2} \\ &= (w_3 w_1 + w_3 w_2 + w_3^2 + w_3 w_4 + w_4 w_1 + w_4 w_2 + w_3 w_4 + w_4^2) - (w_3^2 + w_4^2). \end{aligned} \tag{4.13}$$

It can be seen that all the self correlations are trivially removed. However, the POI can be an identified particle. In that case, the distribution of $N(\eta, \varphi)$ might be different of the one of inclusive charged particles, which subsequently can lead to $w' \neq w$, where w' is the weight of POI. In order to represent the new weight, the Eq. 4.13 has to be modified to

$$\mathrm{D}\langle 2' \rangle = (w'_3 w_1 + w'_3 w_2 + w'_3 w_3 + w'_3 w_4 + w'_4 w_1 + w'_4 w_2 + w'_3 w_4 + w'_4 w_4) - (w'^2_3 + w'^2_4). \tag{4.14}$$

Unlike the previous case, the self correlations are not subtracted. The difference between these two approaches is shown in Fig. 4.11 for the flow coefficients of $v_2\{2\}$ (left) and $v_2\{4\}$ (right) of $\mathrm{K}^{\pm}$ in peripheral Pb–Pb collisions at $\sqrt{s_{\mathrm{NN}}} = 5.02$ TeV. The weights without considering the particle species are marked as GF weights as they originate from the generic framework without the proposed modification. In the new approach, marked in the legend as PID weights, the species of the particle is known prior to its contribution to the Q-vector. The PID weight w' is used when calculating the Q-vector. With this modification, the self correlations in Eq. 4.14 are removed. The importance of

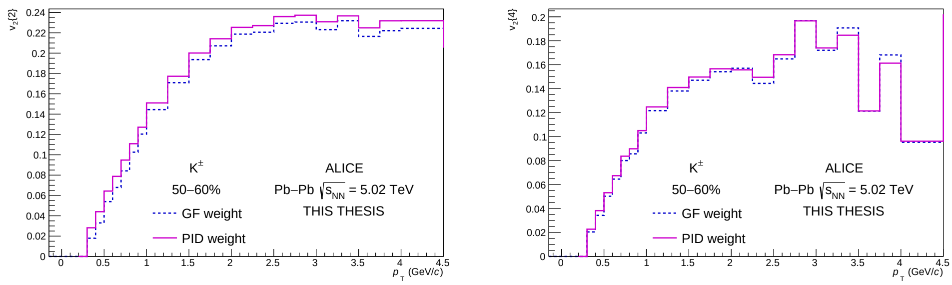

FIGURE 4.11: Flow coefficients $v_2\{2\}$ (left) and $v_2\{4\}$ (right) using two different weight approaches in peripheral Pb–Pb collisions for $K^{\pm}$.

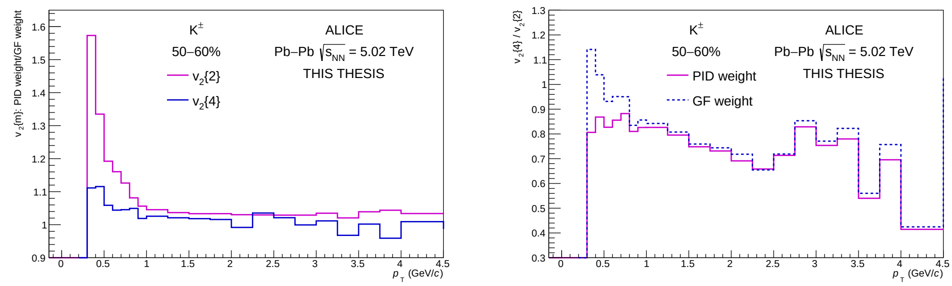

FIGURE 4.12: Left: Ratio of two different weight approaches for $v_2\{2\}$ and $v_2\{4\}$ in peripheral Pb–Pb collisions for $K^{\pm}$. Right: $v_2\{4\}/v_2\{2\}$ with two different weight approaches in peripheral Pb–Pb collisions for $K^{\pm}$.

the modification can be seen from the ratios of $v_2\{2\}$ (left) and $v_2\{4\}$ (right) with two different weights approaches, shown in Fig. 4.12 (left). It can be seen that the relative difference in low p_T is up to 60%. In addition, the modification is crucial for calculating the correct value of $v_2\{4\}/v_2\{2\}$, shown in Fig. 4.12 (right). The results of the ratio between the flow coefficients obtained from two- and four-particle cumulants are discussed in Sec. 5.1.7. Finally, when the pseudorapidity separation (η gap) is applied, both weight modes of $v_2\{2\}$ provide the same result as there is no self-correlation by construction. However, in the higher order correlations, the self-correlation is present even when an η gap is applied. For that reason, the default mode in this analysis is to use identified weights w'.

The correction of non-uniform acceptance using particle weights is used in the analysis using the generic framework, i.e. the two- and multi-particle cumulants and flow coefficients. In the measurement of di-hadron correlations, the effects of the detector acceptance are removed during the event mixing procedure described in Sec. 3.4. Once applied, all the non-physical correlations are removed from the correlation function

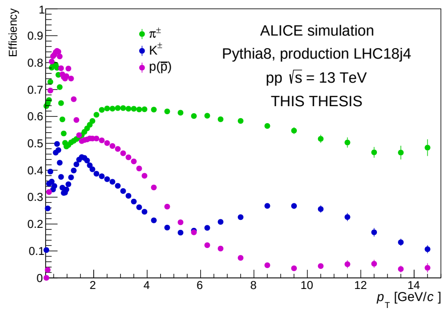

FIGURE 4.13: Reconstruction efficiency of primary charged particles $\pi^{\pm}$, $K^{\pm}$, and $p(\bar{p})$ in pp collisions.

$C(\Delta\eta, \Delta\varphi)$.

4.7.2 Reconstruction efficiency

In addition to the non-uniform acceptance correction, a correction of the reconstruction efficiency has to be applied for all the tracks originating from the central barrel, as it is not uniform across the studied p_T range. The reconstruction efficiency is calculated from a Monte Carlo (MC) simulation with GEANT4 toolkit [155] for simulating passage of the particles through the matter as

$$\varepsilon_{\mathrm{PID}}(p_{\mathrm{T}}) = \frac{N_{\mathrm{true,reconstructed,PID}}}{N_{\mathrm{generated,PID}}}, \tag{4.15}$$

where $N_{\mathrm{true,reconstructed,PID}}$ is the number of identified particles that are correctly reconstructed and $N_{\mathrm{generated,PID}}$ is the number of generated identified particles. The efficiency of charged particles is calculated using the efficiencies of identified particles, including the correction for the particle composition. The particle composition correction (PCC) factors are estimated in a data-driven way by comparing the measured relative hadron abundances to those in MC generator. Afterwards, PID efficiencies are weighted by the correction factors and summed to calculate the efficiency of all charged hadrons. The feed-down contribution for both identified and inclusive charged hadrons is estimated by weighting each secondary particle by the PCC weight of their mother particle. The reconstruction efficiency as a function of p_T is shown in Fig. 4.13 for $\pi^{\pm}$, $K^{\pm}$, and $p(\bar{p})$.

While the efficiency correction is important in the p_T-integrated flow measurements [159], it has been shown [102] that the effects are negligible in the case of p_T-differential flow measurements, including those of the identified particles. Thus, the p_T-differential flow coefficients are consistent within uncertainties with or without applying track-by-track reconstruction efficiency. Therefore, by default the results obtained using two- and multi-particle cumulants are calculated without this correction.

However, the aforementioned measurement uses particles from the central barrel only, i.e. both RFP and POI in cumulants and trigger and associated particles in the di-hadron correlations originate from the pseudorapidity $\eta| < 0.8$. Nevertheless, no such study has been done using associate particles from the forward pseudorapidity region in small collision systems. For that reason, the calculation of the ultra-long-range correlations and subsequent flow extraction is done both with and without applying track-by-track reconstruction efficiency correction. The correction is applied in a form of a weight of the studied particle pair,

$$w = \frac{1}{\varepsilon_{\text{trig}} \cdot \varepsilon_{\text{ass}}}, \tag{4.16}$$

where subscripts stands for trigger and associate particles, respectively.

For pp collisions, a general purpose MC production with the PYTHIA event generator [90] is used in order to obtain the reconstruction efficiency. The efficiencies applied in the analysis are period dependent and separately created for minimum bias and high multiplicity triggered collisions. In addition to the period dependence, the track-by-track efficiency is p_{T} and multiplicity dependent.

Similarly, for p–Pb collisions, a general purpose MC production anchored to relevant p–Pb data has been used with the DPMJET particle generator [160]. The efficiencies of the produced particles are p_{T} and centrality dependent. Moreover, as the η dependence is vital in non-symmetric p–Pb collisions, the pseudorapidity is also considered in the efficiency correction.

It is important to note that the efficiency correction, applied on a track-by-track basis, is applied only to the particles in the central pseudorapidity region ($|\eta| < 0.8$ in this analysis). The associated particles originate from the forward region. Since they are recorded with the FMD detector, described in Sec. 2.5, no tracking information is available. Thus the reconstruction efficiency correction is not possible. Instead, the possible effects from the nonuniform efficiency are studied during the closure test, described in Sec. 4.8.

The correlation function $C(\Delta\eta, \Delta\varphi)$ from ultra-long-range correlations does not significantly differ neither in magnitude nor in shape when calculated with or without applying reconstruction efficiency correction, as shown in Fig. 4.14. As a consequence, the flow coefficient $v_2\{2\text{PC}\}$ extracted using the template fit method out of $C(\Delta\eta, \Delta\varphi)$ with or without applying the efficiency correction does not differ. It can be seen in Fig. 4.15 where $v_2\{2\text{PC}\}$ is shown in central (0–20%) p–Pb collisions with the base of the template fit from the centrality 60–100%. The difference between the results obtained

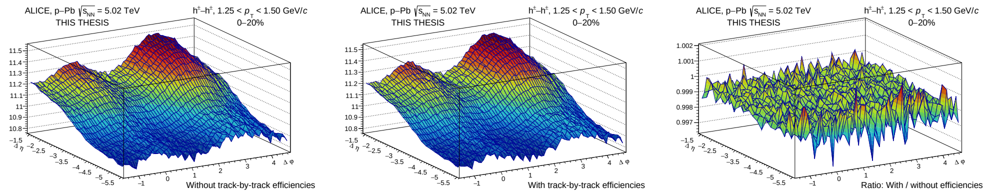

FIGURE 4.14: Correlation function $C(\Delta\eta, \Delta\varphi)$ from ultra-long-range correlations without (left) and with (middle) track-by-track particle efficiencies and their ratio (right) in central p–Pb collisions at $\sqrt{s_{NN}} = 5.02$ TeV.

with and without efficiency correction is shown in Fig. 4.15 (right) using the ratio of both approaches. It can be seen the results are consistent within uncertainties and statistical fluctuations, with the overall difference being $\approx 0.1\%$. The agreement confirms $v_2\{2PC\}(p_T)$ is not affected by the reconstruction efficiency correction also in the case of ultra-long-range correlations. To further confirm the conclusion, the study with or without applying reconstruction efficiency is done using MC events generated using AMPT simulation [161]. The conclusion, i.e. the independence on the weight usage, is confirmed. Nevertheless, the final results of $v_2\{2PC\}(p_T)$ from ultra-long-range correlations are obtained with applying the efficiency correction in order to be consistent with other correlation analyses using the FMD detector.

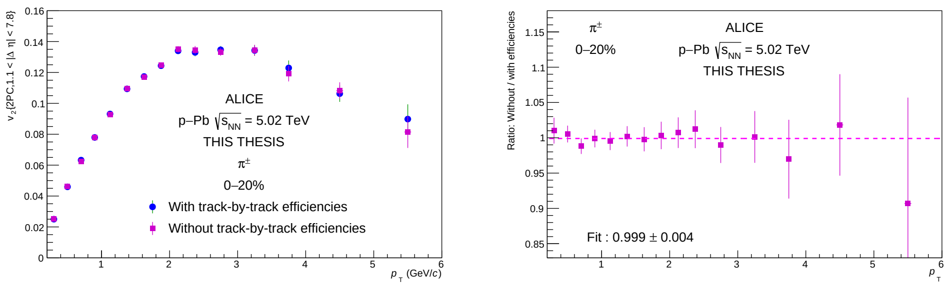

FIGURE 4.15: Left: Flow coefficients $v_2\{PC\}$ from ultra-long-range correlations obtained with the template fit method with and without track-by-track particle efficiencies in central p–Pb collisions at $\sqrt{s_{NN}} = 5.02$ TeV. Right: Ratio of $v_2\{PC\}$ with and without track-by-track particle efficiencies.

4.7.3 Secondary contamination

Alongside primary particles produced directly in the collision, a non-negligible amount of secondary particles is detected. They can originate, e.g. from decays of heavier particles and can be linked to either a secondary vertex or, in a case of a cascade decay, more vertices. Nevertheless, only the primary particles are of interest when reconstructing the collision. Therefore, a set of strict criteria is applied on reconstructed particles in order to remove as many secondary particles as possible.

Within the central barrel, thanks to the individual track reconstruction and good spatial resolution, described in Sec. 4.4, most of the secondary particles are removed, as can be seen in Fig. 4.5 (left) with the fraction of primary particles of $\pi^{\pm}$, $\mathrm{K}^{\pm}$, and $\mathrm{p}(\bar{\mathrm{p}})$. However, since the FMD detector, described in Sec. 2.5, does not provide any tracking information, it is impossible to distinguish between primary and secondary particles. The various sources of the contamination in this detector can be seen in Fig. 2.5. The simulation used for the sources of the secondary contamination in the FMD detector originates from Pb–Pb collisions. However, the contamination is expected to depend only weakly on the collision system [117].

The study of the effects of the secondary contamination in the FMD in this analysis is done using a MC simulation. The AMPT [161] event generator is used with the GEANT4 [155] toolkit for simulating the interaction of particles with the FMD detector. In addition to the simulation of standard reconstruction with the FMD detector, two MC simulations with an enhanced or reduced material budget of the FMD by 10% are used. As fewer events are generated with the MC simulations with the modified material budget, the statistical stability of the obtained results of $v_2\{2\mathrm{PC}\}(\mathrm{p_T})$ is affected, especially in the higher p_{T} region. The comparison of $v_2\{2\mathrm{PC}\}(p_{\mathrm{T}})$ coefficients calculated using the template fit method from three different MC simulations is shown in Fig. 4.16 (left). The ratio between the enhanced/reduced and default material budget simulations is shown in the right panel of Fig. 4.16. In order to obtain the deviation from the default simulation, and thus the possible effects of the secondary contamination in FMD, the ratio is fitted with a constant, as the FMD is p_{T}-independent. The deviation is 0.5% and 0.9% for +10% and -10%, respectively. A constant systematic uncertainty of 1% is added into the final systematic uncertainty for all the particle species to compensate for this contamination.

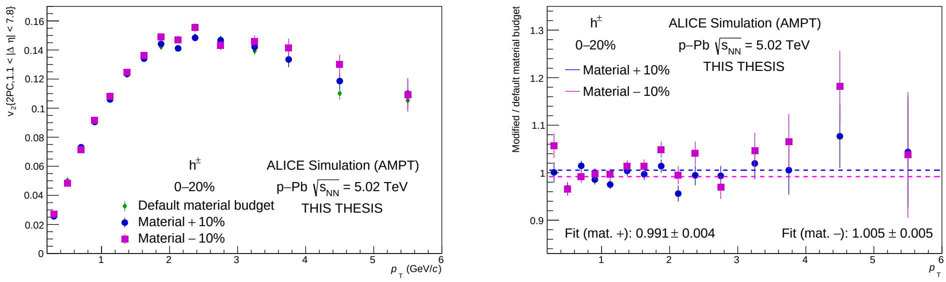

FIGURE 4.16: Left: Comparison of $v_2\{2\}(p_\mathrm{T})$ coefficients from the template fit method from the standard and material budget modified AMPT simulation in p–Pb collisions. Right: Ratio of different material budgets fitted with a constant function.

4.8 Monte Carlo closure test

To ensure no selection bias is introduced in the experimental measurements, the Monte Carlo closure test is performed. During the test, two sets of distributions of the particles are used to calculate the final observables. The first originates from the MC simulation where all the particles are generated using a specific event generator. This simulation, referred to as MC truth, contains only the effects mimicking the physical behaviour of the collision system. The second set of particle distributions combines MC simulated events and a simulation of the particle interaction with the detector using the GEANT4 [155] framework. Subsequently, the signal from the detector is reconstructed, obtaining a MC reconstrusted set. If no experimental bias is present, MC truth and MC reconstructed sets are in agreement within uncertainties.

The MC closure test is done for all the analyses and is demonstrated on an example of $v_2\{2\mathrm{PC}\}$ extracted with the template fit from the ultra-long-range correlations. This example is selected as it contains particles from two different pseudorapidities, thus the test consists of more steps compared to the MC closure test with particles from the central barrel only, i.e. other analyses presented in this thesis. In this case, the closure test is done separately for central and forward pseudorapidity, i.e. testing the reconstruction of detectors in this η coverages separately. Moreover, the closure test is performed for the entire detector in order to ensure the result corresponds to the combination of two separate closure tests and no remaining bias is present. To further ensure the correctness of the test, two different event generators, AMPT [161] and EPOS-LHC [154] are used to crosscheck the obtained results.

The comparison of $V_{n\Delta}$ coefficients extracted using the template fit method from the

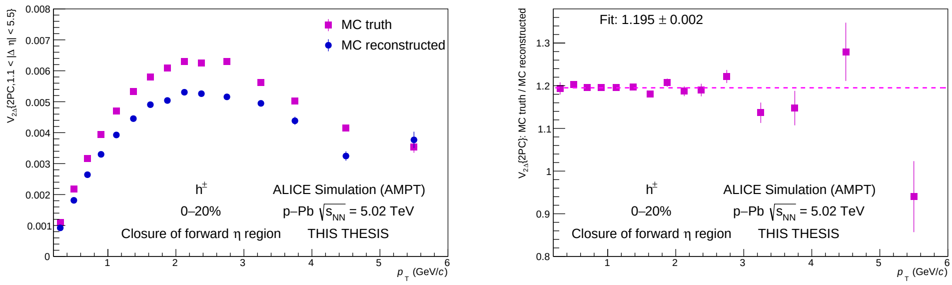

FIGURE 4.17: Left: Comparison of $V_{n\Delta}\{2\text{PC}\}$ coefficients from the template fit method of the ultra-long-range correlations (TPC–FMDA) from the MC simulation using AMPT event generator for the MC truth and MC reconstructed. Right: Ratio between MC truth and MC reconstructed and its fit with a constant.

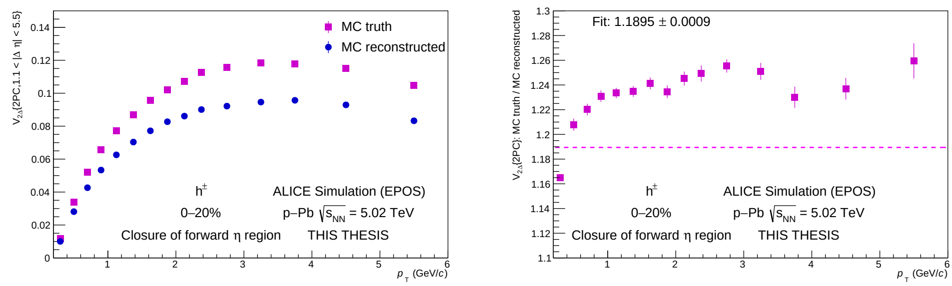

FIGURE 4.18: Left: Comparison of $V_{n\Delta}\{2\text{PC}\}$ coefficients from the template fit method of the ultra-long-range correlations (TPC–FMDA) from the MC simulation using EPOS event generator for the MC truth and MC reconstructed. Right: Ratio between MC truth and MC reconstructed and its fit with a constant.

ultra-long-range correlations is shown in Fig. 4.17 and 4.18 for AMPT and EPOS, respectively, for the closure test of forward pseudorapidity region. The trigger particle originates from the central pseudorapidity $|\eta| < 0.8$ while the associate particle originates from the forward pseudorapidity, $1.8 < \eta < 4.8$. The shown test studies the performance of the FMD detector with known large contamination of secondary particles. It can be seen from the ratio plots in right panels of Fig. 4.17 and 4.18 that the difference between MC truth and MC reconstructed is approximately 19%. The ratio plots are fitted with a constant as the signal from the FMD does not contain any information of the p_{T} of the particle. Analogically, the test is performed for the trigger particle originating from the central pseudorapidity $|\eta| < 0.8$ and the associated particle originating from the backward region, $-3.4 < \eta < -1.8$. The final contribution to the closure test of the FMD detector is performed with the trigger and associate particles from the forward and

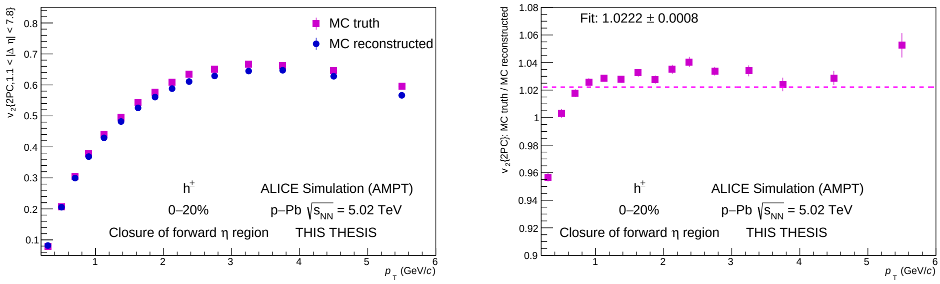

FIGURE 4.19: Left: Comparison of $v_2\{2\text{PC}\}$ coefficients from the template fit method of the ultra-long-range correlations from the MC simulation using AMPT event generator for the MC truth and MC reconstructed. Right: Ratio between MC truth and MC reconstructed and its fit with a constant.

backward pseudorapidity, respectively. The results of the fits with a constant from the tests are:

- $V_{n\Delta}$ from TPC – FMDA correlations, 19% for AMPT, 20% for EPOS,
- $V_{n\Delta}$ from TPC – FMDC correlations, 22% for AMPT, 24% for EPOS,
- $V_{n\Delta}$ from FMDA – FMDC correlations, 46% for AMPT, 49% for EPOS,

where TPC, FMDA, and FMDC represents central, forward, and backward pseudorapidities, respectively. These values agree with the corrections done in [150].

When inserting $V_{n\Delta}$ from TPC – FMDA, TPC – FMDC, and FMDA – FMDC into $v_2\{2\text{PC}\}$ using Eq. 3.53, the difference between MC truth and MC reconstructed, mostly caused by the secondary contamination in FMD, is reduced to 2%, thus almost cancels out as can be seen in Fig. 4.19.

Analogical test is performed to test the possible reconstruction bias in the central pseudorapidity region. The result of the closure test using $v_2\{2\text{PC}\}$ obtained from the template fit method is shown in Fig. 4.20. It can be seen that MC truth and MC reconstructed are in agreement within uncertainties. While the test is shown only for EPOS event generator, AMPT offers the same conclusion.

Finally, to ensure no additional selection bias affects the analysis, an overall MC closure test is performed studying the entire pseudorapidity. Its result is shown in Fig. 4.21. The difference is approximately in agreement with the closure test of the forward region only. Both AMPT and EPOS closure tests are considered in the final closure test. The 2% difference between MC truth and MC reconstructed is used as a correction of the final data points that is particle species independent. Such a MC-driven correction is a standard approach in analyses using the FMD detector.

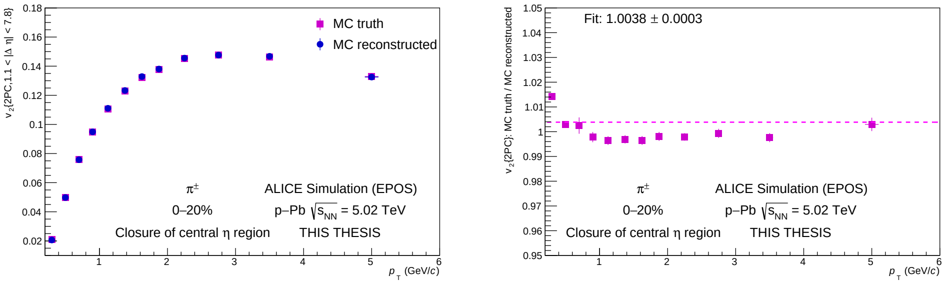

FIGURE 4.20: Left: Comparison of $v_2\{2\text{PC}\}$ coefficients from the template fit method of the ultra-long-range correlations from the MC simulation using EPOS event generator for the MC truth and MC reconstructed. Right: Ratio between MC truth and MC reconstructed and its fit with a constant.

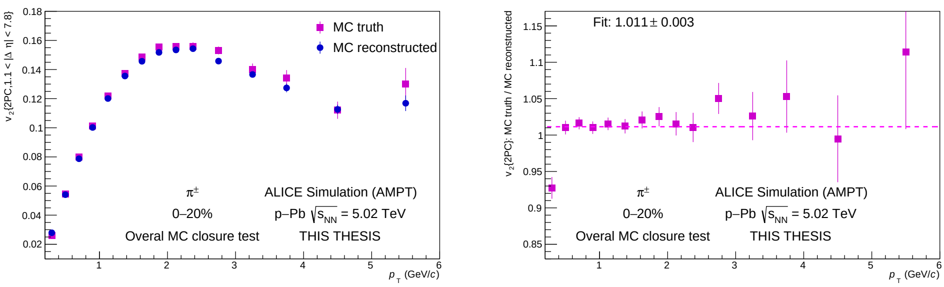

FIGURE 4.21: Left: Comparison of $v_2\{2\text{PC}\}$ coefficients from the template fit method of the ultra-long-range correlations from the MC simulation using AMPT event generator for the MC truth and MC reconstructed. Right: Ratio between MC truth and MC reconstructed and its fit with a constant.

4.9 Uncertainties

No measurement in physics can be discussed if it does not have assigned a correct uncertainty. For that reason, a detailed description of the methods of evaluating both statistical and systematic uncertainties is provided below.

4.9.1 Statistical uncertainties

It can be seen in Chapter 3 that for obtaining flow coefficients $v_2\{2\}(p_\mathrm{T})$, $v_2\{4\}(p_\mathrm{T})$, and $v_2\{2\mathrm{PC}\}(p_\mathrm{T})$, or mixed harmonic cumulants $MHC(v_m^2, v_n^2)$, several terms enter the equations for obtaining the final result. While the correlation between some of them can be or is known, it is not always trivial to obtain correlations between all of them. Therefore, the standard error propagation using partial derivatives cannot be used in this case as the correlation coefficients are unknown. Consequently, the bootstrapping method [162] is used for the final statistical uncertainty. The method is used to calculate the uncertainty of the flow coefficients using two- and multi-particle cumulants and di-hadron correlations, i.e. all the methods used for the results discussed in this thesis.

In the online part of the analysis, all the events randomly divided into equal samples. The central value is obtained from all the data without the additional sub-sampling. Keeping all the data is crucial as it can help with the stability of specific steps of the post-process, such as fitting. Nevertheless, a general rule applies that if a sub-sample provides a result significantly inconsistent with the rest of the data and it is impossible to identify the reason for the deviation, the sub-sample can be excluded.

With 10 sub-samples, b data samples are created by combining 10 sub-samples using a random selection with repetition. Typically in this analysis, $b = 100$. They are combined as a weighted average w_i, with the weight being $\frac{1}{\sigma^2}$. The σ is the estimated uncertainty from the standard error propagation, assuming no correlation exists between the variables. It should be emphasized that this estimate is not perfect and is only used as the inverse weight to reduce the contribution of statistically unstable samples. All the weighted averages w_i are combined into a standard average m. The final uncertainty is then

$$\sigma = \sqrt{\frac{\sum_i^b (w_i - m)^2}{b-1}}. \tag{4.17}$$

The distribution of samples and ratio between propagated and bootstrapped uncertainty can be seen in Fig. 4.22. The ratio, clearly deviated from one, shows the importance of using such a method for the final statistical uncertainty and the non-zero correlation between different components of the final result.

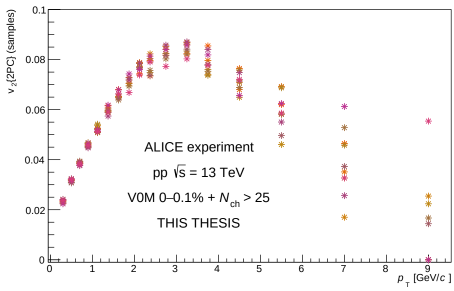

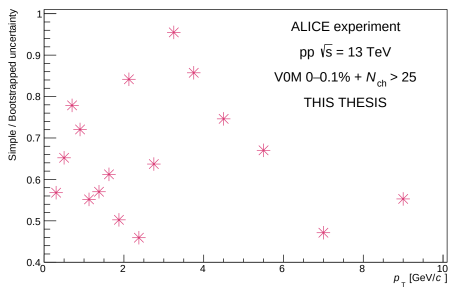

FIGURE 4.22: Comparison of $v_2\{2\mathrm{PC}\}(p_\mathrm{T})$ coefficients from different sub-samples (left) and ratio between simply propagated and bootstrapped statistical uncertainty (right) from the template fit method in pp collisions.

4.9.2 Systematic uncertainties

The systematic uncertainties are evaluated by varying the event and track selection criteria, requirements for the particle identification and the topological criteria for reconstruction of the V^0 particles[1] The evaluation is done separately for every method (cumulants, di-hadron correlations) and observable. Moreover, it is evaluated independently in every collision system, p_T region, and centrality interval for every particle species. Nevertheless, the procedure always follows the same steps and is described in the example below.

For every step, one selection criterion is modified at a time. An example of modifying an event selection criterion from the correlation of V0 and FMD multiplicities is shown in Fig. 4.23. The default criterion is 3σ cut, as shown in Fig. 4.2. For the study of the systematic uncertainty of this cut, this criterion is tightened to 1σ. First, the result with a varied event selection is compared to the default result, as shown in the top left panel. Their ratio is shown in the top right panel. The deviation, calculated as $|1 - \mathrm{default/syst}|$, is shown in the bottom left panel. The final panel in Fig. 4.23 (bottom right) shows a statistical significance of the difference, calculated as

$$B = \frac{|v_2(p_\mathrm{T})_{default} - v_2(p_\mathrm{T})_{syst}|}{\sqrt{|\sigma^2_{default} \mp \sigma^2_{syst}|}}. \tag{4.18}$$

This criterion is commonly referred to as the Barlow check, as it has been introduced in [163]. The subtraction in the denominator is used if the default and varied values are fully correlated, e.g. if one is a subset of the other when tightening or losing the selection criteria. The addition is chosen otherwise. For this analysis, if at least 1/3 of all the

[1]The effect from the secondary contamination in the FMD is added to the systematic uncertainty of $v_2\{2\mathrm{PC}\}(p_\mathrm{T})$ from ultra-long-range correlations, as discussed in Sec. 4.7.3.

points are above 1 (shown by the dashed line), the uncertainty is considered significant. The deviations from the default values from all the independent sources that pass the Barlow criterion are added in quadrature to obtain the final systematic uncertainty.

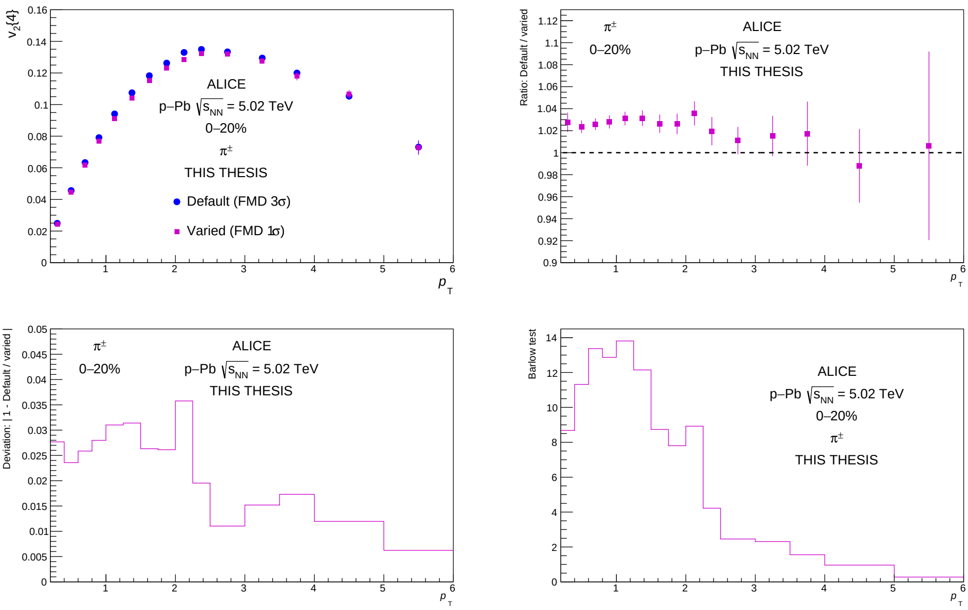

FIGURE 4.23: Study of systematic uncertainty - an example.

For the event selection criteria, in addition to the FMD cut, the requirement on the primary vertex position in the beam axis is modified from 10 cm to 8 cm. In Pb–Pb , the centrality determination is based on the multiplicity measurements in the forward pseudorapidity using the V0 detector in the default analysis. For the systematic uncertainty evaluation, the centrality determination is based on the multiplicity measurement in the central pseudorapidity using the first layer of the ITS detector. The effect of the polarity of the magnetic field within the detector is investigated by studying the opposite polarities independently.

The track quality requirements are varied as follows. The changes of the track reconstruction include the increase of the minimum number of required TPC space points from 70 to 90 and tightening of the DCA in the z axis from 2 cm to 0.5 cm and 0.2 cm in small and large systems, respectively. For the primary identified particles ($\pi^{\pm}$, $K^{\pm}$, and $p(\bar{p})$), the threshold for the minimal probability of the Bayesian particle identification is increased from 0.95 to 0.98 for $\pi^{\pm}$ and from 0.85 to 0.9 for both $K^{\pm}$ and $p(\bar{p})$. A example of final systematic uncertainty is illustrated on $v_2\{2, |\Delta\eta| > 0.8\}$ and $v_2\{4\}$ calculated using two- and four-particle cumulants. A summary of the minimum and maximum

	$v_2\{2, \|\Delta\eta\| > 0.8\}$			$v_2\{4\}$		
Uncertainty source	$\pi^{\pm}$	$K^{\pm}$	$p(\bar{p})$	$\pi^{\pm}$	$K^{\pm}$	$p(\bar{p})$
Centrality estimator	0–1%	0–1%	0–1%	0–1%	0–1%	0–1%
Magnetic field polarity	0–1%	0–1%	0–1%	0–1%	1–3%	0–3%
Tracking mode	0–2%	0–5%	0–5%	0–1%	0–1%	0–2%
Bayesian particle identification	0–5%	0–5%	0–4%	0–5%	0–4%	0–4%

TABLE 4.1: The minimum and maximum values of the relative systematic uncertainties from each individual source for $\pi^{\pm}$, $K^{\pm}$, and $p(\bar{p})$. Percentage ranges are given to account for variations with p_T and centrality.

contributions of individual sources to the the relative systematic uncertainties for primary identified particles is shown in Tab. 4.1.

For V^0 particles, the topological criteria are modified together in two different sets to tighten or loosen the requirements for the candidates. The modified cuts are chosen from Ref. [164]. In addition to the topological criteria, the fitting function of the signal and background are modified in the extraction of the multi-particle correlation of V^0 candidates from $\langle\langle X' \rangle\rangle_n^{\text{total}}(m_{\text{inv}})$ as described by Eq. 4.8. In the di-hadron correlation study, instead of a different fitting function, the signal range of V^0 is modified from 3 to 2σ. In addition, the fitting function of the signal is changed from the double-Gaussian to the standard Gaussian distribution.

In the study of flow fluctuations, the evaluation of the systematic uncertainty is performed based on all final the observables, such as $\langle v_n \rangle$, $\sigma(v_n)$, $F(v_n)$, in order to not introduce a bias from the correlation between systematic uncertainties of $v_2\{2\}$ and $v_2\{4\}$ that are used for their calculation.

Finally, for the flow coefficients $v_2\{2\text{PC}\}$ obtained with the template fit method, a different base (low multiplicity region) is tested in the non-flow treatment method during the evaluation of the systematic uncertainty.

If not stated otherwise, all the results presented in the following two chapters are shown with a systematic uncertainty plotted as a box around the central value, while the statistical uncertainty is shown as a vertical error bar.

5 Results and discussion

The measurements of anisotropic flow in Pb–Pb collisions help to investigate the initial conditions and the transport properties of QGP. Various flow observables are used for such a study. In particular, mixed harmonic cumulants $MHC(v_m^2, v_n^2)$ with a unique sensitivity to the initial conditions, and the flow of identified particles that can probe the particle production mechanisms.

While minimum bias pp collisions are considered a base for heavy-ion measurements, collective behaviour is observed in small collision systems at very high multiplicities. Such a behaviour is associated with the production of a droplet of QGP. Thus, measuring flow coefficients in p–Pb and pp collisions can help to understand the development of flow from the initial geometry.

Measurements in both large and small systems are performed using methods presented in Chap. 3. The analysis of experimental data is described in Chap. 4. This chapter focuses on the results in Pb–Pb, p–Pb, and pp collisions at $\sqrt{s_{\mathrm{NN}}} = 5.02, 5.02,$ and 13 TeV, respectively. Measurements are also compared to predictions from several different models in order to study the properties of QGP in Pb–Pb collisions as well as the possibility of QGP production in small systems.

This chapter reports on flow measurements in large and small systems. In the first part, the flow coefficients measured in Pb–Pb collisions are discussed. First, a new algorithm for calculating multi-particle correlations is presented. A comparison between the standard and the new implementation is provided, and further performance optimisation is discussed. Calculated multi-particle correlations are used to measure flow coefficients using multi-particle cumulants. The higher orders of multi-particle cumulants are obtained using the generic algorithm. The tests of the algorithm are performed using a toy Monte Carlo simulation with which both flow coefficients from multi-particle cumulants and mixed harmonic cumulants are calculated. The first results in the experimental data are presented for both observables. In addition, mixed harmonic cumulants are compared to theoretical predictions. Second, the measurement of flow of identified particles in Pb–Pb collisions is discussed in detail. The reported flow coefficients are measured for 14 identified particle species using two- and four-particle cumulants. In addition, the first two moments of the probability density function of flow are discussed. Furthermore, the model comparison is provided to examine the contribution of the quark coalescence mechanism.

The flow coefficients of identified particles in small collision systems, p–Pb and pp, are calculated using two- and four-particle cumulants and the di-hadron correlations method considering various non-flow treatments. The advantages and disadvantages of each method are discussed. Next, measurements of flow for nine different particle species are reported that have been performed using the template fit method on ultra-long-range di-hadron correlations. Striking similarities between small and large collision systems are observed and discussed in detail. Finally, the obtained results are compared to the models in order to study the mechanisms contributing to the flow in small systems.

5.1 Flow in large collision systems

The flow coefficients in large collision systems are studied at the LHC in Pb–Pb collisions. The flow coefficients of single harmonics from multi-particle cumulants, $v_n\{m\}$, are obtained using the generic algorithm from the multi-particle correlations. The calculation of multi-particle correlations is discussed in the context of the new formulation of the recursive algorithm. In addition, the generic algorithm can be used to calculate an arbitrary order of multi-particle cumulants with mixed harmonics. In this section, observables with both single and mixed harmonics are presented. The measured mixed harmonic cumulants are compared to hydrodynamic calculations with different initial conditions. The anisotropic flow in large collision systems is further studied using the measurements of flow of identified particles using various observables.

5.1.1 Multi-particle correlations

As introduced in Sec. 3.1.1, calculating m-particle correlations from Q-vectors leads to the number of terms that follow a Bell sequence (see Eq. 3.15). For that reason, a recursive algorithm presented in [80] is typically used to calculate the m-particle correlation $N\langle m\rangle$. One of the shortcomings of the recursive approach is that there are a lot of recurring terms that are evaluated, thus inflating the computational time. This becomes a significant issue especially when considering more than eight-particle correlations. An new version of the recursive formula is presented in [134] and described in Sec. 3.2.1. The new algorithm improves upon old by ensuring that each recurrent term is evaluated only once, hence greatly reducing the CPU time. The new implementation of the algorithm is tested in a Toy Monte Carlo simulation, where $v_2 = 0.1$ and $v_3 = 0.05$, and no fluctuations nor correlations between harmonics are considered. Overall, 10^5 events are simulated, where the number of tracks in each event is drawn from a uniform distribution and is between 200 and 1000.

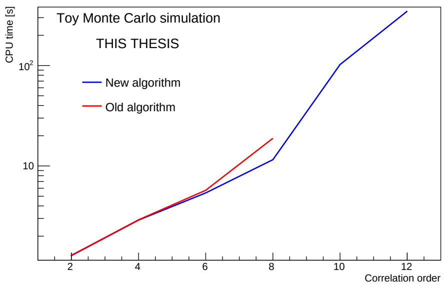

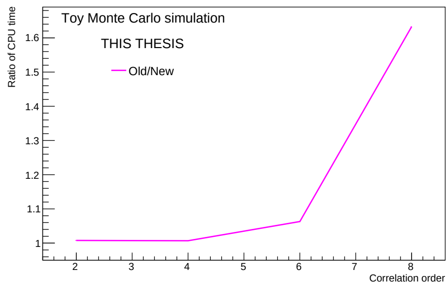

FIGURE 5.1: Comparison of elapsed CPU time for different orders of m-particle correlations for 10^5 events simulated with Toy Monte Carlo.

Once the simulation is finished, the test on the correlation algorithm start. The elapsed CPU time for the previous and new implementations of the algorithm and their ratios are shown in Fig. 5.1. The old algorithm is used only up to $\langle\langle 8\rangle\rangle$. With the new implementation of the algorithm, the average time per event for $\langle\langle 2\rangle\rangle$ is $\sim 12\mu$s, while for $\langle\langle 12\rangle\rangle$ it is $\sim$ 3 ms, i.e., there is a magnitude difference of three orders. Due to the long average CPU time per event, higher orders of correlations, such as $\langle\langle 14\rangle\rangle$ and $\langle\langle 16\rangle\rangle$, are not calculated.

In addition to the calculation of correlation using the recursive algorithm, the total CPU time includes the process of filling the Q-vector with generated particles. Nevertheless, the process of filling the Q-vector is the same for both implementations. Therefore it does not affect the difference in the total elapsed CPU time. Moreover, the filling of the Q-vector process is optimised, i.e., the combination of harmonics n and power p of Q-vector $Q_{n,p}$ is filled only if used in the final combination. For example, four-particle correlations with single harmonic 2, or $N\langle 4\rangle_{2,2,-2,-2}$, is calculated using $Q_{n,p}$ as shown in Eq. 3.8. For single harmonic 2, the possible ranges of n and p are 0–4 for both parameters. The standard approach in the generic framework calculation is to fill $(4+1)\times(4+1)$ terms for every generated particle. Every term contains a sine and cosine operation, and a complex addition of two numbers[1]. For $N\langle 4\rangle_{2,2,-2,-2}$, only $Q_{4,2}$, $Q_{2,3}$, $Q_{2,1}$, $Q_{0,4}$ and $Q_{0,2}$ are needed, i.e. 5 terms instead of 25. Nevertheless, to keep the algorithm as general as possible, a vector with maximum power for harmonic is introduced. Then, for harmonics $\{0,1,2,3,4\}$, the maximum power vector is $\{4,0,3,0,2\}$. In total, 9 terms are filled instead of 25. Generally, for single harmonic n and the correlation of m particles, the vector of maximum powers is $\{m, m-1, m-2, ...\}$ for harmonics $\{0, n, 2n, ...\}$ and zero otherwise. For the highest possible order of multi-particle correlations used in the calculation, $m = 12$, 63 terms are filled instead of 169.

[1]For further optimisation, ROOT's `TComplex` class is replaced by standard C++ `std::complex`.

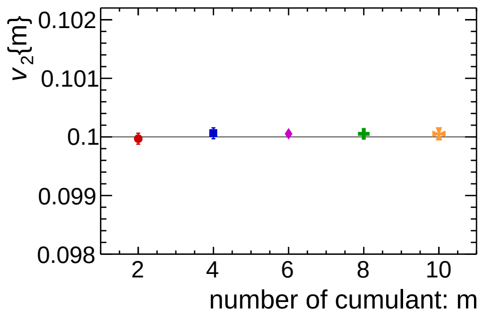

FIGURE 5.2: Flow coefficients $v_2\{m\}$ from different orders of multi-particle cumulants m obtained from Toy Monte Carlo simulation. Taken from [134].

5.1.2 Flow coefficients from multi-particle cumulants

Multi-particle correlations can be used to calculate multi-particle cumulants and flow coefficients. Using the notation $\langle\langle m\rangle\rangle_n = \langle v_n^m\rangle$ for a single harmonic n, flow coefficients $v_n\{m\}$ are calculated from m-particle cumulants as

$$v_n\{2\} = \sqrt{\langle v_n^2\rangle}, \tag{5.1}$$

$$v_n\{4\} = \sqrt[4]{-\left(\langle v_n^4\rangle - 2\langle v_n^2\rangle^2\right)}, \tag{5.2}$$

$$v_n\{6\} = \sqrt[6]{\frac{1}{4}\left(\langle v_n^6\rangle - 9\langle v_n^4\rangle\langle v_n^2\rangle + 12\langle v_n^2\rangle^3\right)}, \tag{5.3}$$

$$v_n\{8\} = \sqrt[8]{-\frac{1}{33}\left(\langle v_n^8\rangle - 16\langle v_n^6\rangle\langle v_n^2\rangle - 18\langle v_n^4\rangle^2 + 144\langle v_n^4\rangle\langle v_n^2\rangle^2 - 144\langle v_n^2\rangle^4\right)}, \tag{5.4}$$

$$\begin{aligned} v_n\{10\} = {} & \left[\frac{1}{456}\left(\left\langle v_n^{10}\right\rangle - 25\left\langle v_n^8\right\rangle\left\langle v_n^2\right\rangle - 100\left\langle v_n^6\right\rangle\left\langle v_n^4\right\rangle + 400\left\langle v_n^6\right\rangle\left\langle v_n^2\right\rangle^2\right.\right. \\ & \left.\left.+900\left\langle v_n^4\right\rangle^2\left\langle v_n^2\right\rangle - 3600\left\langle v_n^4\right\rangle\left\langle v_n^2\right\rangle^3 + 2880\left\langle v_n^2\right\rangle^5\right)\right]^{1/10}, \end{aligned} \tag{5.5}$$

$$\begin{aligned} v_n\{12\} = {} & \left[-\frac{1}{9460}\left(\left\langle v_n^{12}\right\rangle - 36\left\langle v_n^{10}\right\rangle\left\langle v_n^2\right\rangle - 225\left\langle v_n^8\right\rangle\left\langle v_n^4\right\rangle + 900\left\langle v_n^8\right\rangle\left\langle v_n^2\right\rangle^2\right.\right. \\ & -200\left\langle v_n^6\right\rangle^2 + 7200\left\langle v_n^6\right\rangle\left\langle v_n^4\right\rangle\left\langle v_n^2\right\rangle - 14400\left\langle v_n^6\right\rangle\left\langle v_n^2\right\rangle^3 + 2700\left\langle v_n^4\right\rangle^3 \\ & \left.\left.-48600\left\langle v_n^4\right\rangle^2\left\langle v_n^2\right\rangle^2 + 129600\left\langle v_n^4\right\rangle\left\langle v_n^2\right\rangle^4 - 86400\left\langle v_n^2\right\rangle^6\right)\right]^{1/12}. \end{aligned} \tag{5.6}$$

The Toy Monte Carlo simulation introduced above is used to test the equations obtained from the generic algorithm. The results of $v_2\{m\}$ for m between 2 and 10 are

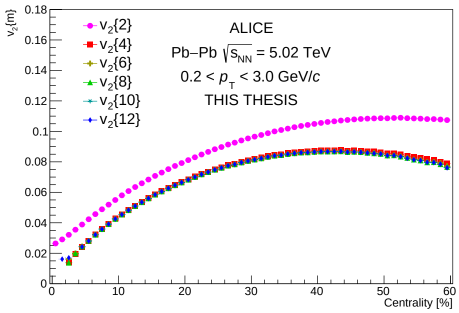

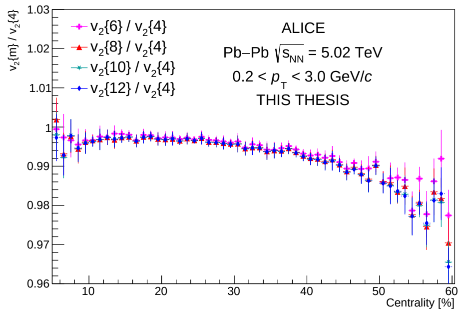

FIGURE 5.3: Left: Flow coefficients $v_2\{m\}$ from different orders of multi-particle cumulants m as a function of collision centrality in Pb–Pb collisions at $\sqrt{s_{\rm NN}} = 5.02$ TeV. Right: Ratio $v_2\{m\}/v_2\{4\}$ in Pb–Pb collisions at $\sqrt{s_{\rm NN}} = 5.02$ TeV.

shown in Fig. 5.2. It can be seen that the values of v_2 are consistent with the input flow signal, which is 0.1. Thus, the equations for calculating flow coefficients from different orders of multi-particle correlations are validated and can be used for the flow measurements.

The first application of the algorithm in experiments is done in Pb–Pb collisions at $\sqrt{s_{\rm NN}} = 5.02$ TeV. The results of flow coefficients $v_2\{m\}$ for m between 2 and 12 are shown in Fig. 5.3. Due to the high CPU consumption, flow coefficients $v_2\{m\}$ for $m \geq 14$ are not calculated. For m in the range 2 to 8, the flow coefficients are in agreement with the published results in the same kinematic region ($p_{\rm T}, \eta$), shown in Fig. 1.16. The difference between $v_2\{2\}$ and flow coefficients $v_2\{m\}$ from higher orders of m-particle cumulants is mainly explained by their different sensitivities to the flow fluctuations. Moreover, the non-flow contributes to the measured flow coefficients $v_2\{2\}$ while non-flow effects are sufficiently suppressed in higher orders cumulants. Flow coefficients from higher orders cumulants, v_2m from $m \geq 4$, are approximately in agreement, i.e. $v_2\{4\} \approx v_2\{6\} \approx ... \approx v_2\{12\}$. Their relative differences expressed in the form of their ratios $v_2\{m\}/v_2\{4\}$ are shown in Fig. 5.3 (right). The results in the most central collisions are not reported due to the significant statistical uncertainty of the ratio. The differences between higher orders of flow coefficients vary with the event centrality, from approximately 0.5% in central collisions to up to 3.5% in peripheral collisions. Such results are in agreement with [165]. The differences are believed to originate from the deviation of the flow $p.d.f.$ from the Bessiel-Gaussian distribution [166].

The higher order cumulants can be used for suppressing the non-flow contamination, as addressed in Sec. 3.5. A comparison of cumulants $c_2\{m\}$ for m between 2 and 12 is shown in Fig. 5.4 together with cumulants from the HIJING simulation [83] in order

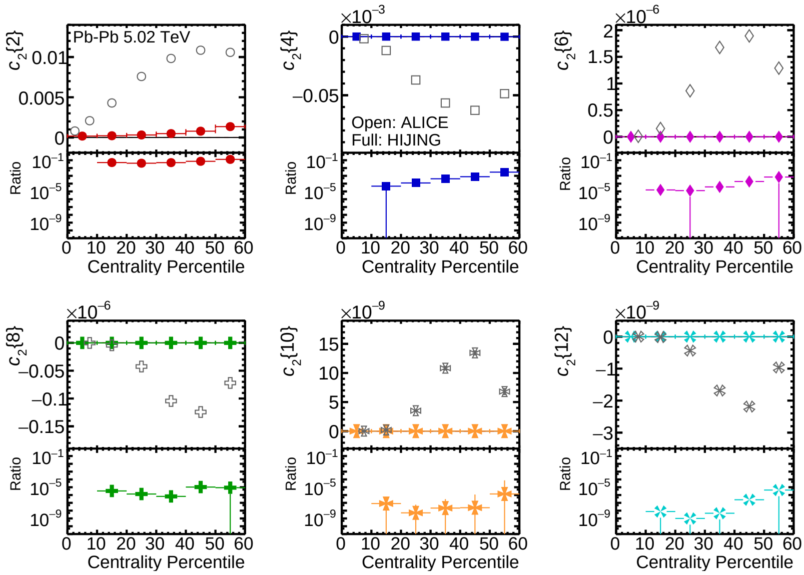

FIGURE 5.4: Multi-particle cumulants $c_2\{m\}$ for different m as a function of collision centrality in Pb–Pb collisions at $\sqrt{s_{\rm NN}} = 5.02$ TeV from the ALICE experiment and from HIJING simulation. Taken from [134].

to test the non-flow contribution. HIJING is selected as it does not contain any anisotropic flow signal. Thus the obtained result from HIJING simulations contains only the non-flow. For that reason, cumulants are shown instead of flow coefficients, as HIJING is expected to be very close to zero. Hence, it might be problematic to obtain the final $v_n\{m\}$ results, i.e., if the corresponding cumulants has a wrong sign. It is observed in Fig. 5.4 that the cumulants in Pb–Pb collisions from ALICE are non-zero and show the characteristic sign change – $c_2\{2\}$, $c_2\{6\}$, and $c_2\{10\}$ are positive while $c_2\{4\}$, $c_2\{8\}$, and $c_2\{12\}$ are negative, while the cumulants results from HIJING simulations are compatible with zero for $c_2\{m\}$ with $m \geq 4$. The results of $c_2\{2\}$ from HIJING simulation is non-zero in peripheral collisions. However, it is significantly smaller compared to the $c_2\{2\}$ from the experimental data.

5.1.3 Mixed harmonic cumulants

Besides the calculation of $v_n\{m\}$ with arbitrary m and n, the generic algorithm can be used to calculate the correlation between different moments $2k, 2l$ of different flow harmonics v_m, v_n using the observable Mixed Harmonic Cumulant $MHC(v_m^{2k}, v_n^{2l})$ [134].

The lowest order, $MHC(v_m^2, v_n^2)$, is a four-particle cumulant that is identical to the symmetric cumulant $SC(m,n)$, defined as

$$MHC(v_m^2, v_n^2) = SC(m,n) = \langle v_m^2 v_n^2 \rangle - \langle v_m^2 \rangle \langle v_n^2 \rangle. \tag{5.7}$$

A six-particle cumulant is used to study correlations between higher moments of different flow harmonics. For simplicity, specific harmonics ($m = 2, n = 3$) are used in the equations below. The $MHC(v_2^4, v_3^2)$ is defined as

$$MHC(v_2^4, v_3^2) = \left\langle v_2^4 v_3^2 \right\rangle - 4 \left\langle v_2^2 v_3^2 \right\rangle \left\langle v_2^2 \right\rangle - \left\langle v_2^4 \right\rangle \left\langle v_3^2 \right\rangle + 4 \left\langle v_2^2 \right\rangle^2 \left\langle v_3^2 \right\rangle. \tag{5.8}$$

Furthermore, it is possible to construct an eight-particle cumulant, either for different moments of correlations, as

$$\begin{aligned} MHC(v_2^6, v_3^2) = &\left\langle v_2^6 v_3^2 \right\rangle - 9 \left\langle v_2^4 v_3^2 \right\rangle \left\langle v_2^2 \right\rangle - \left\langle v_2^6 \right\rangle \left\langle v_3^2 \right\rangle - 9 \left\langle v_2^4 \right\rangle \left\langle v_2^2 v_3^2 \right\rangle \\ &- 36 \left\langle v_2^2 \right\rangle^3 \left\langle v_3^2 \right\rangle + 18 \left\langle v_2^2 \right\rangle \left\langle v_3^2 \right\rangle \left\langle v_2^4 \right\rangle + 36 \left\langle v_2^2 \right\rangle^2 \left\langle v_2^2 v_3^2 \right\rangle. \end{aligned} \tag{5.9}$$

or with the same moments of correlations, as in

$$\begin{aligned} MHC(v_2^4, v_3^4) = &\left\langle v_2^4 v_3^4 \right\rangle - 4 \left\langle v_2^4 v_3^2 \right\rangle \left\langle v_3^2 \right\rangle - 4 \left\langle v_2^2 v_3^4 \right\rangle \left\langle v_2^2 \right\rangle - \left\langle v_2^4 \right\rangle \left\langle v_3^4 \right\rangle - 8 \left\langle v_2^2 v_3^2 \right\rangle^2 \\ &- 24 \left\langle v_2^2 \right\rangle^2 \left\langle v_3^2 \right\rangle^2 + 4 \left\langle v_2^2 \right\rangle^2 \left\langle v_3^4 \right\rangle + 4 \left\langle v_2^4 \right\rangle \left\langle v_3^2 \right\rangle^2 + 32 \left\langle v_2^2 \right\rangle \left\langle v_3^2 \right\rangle \left\langle v_2^2 v_3^2 \right\rangle. \end{aligned} \tag{5.10}$$

In addition, it is possible to study the correlation between more than two different harmonics, such as a correlation between v_m^2, v_n^2, and v_p^2. For specific harmonics ($m = 2, n = 3, p = 4$), it is defined as

$$\begin{aligned} MHC(v_2^2, v_3^2, v_4^2) = &\left\langle v_2^2 v_3^2 v_4^2 \right\rangle - \left\langle v_2^2 v_3^2 \right\rangle \left\langle v_4^2 \right\rangle - \left\langle v_2^2 v_4^2 \right\rangle \left\langle v_3^2 \right\rangle \\ &- \left\langle v_3^2 v_4^2 \right\rangle \left\langle v_2^2 \right\rangle + 2 \left\langle v_2^2 \right\rangle \left\langle v_3^2 \right\rangle \left\langle v_4^2 \right\rangle \end{aligned} \tag{5.11}$$

It is important to note that it is not possible to construct $MHC(v_m^2, v_n^2, v_p^2)$ where $m + n = p$ as it contains a non-vanishing correlation with the flow symmetry planes. Such observable is discussed in details in Appendix B of [134].

Analogically, the idea behind mixed harmonic cumulants is first tested using the Toy Monte Carlo simulation. Such a study serves as a validation of the equations obtained from the generic algorithm. Mixed harmonic cumulants $MHC(v_2^m, v_3^n)$ for different moments of the correlations are shown in Fig. 5.5. Both v_2 and v_3 have fixed values in the simulation. As no correlation between v_2 and v_3 is inserted in the Toy MC, all the results are consistent with zero, which confirms the correctness of the used equations.

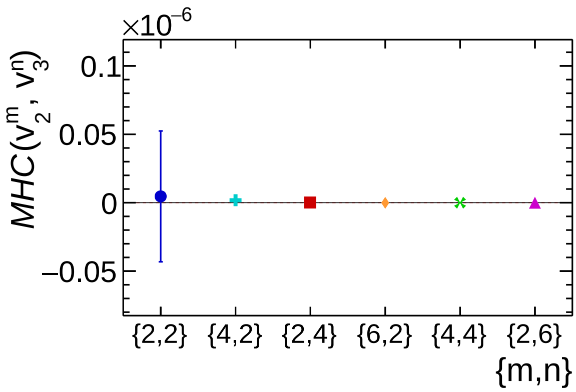

FIGURE 5.5: Mixed harmonic cumulants $MHC(v_2^m, v_3^n)$ for different moments of the correlations obtained from Toy Monte Carlo simulation. Taken from [134].

While the optimisation of filling of the Q-vector is straightforward for the case of multi-particle correlations with a single harmonic, it is much less trivial in the case for mixed harmonics. The vector of maximum powers, discussed in Sec. 5.1.1, is calculated case-by-case for higher order correlations. For example, the maximum power vector needed for the calculation of $MHC(v_2^2, v_3^2)$ that corresponds to the vector of maximum harmonics $\{0, 1, 2, 3, 4, 5\}$ is $\{4, 2, 3, 3, 0, 2\}$, i.e., no obvious trend is present.

In order to study genuine multi-particle correlations independent of the flow magnitudes, the results are normalised as

$$nMHC(v_m^k, v_n^l) = \frac{MHC(v_m^k, v_n^l)}{\langle v_m^k \rangle \langle v_n^l \rangle}. \tag{5.12}$$

A comparison of different normalised mixed harmonic cumulants measurements in Pb–Pb at $\sqrt{s_{\mathrm{NN}}} = 5.02$ TeV is shown in Fig. 5.6. The negative sign of $MHC(v_2^2, v_3^2)$ is consistentwith in the published measurement of symmetric cumulants from [82], though, the measurement originates from Pb–Pb collisions at $\sqrt{s_{\mathrm{NN}}} = 2.76$ TeV. Mixed harmonic cumulants from six-particle cumulants, $MHC(v_2^4, v_3^2)$ and $MHC(v_2^2, v_3^4)$, are positive, while the mixed harmonic cumulants from eight-particle cumulants, i.e., $MHC(v_2^6, v_3^2)$, $MHC(v_2^4, v_3^4)$, and $MHC(v_2^2, v_3^6)$, are negative. The higher order MHC show the characteristic sign changes for four-, six-, and eight-particle cumulants. The observation is consistent with the four-, six-, and eight-particle cumulants of single harmonic as shown in Fig. 5.4. Finally, analogically to multi-particle cumulants, the residual non-flow contribution is tested using HIJING simulation. The results, shown in [134], are consistent with zero and confirm that the non-flow suppression in multi-particle cumulants is sufficient.

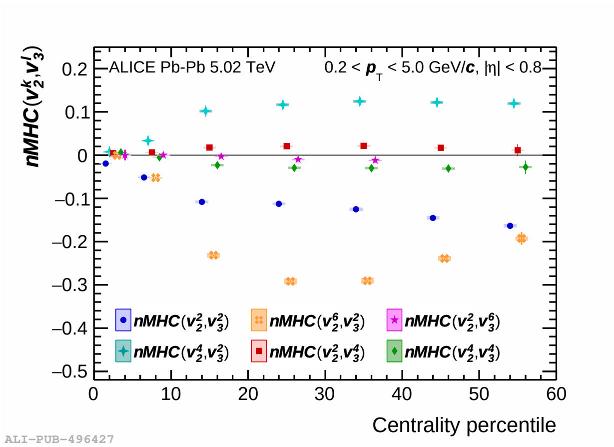

FIGURE 5.6: Normalized mixed harmonic cumulants $nMHC(v_2^m, v_3^n)$ for different moments of the correlations as a function of collision centrality in Pb–Pb collisions at $\sqrt{s_{\rm NN}} = 5.02$ TeV from the ALICE experiment. Taken from [167].

5.1.4 Model comparison and discussion

The obtained results of all the combinations of different moments and different harmonics of mixed harmonic cumulants $MHC(v_2^m, v_3^n)$ and $MHC(v_2^m, v_3^n, v_4^p)$ are discussed together with the comparison to the hydrodynamic model calculations from Ref. [168]. The model comparison is crucial to study the initial conditions and transport properties of the created QCD medium. The model contains a hydrodynamic part using a hybrid iEBE-VISHNU model [169] that uses event-by-event (2+1)-dimensional viscous hydrodynamics to describe the evolution of the medium. The hydrodynamic simulation ends with a freeze-out in which the particle sampler iSS is used to convert the medium into individual particles. Finally, the evolution of created hadrons is simulated using the UrQMD (Ultrarelativistic Quantum Molecular Dynamic) model [96]. Two sets of initial conditions are used as the input to the hydrodynamic model – TRENTo and AMPT, with their details discussed below. The model with these initial conditions can describe the particle $p_{\rm T}$ spectra and $v_n\{2\}$ of $\pi^{\pm}$, $K^{\pm}$, and $p(\bar{p})$ very well [170].

The first initial state model, TRENTo (Reduced Thickness Event-by-event Nuclear Topology model) [171], generates realistic Monte Carlo initial entropy density without specifying additional physics mechanisms that are addressed later in the hydrodynamic evolution of the system. The shear η/s and bulk ζ/s viscosities expressed as a dimensionless ratio to entropy density are temperature dependent in the model. The dependency, shown in Fig. 5.7, starts at 154 MeV for $\eta/s(T)$, which is the critical temperature T_c in the model, and at 150 MeV for $\zeta/s(T)$. The dependence and parametrisation of

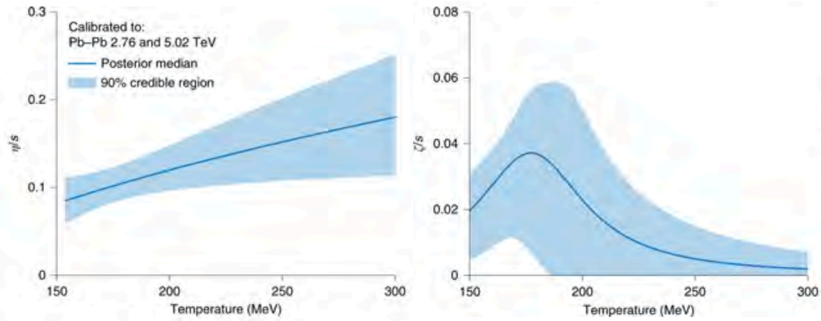

FIGURE 5.7: Specific shear η/s and bulk ζ/s viscosity as a function of temperature estimated for Pb–Pb collisions at LHC energies with 90% confidence interval. Taken from [172].

both viscosities are crucial, as they are the key transport coefficients of QGP. Understanding the behaviour of anisotropic flow and observables connected with it, such as mixed harmonic cumulants, contributes to the understanding of η/s and ζ/s, and thus, the properties of QGP. The temperature dependency is obtained from the Bayesian analysis [172]. In this approach, free parameters, including those describing $\eta/s(T)$ and $\zeta/s(T)$, are tuned simultaneously. In total, nine parameters are used in the model [173].

The second set of initial conditions originates from the AMPT (A Multi-Phase Transport) model [161, 174, 175]. The model provides fluctuating initial conditions, including the positions of point-like partons that are smeared according to a two-dimensional Gaussian distribution in the transverse plane. The shear viscosity is constant and set to $\eta/s = 0.08$ while the bulk viscosity is zero, $\zeta/s = 0.0$. The critical temperature is $T_c = 148$ MeV. The model describes the flow coefficients $v_n\{2\}$ and p_{T} spectra well. In addition, calculations with $\eta/s = 0.2$ are also used for comparison. While the model with such a setup does not describe flow coefficients nor p_{T} spectra, it can bring additional information on the sensitivity of the variable to the transport coefficient η/s of the hydrodynamic evolution of the QGP.

The measurements of normalized mixed harmonic cumulants $nMHC(v_2^m, v_3^n)$ are compared to the hydrodynamic model calculations using different settings of initial conditions and/or transport coefficients. The results are presented in Figs. 5.8 – 5.12. Assuming $v_n \propto \varepsilon_n$, which is known to be true for $n = 2, 3$ in central and semi-central Pb–Pb collisions, $nMHC(v_2^m, v_3^n) = nMHC(\varepsilon_2^m, \varepsilon_3^n)$, which enables a direct comparison between the two observables. Therefore, the initial state calculations of $nMHC(\varepsilon_2^m, \varepsilon_3^n)$ are also presented. In order to compare the models and the data better, the ratio between them is shown in the bottom panel of the figures.

The comparisons between the data and the model for $nMHC(v_2^2, v_3^2)$ and $nMHC(v_2^2, v_4^2)$ are shown in Fig. 5.8. For both observables, the measurements from two different

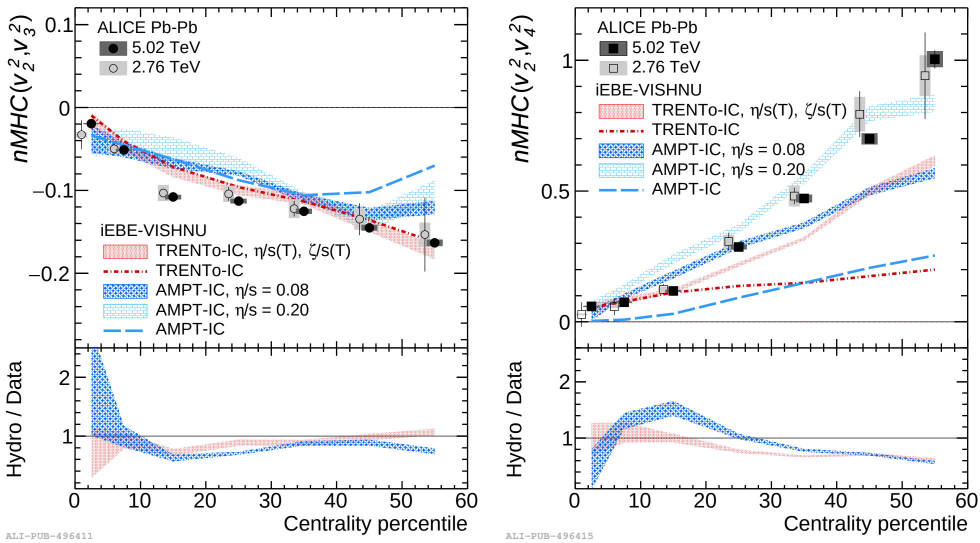

FIGURE 5.8: Mixed harmonic cumulants $nMHC(v_2^2, v_3^2)$ (left) and $nMHC(v_2^2, v_4^2)$ (right) as a function of collision centrality in Pb–Pb collisions at $\sqrt{s_{NN}} = 2.76$ and 5.02 TeV compared to hydrodynamic model calculations. Taken from [167].

collision energies, $\sqrt{s_{NN}} = 2.76$ and 5.02 TeV, are consistent within uncertainties. For $nMHC(v_2^2, v_3^2)$ measurement, the centrality dependence is well described by the hydrodynamic model calculations using both AMPT and TRENTo initial conditions. Furthermore, no difference between hydrodynamic calculations with AMPT initial conditions with two different η/s configurations is seen. The negative correlation between the flow coefficients v_2 and v_3, i.e. $nMHC(v_2^2, v_3^2)$, is also compatible with the correlation between the initial geometry ε_2 and ε_3, i.e. $nMHC(\varepsilon_2^2, \varepsilon_3^2)$. This further confirms the linear relation between v_n and ε_n for $n = 2, 3$. The calculations of $nMHC(v_2^2, v_4^2)$ with both AMPT and TRENTo initial conditions underestimate the data from semi-central to peripheral collisions. In central collisions, calculations with TRENTo initial conditions describe the data better. This linear relation between v_n and ε_n does not hold for $n \geq 4$, which explains the difference between $nMHC(v_2^2, v_4^2)$ and $nMHC(\varepsilon_2^2, \varepsilon_4^2)$. Additionally, it supports the hypothesis of the non-linear flow components in v_n coefficients for $n \geq 4$.

The last observable from four-particle MHC is $nMHC(v_3^2, v_4^2)$, shown in Fig. 5.9 (left). The differences between the observable at two different collision energies, $\sqrt{s_{NN}} = 2.76$ and 5.02 TeV, increase towards the central collisions. The change of sign in most central collision is observed only at $\sqrt{s_{NN}} = 5.02$ TeV. Hydrodynamic models with different initial conditions describe the centrality dependence qualitatively. Nonetheless, only

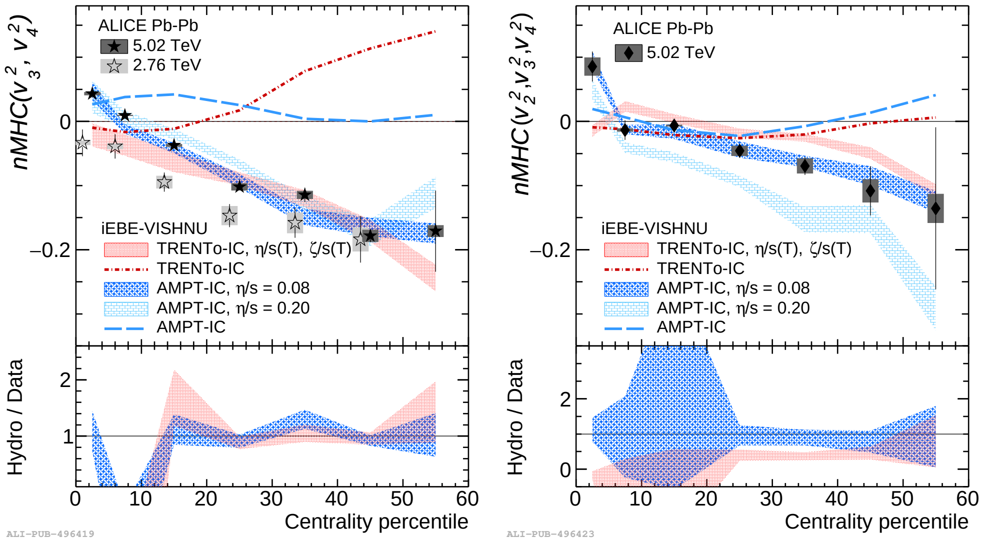

FIGURE 5.9: Left: Mixed harmonic cumulant $nMHC(v_3^2, v_4^2)$ as a function of collision centrality in Pb–Pb collisions at $\sqrt{s_{NN}} = 2.76$ and 5.02 TeV. Right: $nMHC(v_2^2, v_3^2, v_4^2)$ as a function of collision centrality in Pb–Pb collisions at $\sqrt{s_{NN}} = 5.02$ TeV. Both are compared to hydrodynamic model calculations. Taken from [167].

AMPT predicts the sign change in the most central collisions, while TRENTo calculations are negative across the studied centrality range. The correlation between initial eccentricities $nMHC(\varepsilon_3^2, \varepsilon_4^2)$ does not predict the trend. The TRENTo calculation starts with negative values and increases towards positive ones, while AMPT one starts with positive values and, with increasing centrality, gets closer to zero. This behaviour again confirms the non-linear relation between the initial geometry and the final flow coefficient v_4.

The relation between the second moments of all studied harmonics, i.e. v_2^2, v_3^2, v_4^2, can be studied using six-particle mixed harmonic cumulant $nMHC(v_2^2, v_3^2, v_4^2)$, shown in Fig. 5.9 (right). The $nMHC(v_2^2, v_3^2, v_4^2)$ from hydrodynamic calculations agrees qualitatively with the experimental data. The initial state calculations of $nMHC(\varepsilon_2^2, \varepsilon_3^2, \varepsilon_4^2)$ show a change of sign which is not observed in the data nor in hydrodynamic calculations. The deviation between initial and final state models is expected from the non-linear hydrodynamic response of v_4 to the initial geometry that increases with the increasing centrality of the collision. The comparison with the hydrodynamic calculations with different initial conditions shows a difference between AMPT with $\eta/s = 0.08$ and $\eta/s = 0.2$. The former describes the data well in the studied centrality range. Thus, the measurement of the correlation between three different harmonics offers a possibility to constrain the

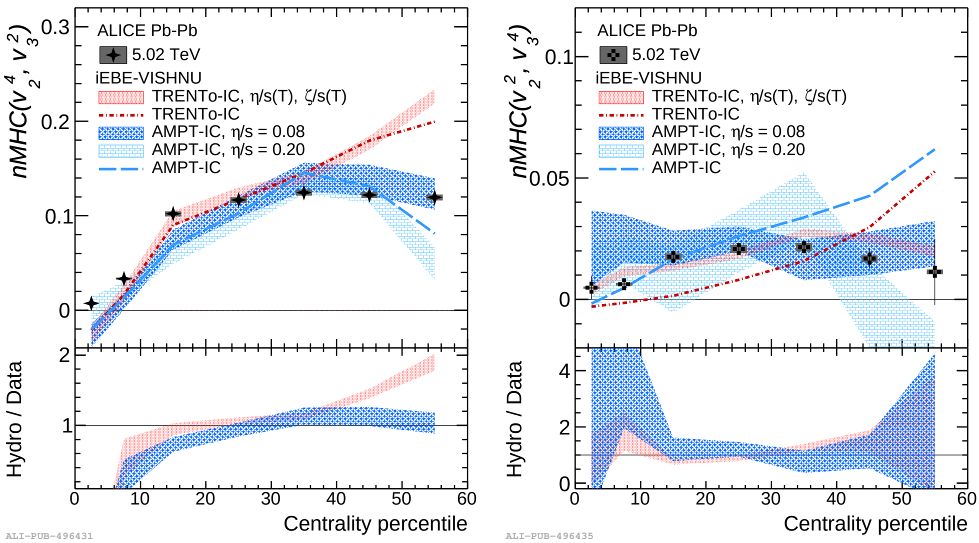

FIGURE 5.10: Mixed harmonic cumulants $nMHC(v_2^4, v_3^2)$ (left) and $nMHC(v_2^2, v_3^4)$ (right) as a function of collision centrality in Pb–Pb collisions at $\sqrt{s_{\mathrm{NN}}} = 5.02$ TeV compared to hydrodynamic model calculations. Taken from [167].

transport properties of the QGP further. The hydrodynamic calculation with TRENTo initial conditions qualitatively describes four-particle $nMHC$ of different harmonics, but underestimates the $nMHC(v_2^2, v_3^2, v_4^2)$ measurement. The presented new measurements could be used to tune better the parameters of the Bayesian analysis.

Comparing the measurements and the model calculations on correlations between higher moments of flow harmonics v_2 and v_3 allows to further study potential non-linearity between v_n and ε_n for $n = 2, 3$ in peripheral collisions. Additionally, higher orders can provide deeper insight into the hydrodynamic response of the system. The results of six-particle mixed harmonic cumulants $nMHC(v_2^4, v_3^2)$ and $nMHC(v_2^2, v_3^4)$ are shown in the left and right panel of Fig. 5.10, respectively. The hydrodynamic calculations of $nMHC(v_2^4, v_3^2)$ with different initial conditions qualitatively describe the data in central and semi-central collisions. The deviation between different model calculations of $nMHC(v_2^4, v_3^2)$ occurs in peripheral collisions, where the hydrodynamic model with AMPT initial conditions with $\eta/s = 0.08$ agrees with the data. In contrast, the model with TRENTo initial conditions overestimates the data. The agreements between $nMHC(\varepsilon_2^4, \varepsilon_3^2)$ from initial conditions and $nMHC(v_2^4, v_3^2)$ from hydrodynamic models with the same initial conditions are almost perfect for both sets of initial conditions, respectively. The model comparison of $nMHC(v_2^2, v_3^4)$ follows a similar trend and fairly

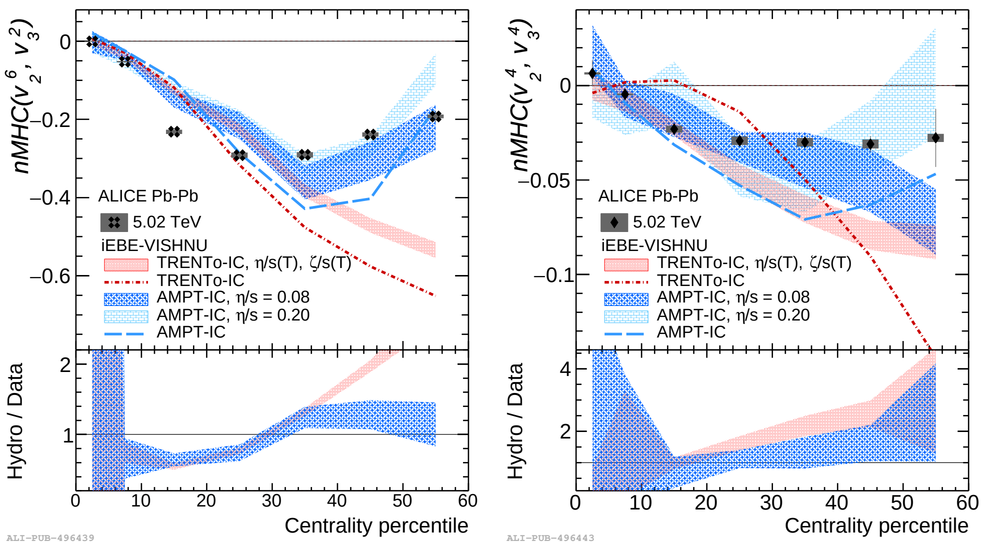

FIGURE 5.11: Mixed harmonic cumulants $nMHC(v_2^6, v_3^2)$ (left) and $nMHC(v_2^4, v_3^4)$ (right) as a function of collision centrality in Pb–Pb collisions at $\sqrt{s_{\mathrm{NN}}} = 5.02$ TeV compared to hydrodynamic model calculations. Taken from [167].

well describes the data across the entire studied centrality region. However, the uncertainties of the calculations are significantly larger compared to the previously presented results. Furthermore, the initial state calculations $nMHC(\varepsilon_2^2, \varepsilon_3^4)$ do not follow the same trend as in data, unlike $nMHC(\varepsilon_2^4, \varepsilon_3^2)$. This can be explained by the linearity between v_3 and ε_3 being weaker than the linearity between v_2 and ε_2 [72].

The eight-particle cumulants can study even higher moments of correlations between v_2 and v_3. For all studied cases, i.e. $nMHC(v_2^6, v_3^2)$, $nMHC(v_2^4, v_3^4)$, and $nMHC(v_2^2, v_3^6)$, shown in Fig. 5.11 and 5.12, the hydrodynamic calculations with AMPT initial conditions describe the trends seen in the data quantitatively. The calculation with TRENTo initial conditions shows a qualitative agreement in central and semi-central collisions, but it overestimates the data by a factor of two in peripheral collisions. The correlations between $nMHC(\varepsilon_2^6, \varepsilon_3^2)$ obtained from initial state models follow the trends seen in the data in central and semi-central collisions. In the peripheral collisions, it is not the case anymore for TRENTo initial conditions. Similarly, the hydrodynamic models qualitatively follows $nMHC(v_2^4, v_3^4)$ in central, but a large discrepancy can be seen in non-central collisions. Nevertheless, more hydrodyanmic simulations are needed to draw a firm conclusion.

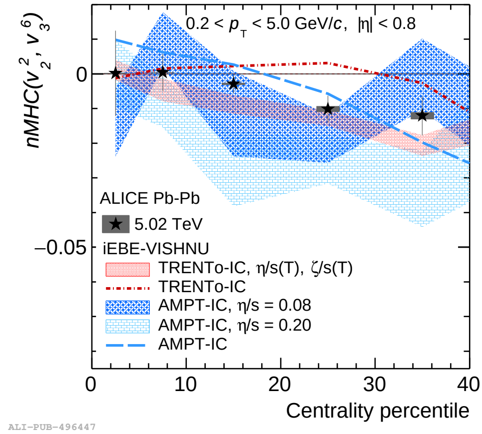

FIGURE 5.12: Mixed harmonic cumulant $nMHC(v_2^2, v_3^6)$ as a function of collision centrality in Pb–Pb collisions at $\sqrt{s_{NN}} = 5.02$ TeV compared to hydrodynamic model calculations. Taken from [167].

5.1.5 Flow of identified particles in Pb–Pb collisions

A different approach to study the transport properties and initial conditions of QGP is by measuring the p_T-differential flow coefficients of identified particles. The results are shown for inclusive charged hadrons $h^\pm$, and identified mesons $\pi^\pm$, $K^\pm$, K^0_S, and ϕ, and baryons $p(\bar{p})$, $\Lambda(\bar{\Lambda})$, $\Xi(\bar{\Xi})$, and $\Omega(\bar{\Omega})$[2]. The flow coefficients obtained using two-particle cumulants with pseudorapidity separation (η gap), $v_2\{2, |\eta| > 0.8\}$, are shown in Fig. 5.13. Different panels show the results in different centrality classes, from central (10–20%) to peripheral (50–60%) collisions. For most peripheral collisions shown, only primary identified particles ($\pi^\pm$, $K^\pm$, and $p(\bar{p})$) are presented as the reconstructions of other particle species are not statistically stable. The measured $v_2\{2, |\eta| > 0.8\}$ show the same behaviour as the previously published flow coefficients $v_2\{2, |\Delta\eta| > 2\}$ obtained with a scalar product method [86], that is shown in Fig. 1.19. More specifically, the increase of v_2 with the increasing centrality is observed due to the linear response of v_2 to the initial eccentricity ε_2. The anisotropy of the initial distribution is greater towards more peripheral collisions as central collisions are more symmetric. The flow coefficients reach their maximum in 40–50% centrality class. In more peripheral collisions, the v_2 results slowly decrease. In addition, the behaviour suggests a lack of final state interaction in more peripheral collisions. Hence the observed v_2 is smaller. In the low $p_T < 3$ GeV/c region, a mass ordering phenomenon is observed, i.e., v_2 is ordered based on the masses of various identified species. Heavier particles have larger v_2, which

[2]Reconstruction of $\Xi(\bar{\Xi})$and $\Omega(\bar{\Omega})$is done by a different analyser thus is not described in this thesis. My contribution to the paper and the analysis is described in the preface.

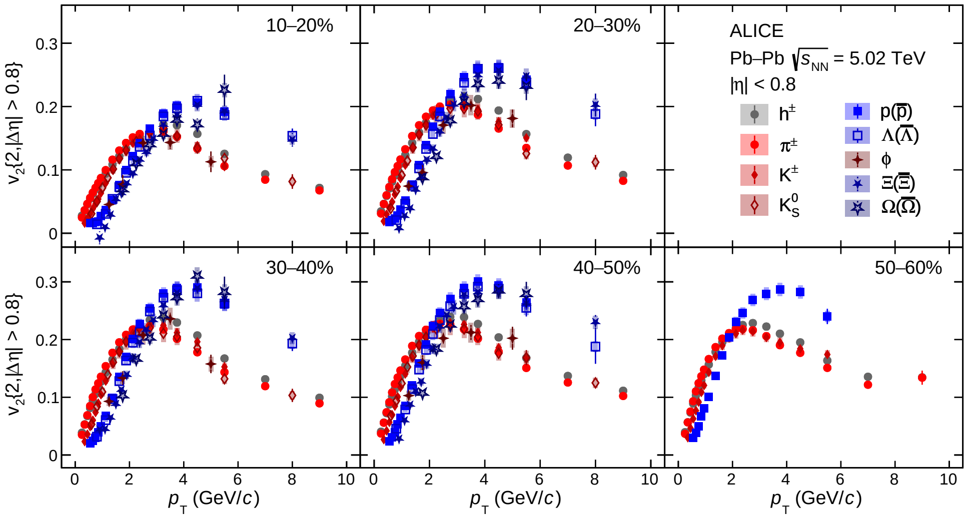

FIGURE 5.13: Flow coefficients $v_2\{2, |\eta| > 0.8\}$ for identified particles in various centrality classes of Pb–Pb collisions at $\sqrt{s_{NN}} = 5.02$ TeV. Taken from [135].

is explained by the interplay between radial and elliptic flow, as heavier particles have harder p_T spectra with $\langle p_T \rangle$ shifted towards the larger values. In the intermediate p_T region, $3 < p_T < 8$ GeV/c, a grouping of v_2 of baryons and mesons is observed for all presented centrality classes[3]. This behaviour favours the hypothesis of the anisotropic flow being developed at the partonic level, known as the partonic collectivity, and subsequent hadron production via quark coalescence. The crossing between v_2 of different particle species do not occur at the same p_T in different centrality classes. In the central collisions, the crossing takes place at higher p_T due to the stronger radial flow compared to the peripheral collisions. The measurement is performed up to $p_T = 10$ GeV/c. This is because the decreasing purity of particles' reconstruction and the limited number of particles taken from the middle pseudorapidity $|\eta| < 0.8$. Thus, it is impossible to observe the phenomenon of the disappearance of the species dependence at the high p_T, as shown in Fig. 1.19.

In addition to $v_2\{2, |\eta| > 0.8\}$, the measurement of flow coefficients using a four-particle cumulant $v_2\{4\}$ is needed in order to study flow fluctuations in Pb–Pb collisions. The measured $v_2\{4\}$ coefficients are shown in Fig. 5.14 for the same particle species and centrality classes as in Fig. 5.13. The difference between $v_2\{2, |\eta| > 0.8\}$ and $v_2\{4\}$ originates from the flow fluctuations and the potential non-flow contamination in

[3] In the peripheral collisions (50–60%), the splitting between baryons and mesons is observed instead of baryon-meson grouping, as the p(p̄) are only measured baryons.

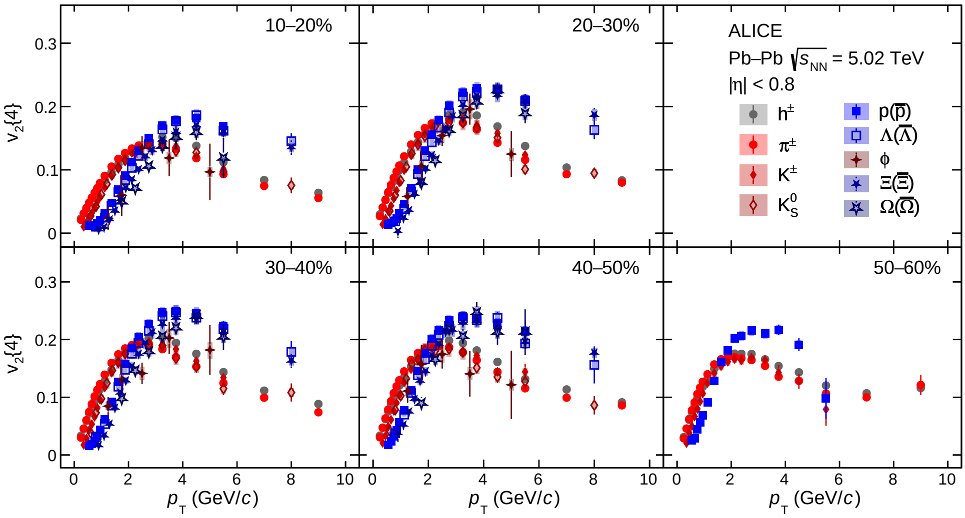

FIGURE 5.14: Flow coefficients $v_2\{4\}$ for identified particles in various centrality classes of Pb–Pb collisions at $\sqrt{s_{NN}} = 5.02$ TeV. Taken from [135].

$v_2\{2, |\eta| > 0.8\}$. The phenomena observed in flow coefficients $v_2\{2, |\eta| > 0.8\}$ of identified particles, i.e. mass ordering at the lower p_T and baryon-meson grouping at the intermediate p_T, are seen in $v_2\{4\}$ as well. The measured $v_2\{4\}$, which are free of non-flow contamination, further confirms the partonic collectivity established in high-energy heavy-ion collisions at the LHC.

5.1.6 Scaling with number of constituent quarks

The first results of v_2 from RHIC suggested the perfect scaling with number of constituent quarks (NCQ) over the entire studied p_T range [176, 177]. Such an observation provided an evidence of the partonic collectivity in heavy-ion collisions. In more recent publications, e.g., [86], the scaling is only approximate, with deviation up to 20%. Nevertheless, it is still used to test the contribution of the quark coalescence that should be dominant in $1 < p_T/n_q < 3$ GeV/c. Therefore, the results of $v_2\{2, |\eta| > 0.8\}$ and $v_2\{4\}$ are scaled in terms of the number of constituent quarks n_q in order to test the baryon-meson grouping phenomenon. The results are shown in Fig. 5.15 and 5.16 for $v_2\{2, |\eta| > 0.8\}/n_q$ and $v_2\{4\}/n_q$, respectively. It can be seen the scaling holds approximately for both studied observables, i.e., $v_2\{2, |\eta| > 0.8\}/n_q$ and $v_2\{4\}/n_q$. Such observation supports the hypothesis of the partonic collectivity and the quark coalescence as the dominant particle production mechanism.

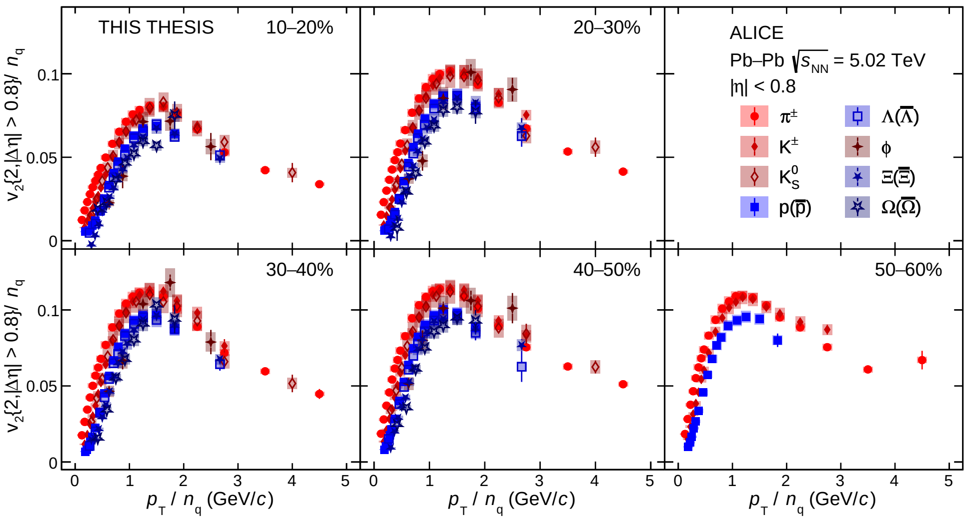

FIGURE 5.15: Flow coefficients $v_2\{2, |\Delta\eta| > 0.8\}$ scaled with number of constituent quarks n_q for identified particles in various centrality classes of Pb–Pb collisions at $\sqrt{s_{NN}} = 5.02$ TeV.

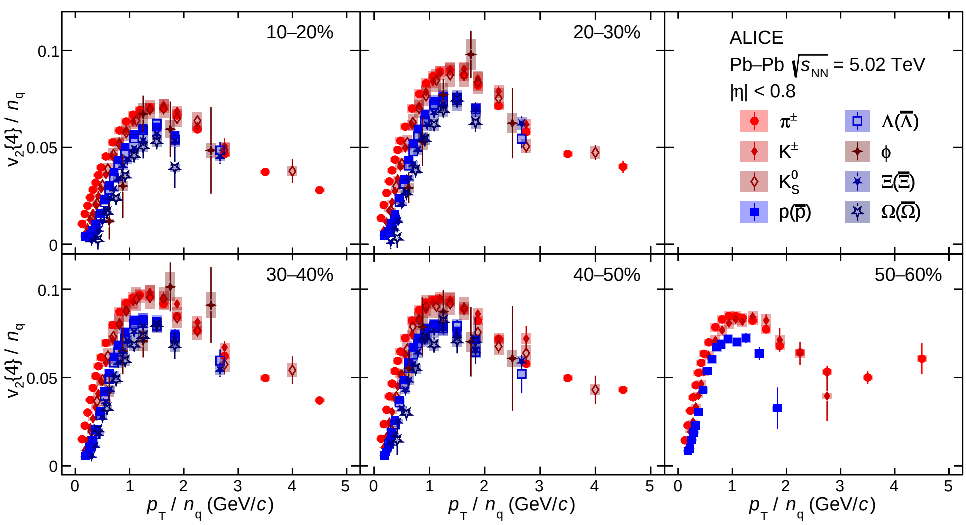

FIGURE 5.16: Flow coefficients $v_2\{4\}$ scaled with number of constituent quarks n_q for identified particles in various centrality classes of Pb–Pb collisions at $\sqrt{s_{NN}} = 5.02$ TeV. Taken from [135].

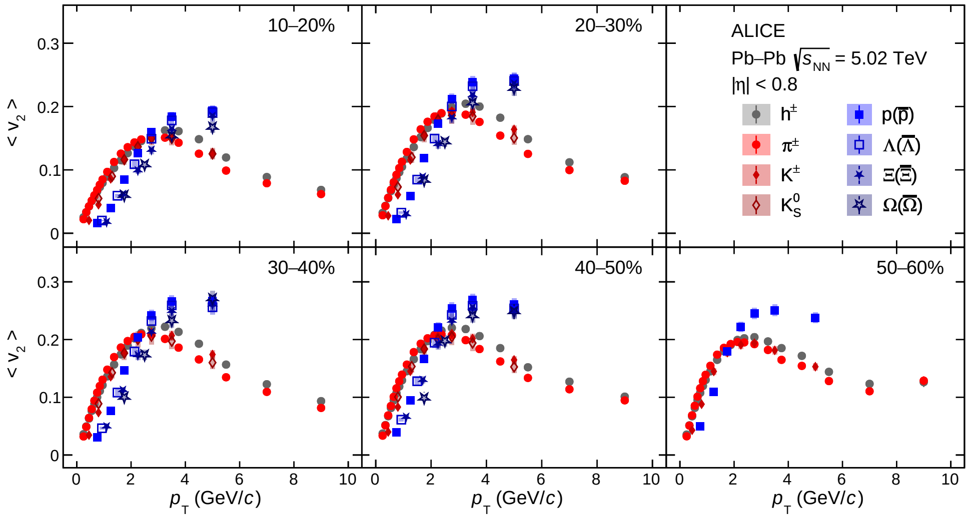

FIGURE 5.17: Mean elliptic flow $\langle v_2 \rangle$ for identified particles in various centrality classes of Pb–Pb collisions at $\sqrt{s_{\rm NN}} = 5.02$ TeV. Taken from [135].

5.1.7 Flow fluctuations

The measured flow coefficients $v_2\{2, |\Delta\eta| > 0.8\}$ and $v_2\{4\}$ can be used to obtain the first two moments of the probability density function of v_2 using relations introduced in Sec. 3.3. The results of the first and the second moments of the distribution, mean elliptic flow $\langle v_2 \rangle$ and its variance σ_{v_2}, in Pb–Pb collisions at $\sqrt{s_{\rm NN}} = 5.02$ TeV are shown in Figs. 5.17 and 5.18, respectively. As in previous cases, the measurements are shown for different identified particles and centrality classes. The mass ordering in the low $p_{\rm T}$ region and baryon-meson grouping and splitting in the intermediate $p_{\rm T}$ region, which are observed in $v_2\{2, |\Delta\eta| > 0.8\}$ and $v_2\{4\}$, can be seen in both $\langle v_2 \rangle$ and σ_{v_2}.

The relative flow fluctuations $F(v_2)$ can be obtained from $\langle v_2 \rangle$ and σ_{v_2} as

$$F(v_2) = \frac{\sigma_{v_2}}{\langle v_2 \rangle}. \tag{5.13}$$

The results are shown in Fig. 5.19 for various identified particles in different centrality classes of Pb–Pb collisions. In addition, the ratio $v_2\{4\}/v_2\{2, |\Delta\eta| > 0.8\}$ is shown in Fig. 5.20. The study of these two observables can bring further insight into the fluctuation of the initial state. The event-by-event fluctuations of ε_2 are transported to the final state via the QGP, and thus $v_2\{4\}/v_2\{2, |\Delta\eta| > 0.8\}$ represents $\varepsilon_2\{4\}/\varepsilon_2\{2\}$. While $v_2\{2, |\Delta\eta| > 0.8\}$, $v_2\{4\}$, $\langle v_2 \rangle$, and σ_{v_2} show species and $p_{\rm T}$ dependence across all studied centrality classes, it is not the case for neither $F(v_2)$ nor $v_2\{4\}/v_2\{2, |\Delta\eta| > 0.8\}$ in

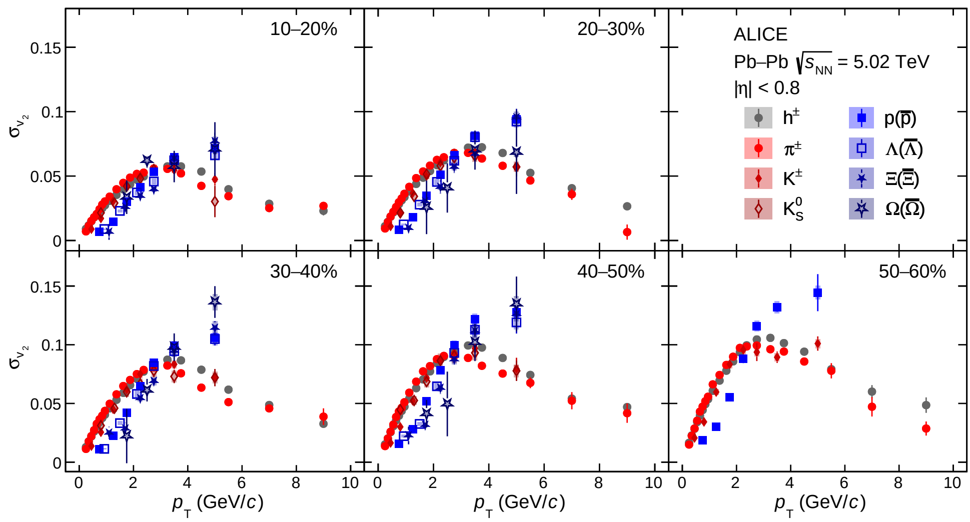

FIGURE 5.18: Variance of the elliptic flow σ_{v_2} for identified particles in various centrality classes of Pb–Pb collisions at $\sqrt{s_{\mathrm{NN}}} = 5.02$ TeV. Taken from [135].

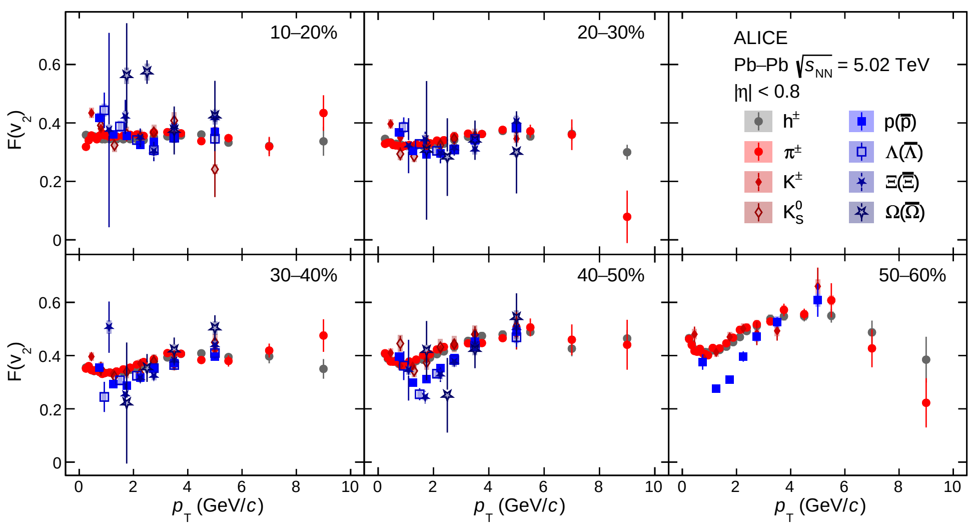

FIGURE 5.19: Relative flow fluctuations $F(v_2)$ for identified particles in various centrality classes of Pb–Pb collisions at $\sqrt{s_{\mathrm{NN}}} = 5.02$ TeV. Taken from [135].

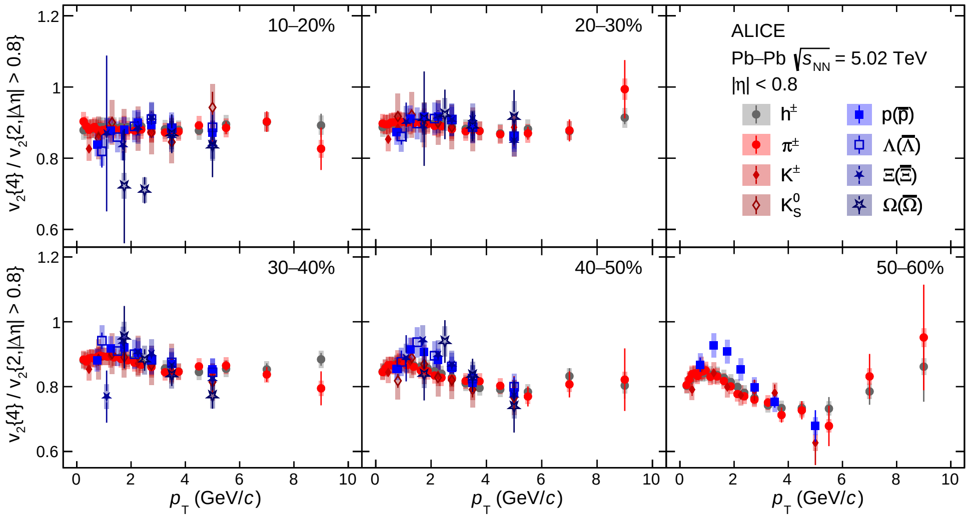

FIGURE 5.20: Ratio between $v_2\{4\}$ and $v_2\{2, |\Delta\eta| > 0.8\}$ for identified particles in various centrality classes of Pb–Pb collisions at $\sqrt{s_{NN}} = 5.02$ TeV. Taken from [135].

central collisions. A non-monotonic p_T dependence can be observed starting from semi-central collisions (30–40%). The minimum $F(v_2)$ and maximum $v_2\{4\}/v_2\{2, |\Delta\eta| > 0.8\}$ occur in lower p_T for mesons compared to baryons. The baryon-meson grouping occurs in the intermediate p_T region for flow coefficients $v_2\{2, |\Delta\eta| > 0.8\}$, $v_2\{4\}$, and flow *p.d.f.* moments $\langle v_2 \rangle$ and σ_{v_2} shown above. However, no such grouping is observed in the results of $F(v_2)$ and $v_2\{4\}/v_2\{2, |\Delta\eta| > 0.8\}$. A hint of grouping, i.e. a difference between baryons and mesons, can be observed in the low p_T region, $p_T < 3$ GeV/c where a systematic difference is seen between the two groups. Such differences might be explained by different origins of the observed baryon-meson grouping phenomena. The particle species dependence confirms the non-negligible contribution of the final state effects to the studied observables.

5.1.8 Model comparison and discussion

The results of $v_2\{2, |\Delta\eta| > 0.8\}$, $v_2\{4\}$, $\langle v_2 \rangle$, σ_{v_2}, $F(v_2)$ and $v_2\{4\}/v_2\{2, |\Delta\eta| > 0.8\}$ are compared to hydrodynamic models to constrain the initial state and transport properties of the QGP. The calculations are done for $\pi^{\pm}$, $K^{\pm}$, and $p(\bar{p})$, i.e. the primary identified particles. The hydrodynamic model iEBE-VISHNU with two sets of initial conditions, AMPT and TRENTo, is introduced in Sec. 5.1.4. The hydrodynamic model with AMPT initial conditions uses the shear viscosity to entropy density with a constant value of $\eta/s = 0.08$ and bulk viscosity to entropy density $\zeta/s = 0$. For the model with TRENTo

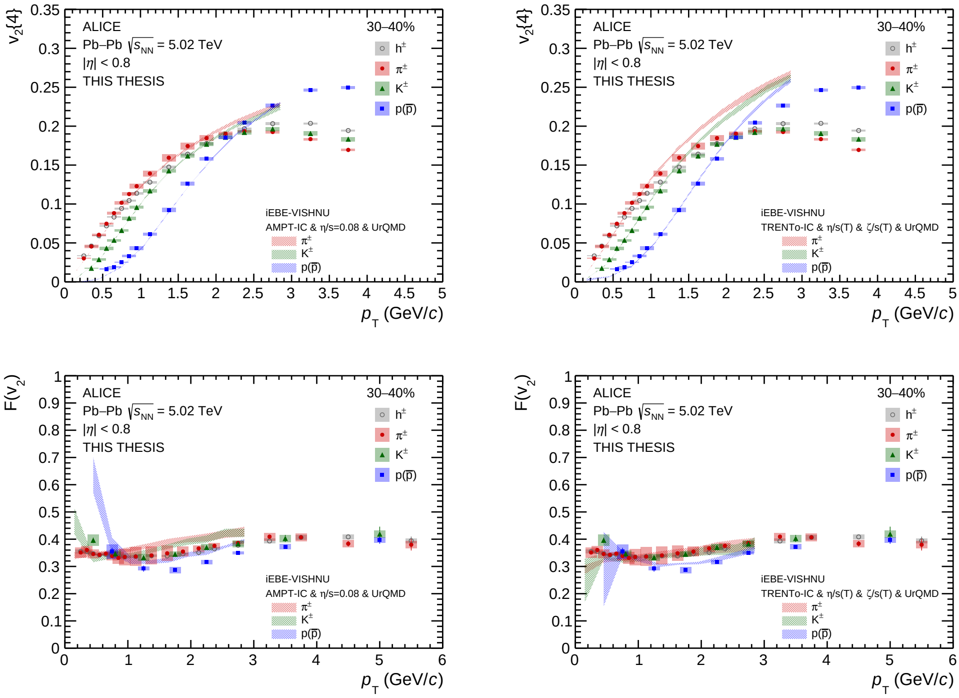

FIGURE 5.21: Flow coefficients $v_2\{4\}$ (top row) and relative flow fluctuations $F(v_2)$ (bottom row) of $\pi^{\pm}$, $K^{\pm}$, and $p(\bar{p})$ in 30–40% centrality class of Pb–Pb collisions at $\sqrt{s_{NN}} = 5.02$ TeV compared to the hydrodynamic iEBE-VISHNU model with initial conditions from AMPT (left column) and TRENTo (right column).

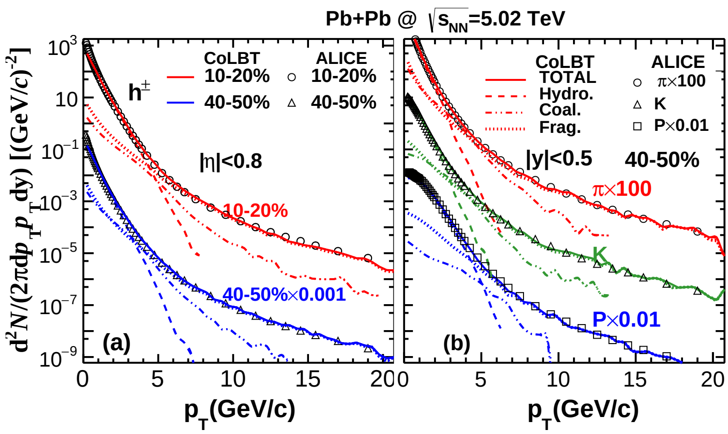

FIGURE 5.22: Particle spectra of inclusive charged particles (left) and primary identified particles (right) in Pb–Pb collisions together with fit with the hybrid CoLBT model combining hydrodynamics, quark coalescence, and jet fragmentation. Taken from [178].

initial conditions, both η/s and ζ/s change as a function of temperature. The comparison of $v_2\{4\}$ in the centrality class 30–40% of Pb–Pb collisions at $\sqrt{s_{\mathrm{NN}}} = 5.02$ TeV is shown in Fig. 5.21 for both AMPT (left) and TRENTo (right) initial conditions. In the low p_{T} region, approximately $p_{\mathrm{T}} < 1.5$ GeV/c, both models agree with the experimental data points and show mass ordering of the presented particle species – $\pi^{\pm}$, $\mathrm{K}^{\pm}$, and $\mathrm{p}(\bar{\mathrm{p}})$. Above this p_{T} range, only AMPT calculation can describe the data in the highest p_{T} region, while TRENTo calculation significantly overestimates the measurements. In both models, $v_2\{4\}$ results for all studied particle species are the same at $p_{\mathrm{T}} = 3$ GeV/c. No crossing between v_2 of different particles and no splitting between baryons and mesons is observed in the models. Nevertheless, the models are available only in the limited p_{T} range up to 3 GeV/c. The comparisons of relative flow fluctuations $F(v_2)$ of $\pi^{\pm}$, $\mathrm{K}^{\pm}$, and $\mathrm{p}(\bar{\mathrm{p}})$ from the data and from the hydrodynamic model with AMPT and TRENTo initial conditions are shown in Fig. **??**. For the calculations with AMPT initial conditions, $\mathrm{K}^{\pm}$ and $\mathrm{p}(\bar{\mathrm{p}})$ show non-trivial p_{T} dependence at the low p_{T} region that is not observed in the data, while the model qualitatively describes the data for $\pi^{\pm}$ in the entire p_{T} range and $\mathrm{K}^{\pm}$ and $\mathrm{p}(\bar{\mathrm{p}})$ above $p_{\mathrm{T}} > 1$ GeV/c. The agreement is better for the model with TRENTo initial conditions as the model calculations with AMPT overestimate the data in the p_{T} range $1 < p_{\mathrm{T}} < 3$ GeV/c. As in the case of $v_2\{4\}$ discussed above, the hydrodynamic model is not shown for $p_{\mathrm{T}} > 3$ GeV/c.

The p_{T} limitation of the purely hydrodynamic model can be overcome by introducing a hybrid model that can provide a unified picture of the flow coefficients at a wider p_{T} range. The hybrid CoLBT-hydro model consists of a LBT (linear Boltzmann transport) model for describing the jet propagation coupled with the dynamic (3+1)-D hydrodynamic evolution with $\eta/s = 0.1$ [179]. Besides the hydrodynamic and jet fragmentation parts, quark coalescence mechanism is included in the hybrid model. The relative contribution to individual mechanisms is obtained from the fit of particle spectra in Pb–Pb collisions, shown in Fig. 5.22. The spectra are shown for inclusive charged particles (left) in 10–20% and 40–50% centrality class and for primary identified particles $\pi^{\pm}$, $\mathrm{K}^{\pm}$, and $\mathrm{p}(\bar{\mathrm{p}})$ (right) in 40–50% centrality class. It can be seen that the hydrodynamic contribution is dominant in low p_{T}, i.e., $p_{\mathrm{T}} < 2$ GeV/c. In the high p_{T}, i.e., $p_{\mathrm{T}} > 8$ GeV/c, the fragmentation process has the dominant contribution. The transition from hydrodynamics to different mechanisms occurs at higher p_{T} for more central collisions due to the stronger radial flow. As the lower limit for participation in the coalescence is $p_{\mathrm{T}} > 1.5$ GeV/c for quarks, the effect is different for mesons and baryons because of a different number of constituent quarks [178].

The comparison of $v_2\{4\}$ of $\pi^{\pm}$, $\mathrm{K}^{\pm}$, and $\mathrm{p}(\bar{\mathrm{p}})$ between the hybrid model, marked as Hydro+coal+frag, is shown in Fig. 5.23 for 10–20% (left) and 40–50% (right) centrality classes of Pb–Pb collisions. The model describes the p_{T} dependence over the entire p_{T}

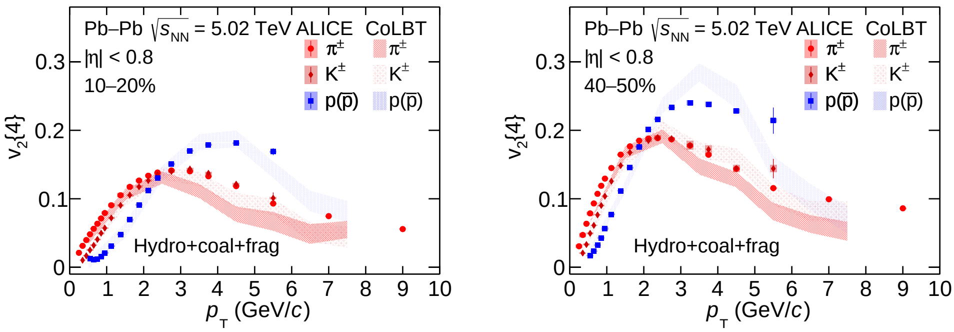

FIGURE 5.23: Flow coefficients $v_2\{4\}$ of $\pi^{\pm}$, $K^{\pm}$, and $p(\bar{p})$ in 10–20% (left) and 40–50% (right) centrality classes of Pb–Pb collisions at $\sqrt{s_{NN}} = 5.02$ TeV compared to the hybrid CoLBT model combining hydrodynamics, quark coalescence, and jet fragmentation. Taken from [135].

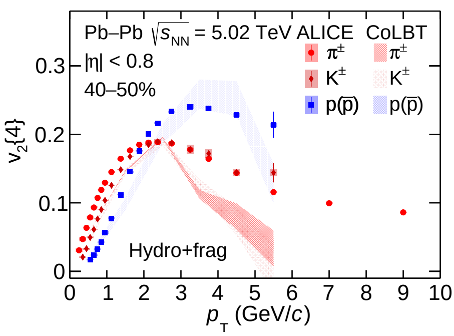

FIGURE 5.24: Flow coefficients $v_2\{4\}$ of $\pi^{\pm}$, $K^{\pm}$, and $p(\bar{p})$ in 40–50% centrality class of Pb–Pb collisions at $\sqrt{s_{NN}} = 5.02$ TeV compared to the hybrid CoLBT model combining hydrodynamics and jet fragmentation. Taken from [135].

range. In both the experimental data and the model, it can be seen

- the mass ordering of $v_2\{4\}$ based on particle species at low p_T, originating from the radial hydrodynamic expansion of the medium,
- the maximum $v_2\{4\}$ at $p_T \approx 3$ GeV/c for mesons and $p_T \approx 4.5$ GeV/c for baryons,
- the decreasing of $v_2\{4\}$ with p_T above the maximum,
- the splitting between baryon and mesons at intermediate p_T, suggesting the presence of the collectivity at the partonic level and subsequent hadronisation via quark coalescence.

From the fit of the particle spectra, it is known that the relative contribution of the coalescence is up to 25% in the intermediate p_T region, i.e., $4 < p_T < 6$ GeV/c. The model is

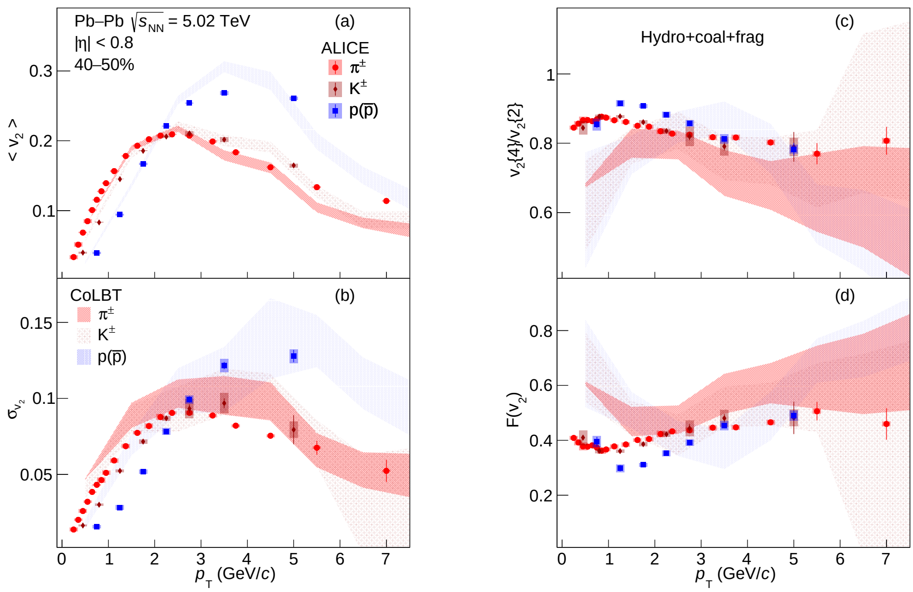

FIGURE 5.25: Mean elliptic flow $\langle v_2 \rangle$ (a), variance of the elliptic flow σ_{v_2} (b), ratio $v_2\{4\}/v_2\{2, |\Delta\eta| > 0.8\}$ (c), and relative flow fluctuations $F(v_2)$ (d) 40–50% centrality class of Pb–Pb collisions at $\sqrt{s_{\mathrm{NN}}} = 5.02$ TeV of $\pi^{\pm}$, $\mathrm{K}^{\pm}$, and $\mathrm{p}(\bar{\mathrm{p}})$ compared to the hybrid CoLBT model combining hydrodynamics, quark coalescence, and jet fragmentation. Taken from [135].

also tested in a configuration without any contribution of the quark coalescence, marked as Hydro+frag. The results of $v_2\{4\}$ from the Hydro+frag calculations are shown in Fig. 5.24 in the centrality class 40–50%. Only the jet fragmentation mechanism contributes to the high p_{T} region. While the low p_{T} qualitatively describes the data, the model significantly underestimates the experimental data above $p_{\mathrm{T}} > 3$ GeV$/c$. Nevertheless, the splitting between baryons and mesons and the crossing between v_2 of different particles are observed in the model without the contribution of the quark coalescence. In the presented configuration of the model, the splitting originates from the particle species dependent value of the relative contribution of individual processes, i.e. hydrodynamics and fragmentation.

The hybrid model is also used to calculate the mean elliptic flow $\langle v_2 \rangle$, variance of the elliptic flow σ_{v_2}, ratio $v_2\{4\}/v_2\{2, |\Delta\eta| > 0.8\}$, and relative flow fluctuations $F(v_2)$. The comparisons of the experimental data and Hydro+coal+frag model calculations are shown in Fig. 5.25. To test the contribution of quark coalescence mechanism, the Hydro+frag model with the contributions only from hydrodynamics and jet fragmentation, i.e., without the quark coalescence, is compared to the experimental data, which

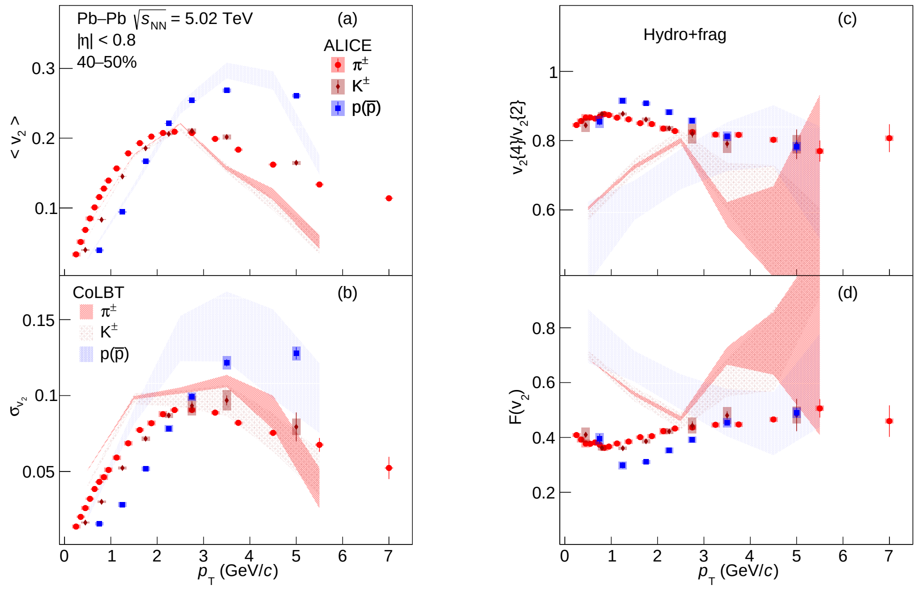

FIGURE 5.26: Mean elliptic flow $\langle v_2 \rangle$ (a), variance of the elliptic flow σ_{v_2} (b), ratio $v_2\{4\}/v_2\{2, |\Delta\eta| > 0.8\}$ (c), and relative flow fluctuations $F(v_2)$ (d) 40–50% centrality class of Pb–Pb collisions at $\sqrt{s_{NN}} = 5.02$ TeV of $\pi^{\pm}$, $K^{\pm}$, and $p(\bar{p})$ compared to the hybrid CoLBT model combining hydrodynamics and jet fragmentation. Taken from [135].

is shown in Fig. 5.26. Similarly to the comparison of $v_2\{4\}$, the model without quark coalescence underestimates $\langle v_2 \rangle$ of $\pi^{\pm}$ and $K^{\pm}$ above $p_T > 3$ GeV/c. The model with coalescence qualitatively agrees with the measurement. In the low p_T, σ_{v_2} results are not described well by either configuration of the model. In the intermediate p_T region, the description of the model with quark coalescence is better. Neither model configuration can describe the experimental results of $v_2\{4\}/v_2\{2, |\Delta\eta| > 0.8\}$ and $F(v_2)$. In addition, the calculations of σ_{v_2}, $v_2\{4\}/v_2\{2, |\Delta\eta| > 0.8\}$ and $F(v_2)$ have significant uncertainties. Therefore, no strong conclusion can be made. Nevertheless, from the results of $v_2\{2, |\Delta\eta| > 0.8\}$, $v_2\{4\}$, and $\langle v_2 \rangle$, the configuration with quark coalescence is favored.

5.2 Flow in small collision systems

The observation of the double ridge in the correlation function $C(\Delta\eta, \Delta\varphi)$ in high multiplicity pp and p–Pb collisions meant a significant shift in the understanding of small systems. Until that point, in the high-energy heavy-ion physics community, small systems were often understood as the reference system, free from anisotropic flow and without any potential QCD medium. Nowadays, the anisotropic flow coefficients are measured across collision systems of all sizes [93]. The origin of the collective behaviour in large collision systems is known to correspond to the effects of the initial geometry and the medium expansion [98]. Thus, the measurement of flow coefficients helps constrain the calculations describing the initial state and transport properties of the created medium. However, in the small collision systems, the development of the anisotropic flow from the initial conditions is not known. In addition, the flow measurements are more challenging compared to the large collision systems due to the much larger non-flow contamination, which must be suppressed as much as possible. Several different methods, introduced in Sec. 3.5, are used to test the effects of non-flow contamination and the statistical stability of the results. Therefore, these results from individual methods are not reported with the systematic uncertainty nor for both studied systems, i.e., p–Pb and pp. The final results of flow coefficients of $\pi^{\pm}$, $\mathrm{K}^{\pm}$, $\mathrm{p}(\bar{\mathrm{p}})$, $\mathrm{K}^0_{\mathrm{S}}$, and $\Lambda(\bar{\Lambda})$, obtained using the best non-flow suppression method, are presented with both statistical and systematic uncertainties. Such measurements are discussed at the end of the section together with the comparison with model calculations to test the particle production mechanism.

5.2.1 $v_2\{2\}$ with pseudorapidity separation

In Pb–Pb collisions, the pseudorapidity separation (η gap) method sufficiently suppresses non-flow in the studies of the flow coefficients from two-particle cumulants method. The differences between $v_2\{2\}$ measurements with larger η gaps are getting smaller, showing a clear saturation in Pb–Pb collisions. It can be seen in Fig. 5.27 that the η gap saturation does not occur in p–Pb collisions or smaller systems. With larger η gap between individual sub-events, the results of $v_2\{2\}$ decrease, i.e. $v_2\{2, |\Delta\eta| > a\} > v_2\{2, |\Delta\eta| > b\}$ for $b > a$. Nevertheless, as the η gaps cannot be infinitely large due to the limited detector acceptance, the clear saturation of v_2 results is not observed. Moreover, the v_2 results exhibit the increasing trend across the entire studied p_{T} range. Unlike the measurements in heavy-ion collisions, no decreasing trend after peaking at $p_{\mathrm{T}} \approx 3$ GeV/c is observed in small systems. The increasing trend is observed in low multiplicity pp collisions and models with pure non-flow. Therefore, such a trend is explained by a significant contamination from the non-flow effects. Apparently, the pseudorapidity separation method alone is not sufficient for the flow measurements in small systems.

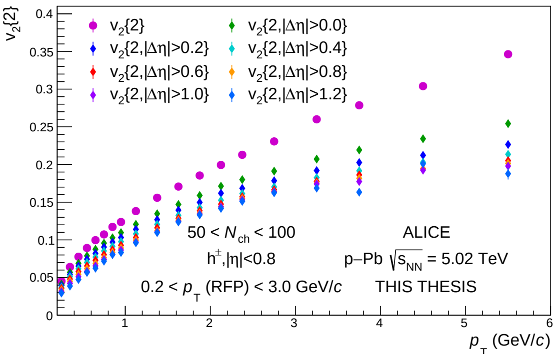

FIGURE 5.27: Flow coefficients $v_2\{2\}$ with different pseudorapidity separations in p–Pb collisions at $\sqrt{s_{\mathrm{NN}}} = 5.02$ TeV as a function of the transverse momentum.

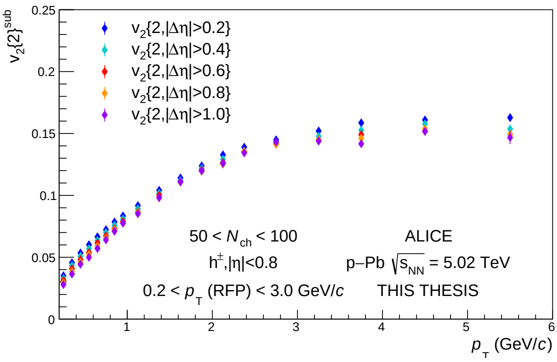

FIGURE 5.28: Flow coefficients $v_2\{2\}$ with different pseudorapidity separations in p–Pb collisions at $\sqrt{s_{\mathrm{NN}}} = 5.02$ TeV as a function of the transverse momentum.

5.2.2 $v_2\{2\}$ with additional non-flow subtraction

While the η gap method alone is insufficient for the non-flow subtraction in the two-particle cumulants method, it can be combined with the method of subtraction of non-flow, estimated from low multiplicity events. The subtraction is done separately for reference cumulant $c_2\{2\}$ and p_{T}-differential cumulants $d_2\{2\}$, as described by Eq. 3.56. The minimum bias pp collisions are considered as the low multiplicity base in the subtraction process. The scaling factor k is obtained as the ratio of the mean charged particles multiplicities $\langle M \rangle$ integrated in the p_{T} range $0.2 < p_{\mathrm{T}} < 3$ GeV/c separately for high and low multiplicity collisions, as described by Eq. 3.57. Furthermore, to avoid any possible bias from the multiplicity fluctuations [144], the subtraction is performed in every multiplicity class separately, i.e. the subtraction takes place in narrow N_{ch} intervals. The

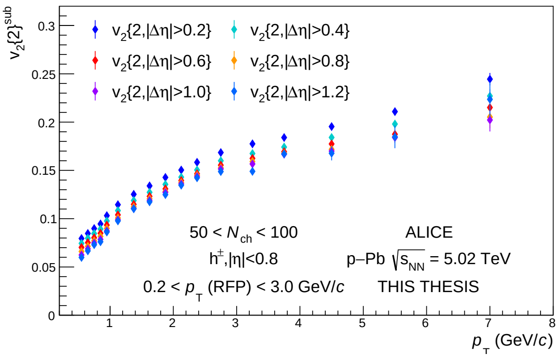

FIGURE 5.29: Flow coefficients $v_2\{2\}$ with different pseudorapidity separations in p–Pb collisions at $\sqrt{s_{NN}} = 5.02$ TeV as a function of the transverse momentum.

final result is obtained from the combination of all considered N_{ch} classes. The result of subtracted $v_2\{2\}$ is shown in Fig. 5.28. The increase with p_T is less steep compared to the non-subtracted results shown in Fig. 5.27 with an approximately constant value of the flow coefficients above $p_T > 3$ GeV/c. The expected decrease after the peak at $p_T \approx 3$ GeV/c, typical for $v_2\{2\}(p_T)$ in Pb–Pb collisions, is still not observed. Such a behaviour is likely caused by the remaining non-flow contamination, which increases with the increasing p_T.

The reported results consider $d_2\{2\}$ as a function of the p_T. However, the used scaling factor k is p_T independent. Thus, in order to improve the non-flow subtraction, it is possible to modify Eq. 3.56 to

$$v_n\{2\}^{\mathrm{sub}}(p_T) = \frac{d_n\{2\}(p_T)^{\mathrm{HM}} - \sqrt{k(p_T)k} \cdot d_n\{2\}(p_T)^{\mathrm{LM}}}{\sqrt{c_n\{2\}^{\mathrm{HM}} - k \cdot c_n\{2\}^{\mathrm{LM}}}}, \tag{5.14}$$

with p_T-differential scaling factor $k(p_T)$, defined as

$$k(p_T) = \frac{\langle M \rangle^{\mathrm{LM}}(p_T)}{\langle M \rangle^{\mathrm{HM}}(p_T)}. \tag{5.15}$$

However, the results of $v_n\{2\}^{\mathrm{sub}}(p_T)$ with k and $k(p_T)$ are in agreement within uncertainties as no significant pt-dependence of $\langle M \rangle$ is observed. Therefore, a further extension of the study is made with the near-side jet yields, extracted from the correlation function $C(\Delta\eta, \Delta\varphi)$. After the projection of $C(\Delta\eta, \Delta\varphi)$ into $\Delta\varphi$ direction, the subtraction of minimum is applied across the entire $\Delta\varphi$ region in order to obtain $Y(\min) = 0$, i.e., in order to obtain zero yield at minimum. The yield is then obtained as an integral of the region $|\Delta\varphi - \pi| < 1.4$, separately for high and low multiplicity collisions and every p_T

range. The scaling factor $k(p_{\mathrm{T}})$ is then

$$k(p_{\mathrm{T}}) = \frac{\int_{\pi-1.4}^{\pi+1.4} \left(Y(\Delta\varphi) - Y(\mathrm{min})\right)^{\mathrm{LM}}(p_{\mathrm{T}})}{\int_{\pi-1.4}^{\pi+1.4} \left(Y(\Delta\varphi) - Y(\mathrm{min})\right)^{\mathrm{HM}}(p_{\mathrm{T}})}. \tag{5.16}$$

The results of $v_2\{2\}^{\mathrm{sub}}(p_{\mathrm{T}})$ with such subtraction are shown in Fig. 5.29 for different pseudorapidity separations (η gaps) between sub-events. The values of $v_2\{2\}^{\mathrm{sub}}(p_{\mathrm{T}})$ differ with different η gaps, however, a certain saturation with a larger η gap can be observed. Similarly to the previous cases, no peak at $p_{\mathrm{T}} \approx 3$ GeV/c and no subsequent decrease of $v_2\{2\}^{\mathrm{sub}}$ with p_{T} are observed. Therefore, the method of subtraction with relative jet-yield scaling is also not considered to provide a sufficient non-flow suppression.

5.2.3 $v_2\{4\}$ with sub-events

An alternative way of non-flow suppression is using multi-particle cumulants. In order to obtain a real value of $v_2\{4\}$ using Eq. 3.24, the p_{T}-integrated cumulant of reference particles, $c_2\{4\}$, has to be negative To ensure such behaviour, the four-particle cumulant $c_2\{4\}$ is studied as a function of multiplicity with different sub-events methods in Pb–Pb collisions in Fig. 5.30 (left), in p–Pb collisions in Fig. 5.30 (right), and in pp collisions in Fig. 5.31. The relative non-flow contribution is expected to be similar in the same multiplicity region of pp and p–Pb collisions. All studied configurations, i.e., $c_2\{4\}$ with one, two, and three sub-events, give consistent results in Pb–Pb collisions except in the lowest multiplicity. In p–Pb collisions, for $N_{\mathrm{ch}} < 50$, only $c_2\{4\}_{3-\mathrm{sub}}$ is negative, while $c_2\{4\}$ with one and two sub-events remain positive. In higher multiplicities, all $c_2\{4\}$ results become negative. In pp collisions, the results of $c_2\{4\}$ from minimum bias pp collisions or results from PYTHIA event generator without multi-particle correlations give $c_2\{4\} > 0$ with all studied sub-events. Nevertheless, the results reported in Fig. 5.31 are from pp collisions with the high multiplicity trigger using the forward V0 detector, described in Sec. 2.4. With this configuration, $c_2\{4\}_{3-\mathrm{sub}}$ gives the negative values over the full studied multiplicity range, which is consistent with the results from [93]. The four-particle cumulant with η separation, $c_2\{4, |\Delta\eta| > 0.8\}$, is negative in most of the multiplicity range, however, it is not statistically stable. Therefore, the measurement of $v_2\{4\}$ of identified particles is done using the three sub-events method.

The method is validated in low multiplicity Pb–Pb collisions where $v_2\{4\}$, $v_2\{4, |\Delta\eta| > 0.0\}$, and $v_2\{4\}_{3-\mathrm{sub}}$ are consistent within statistical uncertainties, which can be seen already from the reported results of $c_2\{4\}$, shown in Fig. 5.30 (left). The

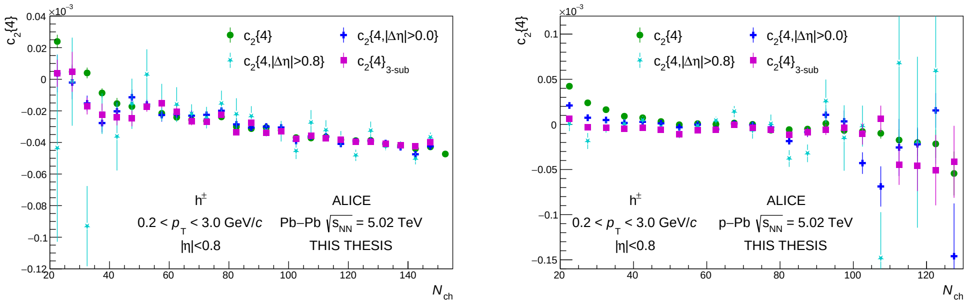

FIGURE 5.30: Four-particle cumulants $c_2\{4\}$ with different pseudorapidity separations in Pb–Pb (left) and p–Pb (right) collisions at $\sqrt{s_{\mathrm{NN}}} = 5.02$ TeV as a function of the multiplicity.

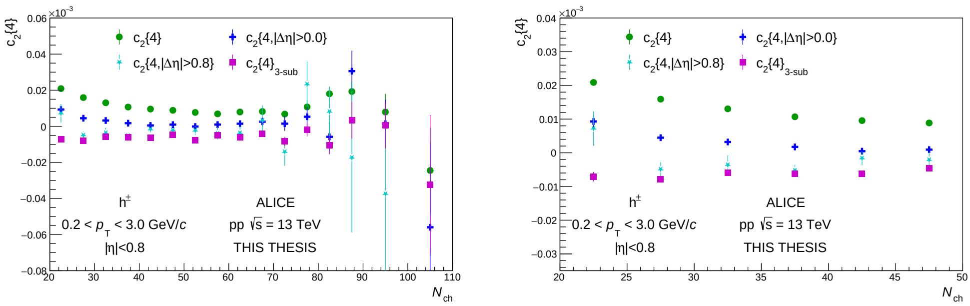

FIGURE 5.31: Four-particle cumulants $c_2\{4\}$ with different pseudorapidity separations in pp collisions at $\sqrt{s} = 13$ TeV as a function of the event multiplicity. The right panel is zoomed low multiplicity region of the left panel.

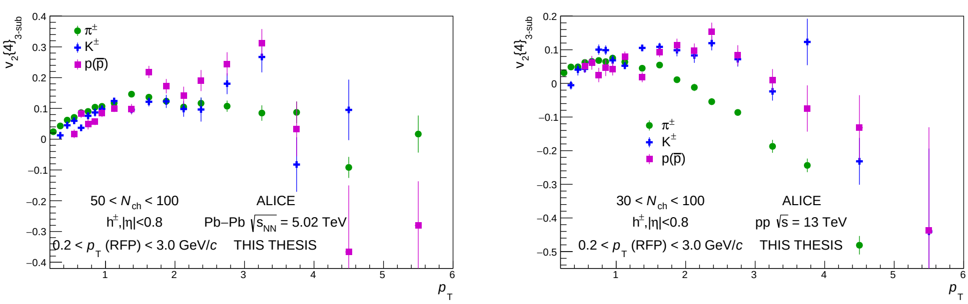

FIGURE 5.32: Flow coefficients $v_2\{4\}$ of $\pi^{\pm}$, $\mathrm{K}^{\pm}$, and $\mathrm{p}(\bar{\mathrm{p}})$ in Pb–Pb (left) and pp low multiplicity collisions.

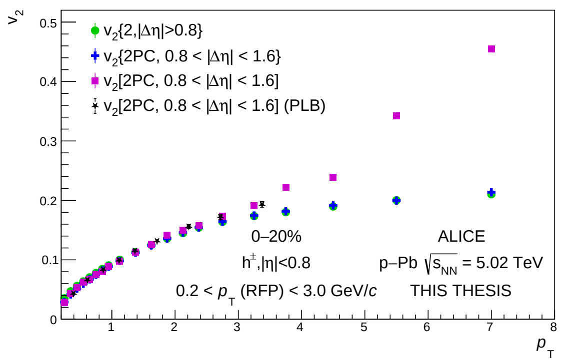

FIGURE 5.33: Flow coefficients $v_2\{2\}$, $v_2\{2\text{PC}\}$ and $v_2[2\text{PC}]$ of inclusive charged hadrons in central p–Pb collisions at $\sqrt{s_{\text{NN}}} = 5.02$ TeV. The data points marked as PLB originates from Ref. [102].

flow coefficients of primary identified particles $\pi^{\pm}$, $\text{K}^{\pm}$, and $\text{p}(\bar{\text{p}})$ measured using four-particle cumulants with three sub-events method are shown in low multiplicity Pb–Pb and pp collisions in Fig. 5.32 in left and right panel, respectively. It can be seen that the results in both systems are steeply decreasing towards negative values. Such a phenomenon is expected to originate from insufficient subtraction of the contributions from jets. A similar trend is also found in $v_2\{4\}_{3-\text{sub}}$ measured in p–Pb collisions. However, the results in p–Pb collisions are much less statistically stable and thus not shown here. The instability originates from the four-particle cumulant method which is known to require larger statistical sample. Despite the large uncertainties, a hint of mass ordering can be observed in the low p_{T} region of Pb–Pb collisions.

5.2.4 $v_2\{2\text{PC}\}$

The previously described results obtained using two- and four-particle cumulants show non-negligible non-flow contamination. Therefore, an alternative approach is used in order to obtain unbiased flow coefficients in small systems. The flow coefficients are extracted from the di-hadron correlation function $C(\Delta\eta, \Delta\varphi)$. The comparisons of the di-hadron correlations and two-particle cumulants methods are done in central (0–20%) p–Pb collisions without any non-flow subtraction. A comparison of $v_2\{2, |\Delta\eta| > 0.8\}$ from two-particle cumulants and $v_2\{2\text{PC}, 0.8 < |\Delta\eta| < 1.6\}$ from di-hadron correlations is shown in Fig. 5.33. The reference flow and associate particles in the calculation of $v_2\{2, |\Delta\eta| > 0.8\}$ and $v_2\{2\text{PC}, 0.8 < |\Delta\eta| < 1.6\}$, respectively, are taken from the same p_{T} region of $0.2 < p_{\text{T}} < 3\,\text{GeV}/c$. It can be seen that the flow coefficients calculated using different methods are in agreement. In addition, $v_2[2\text{PC}]$, in which both trigger and associate particles are taken from the same p_{T} region, is shown. While obtaining $v_2[2\text{PC}]$

using two-particle cumulants is possible, the measurement of $v_2[2PC]$ in this analysis is done only using the di-hadron correlation method. The data is compared to $v_2[2PC]$ from Ref. [102] and are in agreement within uncertainties. It can be seen that all four sets of flow coefficients are consistent with each other in the low p_T region. From $p_T \approx 3\,\text{GeV}/c$, the observed difference between $v_2[2PC]$ and $v_2\{2PC\}$ is explained mostly by the non-flow effects and the event selection bias. After the non-flow suppression, the difference between these two observables can be used to study the flow vector fluctuations [139].

5.2.5 $v_2\{2PC\}$ with peripheral subtraction method

With the two-dimensional information on the shape of correlation function $C(\Delta\eta, \Delta\varphi)$, it is possible to use different non-flow treatment methods, e.g., using peripheral subtraction and template fit methods, described in Sec. 3.5. Such study is made using two different correlations functions – long-range correlations, where both trigger and associate particles originate from the middle pseudorapidity, $|\eta| < 0.8$, and ultra-long-range correlations, where the trigger particles originate from the middle pseudorapidity and the associate particles originate from the forward pseudorapidity region. The subtraction of peripheral or low multiplicity collisions is made at the level of correlation functions, as discussed in Sec. 3.5.2. The low multiplicity collisions are assumed to have weak to no flow signal, thus, they are used to approximate the non-flow contribution. In this method, $C(\Delta\eta, \Delta\varphi)$ from peripheral (60–100%) p–Pb collisions is subtracted from the $C(\Delta\eta, \Delta\varphi)$ from central (0–20%) p–Pb collisions. The subtracted long-range correlation function is shown in Fig. 3.4. The correlation function is subsequently projected into $\Delta\varphi$ and fitted with Eq. 3.38 in order to extract coefficients $V_{n\Delta}$ that are used to calculate the flow coefficients. Nevertheless, in order to remove the contribution from the short-range correlations, the correlation function $C(\Delta\eta, \Delta\varphi)$ is projected only within a certain pseudorapidity region. From both the correlation function and its projections in Fig. 3.4 and 3.5, it can be seen that the jet peak at $\Delta\varphi \approx 0$ is not entirely subtracted. The peak is wider and more significant in the low p_T region. In order to test the residual non-flow effects between $v_2\{2PC\}$ extracted from different coverage in pseudorapidities, a ratio of various pseudorapidity ranges to the range $0.8 < |\Delta\eta| < 1.6$ is shown in Fig. 5.34 (right). It can be seen that the most significant difference is in the low p_T region due to the wider jet peak, as discussed above. While the flow coefficients extracted from long-range correlations with $1.4 < |\Delta\eta| < 1.6$ have the smallest contribution of the non-flow, the results are not statistically stable in the intermediate p_T. The statistical stability is further affected by studying the flow of identified particles. For such a measurement, the pseudorapidity coverage of $0.8 < |\Delta\eta| < 1.6$ is selected for the projection, despite the fact the correlation function contains a jet peak wider than $|\Delta\eta| \approx 0.8$. The flow coefficients of $\pi^{\pm}$, $K^{\pm}$, and $p(\bar{p})$ are shown in Fig. 5.35. In the low p_T region, the mass ordering, typical for

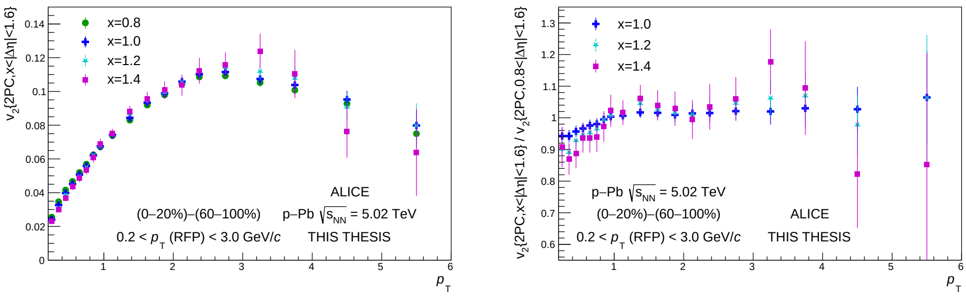

FIGURE 5.34: Left: Flow coefficients $v_2\{2\text{PC}\}$ of inclusive charged hadrons in central p–Pb collisions at $\sqrt{s_{\text{NN}}} = 5.02$ TeV from the peripheral subtraction method with different ranges of $\Delta\eta$ projections. Right: Ratio of $v_2\{2\text{PC}\}$ with different $\Delta\eta$ projections to $v_2\{2\text{PC}, 0.8 < |\Delta\eta| < 1.6\}$.

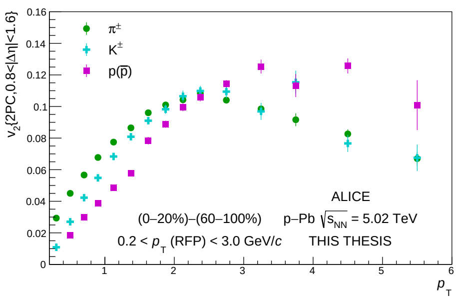

FIGURE 5.35: Flow coefficients $v_2\{2\text{PC}\}$ of $\pi^\pm$, $\text{K}^\pm$, and $\text{p}(\bar{\text{p}})$ in central p–Pb collisions at $\sqrt{s_{\text{NN}}} = 5.02$ TeV from the peripheral subtraction method.

the Pb–Pb collisions, can be seen. In intermediate p_{T} region, a baryon-meson splitting is observed with an exception of $3.5 < p_{\text{T}} < 4.0$ GeV/c in which $\text{K}^\pm$ and $\text{p}(\bar{\text{p}})$ are in agreement within uncertainties. The flow coefficients of identified particles at the intermediate and high p_{T} are not statistically stable. The instability can be explained by the rejection of approximately 75% particle pairs within the middle pseudorapidity in the $v_2\{2\text{PC}, 0.8 < |\Delta\eta| < 1.6\}$ calculation.

Suppressing non-flow effects with a sufficient η gap and still maintaining statistical stability in the calculation of flow coefficients of identified particles is possible using the three sub-event method in which associate particles are taken from forward and backward pseudorapidity regions. The comparison of $v_2\{2\text{PC}\}$ of inclusive charged hadrons from long-range correlations from $0.8 < |\Delta\eta| < 1.6$ and ultra-long-range correlations from $1.1 < |\Delta\eta| < 7.8$ is shown in Fig. 5.36. In the former, both the trigger and associated particles are taken from the middle pseudorapidity, $|\eta| < 0.8$. In the latter, the

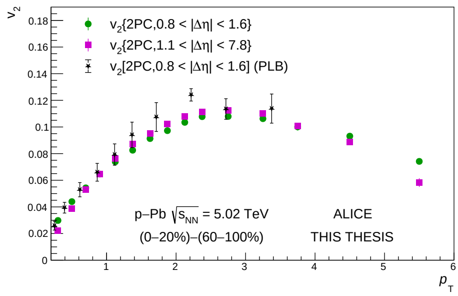

FIGURE 5.36: Flow coefficients $v_2\{2\mathrm{PC}\}$ of inclusive charged hadrons in central p–Pb collisions at $\sqrt{s_{\mathrm{NN}}} = 5.02$ TeV from the peripheral subtraction method with two different $\Delta\eta$ ranges. The data points marked as PLB originates from Ref. [102].

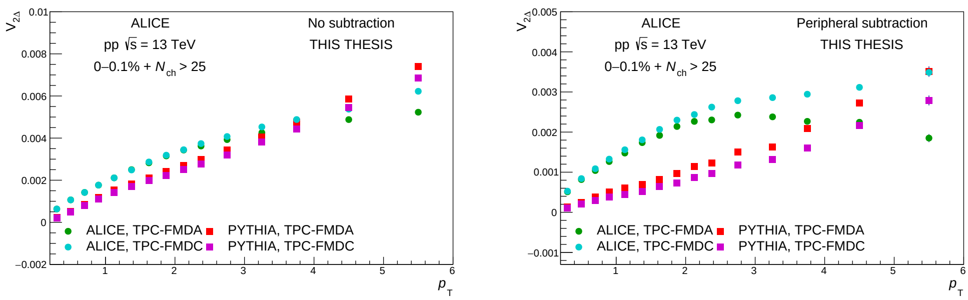

FIGURE 5.37: Flow coefficients $V_{2\Delta}\{2\mathrm{PC}\}$ of inclusive charged hadrons in high multiplicity pp collisions without (left) and with (right) peripheral subtraction in the data and from the MC simulation using PYTHIA event generator.

three sub-event method is used with FMD detector situated in the forward and backwards pseudorapidity with coverages $1.7 < \eta < 5.0$ and $-3.4 < \eta < -1.7$, respectively. It can be seen the p_{T} dependence of $v_2\{2\mathrm{PC}\}$ from both pseudorapidity regions is similar. The difference in low p_{T} originates mostly from the remaining jet peak in the long-range correlations. As the relative non-flow contribution increases with p_{T}, in the highest presented p_{T} bin, a difference between long- and ultra-long-range correlations likely originates from the non-sufficient non-flow subtraction in the former case. Moreover, comparisons of $v_2\{2\mathrm{PC}, 0.8 < |\Delta\eta| < 1.6\}$ and $v_2\{2\mathrm{PC}, 1.1 < |\Delta\eta| < 7.8\}$ to $v_2[2\mathrm{PC}, 0.8 < |\Delta\eta| < 1.6]$ from peripheral subtraction method from [102] are shown. The published results of $v_2[2\mathrm{PC}, 0.8 < |\Delta\eta| < 1.6]$ are in agreement with $v_2\{2\mathrm{PC}\}$ from long-range and ultra-long-range two-particle correlations.

The peripheral subtraction method assumes negligible flow signal in the correlation function in the low multiplicity collisions. For that reason, the low multiplicity base is

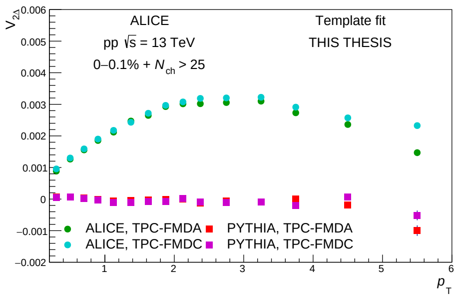

FIGURE 5.38: Flow coefficients $V_{2\Delta}\{2PC\}$ of inclusive charged hadrons in high multiplicity pp collisions from the template fit method from the data and the MC simulation using PYTHIA event generator.

subtracted from the correlation function in the high multiplicity collisions, assuming the subtraction of the entire non-flow contribution. To validate this non-flow subtraction method, $V_{2\Delta}$ coefficients extracted from the ultra-long-range correlations with coverage $-4.1 < \Delta\eta < -1.1$ and $1.1 < \Delta\eta < 3.9$ marked as TPC–FMDA and TPC–FMDC, respectively, are compared to the calculations from PYTHIA simulation [90]. PYTHIA is selected as it does not contain any anisotropic flow, i.e. the flow coefficients obtained from this model contain the non-flow exclusively. The comparison is shown in Fig. 5.37. In the left panel, it can be seen that if no subtraction is applied, $V_{2\Delta}$ increases with p_T in both the data and the model. After applying the peripheral subtraction, only the flow signal should remain. Therefore, it is expected that the $V_{2\Delta}$ coefficients extracted from PYTHIA should be consistent with zero. However, the results from the PYTHIA simulation are non-zero and keep increasing with the increasing p_T, as shown in Fig. 5.37 (right), and thus, the peripheral subtraction does not remove sufficiently the non-flow contribution in small systems. For that reason, an alternative approach of a non-flow treatment is used – the template fit method.

5.2.6 $v_2\{2PC\}$ with template fit method

If the assumption of no flow signal in low multiplicity collisions is broken, i.e., if there is a flow signal in low multiplicity collisions, an over-subtraction of the flow signal can occur during the peripheral subtraction. To avoid any potential effects from the over-subtraction, a template fit method, proposed in [145], is used. In this method, no explicit subtraction takes place and the flow signal is allowed in low multiplicity collisions. Details of this method are introduced in 3.5.3.

A MC study using the PYTHIA event generator is performed to test the non-flow suppression. Coefficients $V_{2\Delta}$, extracted from ultra-long-range correlations with the pseudorapidity coverage described in the previous section, are shown in Fig. 5.38 for

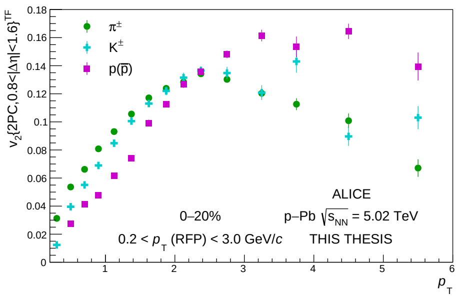

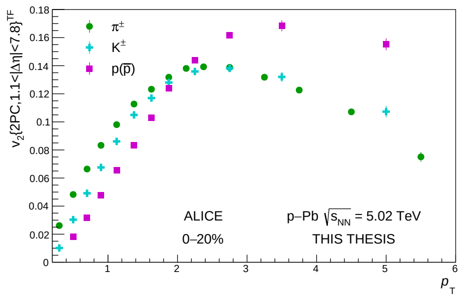

FIGURE 5.39: Flow coefficients $v_2\{2PC, 0.8 < |\Delta\eta| < 1.6\}$ from long-range correlations (left) and $v_2\{2PC, 1.1 < |\Delta\eta| < 7.8\}$ from ultra-long-range correlations (right) of $\pi^{\pm}$, $K^{\pm}$, and $p(\bar{p})$ in central p–Pb collisions at $\sqrt{s_{NN}} = 5.02$ TeV obtained with the template fit method.

both the experimental data and PYTHIA simulation. The results from PYTHIA obtained using the peripheral subtraction method are non-zero and keep increasing with the p_T, as shown in Fig. 5.37. Such a behaviour suggests some non-flow contamination remains. This is not the case for the template fit method as both $V_{2\Delta}$ coefficients from PYTHIA are consistent with zero. Therefore, no significant non-flow contamination is present when using the template fit method with the ultra-long-range correlations.

While it is shown in the previous section the long-range correlations contain residual contribution from the jet peak, the method is used together with the template fit method for the testing purposes. The measurements of flow coefficients $v_2\{2PC, 0.8 < |\Delta\eta| < 1.6\}$ from the template fit method for $\pi^{\pm}$, $K^{\pm}$, and $p(\bar{p})$ in 0–20% central p–Pb collisions at $\sqrt{s_{NN}} = 5.02$ TeV are shown in Fig. 5.39 (left). The mass ordering and baryon-meson grouping, typical for Pb–Pb collisions, can be observed at the low and intermediate p_T regions, respectively. The presented results from long-range correlations consider both the trigger and associated particles from the central pseudorapidity. To extend the pseudorapidity separation between correlated particles and to improve the statistical stability of the v_2 results for the identified particles, measurements using the forward pseudorapidity detectors are performed. The results of $v_2\{2PC, 1.1 < |\Delta\eta| < 7.8\}$ from ultra-long-range correlations using the template fit method for $\pi^{\pm}$, $K^{\pm}$, and $p(\bar{p})$ in 0–20% central p–Pb collisions at $\sqrt{s_{NN}} = 5.02$ TeV are shown in Fig. 5.39 (right). The method is chosen and used for extracting the final flow coefficients of identified particles in p–Pb and pp collisions. The results of $v_2\{2PC\}$ from ultra-long-range correlations with template fit method for $\pi^{\pm}$, $K^{\pm}$, $p(\bar{p})$, K^0_S, and $\Lambda(\bar{\Lambda})$ in both systems are discussed later.

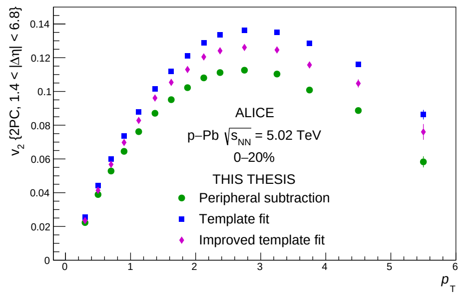

FIGURE 5.40: Flow coefficients $v_2\{2\mathrm{PC}\}$ from ultra-long-range correlations with three different methods of non-flow suppression.

5.2.7 $v_2\{2\mathrm{PC}\}$ with improved template fit method

The measurement of flow coefficients is also tested using the improved template fit method [146], introduced in Sec. 3.5.3. The improved template fit method parametrises the multiplicity dependence of the flow coefficients. It the method, it is assumed the jet component of any multiplicity class can be expressed using a jet component of a different multiplicity class with an appropriate scaling factor F, i.e.,

$$Y_{\mathrm{jet}}\left(\Delta\varphi\right) = FY'_{\mathrm{jet}}\left(\Delta\varphi\right), \tag{5.17}$$

where $'$ stands for a different multiplicity class. An analogical relation between multiplicity classes has been already introduced in Eq. 3.61. In addition, the method assumes that the jet components in two lowest multiplicity classes, $Y_{\mathrm{jet}}^{\mathrm{1st\ LM}}$ and $Y_{\mathrm{jet}}^{\mathrm{2nd\ LM}}$, are the same, i.e.,

$$Y_{\mathrm{jet}}^{\mathrm{1st\ LM}} = F^{\mathrm{LM}} Y_{\mathrm{jet}}^{\mathrm{2nd\ LM}}, \tag{5.18}$$

with the parameter F^{LM} describing the scale of the jet component in the second-lowest multiplicity bin with respect to the lowest multiplicity bin with a fix value

$$F^{LM} = 1. \tag{5.19}$$

The comparisons of results obtained using improved template fit method, template fit method, and peripheral subtraction method in p–Pb collisions at $\sqrt{s_{\mathrm{NN}}} = 5.02$ TeV are shown in Fig. 5.40. The ordering of methods, i.e., $v_2^{\mathrm{sub}} < v_2^{\mathrm{ITF}} < v_2^{\mathrm{TF}}$ is in agreement with [150].

The assumption of $F^{LM} = 1$ is broken in pp collisions, as has been shown, e.g., in [147]. For that reason, the improved template fit method is tested with two different

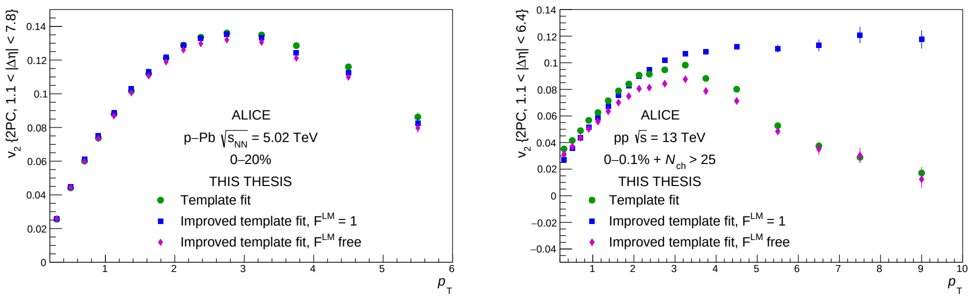

FIGURE 5.41: Flow coefficients $v_2\{2PC\}$ of inclusive charged particles from ultra-long-range correlations in high multiplicity p–Pb (left) and pp (right) collisions with template fit method and two different configurations of the improved template fit methods.

configurations in which parameters F^{LM} are different. In the first configuration, originally introduced in [146], the parameter F^{LM} is fixed to 1. In the second configuration, the parameter F^{LM} is free during the fitting procedure. The comparisons of the $v_2\{2PC, 1.1 < |\Delta\eta| < 7.8\}$ results for inclusive charged particles from both configurations of the improved template fit method in p–Pb and pp collisions are shown in Fig. 5.41 in left and right panel, respectively. In addition, the results from the template fit method are shown. It can be seen the results from template fit method and both configurations of the improved template fit methods are consistent in p–Pb collisions where the assumptions of the improved template fit method are not broken. However, in pp collisions, the differences between the results from two configurations of the improved template fit, i.e., with fixed and free F^{LM}, are significant in both the intermediate and high p_T. This further confirms the jet components in two lowest multiplicity classes are different. Thus, the originally proposed improved template fit method with $F^{LM} = 1$ cannot be used to study p_T-differential flow coefficients in pp collisions. As the configuration of the improved template fit with free F^{LM} parameter has not been used before by anybody and is not carefully tested using MC studies, only the template fit method is used in pp and p–Pb collisions to obtain the final results of flow coefficients with identified particles to stay consistent.

5.2.8 Results and scaling with number of constituent quarks

Based on the discussion above, it is clear that the best available method for obtaining the flow coefficients of identified particles with good statistical stability and a sufficient non-flow suppression is by using ultra-long-range two-particle correlations with the template fit method. The results of flow coefficients of $\pi^{\pm}$, $K^{\pm}$, $p(\bar{p})$, K^0_S, and $\Lambda(\bar{\Lambda})$ in

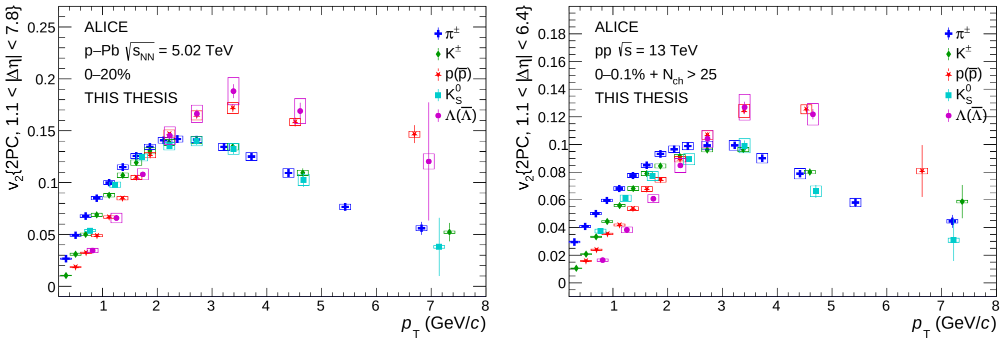

FIGURE 5.42: Flow coefficients $v_2\{2PC\}$ of $\pi^{\pm}$, $K^{\pm}$, $p(\bar{p})$, K^0_S, and $\Lambda(\bar{\Lambda})$ from the template fit method using ultra-long-range correlations in high multiplicity pp and p–Pb collisions.

	$\pi^{\pm}$	$K^{\pm}$	$p(\bar{p})$	K^0_S	$\Lambda(\bar{\Lambda})$
$\pi^{\pm}$	x	0.93	6.73	0.11	4.18
$K^{\pm}$	0.93	x	5.49	0.44	3.66
$p(\bar{p})$	6.73	5.49	x	4.64	0.88
K^0_S	0.11	0.44	4.64	x	3.64
$\Lambda(\bar{\Lambda})$	4.18	3.66	0.88	3.64	x

TABLE 5.1: The separation between $v_2\{2PC\}(p_T)$ of different particle species in $3 < p_T < 6$ GeV/c in high multiplicity p–Pb collisions in units of σ.

high multiplicity p–Pb and pp collisions are shown in 5.42 in left and right panels, respectively[4]. The ultra-long-range correlations cover large range in pseudorapidity, in particular, $1.1 < |\Delta\eta| < 7.8$ and $1.1 < |\Delta\eta| < 6.4$ in p–Pb and pp collisions, respectively. The smaller $|\Delta\eta|$ coverage is considered in pp collisions due to the known issue in the outer ring of the forward side of the FMD detector. As described in Sec. 4.3.1, a criterion on N_{ch} is applied in high multiplicity pp collisions in order to obtain approximately the same mean multiplicity as is in 0–20% p–Pb collisions. In both cases, the low multiplicity base originates from the same system as the high multiplicity collisions, i.e., for high multiplicity p–Pb collisions, 60–100% centrality class is considered for the base with an additional criterion on multiplicity, $N_{ch} < 20$. For high multiplicity pp collisions, minimum bias pp collisions with $N_{ch} < 20$ serve as the low multiplicity base.

In both p–Pb and pp collisions, the same phenomena are observed as in the measurement of the flow coefficients of identified particles in Pb–Pb collisions, in particular,

[4]As the set of results in Fig. 5.42 is part of the publication that is under preparation, the results contain systematic uncertainty. The results presented earlier in this section are shown to discuss individual methods of flow extraction in small systems, thus, no systematic uncertainty is evaluated for the presented measurements. In addition, unlike the previously discussed results, the position of points on the x-axis in Fig. 5.42 is not in the centre of the bin but corresponds to the mean value of the p_T in the studied bin.

	$\pi^{\pm}$	$K^{\pm}$	$p(\bar{p})$	K^0_S	$\Lambda(\bar{\Lambda})$
$\pi^{\pm}$	x	0.96	5.20	0.34	4.22
$K^{\pm}$	0.96	x	6.24	0.99	3.71
$p(\bar{p})$	5.20	6.24	x	4.99	0.26
K^0_S	0.34	0.99	4.99	x	3.81
$\Lambda(\bar{\Lambda})$	4.22	3.71	0.26	3.81	x

TABLE 5.2: The separation between $v_2\{2PC\}(p_T)$ of different particle species in $3 < p_T < 6$ GeV/c in high multiplicity pp collisions in units of σ.

the mass ordering in the low p_T region and baryon-meson grouping in the intermediate p_T region. The mass ordering in Pb–Pb collisions is explained by the collective expansion of produced particles by the interplay between the radial flow and v_2. This phenomenon has been observed before in p–Pb and pp collisions, e.g., in [102] and [103], respectively. The measured flow coefficients are shown for $\pi^{\pm}$, $K^{\pm}$, and $p(\bar{p})$ in p–Pb collisions at $\sqrt{s_{NN}} = 5.02$ TeV and for K^0_S and $\Lambda(\bar{\Lambda})$ pp collisions at $\sqrt{s} = 13$ TeV in Figs. 1.26 and 1.27. The results presented in this thesis contain flow coefficients of $\pi^{\pm}$, $K^{\pm}$, $p(\bar{p})$, K^0_S, and $\Lambda(\bar{\Lambda})$ in both collision systems. Therefore, the mass ordering can be studied with more particle species. Such phenomenon can be seen in the low p_T region, $pt < 2.5$ GeV/c, in the measurements of flow coefficients of identified particles in both p–Pb and pp collisions, shown in Fig. 5.42. The v_2 of different particle species crosses at $2 < p_T < 3$ GeV/c in both studied systems. At $3 < p_T < 6$ GeV/c, the evidence of baryon-meson grouping is seen in both p–Pb and pp collisions for the first time. The splittings between pairs of all particle species in the p_T region $3 < p_T < 6$ GeV/c are shown in Tabs. 5.1 and 5.2 in the units of statistical significance σ for p–Pb and pp collisions, respectively. In the intermediate p_T region, the splittings of the measured v_2 within the group of mesons are $0.11 - 0.93\ \sigma$ while the splitting within baryons is $0.88\ \sigma$ in high multiplicity p–Pb collisions. The splittings between individual baryons and mesons are $3.71 - 6.24\ \sigma$. In the same p_T region but in high multiplicity pp collisions, the splittings between different mesons are $0.34 - 0.99\ \sigma$. The separation between two reported baryons is $0.26\ \sigma$. The splittings between individual baryons and mesons are $3.71 - 6.73\ \sigma$. Therefore, in both p–Pb and pp collisions at high multiplicities, the evidence of the baryon-meson grouping and splitting is observed for the first time. Such phenomenon in Pb–Pb collision originates from the collectivity at the partonic level and the particle production via the quark coalescence mechanism. The similarities between large and small collision systems, especially the clear baryon-meson grouping, show strong evidence of partonic collectivity in small sysstems, and therefore, a possible creation of droplet of QGP in small collision systems at high multiplicities.

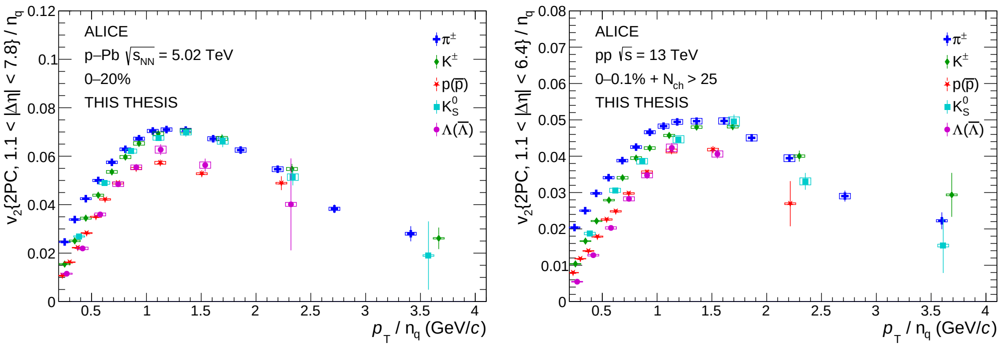

FIGURE 5.43: Flow coefficients $v_2\{2PC\}$ of $\pi^{\pm}$, $K^{\pm}$, $p(\bar{p})$, K^0_S, and $\Lambda(\bar{\Lambda})$ scaled with number of constituent quarks in high multiplicity p–Pb (left) and pp (right) collisions from the template fit method using ultra-long-range correlations.

The phenomenon of baryon-meson grouping is further tested by the number of constituent quarks (NCQ) scaling. The results of $v_2\{2PC\}/n_q$ for various particle species in high multiplicity p–Pb and pp collisions are shown in Fig. 5.43. The scaled flow coefficients $v_2\{2PC\}/n_q$ have similar values from $p_T > 1$ GeV$/c$ for all the particle species. The NCQ scaling holds approximately in Pb–Pb collisions, as reported in $v_2\{2, |\Delta\eta| > 0.8\}/n_q$ and $v_2\{4\}/n_q$, shown in Figs. 5.15 and 5.16, respectively, with the difference $\geq 20\%$. The scaling in p–Pb and pp collisions holds with an approximate difference up to 36% and 21%, respectively, thus, the scaling is slightly worse than the one reported in Pb–Pb collisions, possibly due to the smaller relative contribution from the quark coalescence. Such behaviour can be better understood by the comparison between the experimental measurements and the models, discussed in the following subsection.

5.2.9 Model comparison and discussion

In order to further study the obtained results of the flow of identified particles in small collision systems, comparisons with various models are made, with an emphasis on the hybrid model with two different configurations, similar to the one described in Sec. 5.1.8. In the first configuration, marked as Hydro+coal+frag, the model combines hydrodynamics at the low p_T region, quark coalescence at the intermediate p_T, and jet fragmentation at the high p_T. In the second configuration, marked as Hydro+frag, no contribution of the coalescence is included. The model consists only of hydrodynamics and fragmentation. The partons in both configurations of the models are generated using two different approaches. The hydrodynamic model VISH2+1 [180] is used for generating the thermal partons, i.e., the partons with low p_T, using the TRENTo initial

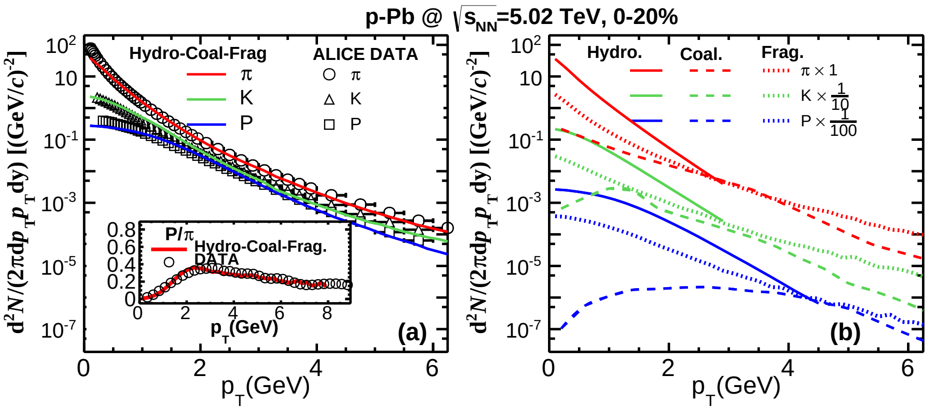

FIGURE 5.44: Left: p_{T} spectra of $\pi^{\pm}$, $\mathrm{K}^{\pm}$, and $\mathrm{p}(\bar{\mathrm{p}})$ in high multiplicity p–Pb collisions from the data and the Hydro+coal+frag model. The proton-to-pion ratio is in the inserted panel. Right: Contributions from individual components of the Hydro+coal+frag model into the flow of $\pi^{\pm}$, $\mathrm{K}^{\pm}$, and $\mathrm{p}(\bar{\mathrm{p}})$ in high multiplicity p–Pb collisions. Figure taken from [183]. The ALICE data originate from [184].

conditions [171]. The hard partons, i.e., partons with high p_{T}, are generated using initial jet shower partons from PYTHIA [90]. Subsequently, the LBT model simulates their energy loss via elastic and inelastic interactions with the evolving medium [181, 182]. The recombination of partons is possible with all available combinations, i.e., thermal-thermal, thermal-hard, and hard-hard. For the Hydro+coal+frag model, the hard partons not used in coalescence are fragmented into hard hadrons. The final state hadronic rescattering is described using the UrQMD [96] model. The relative contribution of individual components into the Hydro+coal+frag and Hydro+frag models is determinated by fitting the p_{T} spectra of $\pi^{\pm}$, $\mathrm{K}^{\pm}$, and $\mathrm{p}(\bar{\mathrm{p}})$, shown in Fig. 5.44 in high multiplicity (0–20%) p–Pb collisions. It can be seen that the Hydro+coal+frag model describes the p_{T} spectra well. In Fig. 5.44 (right), the individual contributions of hydrodynamics, quark coalescence, and jet fragmentation are shown. The hydrodynamics is dominant in the low p_{T} region with $p_{\mathrm{T}} < 2$ GeV/c while the jet fragmentation is dominant in the higher p_{T} with a different p_{T} threshold for different particle species. In the intermediate region, i.e., $2 < p_{\mathrm{T}} < 4$ GeV/c, all three components contribute to the total description of p_{T} spectra [183]. Nevertheless, the relative contribution of the quark coalescence mechanism is smaller in p–Pb collisions compared to the one in Pb–Pb collisions, which can possibly explain the worse NCQ scaling.

The measured flow coefficients $v_2\{2\mathrm{PC}\}(p_{\mathrm{T}})$ for $\pi^{\pm}$, $\mathrm{K}^{\pm}$, $\mathrm{p}(\bar{\mathrm{p}})$, $\mathrm{K}^0_{\mathrm{S}}$, and $\Lambda(\bar{\Lambda})$ from the template fit method in high multiplicity p–Pb collisions are compared to the calculations from Hydro+coal+frag and Hydro+frag in Fig. 5.45. The model calculations are available only for $\pi^{\pm}$, $\mathrm{K}^{\pm}$, and $\mathrm{p}(\bar{\mathrm{p}})$. The characteristic mass ordering is seen in both

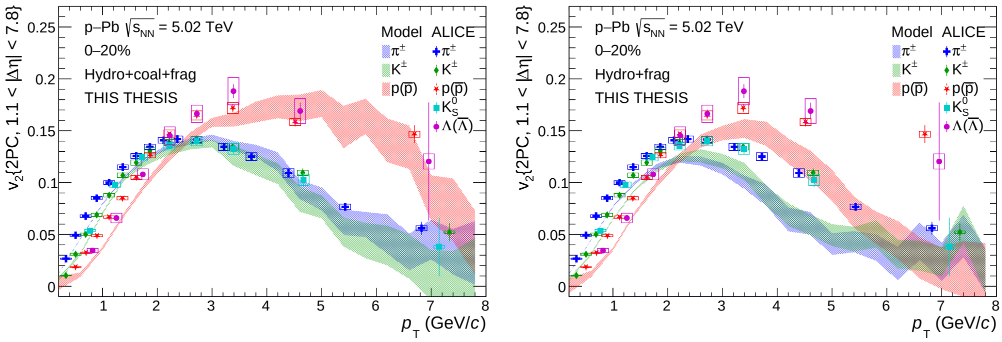

FIGURE 5.45: Flow coefficients $v_2\{2PC\}$ of $\pi^{\pm}$, $K^{\pm}$, $p(\bar{p})$, K^0_S, and $\Lambda(\bar{\Lambda})$ from the template fit method using ultra-long-range correlations in high multiplicity p–Pb collisions compared to hybrid models combining hydrodynamics, quarks coalescence, and jet fragmentation (left) and hydrodynamics and jet fragmentation (right).

	$\pi^{\pm}$	$K^{\pm}$	$p(\bar{p})$
Hydro+coal+frag	0.77	1.4	1.11
Hydro+frag	3.9	3.5	2.1

TABLE 5.3: The separation between $v_2\{2PC\}(p_T)$ of $\pi^{\pm}$, $K^{\pm}$, and $p(\bar{p})$ in $3 < p_T < 6$ GeV/c between the data and two configurations of models in high multiplicity p–Pb collisions in units of σ.

configurations of the model and the data at $p_T < 2$ GeV/c. The crossing of v_2 of different particle species is observed in the same p_T region, $2 < p_T < 3$ GeV/c, in models and the data. At the intermediate p_T region, the baryon-meson grouping is observed. The splittings between the baryons and mesons in both Hydro+coal+frag model calculations and the experimental measurements persist until ~ 8 GeV/c, while in the model without coalescence, Hydro+frag, the splitting disappears at ~ 6 GeV/c. The separation between models and the data in $3 < p_T < 6$ GeV/c is shown in Tab. 5.3. It can be seen in both the table and Fig. 5.45 that the Hydro+coal+frag model agrees with the data within $\approx 1\,\sigma$ while the deviation between the data and Hydro+frag model is greater. The model without quark coalescence significantly underestimates the data in the intermediate p_T region. In addition, with the Hydro+frag model, it is not possible to simultaneously describe the p_T spectra and the flow coefficients [183]. Therefore, it further confirms the importance of the quark coalescence mechanism in the description of p–Pb collisions and strongly suggests a presence of a small droplet of the QGP in this system.

The Hydro+coal+frag and Hydro+frag predictions are available in pp collisions as well[5]. The comparison with the data is shown in Fig. 5.46. In the low p_T region, the mass

[5]The current models originate from the private communication with the authors. The publication with the presented models is expected to be released after the submission of this thesis.

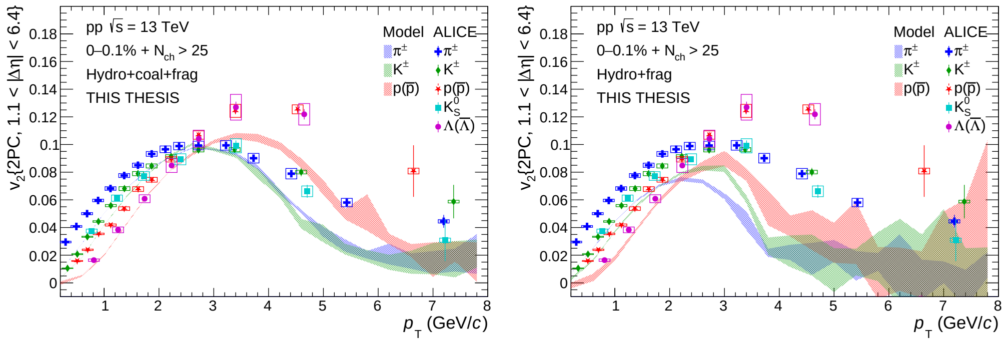

FIGURE 5.46: Flow coefficients $v_2\{2PC\}$ of $\pi^{\pm}$, $K^{\pm}$, $p(\bar{p})$, K^0_S, and $\Lambda(\bar{\Lambda})$ from the template fit method using ultra-long-range correlations in high multiplicity pp collisions compared to hybrid models combining hydrodynamics, quarks coalescence, and jet fragmentation (left) and hydrodynamics and jet fragmentation (right)

	$\pi^{\pm}$	$K^{\pm}$	$p(\bar{p})$
Hydro+coal+frag	3	4.6	5
Hydro+frag	7.5	6.7	6.5

TABLE 5.4: The separation between $v_2\{2PC\}(p_T)$ of $\pi^{\pm}$, $K^{\pm}$, and $p(\bar{p})$ in $3 < p_T < 6$ GeV/c between the data and two configurations of models in high multiplicity pp collisions in units of σ.

ordering phenomenon is observed in the data and both presented configurations of the model. The crossing between $v_2(p_T)$ of different particles occurs at the lower p_T in the Hydro+frag model calculations compared to the data and the Hydro+coal+frag model calculations. The splitting between baryons and mesons is seen in the data and the Hydro+coal+frag model calculations across $3 < p_T < 6$ GeV/c, while no such phenomenon is observed in Hydro+frag model calculations. The difference between both configurations of the model and the experimental measurements in the intermediate p_T region, $3 < p_T < 6$ GeV/c, is presented in Tab. 5.4 in the units of the statistical deviation σ. It can be seen in both Fig. 5.46 and Tab. 5.4 that neither of the models describes the data quantitatively. Nevertheless, the calculation from Hydro+coal+frag is closer to the measurements. Thus, the quark coalescence mechanism has to be added to the calculation to improve the model's overall performance. However, while introducing the mechanism of quark coalescence helps to describe the data better, additional mechanisms may miss in the theoretical description.

In addition to the presented Hydro+coal+frag and Hydro+frag models, comparisons to AMPT model [161] with the string melting configuration [185] and EPOS-LHC model [154] in high multiplicity p–Pb collisions are shown in Fig. 5.47 in left and right panels, respectively. In the AMPT model, high multiplicity collisions produce very high

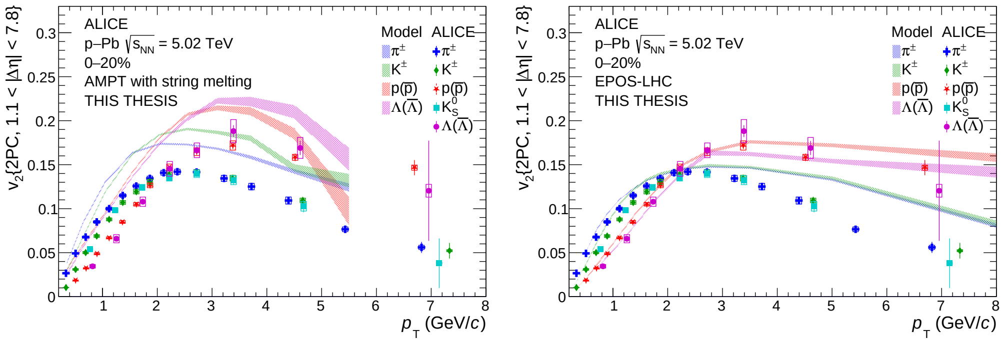

FIGURE 5.47: Flow coefficients $v_2\{2PC\}$ of $\pi^{\pm}$, $K^{\pm}$, $p(\bar{p})$, K^0_S, and $\Lambda(\bar{\Lambda})$ from the template fit method using ultra-long-range correlations in high multiplicity p–Pb collisions compared to AMPT model with string melting (left) and EPOS-LHC model (right).

energy density regions. Hadrons in AMPT are initially produced in inelastic scatterings. Those produced in the high energy density regions melt into their constituent quarks and interact with the medium via the parton escape mechanism. Finally, partons hadronize via quark coalescence. Typically, parton escape mechanisms produce fewer parton-medium interactions than hydrodynamic models, resulting in lower values of flow coefficients. The EPOS-LHC model follows the core-corona prescription, where particles are produced by two competing mechanisms. In the core, particles are produced thermally using statistical hadronization and follow the dynamics parameterised by previous LHC measurements. Particles in the corona are produced via string breaking. The AMPT model does not describe the measurements across the whole studied p_T region. However, the flow coefficients v_2 in the AMPT model exhibit the characteristic mass ordering, which has been observed already in [186]. The model does not reproduce the baryon-meson grouping either. It is not currently understood whether the absence of baryon-meson grouping in the AMPT model originates from the applied non-flow suppression mechanism. Further model studies are expected to be performed in the future. The flow coefficients v_2 from the EPOS-LHC model qualitatively agree with the experimental measurement in the low p_T region and exhibit clear mass ordering. In addition, the baryon-meson splitting is observed in the intermediate p_T region. However, it underestimates the v_2 of $\pi^{\pm}$ and $K^{\pm}$, and no particle type grouping is observed for baryons. Similarly to the AMPT, further studies are expected using the EPOS-LHC model to better understand the contribution of the quark coalescence mechanism.

6 Conclusions and outlook

Due to the very short lifetime of the quark-gluon plasma, its properties are probed indirectly using different experimental observables. In this thesis, the transport properties of the created medium and initial conditions before the QGP creation are studied using the various anisotropic flow measurements.

The flow coefficients $v_2\{m\}$ from m-particle cumulants are reported for $m = 2, 4, ..., 12$ in Pb–Pb collisions at $\sqrt{s_{\mathrm{NN}}} = 5.02$ TeV from the data and from the HIJING simulation. As HIJING does not contain any collective effects, it is suitable for checking the remaining non-flow effects. It is shown that non-flow contamination is heavily suppressed using multi-particle cumulants.

The mixed-harmonic cumulants $MHC(v_2^k, v_3^l)$ are reported in Pb–Pb collisions at $\sqrt{s_{\mathrm{NN}}} = 5.02$ TeV for various combinations of moments k and l. With these observables, correlations between different moments of different harmonics are investigated. As $MHC(v_2^k, v_3^l)$ shows a unique sensitivity to the initial conditions, they are compared to calculations from a hydrodynamic model with two different initial conditions. It is shown that the linear dependence of the flow coefficients v_n on the initial eccentricities ε_n persists in central and semi-central Pb–Pb collisions for $n = 2, 3$. The linearity between v_2 and ε_2 is stronger than the one between v_3 and ε_3. The linear relation does not hold for higher harmonics, $n \geq 4$, where non-linear contributions from lower harmonics are dominant. The higher orders of mixed harmonic cumulants using six- and eight-particle correlations are studied for the first time. They show a change of sign, which is characteristic to multi-particle cumulants of a single harmonic. Such a study is important as different moments exhibit different sensitivities to the initial conditions. Finally, correlations between three different flow harmonics are studied for the first time using $MHC(v_2^2, v_3^2, v_4^2)$. The large discrepancies between the models with various transport properties of the medium allow constraining the models describing the evolution of the QGP.

The measurement of flow in Pb–Pb collisions at $\sqrt{s_{\mathrm{NN}}} = 5.02$ TeV is further extended by studying flow coefficients v_2 of identified particles using the two- and four-particle cumulants method, $v_2\{2\}$ and $v_2\{4\}$. The results of $v_2\{2\}$ and $v_2\{4\}$ are reported for identified particles $\pi^{\pm}$, $\mathrm{K}^{\pm}$, $\mathrm{p}(\bar{\mathrm{p}})$, $\mathrm{K}^0_{\mathrm{S}}$, $\Lambda(\bar{\Lambda})$, ϕ, $\Xi(\bar{\Xi})$, and $\Omega(\bar{\Omega})$ in different centrality classes from central (10–20%) to peripheral (50–60%) Pb–Pb collisions. Two phenomena are observed in all reported centrality classes – the mass ordering in the low transverse momentum region, $p_{\mathrm{T}} \lesssim 3$ GeV/c, and the baryon-meson grouping in the intermediate transverse momentum region, $3 < p_{\mathrm{T}} < 6$ GeV/c. The mass ordering originates from the radial expansion of the medium and can be described by hydrodynamic models. The baryon-meson grouping originates from the partonic collectivity and subsequent particle production via the quark coalescence mechanism. Using $v_2\{2\}$ and $v_2\{4\}$, the first two moments of the probability density function of elliptic flow v_2, the mean $\langle v_2 \rangle$ and variance σ_{v_2}, are calculated. The observables $\langle v_2 \rangle$, σ_{v_2}, ratio $v_2\{2\}/v_2\{4\}$, and relative flow fluctuations $F(v_2)$ are reported for the same particle species and centrality classes as $v_2\{2\}$ and $v_2\{4\}$. The mass ordering and baryon-meson grouping are observed for $\langle v_2 \rangle$ and σ_{v_2} in all reported centrality classes. No particle type grouping is reported in central collisions of $v_2\{2\}/v_2\{4\}$ and $F(v_2)$. In contrast, a grouping of baryons and mesons is observed in the low transverse momentum region, $p_{\mathrm{T}} < 3$ GeV/c, for both $v_2\{2\}/v_2\{4\}$ and $F(v_2)$ in semi-central and peripheral collisions. The observables $v_2\{4\}$ and $F(v_2)$ are compared to the hydrodynamic model with different initial conditions. In addition, all reported observables are compared to a hybrid model with contributions of hydrodynamics, quark coalescence, and jet fragmentation to probe the particle production mechanism. The model without the contribution of the quark coalescence can not reproduce the experimental data. Thus, it confirms the importance of the quark coalescence in the description of the evolution of the system.

Finally, the measurement of the flow of identified particles is extended to small collision systems, where it can help to understand the development of flow through the dynamic evolution of the colliding system. The measurement is more challenging compared to the study in heavy-ion collisions due to significant non-flow contamination. For that reason, the flow coefficients are extracted using various methods, such as two- and four-particle cumulants with different sub-events, subtraction of low multiplicity collisions, long-range and ultra-long-range two-particle correlations, and the template and improved template fit methods. The flow coefficients obtained using ultra-long-range two-particle correlations with the template fit method are reported for $\pi^{\pm}$, $\mathrm{K}^{\pm}$, $\mathrm{p}(\bar{\mathrm{p}})$, $\mathrm{K}^0_{\mathrm{S}}$, and $\Lambda(\bar{\Lambda})$ in p–Pb and pp collisions at $\sqrt{s_{\mathrm{NN}}} = 5.02$ and 13 TeV, respectively. The flow coefficients v_2 exhibit mass ordering in the low transverse momentum region that is explained as the interplay of radial and elliptic flow. The grouping of v_2 of baryons and mesons occurs in the intermediate transverse momentum region. This phenomenon is associated with partonic collectivity and quark coalescence in heavy-ion collisions. The first observation of baryon-meson grouping with large statistical significance is reported in p–Pb and pp collisions. Due to the many similarities between large and small systems, strong evidence is presented of creating a droplet of QGP in small collision systems at high multiplicities. In addition, the measured flow coefficients are compared to a model with and without the contribution of quark coalescence. The hybrid model with the contribution of quark coalescence quantitatively agrees with the measured data in p–Pb collisions. In pp collisions, the model describes the data only qualitatively. Nevertheless, the description is much better than the model without any contribution of the quark coalescence.

6.1 Outlook and future LHC runs

Further studies of the anisotropic flow of identified particles in small systems are possible using the methods presented in this thesis. First, the current analysis using ultra-long-range two-particle correlation with the template fit method can be extended by adding more particle species. In particular, ϕ can provide an essential test of mass ordering and baryon-meson grouping phenomena, as it has a mass similar to $\mathrm{p}(\bar{\mathrm{p}})$ while it is a meson. In addition, the presented measurement can be extended to a high transverse momentum region with future LHC runs with a larger data sample available, allowing statistical stability in a wider transverse momentum range.

The high multiplicity pp collisions sample with higher integrated luminosity is expected to be obtained during the LHC Run 3 that started mid-2022. The projection of the flow of identified particles, shown in Fig. 6.1 (left), is obtained using four-particle cumulants with three sub-events method. The method, described in detail in this thesis, can be improved by rejecting events that contain di-jets in the central pseudorapidity region. With such improvement, it is expected to receive similar results to the results presented in this thesis obtained using ultra-long-range two-particle correlations with the template fit method instead of the steeply decreasing flow coefficients $v_2\{4\}_{3-\mathrm{sub}}$ in pp collisions, shown in this thesis. Moreover, the four-particle cumulants with three sub-events method is used to project the flow of identified particles in O–O collisions at $\sqrt{s_{\mathrm{NN}}} = 6.37$ TeV, expected to take place at the LHC during Run 3. The projection is shown in Fig. 6.1 (right). Such a study is important to test the hydrodynamic evolution and the particle production in collisions of ^{16}O and to test the contribution of the initial geometry in the system with a similar number of participating nucleons than in p–Pb collisions.

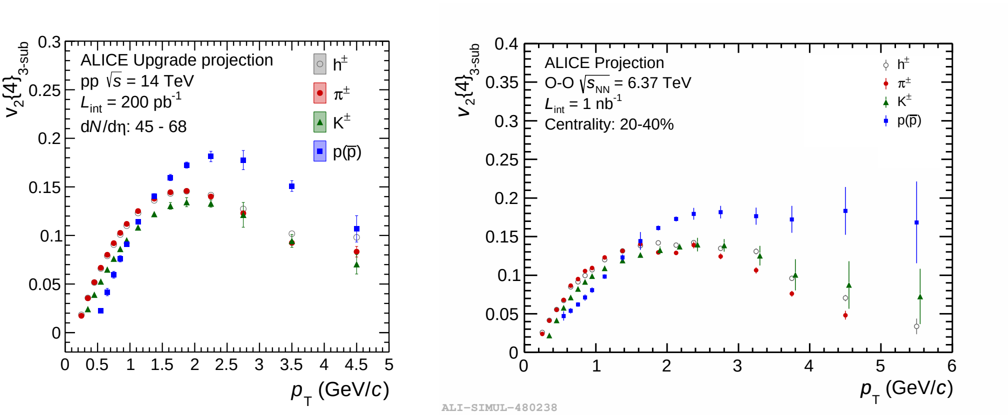

FIGURE 6.1: Left: Upgrade projection of flow coefficients $v_2\{4\}_{3-\mathrm{sub}}$ of $\pi^{\pm}$, $\mathrm{K}^{\pm}$, and $\mathrm{p}(\bar{\mathrm{p}})$ in high multiplicity pp collisions. Taken from [187]. Right: Upgrade projection of flow coefficients $v_2\{4\}_{3-\mathrm{sub}}$ of $\pi^{\pm}$, $\mathrm{K}^{\pm}$, and $\mathrm{p}(\bar{\mathrm{p}})$ in O–O collisions. Taken from [188].

Bibliography

[1] N. Bohr. "On the constitution of atoms and molecules". *The London, Edinburgh, and Dublin Philosophical Magazine and Journal of Science* 26 (1913). DOI: 10.1080/14786441308634955.

[2] B. R. Martin. *Nuclear and Particle Physics: An introduction*. Wiley, 2012. ISBN: 978-0-470-74274-7.

[3] S. L. Kakani et al. *Nuclear and Particle Physics*. Anshan Limiter, 2008. ISBN: 978-1-848290-07-5.

[4] M. Gell-Mann. *The Eightfold Way: A Theory of strong interaction symmetry*. 1961. DOI: 10.2172/4008239.

[5] J. I. Friedman et al. "Deep Inelastic Electron Scattering". *Annual Review of Nuclear Science* 22 (1972). DOI: 10.1146/annurev.ns.22.120172.001223.

[6] D. P. Barber et al. "Discovery of Three-Jet Events and a Test of Quantum Chromodynamics at PETRA". *Physical Review Letters* 43 (1979). DOI: 10.1103/PhysRevLett.43.830.

[7] R. L. Liboff. *Introductory Quantum Mechanics*. Addison-Wesley, 1997. ISBN: 0-201-87879-8.

[8] A. Zee. *Quantum Field Theory in a nutshell*. Princeton University Press, 2010. ISBN: 978-0-691-14034-6.

[9] Particle Data Group. "Review of Particle Physics". *Progress of Theoretical and Experimental Physics* 2020 (2020). DOI: 10.1093/ptep/ptaa104.

[10] Y. Fukuda et al. "Evidence for Oscillation of Atmospheric Neutrinos". *Physical Review Letters* 81 (1998). DOI: 10.1103/PhysRevLett.81.1562.

[11] Q. R. Ahmad et al. "Measurement of the Rate of $\nu_e + d \to p + p + e^-$ Interactions Produced by ^8B Solar Neutrinos at the Sudbury Neutrino Observatory". *Physical Review Letters* 87 (2001). DOI: 10.1103/PhysRevLett.87.071301.

[12] I. Esteban et al. "Global analysis of three-flavour neutrino oscillations: synergies and tensions in the determination of θ_{23}, δ_{CP}, and the mass ordering". *Journal of High Energy Physics* 01 (2019). DOI: 10.1007/JHEP01(2019)106.

[13] S.-K. Choi et al. "Observation of a narrow charmonium-like state in exclusive $B^+ \to K^+\pi^+\pi^- J/\psi$ decays". *Physical Review Letters* 91 (2003). DOI: 10.1103/physrevlett.91.262001.

[14] R. Aaij et al. "Observation of $J/\psi p$ Resonances Consistent with Pentaquark States in $\Lambda_b^0 \to J/\psi K^- p$ Decays". *Physical Review Letters* 115 (2015). DOI: 10.1103/PhysRevLett.115.072001.

[15] F. E. Wietfeldt et al. "The neutron lifetime". *Reviews of Modern Physics* 83 (2011). DOI: 10.1103/RevModPhys.83.1173.

[16] A. D. Martin et al. "Parton distributions for the LHC". *The European Physical Journal C* 63 (2009). DOI: 10.1140/epjc/s10052-009-1072-5.

[17] R. P. Feynman. "Very High-Energy Collisions of Hadrons". *Physical Review Letters* 23 (1969). DOI: 10.1103/PhysRevLett.23.1415.

[18] J. H. Christenson et al. "Evidence for the 2π Decay of the K_2^0 Meson". *Physical Review Letters* 13 (1964). DOI: 10.1103/PhysRevLett.13.138.

[19] C. S. Wu et al. "Experimental Test of Parity Conservation in Beta Decay". *Physical Review* 105 (1957). DOI: 10.1103/PhysRev.105.1413.

[20] C. S. Wu. "The discovery of the parity violation in weak interactions and its recent developments". *Lecture Notes in Physics* 746 (2008). DOI: 10.1007/978-4-431-77056-5_4.

[21] S. L. Glashow. "Partial-symmetries of weak interactions". *Nuclear Physics* 22 (1961). DOI: 10.1016/0029-5582(61)90469-2.

[22] J. Goldstone et al. "Broken Symmetries". *Physical Review* 127 (1962). DOI: 10.1103/PhysRev.127.965.

[23] P. W. Higgs. "Broken Symmetries and the Masses of Gauge Bosons". *Physical Review Letters* 13 (1964). DOI: 10.1103/PhysRevLett.13.508.

[24] F. Englert et al. "Broken Symmetry and the Mass of Gauge Vector Mesons". *Physical Review Letters* 13 (1964). DOI: 10.1103/PhysRevLett.13.321.

[25] G. Aad et al. "Observation of a new particle in the search for the Standard Model Higgs boson with the ATLAS detector at the LHC". *Physics Letters B* 716 (2012). DOI: 10.1016/j.physletb.2012.08.020.

[26] S. Chatrchyan et al. "Observation of a new boson at a mass of 125 GeV with the CMS experiment at the LHC". *Physics Letters B* 716 (2012). DOI: 10.1016/j.physletb.2012.08.021.

[27] D. J. Gross et al. "Ultraviolet Behavior of Non-Abelian Gauge Theories". *Physical Review Letters* 30 (1973). DOI: 10.1103/PhysRevLett.30.1343.

[28] H. D. Politzer. "Reliable Perturbative Results for Strong Interactions?" *Physical Review Letters* 30 (1973). DOI: 10.1103/PhysRevLett.30.1346.

[29] J. Bartke. *Introduction to Relativistic Heavy Ion Physics*. World Scientific Publishing, 2009. ISBN: 978-981-02-1241-5.

[30] K. G. Wilson. "Confinement of quarks". *Physical Review D* 10 (1974). DOI: 10.1103/PhysRevD.10.2445.

[31] B. Andersson et al. "Parton fragmentation and string dynamics". *Physics Reports* 97 (1983). DOI: 10.1016/0370-1573(83)90080-7.

[32] J. C. Collins et al. "Superdense Matter: Neutrons or Asymptotically Free Quarks?" *Physical Review Letters* 34 (1975). DOI: 10.1103/PhysRevLett.34.1353.

[33] N. Cabibbo et al. "Exponential hadronic spectrum and quark liberation". *Physics Letters B* 59 (1975). DOI: 10.1016/0370-2693(75)90158-6.

[34] E.V. Shuryak. "Quark-gluon plasma and hadronic production of leptons, photons and psions". *Physics Letters B* 78 (1978). DOI: 10.1016/0370-2693(78)90370-2.

[35] U. Heinz et al. *Evidence for a New State of Matter: An Assessment of the Results from the CERN Lead Beam Programme*. 2000. DOI: 10.48550/ARXIV.NUCL-TH/0002042.

[36] I. Arsene et al. "Quark–gluon plasma and color glass condensate at RHIC? The perspective from the BRAHMS experiment". *Nuclear Physics A* 757 (2005). First Three Years of Operation of RHIC. DOI: 10.1016/j.nuclphysa.2005.02.130.

[37] K. Adcox et al. "Formation of dense partonic matter in relativistic nucleus–nucleus collisions at RHIC: Experimental evaluation by the PHENIX Collaboration". *Nuclear Physics A* 757 (2005). First Three Years of Operation of RHIC. DOI: 10.1016/j.nuclphysa.2005.03.086.

[38] B.B. Back et al. "The PHOBOS perspective on discoveries at RHIC". *Nuclear Physics A* 757 (2005). First Three Years of Operation of RHIC. DOI: 10.1016/j.nuclphysa.2005.03.084.

[39] J. Adams et al. "Experimental and theoretical challenges in the search for the quark–gluon plasma: The STAR Collaboration's critical assessment of the evidence from RHIC collisions". *Nuclear Physics A* 757 (2005). First Three Years of Operation of RHIC. DOI: 10.1016/j.nuclphysa.2005.03.085.

[40] S. Mukherjee. *QCD phase diagram*. Online. 2016.

[41] D. Tlusty. *The RHIC Beam Energy Scan Phase II: Physics and Upgrades*. 2018. DOI: 10.48550/ARXIV.1810.04767.

[42] Y. Aoki et al. "The order of the quantum chromodynamics transition predicted by the standard model of particle physics". *Nature* 443 (2006). DOI: 10.1038/nature05120.

[43] A. Pandav et al. "Search for the QCD critical point in high energy nuclear collisions". *Progress in Particle and Nuclear Physics* 125 (2022). DOI: 10.1016/j.ppnp.2022.103960.

[44] A. Bazavov et al. "Chiral crossover in QCD at zero and non-zero chemical potentials". *Physics Letters B* 795 (2019). DOI: 10.1016/j.physletb.2019.05.013.

[45] H. Petersen et al. *MADAI collaboration (Models and Data Analysis Initiative): Different stages of the spacetime evolution of a heavy ion collision*. 2022.

[46] M. Kliemant et al. "Global Properties of Nucleus–Nucleus Collisions". *The Physics of the Quark-Gluon Plasma*. 2009. DOI: 10.1007/978-3-642-02286-9_2.

[47] M. L. Miller et al. "Glauber Modeling in High-Energy Nuclear Collisions". *Annual Review of Nuclear and Particle Science* 57 (2007). DOI: 10.1146/annurev.nucl.57.090506.123020.

[48] A. Kurkela et al. "Effective kinetic description of event-by-event pre-equilibrium dynamics in high-energy heavy-ion collisions". *Physical Review C* 99 (2019). DOI: 10.1103/physrevc.99.034910.

[49] T. Hirano et al. "Hydrodynamics and Flow". *The Physics of the Quark-Gluon Plasma*. 2009. DOI: 10.1007/978-3-642-02286-9_4.

[50] R. Pasechnik et al. "Phenomenological Review on Quark–Gluon Plasma: Concepts vs. Observations". *Universe* 3 (2017). DOI: 10.3390/universe3010007.

[51] J. D. Bjorken. "Highly relativistic nucleus-nucleus collisions: The central rapidity region". *Physical Review D* 27 (1983). DOI: 10.1103/PhysRevD.27.140.

[52] P. Romatschke et al. "Viscosity Information from Relativistic Nuclear Collisions: How Perfect is the Fluid Observed at RHIC?" *Physical Review Letters* 99 (2007). DOI: 10.1103/PhysRevLett.99.172301.

[53] U. Heinz et al. "Collective Flow and Viscosity in Relativistic Heavy-Ion Collisions". *Annual Review of Nuclear and Particle Science* 63 (2013). DOI: 10.1146/annurev-nucl-102212-170540.

[54] P. Braun-Munzinger et al. "Particle production in heavy ion collisions". *Quark-Gluon Plasma 3*. 2003. DOI: 10.1142/9789812795533_0008.

[55] S. Acharya et al. "Production of ^{4}He and $^{4}\overline{\mathrm{He}}$ in Pb–Pb collisions at $\sqrt{s_{\mathrm{NN}}} = 2.76$ TeV at the LHC". *Nuclear Physics A* 971 (2018). DOI: 10.1016/j.nuclphysa.2017.12.004.

[56] M. Rybar. *ATLAS Feature: Looking inside trillion degree matter*. 2022. URL: https://cds.cern.ch/images/ATLAS-PHOTO-2022-031-2.

[57] S. Acharya et al. "Direct observation of the dead-cone effect in quantum chromodynamics". *Nature* 605 (2022). DOI: 10.1038/s41586-022-04572-w.

[58] D. d'Enterria et al. "High-p_T Hadron Suppression and Jet Quenching". *The Physics of the Quark-Gluon Plasma*. 2009. ISBN: 978-3-642-02285-2. DOI: 10.1007/978-3-642-02286-9_9.

[59] X.-N. Wang et al. "Gluon shadowing and jet quenching in A+A collisions at $\sqrt{s}$ =200A GeV". *Physical Review Letters* 68 (1992). DOI: 10.1103/PhysRevLett.68.1480.

[60] S. Acharya et al. "Measurements of inclusive jet spectra in pp and central Pb-Pb collisions at $\sqrt{s_{\mathrm{NN}}} = 5.02$ TeV". *Physical Review C* 101 (2020). DOI: 10.1103/PhysRevC.101.034911.

[61] S. Acharya et al. "Prompt D^0, D^+, and D^{*+} production in Pb–Pb collisions at $\sqrt{s_{\mathrm{NN}}} = 5.02$ TeV". *Journal of High Energy Physics* 01 (2022). DOI: 10.1007/JHEP01(2022)174.

[62] P. P. Bhaduri et al. "An Introduction to the Spectral Analysis of the QGP". *The Physics of the Quark-Gluon Plasma*. 2009. DOI: 10.1007/978-3-642-02286-9_5.

[63] T. Matsui et al. "J/Ψ suppression by quark-gluon plasma formation". *Physics Letters B* 178 (1986). DOI: 10.1016/0370-2693(86)91404-8.

[64] S. Chatrchyan et al. "Observation of Sequential Y Suppression in PbPb Collisions". *Physical Review Letters* 109 (2012). DOI: 10.1103/physrevlett.109.222301.

[65] B. Abelev et al. "Multi-strange baryon production at mid-rapidity in Pb–Pb collisions at $\sqrt{s_{\mathrm{NN}}} = 5.02$ TeV". *Physics Letters B* 728 (2014). DOI: 10.1016/j.physletb.2013.11.048.

[66] J. Rafelski et al. "Strangeness Production in the Quark-Gluon Plasma". *Physical Review Letters* 48 (1982). DOI: 10.1103/PhysRevLett.48.1066.

[67] S. Acharya et al. "Production of charged pions, kaons, and (anti-)protons in Pb-Pb and inelastic pp collisions at $\sqrt{s_{NN}} = 5.02$ TeV". *Physical Review C* 101 (2020). DOI: 10.1103/PhysRevC.101.044907.

[68] U. Heinz. "Early Collective Expansion: Relativistic Hydrodynamics and the Transport Properties of QCD Matter". *Relativistic Heavy Ion Physics*. 2010. DOI: 10.1007/978-3-642-01539-7_9.

[69] B. Alver et al. "Collision-geometry fluctuations and triangular flow in heavy-ion collisions". *Physical Review C* 82 (2010). DOI: 10.1103/PhysRevC.82.039903.

[70] H. Mashui. *Elliptic flow – Expansion in plane*. Online. 2008.

[71] A. M. Poskanzer et al. "Methods for analyzing anisotropic flow in relativistic nuclear collisions". *Physical Review C* 58 (1998). DOI: 10.1103/physrevc.58.1671.

[72] H. Niemi et al. "Event-by-event distributions of azimuthal asymmetries in ultrarelativistic heavy-ion collisions". *Physical Review C* 87 (2013). DOI: 10.1103/physrevc.87.054901.

[73] J. Qian et al. "Mode-coupling effects in anisotropic flow in heavy-ion collisions". *Physical Review C* 93 (2016). DOI: 10.1103/physrevc.93.064901.

[74] S. Acharya et al. "Higher harmonic non-linear flow modes of charged hadrons in Pb-Pb collisions at $\sqrt{s_{\mathrm{NN}}} = 5.02$ TeV". *Journal of High Energy Physics* 05 (2020). DOI: 10.1007/JHEP05(2020)085.

[75] J. Noronha-Hostler et al. "Hydrodynamic predictions for 5.02 TeV Pb-Pb collisions". *Physical Review C* 93 (2016). DOI: 10.1103/physrevc.93.034912.

[76] H. Niemi et al. "Predictions for 5.023 TeV Pb+Pb collisions at the CERN Large Hadron Collider". *Physical Review C* 93 (2016). DOI: 10.1103/physrevc.93.014912.

[77] J. Adam et al. "Anisotropic flow of charged particles in Pb-Pb collisions at $\sqrt{s_{\mathrm{NN}}} = 5.02$ TeV". *Physical Review Letters* 116 (2016). DOI: 10.1103/PhysRevLett.116.132302.

[78] H. Niemi et al. "Event-by-event fluctuations in a perturbative QCD + saturation + hydrodynamics model: Determining QCD matter shear viscosity in ultrarelativistic heavy-ion collisions". *Physical Review C* 93 (2016). DOI: 10.1103/PhysRevC.93.024907.

[79] K.J. Eskola et al. "Scaling of transverse energies and multiplicities with atomic number and energy in ultrarelativistic nuclear collisions". *Nuclear Physics B* 570 (2000). DOI: 10.1016/S0550-3213(99)00720-8.

[80] A. Bilandzic et al. "Generic framework for anisotropic flow analyses with multiparticle azimuthal correlations". *Physical Review C* 89 (2014). DOI: 10.1103/physrevc.89.064904.

[81] G. Giacalone et al. "Symmetric cumulants and event-plane correlations in Pb+Pb collisions". *Physical Review C* 94 (2016). DOI: 10.1103/physrevc.94.014906.

[82] J. Adam et al. "Correlated Event-by-Event Fluctuations of Flow Harmonics in Pb-Pb Collisions at $\sqrt{s_{\mathrm{NN}}} = 2.76$ TeV". *Physical Review Letters* 117 (2016). DOI: 10.1103/physrevlett.117.182301.

[83] X.-N. Wang et al. "HIJING: A Monte Carlo model for multiple jet production in pp, pA, and AA collisions". *Physical Review D* 44 (1991). DOI: 10.1103/PhysRevD.44.3501.

[84] P. Huovinen et al. "Radial and elliptic flow at RHIC: further predictions". *Physics Letters B* 503 (2001). DOI: 10.1016/S0370-2693(01)00219-2.

[85] D. Molnár et al. "Elliptic Flow at Large Transverse Momenta from Quark Coalescence". *Physical Review Letters* 91 (2003). DOI: 10.1103/PhysRevLett.91.092301.

[86] S. Acharya et al. "Anisotropic flow of identified particles in Pb–Pb collisions at $\sqrt{s_{\mathrm{NN}}} = 5.02$ TeV". *Journal of High Energy Physics* 09 (2018). DOI: 10.1007/jhep09(2018)006.

[87] S. Chatrchyan et al. "Centrality dependence of dihadron correlations and azimuthal anisotropy harmonics in PbPb collisions at $\sqrt{s_{\mathrm{NN}}} = 2.76$ TeV". *The European Physical Journal C* 72 (2012). DOI: 10.1140/epjc/s10052-012-2012-3.

[88] V. Khachatryan et al. "Observation of long-range, near-side angular correlations in proton-proton collisions at the LHC". *Journal of High Energy Physics* 09 (2010). DOI: 10.1007/jhep09(2010)091.

[89] S. Chatrchyan et al. "Observation of long-range, near-side angular correlations in pPb collisions at the LHC". *Physics Letters B* 718 (2013). DOI: 10.1016/j.physletb.2012.11.025.

[90] T. Sjöstrand et al. "An introduction to PYTHIA 8.2". *Computer Physics Communications* 191 (2015). DOI: 10.1016/j.cpc.2015.01.024.

[91] J. Adam et al. "Enhanced production of multi-strange hadrons in high-multiplicity proton–proton collisions". *Nature Physics* 13 (2017). DOI: 10.1038/nphys4111.

[92] Z. Citron et al. *Future physics opportunities for high-density QCD at the LHC with heavy-ion and proton beams*. 2018. DOI: 10.48550/ARXIV.1812.06772.

[93] S. Acharya et al. "Investigations of Anisotropic Flow Using Multiparticle Azimuthal Correlations in pp, $p-Pb$, Xe-Xe, and Pb-Pb Collisions at the LHC". *Physical Review Letters* 123 (2019). DOI: 10.1103/PhysRevLett.123.142301.

[94] B. Schenke et al. "Fluctuating Glasma Initial Conditions and Flow in Heavy Ion Collisions". *Physical Review Letters* 108 (2012). DOI: 10.1103/physrevlett.108.252301.

[95] B. Schenke et al. "(3+1)D hydrodynamic simulation of relativistic heavy-ion collisions". *Physical Review C* 82 (2010). DOI: 10.1103/physrevc.82.014903.

[96] S. Bass et al. "Microscopic models for ultrarelativistic heavy ion collisions". *Progress in Particle and Nuclear Physics* 41 (1998). DOI: 10.1016/s0146-6410(98)00058-1.

[97] B. Schenke et al. “Running the gamut of high energy nuclear collisions”. *Physical Review C* 102 (2020). DOI: 10.1103/physrevc.102.044905.

[98] C. Aidala et al. “Creation of quark–gluon plasma droplets with three distinct geometries”. *Nature Physics* 15 (2019). DOI: 10.1038/s41567-018-0360-0.

[99] STAR Collaboration. “Measurements of the elliptic and triangular azimuthal anisotropies in central ^{3}He+Au, d+Au and p+Au collisions at $\sqrt{s_{\mathrm{NN}}}$ = 200 GeV” (2022). DOI: 10.48550/ARXIV.2210.11352.

[100] M. Habich et al. “Particle spectra and HBT radii for simulated central nuclear collisions of C + C, Al + Al, Cu + Cu, Au + Au, and Pb + Pb from $\sqrt{s_{\mathrm{NN}}} = 62.4 - 2760$ GeV”. *The European Physical Journal C* 75 (2015). DOI: 10.1140/epjc/s10052-014-3206-7.

[101] C. Shen et al. “Collectivity and electromagnetic radiation in small systems”. *Physical Review C* 95 (2017). DOI: 10.1103/PhysRevC.95.014906.

[102] B. Abelev et al. “Long-range angular correlations of π, K and p in p—Pb collisions at $\sqrt{s_{\mathrm{NN}}} = 5.02$ TeV”. *Physics Letters B* 726 (2013). DOI: 10.1016/j.physletb.2013.08.024.

[103] V. Khachatryan et al. “Evidence for collectivity in pp collisions at the LHC”. *Physics Letters B* 765 (2017). DOI: 10.1016/j.physletb.2016.12.009.

[104] CERN. *CERN Annual report 2020*. 2021. DOI: 10.17181/AnnualReport2020.

[105] E. Lopienska. *The CERN accelerator complex, layout in 2022*. 2022. URL: http://cds.cern.ch/record/2800984.

[106] L. Evans et al. “LHC Machine”. *Journal of Instrumentation* 3 (2008). DOI: 10.1088/1748-0221/3/08/S08001.

[107] E. Regenstreif. *The CERN Proton Synchrotron*. CERN Yellow Reports: Monographs. Geneva: CERN, 1959. ISBN: 020112078X. DOI: 10.5170/CERN-1959-029.

[108] V. Hatton. “Operational history of the SPS collider 1981-1990”. *Conference Record of the 1991 IEEE Particle Accelerator Conference*. 1991. DOI: 10.1109/PAC.1991.165151.

[109] X. C. Vidal et al. *Taking a closer look at LHC*. Online, accessed in May 2022. 2022. URL: www.lhc-closer.es.

[110] *LEP design report*. Geneva: CERN, 1984. URL: https://cds.cern.ch/record/102083.

[111] G. Aad et al. “The ATLAS Experiment at the CERN Large Hadron Collider”. *Journal of Instrumentation* 3 (2008). DOI: 10.1088/1748-0221/3/08/s08003.

[112] S. Chatrchyan et al. "The CMS experiment at the CERN LHC". *Journal of Instrumentation* 3 (2008). DOI: 10.1088/1748-0221/3/08/s08004.

[113] A. A. Alves et al. "The LHCb Detector at the LHC". *Journal of Instrumentation* 3 (2008). DOI: 10.1088/1748-0221/3/08/s08005.

[114] K. Aamodt et al. "The ALICE experiment at the CERN LHC". *Journal of Instrumentation* 3 (2008). DOI: 10.1088/1748-0221/3/08/S08002.

[115] ALICE Collaboration. *Letter of Intent for A Large Ion Collider Experiment [ALICE]*. 1993. URL: http://cds.cern.ch/record/290825.

[116] ALICE Collaboration. *ALICE: Technical proposal for a large ion collider experiment at the CERN LHC*. 1995. URL: http://cds.cern.ch/record/293391.

[117] P. Cortese et al. *ALICE forward detectors: FMD, TO and VO: Technical Design Report*. 2004. URL: https://cds.cern.ch/record/781854.

[118] B. Abelev et al. "Centrality determination of Pb–Pb collision at $\sqrt{s_{\mathrm{NN}}} = 2.76$ TeV with ALICE". *Physical Review C* 88 (2013). DOI: 10.1103/physrevc.88.044909.

[119] S. Acharya et al. "Pseudorapidity distributions of charged particles as a function of mid- and forward rapidity multiplicities in pp collisions at $\sqrt{s} = 5.02$, 7, 13 TeV". *The European Physical Journal C* 81 (2021). DOI: 10.1140/epjc/s10052-021-09349-5.

[120] J. Alme et al. "The ALICE TPC, a large 3-dimensional tracking device with fast readout for ultra-high multiplicity events". *Nuclear Instruments and Methods in Physics Research Section A: Accelerators, Spectrometers, Detectors and Associated Equipment* 622 (2010). DOI: 10.1016/j.nima.2010.04.042.

[121] G. Renault et al. "The Laser of the ALICE Time Projection Chamber". *International Journal of Modern Physics E* 16 (2007). DOI: 10.1142/S0218301307008021.

[122] W. Yu. "Particle identification of the ALICE TPC via dE/dx". *Nuclear Instruments and Methods in Physics Research Section A: Accelerators, Spectrometers, Detectors and Associated Equipment* 706 (2013). DOI: 10.1016/j.nima.2012.05.022.

[123] F. Carnesecchi. "Performance of the ALICE Time-Of-Flight detector at the LHC". *Journal of Instrumentation* 14 (2019). DOI: 10.1088/1748-0221/14/06/c06023.

[124] Z. Moravcova. *Analysis of the TOF single-channel performance by using cosmic rays triggered in the ALICE experiment during the 2016/17 data taking campaign*. 2018. URL: http://cds.cern.ch/record/2635967.

[125] P. Antonioli et al. *Upgrade of the ALICE Readout and Trigger System*. 2013. URL: https://cds.cern.ch/record/1603472.

[126] B. Abelev et al. *Technical Design Report for the Upgrade of the ALICE Inner Tracking System*. 2013. DOI: 10.1088/0954-3899/41/8/087002.

[127] F. Reidt. "Upgrade of the ALICE ITS detector". *Nuclear Instruments and Methods in Physics Research Section A: Accelerators, Spectrometers, Detectors and Associated Equipment* 1032 (2022). DOI: 10.1016/j.nima.2022.166632.

[128] ALICE Collaboration. *Addendum to the Technical Design Report for the Upgrade of the ALICE Time Projection Chamber*. 2015. URL: https://cds.cern.ch/record/1984329.

[129] FIT Collaboration. *Fast Interaction Trigger*. Online, accessed in July 2022. URL: https://alice-collaboration.web.cern.ch/menu_proj_items/FIT.

[130] ALICE Collaboration. *Addendum of the Letter of Intent for the upgrade of the ALICE experiment : The Muon Forward Tracker*. 2013. URL: http://cds.cern.ch/record/1592659.

[131] N. Borghini et al. "Flow analysis from multiparticle azimuthal correlations". *Physical Review C* 64 (2001). DOI: 10.1103/PhysRevC.64.054901.

[132] N. Borghini et al. "New method for measuring azimuthal distributions in nucleus-nucleus collisions". *Physical Review C* 63 (2001). DOI: 10.1103/PhysRevC.63.054906.

[133] A. Bilandzic et al. "Flow analysis with cumulants: Direct calculations". *Physical Review C* 83 (2011). DOI: 10.1103/physrevc.83.044913.

[134] Z. Moravcova et al. "Generic algorithm for multiparticle cumulants of azimuthal correlations in high energy nucleus collisions". *Physical Review C* 103 (2021). DOI: 10.1103/physrevc.103.024913.

[135] ALICE Collaboration. *Anisotropic flow and flow fluctuations of identified hadrons in Pb−Pb collisions at* $\sqrt{s_{\mathrm{NN}}} = 5.02$ *TeV*. 2022. DOI: 10.48550/ARXIV.2206.04587.

[136] S. A. Voloshin et al. "Elliptic flow in the Gaussian model of eccentricity fluctuations". *Physics Letters B* 659 (2008). DOI: 10.1016/j.physletb.2007.11.043.

[137] J. L. Gramling. *Two-track resolution effects for HBT analyses in ALICE*. 2011. URL: https://cds.cern.ch/record/1419204.

[138] U. Heinz et al. "Fluctuating flow angles and anisotropic flow measurements". *Physical Review C* 87 (2013). DOI: 10.1103/physrevc.87.034913.

[139] S. Acharya et al. "Searches for transverse momentum dependent flow vector fluctuations in Pb–Pb and p–Pb collisions at the LHC". *Journal of High Energy Physics* 09 (2017). DOI: 10.1007/jhep09(2017)032.

[140] C. Adler et al. "Elliptic flow from two- and four-particle correlations in Au+Au collisions at $\sqrt{s_{\mathrm{NN}}} = 130$ GeV". *Physical Review C* 66 (2002). DOI: 10.1103/physrevc.66.034904.

[141] Y. Zhou et al. "Investigation of possible hadronic flow in $\sqrt{s_{NN}} = 5.02$ TeV $p - Pb$ collisions". *Physical Review C* 91 (2015). DOI: 10.1103/PhysRevC.91.064908.

[142] J. Jia et al. "Revealing long-range multiparticle collectivity in small collision systems via subevent cumulants". *Physical Review C* 96 (2017). DOI: 10.1103/physrevc.96.034906.

[143] M. Aaboud et al. "Measurement of long-range multiparticle azimuthal correlations with the subevent cumulant method in pp and p+Pb collisions with the ATLAS detector at the CERN Large Hadron Collider". *Physical Review C* 97 (2018). DOI: 10.1103/physrevc.97.024904.

[144] V. Pacík. *Investigation of azimuthal anisotropy using multi-partice correlations of identified hadrons at the LHC with ALICE detector*. PhD thesis. 2020.

[145] G. Aad et al. "Observation of Long-Range Elliptic Azimuthal Anisotropies in $\sqrt{s} = 13$ and 2.76 TeV pp Collisions with the ATLAS Detector". *Physical Review Letters* 116 (2016). DOI: 10.1103/PhysRevLett.116.172301.

[146] M. Aaboud et al. "Correlated long-range mixed-harmonic fluctuations measured in pp, p+Pb and low-multiplicity Pb+Pb collisions with the ATLAS detector". *Physics Letters B* 789 (2019). DOI: 10.1016/j.physletb.2018.11.065.

[147] S. Acharya et al. "Multiplicity dependence of charged-particle jet production in pp collisions at $\sqrt{s} = 13$ TeV". *The European Physical Journal C* 82 (2022). DOI: 10.1140/epjc/s10052-022-10405-x.

[148] ALICE Collaboration. *ALICE Analysis Repository*. URL: https://github.com/alisw/AliPhysics.

[149] R. Brun et al. "ROOT - An Object Oriented Data Analysis Framework". Version v6-18-02. *Nuclear Instruments and Methods in Physics Research Section A: Accelerators, Spectrometers, Detectors and Associated Equipment* 389 (1996). DOI: 10.5281/zenodo.3895860.

[150] Y. Sekiguchi. "Measurement of long-range two- and multi-particle correlations by ALICE". *Nuclear Physics A* 1005 (2021). DOI: 10.1016/j.nuclphysa.2020.121795.

[151] S. Acharya et al. "Pseudorapidity distributions of charged particles as a function of mid- and forward rapidity multiplicities in pp collisions at *sqrts* = 5.02, 7 and 13 TeV". *The European Physical Journal C* 81 (2021). DOI: 10.1140/epjc/s10052-021-09349-5.

[152] J. Adam et al. “Centrality dependence of particle production in $p-\mathrm{Pb}$ collisions at $\sqrt{s_{NN}} = 5.02$ TeV”. *Physical Review C* 91 (2015). DOI: 10.1103/PhysRevC.91.064905.

[153] J. Adam et al. “Particle identification in ALICE: a Bayesian approach”. *The European Physical Journal Plus* 131 (2016). DOI: 10.1140/epjp/i2016-16168-5.

[154] T. Pierog et al. “EPOS LHC: Test of collective hadronization with data measured at the CERN Large Hadron Collider”. *Physical Review C* 92 (2015). DOI: 10.1103/physrevc.92.034906.

[155] S. Agostinelli et al. “Geant4—a simulation toolkit”. *Nuclear Instruments and Methods in Physics Research Section A: Accelerators, Spectrometers, Detectors and Associated Equipment* 506 (2003). DOI: 10.1016/S0168-9002(03)01368-8.

[156] A. Maire. *Topological selections for V0 (K0s, Lambda) and Cascade (Xi, Omega) reconstruction in ALICE*. 2011. URL: https://cds.cern.ch/record/2030272.

[157] J. Podolanski et al. “III. Analysis of V-events”. *The London, Edinburgh, and Dublin Philosophical Magazine and Journal of Science* 45 (1954). DOI: 10.1080/14786440108520416.

[158] S. Acharya et al. “Multiplicity dependence of light-flavor hadron production in pp collisions at $\sqrt{s} = 7$ TeV”. *Physical Review C* 99 (2019). DOI: 10.1103/physrevc.99.024906.

[159] K. Aamodt et al. “Elliptic flow of charged particles in Pb-Pb collisions at 2.76 TeV”. *Physical Review Letters* 105 (2010). DOI: 10.1103/PhysRevLett.105.252302.

[160] S. Roesler et al. “The Monte Carlo event generator DPMJET-III”. *International Conference on Advanced Monte Carlo for Radiation Physics, Particle Transport Simulation and Applications (MC 2000)*. 2000. DOI: 10.1007/978-3-642-18211-2_166.

[161] Z.-W. Lin et al. “A Multi-Phase Transport Model for Relativistic Heavy Ion Collisions”. *Physical Review C* 72 (2005). DOI: 10.1103/physrevc.72.064901.

[162] C. H. Christensen. *Bootstrap: Estimate statistical uncertainties*. 2020. URL: cholmcc.gitlab.io/nbi-python.

[163] R. Barlow. *Systematic Errors: facts and fictions*. 2002. DOI: 10.48550/ARXIV.HEP-EX/0207026.

[164] S. Acharya et al. “K^0_S- and (anti-)Λ-hadron correlations in pp collisions at $\sqrt{s} = 13$ TeV”. *The European Physical Journal C* 81 (2021). DOI: 10.1140/epjc/s10052-021-09678-5.

[165] S. Acharya et al. “Energy dependence and fluctuations of anisotropic flow in Pb-Pb collisions at $\sqrt{s_{\mathrm{NN}}} = 5.02$ and 2.76 TeV”. *Journal of High Energy Physics* 102 (2018). DOI: 10.1007/JHEP07(2018)103.

[166] G. Giacalone et al. “Skewness of elliptic flow fluctuations”. *Physical Review C* 95 (2017). DOI: 10.1103/physrevc.95.014913.

[167] S. Acharya et al. “Measurements of mixed harmonic cumulants in Pb–Pb collisions at $\sqrt{s_{\rm NN}} = 5.02$ TeV”. *Physics Letters B* 818 (2021). DOI: 10.1016/j.physletb.2021.136354.

[168] M. Li et al. “Investigations on mixed harmonic cumulants in heavy-ion collisions at energies available at the CERN Large Hadron Collider”. *Physical Review C* 104 (2021). DOI: 10.1103/PhysRevC.104.024903.

[169] C. Shen et al. “The iEBE-VISHNU code package for relativistic heavy-ion collisions”. *Computer Physics Communications* 199 (2016). DOI: 10.1016/j.cpc.2015.08.039.

[170] Wenbin Z. et al. “Collective flow in 2.76 and 5.02 A TeV Pb+Pb collisions”. *The European Physical Journal C* 77 (2017). DOI: 10.1140/epjc/s10052-017-5186-x.

[171] J. C. Moreland et al. “Alternative ansatz to wounded nucleon and binary collision scaling in high-energy nuclear collisions”. *Physical Review C* 92 (2015). DOI: 10.1103/PhysRevC.92.011901.

[172] J. E. Bernhard et al. “Bayesian estimation of the specific shear and bulk viscosity of quark–gluon plasma”. *Nature Physics* 15 (2019). DOI: 10.1038/s41567-019-0611-8.

[173] J. E. Bernhard et al. “Applying Bayesian parameter estimation to relativistic heavy-ion collisions: Simultaneous characterization of the initial state and quark-gluon plasma medium”. *Physical Review C* 94 (2016). DOI: 10.1103/PhysRevC.94.024907.

[174] H.-J. Xu et al. “High-order flow harmonics of identified hadrons in 2.76A TeV Pb + Pb collisions”. *Physical Review C* 93 (2016). DOI: 10.1103/PhysRevC.93.064905.

[175] R. S. Bhalerao et al. “Collective flow in event-by-event partonic transport plus hydrodynamics hybrid approach”. *Physical Review C* 92 (2015). DOI: 10.1103/PhysRevC.92.014903.

[176] S. S. Adler et al. “Elliptic Flow of Identified Hadrons in Au+Au collisions at $sqrts_{\rm NN} = 200$ GeV”. *Physical Review Letters* 91 (2003). DOI: 10.1103/PhysRevLett.91.182301.

[177] J. Adams et al. “Particle-Type Dependence of Azimuthal Anisotropy and Nuclear Modification of Particle Production in Au+Au collisions at $sqrts_{\rm NN} = 200$ GeV”. *Physical Review Letters* 92 (2004). DOI: 10.1103/PhysRevLett.92.052302.

[178] W. Zhao et al. "From Hydrodynamics to Jet Quenching, Coalescence, and Hadron Cascade: A Coupled Approach to Solving the R_{AA} x v_2 puzzle". *Physical Review Letters* 128 (2022). DOI: 10.1103/physrevlett.128.022302.

[179] W. Chen et al. "Medium modification of γ-jet fragmentation functions in Pb+Pb collisions at LHC". *Physics Letters B* 810 (2020). DOI: 10.1016/j.physletb.2020.135783.

[180] H. Song et al. "Suppression of elliptic flow in a minimally viscous quark–gluon plasma". *Physics Letters B* 658 (2008). DOI: 10.1016/j.physletb.2007.11.019.

[181] X.-N. Wang et al. "Medium Modification of γ Jets in High-Energy Heavy-Ion Collisions". *Physical Review Letters* 111 (2013). DOI: 10.1103/PhysRevLett.111.062301.

[182] Y. He et al. "Linear Boltzmann transport for jet propagation in the quark-gluon plasma: Elastic processes and medium recoil". *Physical Review C* 91 (2015). DOI: 10.1103/PhysRevC.91.054908.

[183] W. Zhao et al. "Probing the Partonic Degrees of Freedom in High-Multiplicity p–Pb collisions at $\sqrt{s_{\mathrm{NN}}} = 5.02$ TeV". *Physical Review Letters* 125 (2020). DOI: 10.1103/PhysRevLett.125.072301.

[184] J. Adam et al. "Multiplicity dependence of charged pion, kaon, and (anti)proton production at large transverse momentum in p–Pb collisions at $\sqrt{s_{\mathrm{NN}}} = 5.02$ TeV". *Physics Letters B* 760 (2016). DOI: 10.1016/j.physletb.2016.07.050.

[185] Z.-W. Lin et al. "Partonic effects on the elliptic flow at relativistic heavy ion collisions". *Physical Review C* 65 (2002). DOI: 10.1103/PhysRevC.65.034904.

[186] A. Bzdak et al. "Elliptic and Triangular Flow in p+Pb and Peripheral Pb+Pb Collisions from Parton Scatterings". *Physical Review Letters* 113 (2014). DOI: 10.1103/physrevlett.113.252301.

[187] ALICE Collaboration. *Future high-energy pp programme with ALICE*. 2020. URL: https://cds.cern.ch/record/2724925.

[188] ALICE Collaboration. *ALICE physics projections for a short oxygen-beam run at the LHC*. 2021. URL: https://cds.cern.ch/record/2765973.